Cosmic-Ray Positron Fraction Measurement with the AMS-02 Detector

Ignacio Cernuda Cangas

Cosmic-Ray Positron Fraction Measurement with the AMS-02 Detector

Medida de la fracción de positrones en los rayos cósmicos con el detector AMS-02

Ignacio Cernuda Cangas

Doctoral Dissertation in Physics

Advisor: Dr. Jorge Casaus Armentano

Ciemat
Centro de Investigaciones Energéticas, Medioambientales y Tecnológicas

Cover Image Credits: NASA, CERN and High School Teachers Programme at CERN.
http://teachers.web.cern.ch/teachers/archiv/hst2002/bubblech/mbitu/electron-positron.htm

UNIVERSIDAD COMPLUTENSE DE MADRID
FACULTAD DE CIENCIAS FÍSICAS
DEPARTAMENTO DE FÍSICA ATÓMICA, MOLECULAR Y NUCLEAR

Memoria de investigación presentada para optar al título de Doctor en Ciencias Físicas

Cosmic-Ray Positron Fraction Measurement with the AMS-02 Detector

Medida de la fracción de positrones en los rayos cósmicos con el detector AMS-02

CANDIDATO A LA OBTENCION DEL TITULO DE DOCTOR:
Ignacio Cernuda Cangas

TESIS DOCTORAL DIRIGIDA POR : *Dr. Jorge Casaus Armentano*

Curso Académico: 2013-2014

Ciemat
Centro de Investigaciones
Energéticas, Medioambientales
y Tecnológicas

Those are my principles, and if you don't like them...
-well, I have others.

–Groucho Marx

Abstract

The study of Cosmic-Rays has proved to be of utmost importance in the understanding of the processes that govern our galaxy and has became a privileged field for the discovery of new physics.

The current availability of precision measurements in a number of recent experiments such as PAMELA or Fermi, and in particular AMS-02, has provided a unique opportunity to challenge the theoretical framework that builds our comprehension of Nature. Certainly, the recent advent of new data on Cosmic-Ray electrons and positrons has raised disagreements with our current knowledge of production and propagation of Cosmic-Rays. The observation of an excess in the Cosmic-Ray electron spectrum has triggered enormous efforts to understand the origin of this anomaly, both from the theoretical and experimental points of view.

In this context, AMS is a long awaited program, that among other objectives, will provide the most accurate measurement of the Cosmic-Ray electron spectrum, making possible to investigate a fundamental open question in particle astrophysics: the physical nature of the Dark Matter content of our galaxy.

The aim of this thesis is to contribute towards this direction from two complementary perspectives:

- From a purely phenomenological point of view, a method to discriminate an exotic contribution to the Cosmic-Ray electron spectrum from an astrophysical one is presented.
- A detailed analysis of the positron fraction with the AMS-02 detector has been carried out, providing the most precise measurement to date in the energy range of 2-350 GeV.

Finally, the ideas presented in the first part of this work are used to inspect the AMS-02 positron fraction measurement.

The outline of this thesis is as follows:

1. **Chapter 1** : This chapter presents an introduction to Cosmic-Ray physics and the problem of Dark Matter with emphasis on indirect Dark Matter detection.

2. **Chapter 2** : In this chapter, potential tests to probe the Cosmic-Ray electron anomalies are presented, and in particular, the potential imprint in the Cosmic-Ray electron arrival directions from DM annihilation and from a collection of astrophysical sources is investigated.

3. **Chapter 3** : This chapter introduces the AMS experiment. A general overview of the AMS-02 detector is followed by a deeper description of the most relevant sub-detectors used in the data analysis.

4. **Chapter 4** : In this chapter, the detector performances for e/p separation are presented for each of the sub-detectors used in the positron fraction analysis: The transition radiation detector, the electromagnetic calorimeter, and tracker detector.

5. **Chapter 5** : The study of the positron fraction is described using four separate analysis. The chapter concludes with the estimation of systematic errors and summary of the results.

6. **Chapter 6** : This chapter is devoted to the phenomenological analysis of the positron excess measured in the previous chapter. Temporal, spatial and spectral features are searched for, and simple models are used to diagnose the excess.

7. **Conclusions and outlook** : A brief summary of the methodology and results, and prospects of future work.

8. **Appendix A** : A description of the shower shape selection with the calorimeter is presented.

9. **Appendix B** : This appendix contains the positron fraction results for the different tracker pattern configurations.

10. **Appendix C** : In this appendix, a comparison with the AMS-02 positron fraction publication result is reflected.

11. **Appendix D** : This appendix contains auxiliary tables from the positron fraction analysis.

List of Selected Publications

The work reported in this thesis has profited to several publications, including peer-reviewed papers and conference reports. This list is not a complete record of the author's publications but rather an abbreviated summary of the works related to the thesis topic.

- AMS Collaboration, "First Result from the Alpha Magnetic Spectrometer on the International Space Station: Precision Measurement of the Positron Fraction in Primary Cosmic Rays of 0.5–350 GeV", *Phys. Rev. Lett.*, vol. 110, p. 141102, Apr 2013.
- I. Cernuda, "Cosmic ray electron Anisotropies as a tool to discriminate between Exotic and Astrophysical sources", *Astropart.Phys.*, vol. 34, pp. 59–69, 2010.
- I. Cernuda, "Anisotropies in the Cosmic-ray electron spectrum: A way to discriminate between exotic and astrophysical sources?", in *Cosmic Rays for Particle and Astroparticle Physics*, vol. 6 of *Proceedings of the 12th ICATPP Conference*, pp. 449–455, World Scientific, 2010.
- I. Cernuda, "Estudio de anisotropías en la difusión de electrones galácticos", in *Simposio de Física de Altas Energías y Física Teórica*, vol. 32 of *Proceedings of the XXXII Bienal de la Real Sociedad Española de Física*, pp. 220–221, 2009.
- A. Kounine on behalf of the AMS Collaboration, "Precision measurement of the positron fraction with AMS", in *Procceedings of the 33rd International Cosmic Ray Conference*, July 2013.
- J. Casaus on behalf of the AMS Collaboration, "Determination of the positron anisotropy with AMS", in *Procceedings of the 33rd International Cosmic Ray Conference*, July 2013.
- M. Aguilar *et al.*, "Relative Composition and Energy Spectra of Light Nuclei in Cosmic Rays. Results from AMS-01", *Astrophys.J.*, vol. 724, pp. 329–340, 2010.

- M. Aguilar et al., “Isotopic composition of light nuclei in cosmic rays: Results from AMS-01”, *The Astrophysical Journal*, vol. 736, no. 2, p. 105, 2011.
- M. Aguilar, L. Arruda, F. Barao, G. Barreira, A. Barrau, *et al.*, “In-beam aerogel light yield characterization for the AMS RICH detector”, *Nucl.Instrum.Meth.*, vol. A614, pp. 237–249, 2010.
- R. Pereira, “The AMS-02 RICH detector: Performance during ground-based data taking at CERN”, *Nuclear Instruments and Methods in Physics Research Section A: Accelerators, Spectrometers, Detectors and Associated Equipment*, vol. In Press, Corrected Proof, pp. –, 2010.

Contents

Abstract **i**

List of figures **viii**

List of tables **xiii**

I The Positron Fraction Phenomenology **1**

1 Introduction **3**
1.1 Cosmic Rays . . . 3
1.1.1 Spectrum and Composition . . . 4
1.1.2 Production and Acceleration . . . 6
1.1.3 Anisotropies . . . 6
1.2 Cosmic Rays in Near Earth Orbit . . . 8
1.2.1 Solar Modulation . . . 8
1.2.2 Earth Magnetic Field . . . 9
1.3 Antimatter in Cosmic Rays . . . 10
1.3.1 The Positron Fraction . . . 12
1.3.2 Dark Matter Source of Cosmic Ray $e^{\pm}$ . . . 14
1.3.3 Astrophysical Sources of Cosmic Ray $e^{\pm}$ . . . 18

2 Signatures in the Electron and Positron Spectra **21**
2.1 Introduction . . . 21
2.2 Cosmic Ray Electron and Positron Propagation . . . 22
2.3 Astrophysical Sources of High Energy Positrons . . . 24
2.4 Dark Matter Source of High Energy Positrons . . . 30

2.5 Anisotropies 36
2.6 Conclusions 42

II The AMS Experiment 42

3 The AMS Experiment 45
3.1 Introduction 45
3.2 The Precursor Flight 47
3.3 Second Phase: The AMS-02 Detector 50
3.3.1 The Permanent Magnet 52
3.3.2 The Silicon Tracker Detector (STD) 52
3.3.3 The Transition Radiation Detector (TRD) 54
3.3.4 The Time of Flight (TOF) 55
3.3.5 The Ring Imaging Cherenkov (RICH) 56
3.3.6 The Anti Coincidence Counter (ACC) 57
3.3.7 The Electromagnetic Calorimeter (ECAL) 57

4 Performances of AMS-02 Detector for e/p Rejection 61
4.1 Introduction 61
4.2 Data Sample 62
4.3 Data Preselection 62
4.4 The Electromagnetic Calorimeter 65
4.4.1 Introduction 65
4.4.2 Selection 67
4.5 The Transition Radiation Detector 75
4.5.1 Selection 75
4.6 Combined performances for e-p rejection 77

5 Determination of the Positron Fraction 81
5.1 Introduction 81
5.2 Positron Fraction Determination 82
5.3 Strategy of the Analysis 83
5.3.1 Event-Counting Method 84
5.3.2 Template-Fitting Method 84
5.4 Corrections 85
5.4.1 Sample Purity 85
5.4.2 Charge Confusion 87
5.5 Positron Fraction Determination with the Event Counting Method 93

5.5.1 Stability of the Result . . . 94
5.6 Positron Fraction Determination with the Template Fitting Method . . . 98
5.7 Additional Systematic Uncertainties . . . 103
5.7.1 Charge Confusion . . . 103
5.7.2 Detector Acceptance . . . 105
5.7.3 Rigidity Cutoff . . . 108
5.7.4 Bin to Bin Migration . . . 109
5.8 Summary and Results . . . 109

III Diagnosis of an Excess 111

6 Characterization of the Positron Excess 119
6.1 Positron Fraction Stability in Time . . . 119
6.2 Spectral Structures . . . 121
6.3 Anisotropy . . . 122
6.3.1 Anisotropy on e^+/e^- . . . 122
6.3.2 Dipole Anisotropy . . . 124
6.3.3 Seasonal Excess . . . 126
6.4 Physics Models . . . 128
6.4.1 Minimal Model . . . 128
6.4.2 Dark Matter Source Scenario . . . 129
6.4.3 Pulsar Source Scenario . . . 130
6.4.4 Anisotropy Expectations . . . 132
6.4.5 Physics Interpretation within the Minimal Model . . . 133

Conclusions and Outlook 135

Acknowledgments 139

Appendices 141

A The Shower Shape Selection 143
A.1 Mip-Finder . . . 143
A.2 Shower Maximum . . . 147
A.3 Longitudinal Leakage . . . 148
A.4 Average Hit Energy . . . 149
A.5 Moliere Radius . . . 150

A.6 Shower Longitudinal Dispersion 151
A.7 Shower FootPrint 152
A.8 Energy Deposited in First 2 Layers 154
A.9 Energy Fraction in 2 Cells around Shower Center of Gravity 155

B Positron Fraction by Track Patterns **157**

C The AMS-02 Positron Fraction Publication **171**
C.1 Comparison with the Published Result 172
C.2 Minimal Model 175

D Tables **177**

Bibliography **185**

List of Figures

1.1 CR Abundances and Hillas Plot 4
1.2 CR Spectrum 5
1.3 Anisotropy Measurements 7
1.4 Antiproton Fluxes 11
1.5 Antimatter Fluxes 12
1.6 Positron Fraction Measurements 13
1.7 Dark Matter Distribution 16
1.8 Fermi LAT Sources Catalog 18

2.1 Pulsar Fluxes 27
2.2 Pulsar Contributions to Positron Spectra and Positron Fraction 28
2.3 Decays Spectra 33
2.4 Dark Matter Contribution to Positron Spectrum and Positron Fraction 35
2.5 Dark Matter Clump Contribution to Positron Spectrum and Positron Fraction . . . 36
2.6 Anisotropy Sensitivity 38
2.7 Pulsar Model Anisotropy 39
2.8 Dipole Anisotropy for a Dark Matter Halo Scenario 40
2.9 Dipole anisotropy in a Dark Matter Clump Scenario 41

3.1 AMS-02 Detector Installed in the ISS Truss. 46
3.2 AMS-02 Number of Reconstructed Events 47
3.3 AMS-01 On Board the NASA Space Shuttle Discovery 48
3.4 AMS-01 $e^{\pm}$ Results 49
3.5 AMS-01 Antimatter Results 49
3.6 AMS-02 Zoom-In View at the ISS Truss. 50
3.7 AMS-02 Schematic Layout 51

3.8 AMS-02 Magnet . . . 52
3.9 AMS-02 Tracker . . . 53
3.10 AMS-02 TRD . . . 54
3.11 AMS-02 TOF . . . 55
3.12 AMS-02 RICH . . . 56
3.13 Anti-Coincidence Counter System . . . 57
3.14 AMS-02 ECAL . . . 58

4.1 Livetime and Geomagnetic Cutoff . . . 63
4.2 TRD Likelihood . . . 63
4.3 Ecal Shower Profiles . . . 66
4.4 Tagged Sample . . . 69
4.5 Ecal Moliere Distribution . . . 70
4.6 BDT Distribution . . . 71
4.7 E/P Distribution . . . 71
4.8 Shower Shape Selection Efficiencies . . . 73
4.9 BDT Selection Efficiencies . . . 74
4.10 TRD p.d.f.s and Likelihood . . . 76
4.11 TRD Selection Efficiencies . . . 77
4.12 Background Estimation . . . 79

5.1 Preselected Sample BDT-E/P . . . 84
5.2 Example of Purity Calculation . . . 86
5.3 Purities . . . 86
5.4 Spillover Monte Carlo Electrons . . . 87
5.5 E/P-TOF Charge . . . 88
5.6 χ^2 and E/|P| of Test Beam Electrons . . . 90
5.7 Charge Confusion Parametrization . . . 91
5.8 Weighted Charge Confusion . . . 92
5.9 Positron Backgrounds . . . 92
5.10 Cut-Based Positron Fraction . . . 93
5.11 Positron Fraction by Tracker Pattern . . . 94
5.12 Stability of the Result . . . 95
5.13 Positron Fraction RMS . . . 96
5.14 Cut-Based PF toyMC . . . 96
5.15 Systematic Error in Selection . . . 97
5.16 Template-Fitting Fit Examples . . . 98
5.17 Npos and Positron Fraction vs χ^2 . . . 99
5.18 Npos and Positron Fraction Template-Fitting . . . 100

5.19 Positron Fraction and Number of Positrons . . . 100
5.20 Positron Fraction in the Template-Fitting Analysis . . . 101
5.21 Statistical Fluctuations in the Template-Fitting analysis . . . 102
5.22 Systematic Error in the Selection . . . 102
5.23 Charge Confusion Uncertainty . . . 104
5.24 Charge Confusion Systematic Error . . . 104
5.25 $e^{\pm}$ Theta-Phi Dependence . . . 105
5.26 Positron Fraction vs Phi . . . 106
5.27 PF for Different Fiducidal Volumes . . . 107
5.28 PF Systematic Error due to an Asymmetry in the Acceptance . . . 107
5.29 $e^{\pm}$ in Geographical Coordinates . . . 108
5.30 Positron Fraction Cutoff Systematic Error . . . 109
5.31 Positron Fraction Errors . . . 110
5.32 Positron Fraction Result . . . 111

6.1 Positron Fraction Temporal Variation . . . 120
6.2 Positron Fraction Temporal Variation Probability . . . 120
6.3 Positron Fraction Fine Structure . . . 121
6.4 $e^{\pm}$ Sky Maps and e^{+}/e^{-} Relative Fluctuations . . . 123
6.5 Amplitudes a_{10} Obtained from Fits of a Dipole Contribution to the Data . . . 124
6.6 Results for the Dipole Coefficient C_1 . . . 125
6.7 AMS Upper Limits on the Dipole Anisotropy Parameter δ . . . 125
6.8 Dipole Coefficients C_1 in Seasonal Searches . . . 126
6.9 Positron Fraction Minimal Model . . . 128
6.10 Example of a Fit to AMS-02 Data for a Dark Matter Model . . . 130
6.11 Example of a Fit to AMS-02 Data for a Pulsar Model . . . 131
6.12 Dark Matter and Pulsar Model Fits χ^2 . . . 131
6.13 Anisotropy Models and AMS Upper Limits . . . 132
6.14 Primary Sources in the Minimal Model and Physics Models . . . 134

A.1 Optimization Example for the Shower Max Cut . . . 144
A.3 Mip Cut Efficiency . . . 145
A.2 Event Display Mip Finder . . . 146
A.4 Shower Maximum Cut Efficiency . . . 147
A.5 RearLeak Cut Efficiency . . . 148
A.6 Average Hit Energy Cut Efficiency . . . 149
A.7 Moliere Cut Efficiency . . . 150
A.8 Shower Longitudinal Dispersion Cut Efficiency . . . 151
A.9 Shower FootPrint Cut Efficiency . . . 153

A.10 Energy Deposition in the First Two Layers Cut Efficiency 154
A.11 Energy Fraction in Two Cells Cut Efficiency 155

C.1 AMS-02 Published Result on the Positron Fraction 171
C.2 Event-Counting Analysis for Both Ecal Selections 172
C.3 Template-Fitting Analysis for Both Ecal Selections 172
C.4 Relative Difference Between Analysis 173
C.5 Statistical Errors Comparison 173
C.6 BDT Selection: Number of Events/GeV Comparison 174
C.7 Shower Shape Selection: Number of Events/GeV Comparison 174
C.8 Positron Fraction Minimal Model Comparison with Published Result 175

List of Tables

2.1 Diffusion Setups 24
2.2 Pulsar Parameters 27
2.3 Gamma-Ray Pulsars from the ATNF Catalog 29
2.4 Parameters of the DM Halo 32
2.5 Anisotropy Dilution Factors 37

4.1 Preselection Efficiencies I 64
4.2 Preselection Efficiencies II 64

5.1 Cuts for Template Construction 87
5.2 Tracker Patterns 89
5.3 Positron Fraction with BDT Selection and Event-Counting 112
5.4 Positron Fraction with Shower Shape Selection and Event-Counting 113
5.5 Positron Fraction with Shower Shape Selection and Template-Fitting 114
5.6 Positron Fraction with BDT Selection and Template-Fitting 115

6.1 Dipole Anisotropy Upper Limits 125
6.2 Minimal Model Parameters 128

B.1 BDT Selection and Inner Tracker within P1 Acceptance 158
B.2 BDT Selection and Inner Tracker + P9 within P1 Acceptance 159
B.3 BDT Selection and Inner Tracker 160
B.4 BDT Selection and Inner Tracker + P1 + P9 161
B.5 BDT Selection and Inner Tracker Out of P1 Acceptance 162
B.6 BDT Selection and Inner Tracker + P9 Out of P1 Acceptance 163
B.7 Shower Shape Selection and Inner Tracker within P1 Acceptance 164
B.8 Shower Shape Selection and Inner Tracker + P9 within P1 Acceptance 165

B.9 Shower Shape Selection and Inner Tracker + P1 166
B.10 Shower Shape Selection and Inner Tracker + P1 + P9 167
B.11 Shower Shape Selection and Inner Tracker Out of P1 Acceptance 168
B.12 Shower Shape Selection and Inner Tracker + P9 Out of P1 Acceptance 169

C.1 Minimal Model Parameters Comparison 175

D.1 Raw data 177
D.2 BDT Selection: Weighted Results 179
D.3 Shower Shape Selection: Weighted Results 180
D.4 Template-Fitting. Shower Shape Selection. Weighted Results 181
D.5 Template-Fitting. BDT Selection. Weighted Results 182
D.6 Charge Confusion uncertainty 183

I

THE POSITRON FRACTION PHENOMENOLOGY

1 Introduction

THE fact that only a small fraction, just about 20%, of the matter content in the Universe is visible constitutes one of the most astounding results of modern cosmology. The remaining 80% is known as Dark Matter, and the path towards its identification, stands among the most important open problems in cosmology and particle physics. In an effort to improve our understanding of it, we study the particles impinging the Earth from outer space. These particles are known as Cosmic Rays, pervade the universe and carry information about the sources that gave birth to them and the path they follow. Their study is a promising tool to probe the unknown, and in particular the particle nature of Dark Matter.

✧ ✧ ✧

1.1 Cosmic Rays

The Earth's atmosphere is constantly bombarded by elementary particles and nuclei with energies spanning 12 orders of magnitude. From the least energetic ones with a few hundreds of MeV to the most energetic events observed with energies of 10^{12} GeV. This cosmic radiation is dubbed as Cosmic Rays (CR) and its existence has been known for a long time. First hints appeared in 1909 when Theodor Wulf first measured higher radiation levels at the top of the Eiffel Tower than at the ground. The discovery is attributed to Victor Hess by the balloon-borne observation of a increase of the ionization rate over the rate at ground level which was explained as *"The results of my observation are best explained by the assumption that a radiation of very great penetrating power enters our atmosphere from above."*.

Since then, a great deal of effort has been put into their study which in turn, has paid out with important advances in the field of particle physics and their interactions, with the discoveries of the positrons, muons, pions and the kaons among others in the 1930-1940s.

1.1.1 Spectrum and Composition

Cosmic rays are charged particles, essentially atomic nuclei and electrons. Many different species are observed at low Earth orbit. The nuclear component is composed of protons (87%), Helium (12%) and heavier nuclei (1%). A small fraction of electrons (1%) and antimatter (positrons and antiprotons) is also observed.

These species are found in a wide range of energy and have different origins. Cosmic rays that reach us unaltered from the sources are known as *primary* CR, whereas those which are the product of the inelastic collisions (spallation) of the primary counterpart with the Inter Stellar Medium (ISM) or from the decay of unstable species, are denoted as *secondary* cosmic rays.

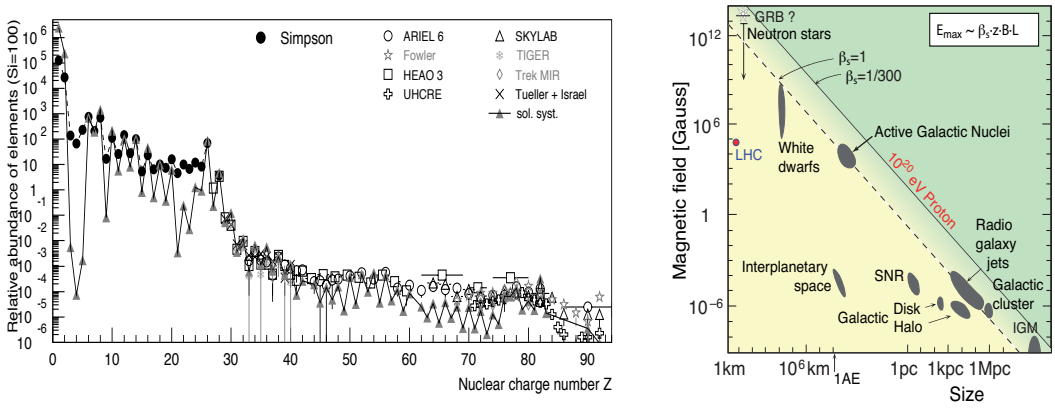

Figure 1.1: Cosmic Ray relative abundances compared to the solar system abundances of elements ([23]) (Left). Hillas Plot: Source's magnetic field strength vs source size for various maximum particles attainable energies E_{max} ([23])

Cosmic rays are a genuine sample of galactic matter. The ratios of the nuclear composition of CR are in good agreement with the relative abundance in the solar system. This is an indication that the production mechanism must be the same, namely fusion of light nuclei in the core of stars at the end of their life cycle. Deviations occur however for some elements, in the Li-Be-B group ($3 \leq Z \leq 5$) and the Sub-Iron group ($22 \leq Z \leq 25$), where an over-abundance is found in CR with respect the solar system (Fig.1.1).

Two effects may play a role in the CR composition in the Galaxy:

- The odd-even effect: Even-even nuclei (even Z and N) are more stable than odd-even and odd-odd nuclei, hence are more copiously produced in the stellar nucleosynthesis. It has been suggested then that peaks in the C,N,O and Fe are of stellar origin.
- Even-nuclei spallation may contribute to the secondary production of lighter nuclei. In fact, Li-Be-B are products of the spallation of carbon and oxygen in the ISM.

In particular, this last point provides an estimate of the average transversed matter, or *grammage*

of a few tens of g/cm^2 that primaries must traverse in order to produce the observed secondaries. In addition, the ratios of secondaries-to-primaries such as B/C constitute an important piece of information to constrain propagation models of CR.

The energy spectrum of cosmic rays is well described by a steeply falling power law:

$$\frac{\mathrm{dN(E)}}{\mathrm{dE}} = k\mathrm{E}^{-\gamma}, \tag{1.1}$$

with a spectral index $\gamma \sim 2.7$ up to 10^6 GeV/nucleon that steepens to $\gamma \sim 3$ for energies above (Fig. 1.2). This implies a very fast decreasing particle rate. For instance , the particle flux at 100 GeV is roughly 1 particle/$\mathrm{m^2 s}$ and about 1 particle/$\mathrm{m^2 yr}$ at $10^7 GeV$ and just 1 particle/$\mathrm{Km^2 yr}$ at $10^{10} GeV$.

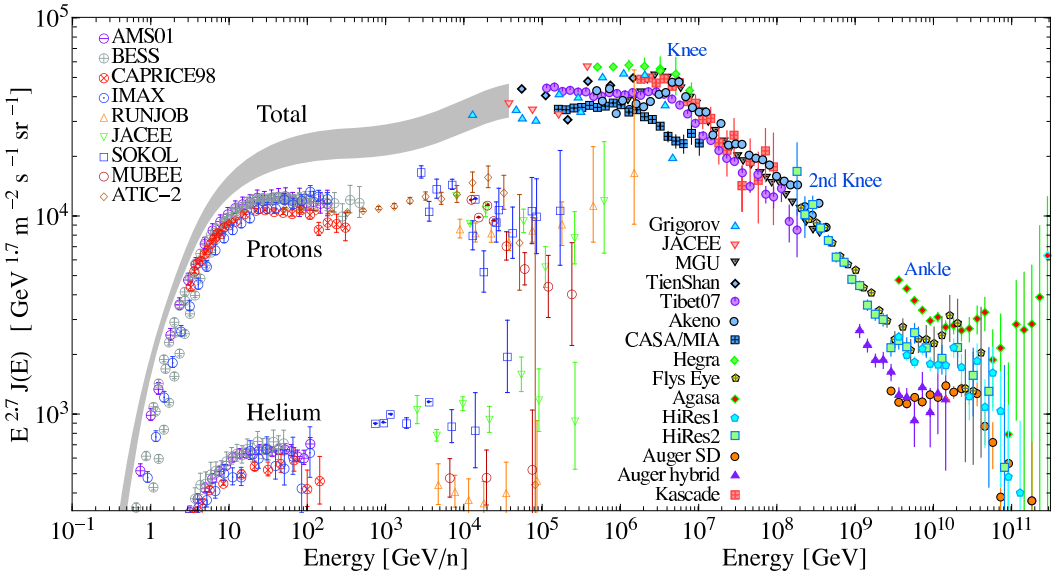

`Figure 1.2:` Cosmic Ray Flux scaled by $E^{2.7}$ from [86]

At the very first part of the spectrum, from a few eV to $\sim$ 1GeV, cosmic rays are produced locally and have a solar origin. They essentially constitute the solar wind. Cosmic rays from $\sim$ 1GeV up to 3×10^6 GeV/nucleon have a spectral index $\gamma \sim 2.75$ and are considered to have a Galactic origin. The low energy cutoff is due to the solar modulation, that is the energy loss produced by the interaction of CR with the electric potential generated by the solar wind [66]. Above those energies, the spectrum steepens to $\gamma \sim 3.1$, feature known as the *"knee"*. At energies above 5×10^8 GeV/nucleon the spectrum further softens to $\gamma \sim 3.3$ (*"second knee"*). Although this feature is still matter of debate, it is attributed to a leakage of CR from the Galaxy. At those energies the Larmor radius is larger than the spatial dimensions of the Galaxy (Fig 1.1), thus particles originated in the Galaxy would not be confined. For this reason, observed cosmic rays above this energy are believed to be of extragalactic origin.

At 3×10^9 GeV/nucleon the spectrum hardens again to $\gamma \sim 2.7$ (*"ankle"*). Finally, a suppression in the flux is observed at 5×10^{10} GeV/nucleon, probably due to the interaction with the cosmic microwave background (CMB). This effect is known as the GZK limit and is due to the background photon (CMB) and CR nucleon center of mass energy exceeding the pion production energy threshold (Eqn. 1.2) [68],[113]:

$$p + \gamma \rightarrow p + \pi^{\circ} \qquad ; \qquad p + \gamma \rightarrow n + \pi^{+}. \tag{1.2}$$

Despite AGASA [111] observation of a significant number of events above the GZK cutoff, the highest energy CRs observed by the Auger [95], HiRes [105], and Yakutsk [10] arrays further supports this explanation.

1.1.2 Production and Acceleration

According to a Hillas-like argument [72], the sources that can accelerate CR particles to such a wide energy range, must be constrained by the extent of the source and magnetic field strength as in Fig. 1.1 [1]. At the energies of interest for this study, below the *knee* in the CR spectrum, it is widely accepted that the sources must be within the galactic scale.

In galactic models, the sources are essentially located in the galactic disc, where the bulk of the visible matter resides. However the determination of the region where CRs are confined (diffusion zone) is a different issue we will not address here.

The origin and acceleration mechanism of CR remains speculative, nonetheless it is very plausible that cosmic rays are accelerated in SNRs shock waves by stochastic scattering on the magnetic turbulence of the expanding plasma. Another conceivable options are pulsars and neutron stars in close binary systems.

From the energetics point of view, these explanations are well grounded. The average CR energy density is $\rho_{CR} \sim 1\mathrm{eV/cm^3}$. If we consider a galactic radius of 15 kpc, a disc height of 200 pc and an average residence time of $\tau \sim 6 \times 10^6$yr then the power needed to keep a stationary CR energy density $P_{CR} = \frac{V \cdot \rho_{CR}}{\tau} \sim 5 \times 10^{40} erg/s$. If we assume a supernova rate of 1/30 years with a typical kinetic energy release of $10^{51}\mathrm{erg}$, then we have a power of $\sim 10^{42}\mathrm{erg/s}$ so a few percent efficiency would be enough.

1.1.3 Anisotropies

The distribution of the arrival directions constitute yet another important piece of information to trace the sources of cosmic rays. The CR arrival directions becomes randomized by the CR scattering on the galactic magnetic fields, hence, very small anisotropies are expected being their measurement very challenging. This CR scattering is directly related to the Larmor radius or gyroradius

[1] Containment in a region requires the size of the region L, to be greater than the Larmor radius $R_L = E/ZeB$, thus setting $E_{max} \sim Ze\beta BL$.

$$R_L = \frac{P_\perp}{ZeB} \simeq 1.08\mathrm{pc}\frac{\mathrm{E}/10^6\mathrm{GeV}}{\mathrm{Ze}\cdot\mathrm{B}/\mu\mathrm{G}}, \tag{1.3}$$

which is $\mathcal{O}(10^{-3}\mathrm{pc})$ for TeV particles (Fig. 1.3).

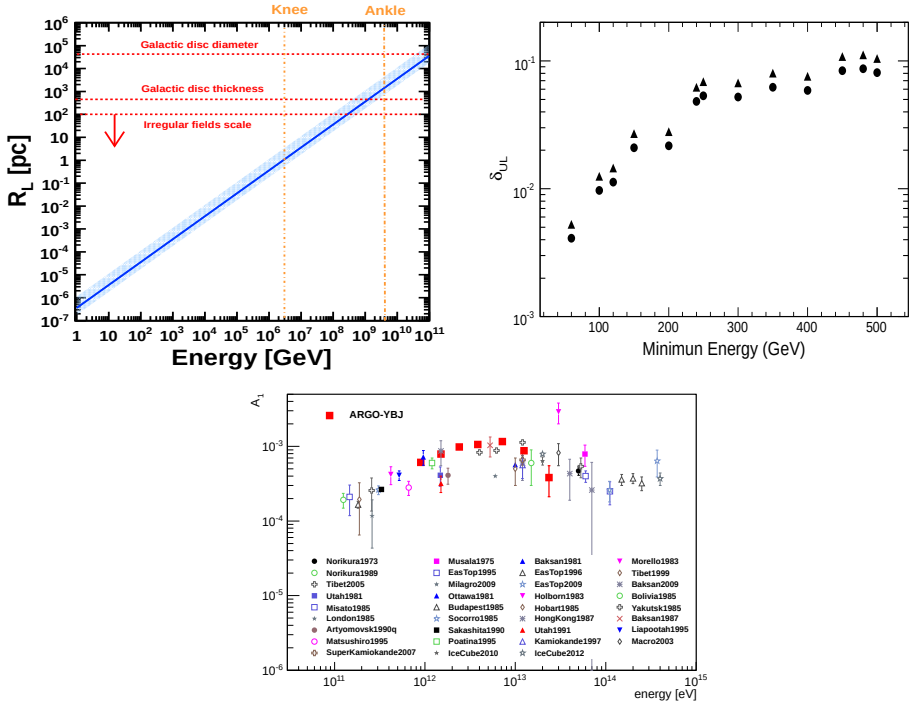

Figure 1.3: (Left): Larmor Radius for Z=1 particles for B=3μG, with upper and lower limits of (1.4-6) μG. (Right): Fermi U.L. on electron + positron dipole anisotropy [54] at 90% and 95% C.L.. (Center) CR anisotropy measurements from [50].

Depending on the energy we are interested in, two aspects can be studied: On the one hand, the small scale where local variations are searched, such as hot-spots, would point to acceleration regions and distinctive sources. On the other hand, the large scale anisotropy may reveal patterns over the full sky such as dipole angular scales. The first one is only possible for energies of $\sim 10^{10}$GeV which have a R_L of a few kpc which is much larger than the scale length of the random component of the galactic magnetic field. This is epitomized in Auger's [95] findings of a correlation between UHECRs and AGNS.

At the lower edge of the spectrum, cosmic rays are highly isotropic, as the Larmor radius is very small compared to the galactic magnetic fields length-scale. In fact, at these energies the CR regime is diffusive. Residual anisotropies may be present however, due to CR leakage from the Galaxy and the stochastic effect of local sources [108].

On top of this, there are additional notable effects that may induce anisotropies in the CR spec-

trum:

- Compton-Getting Effect: The relative motion of the Earth with respect to the CR "local rest-frame" [45] should induce an apparent dipole-like anisotropy of $\sim 0.04\%$ [108] however it has not been observed.
- Latitude and East-West Effect: It is caused by the deflection of primary cosmic rays in the Earth's magnetic field. The integrated cosmic ray intensity increases with latitude.

Such anisotropies can be characterized in first approximation by a pure dipole $I = I_0 + I_1 cos\theta$.

$$\delta = \frac{I_{max} - I_{min}}{I_{max} + I_{min}} = \frac{I_1}{I_0}. \tag{1.4}$$

Current data from Tibet ASγ, IceCube, SuperKamiokande, Milagro, ARGO-YBJ and EAS-top among others, [44], [52],[8],[2],[60],[12] point out the presence of large scale anisotropies at most at the $10^{-4} - 10^{-3}$ level at $10^2 - 10^5$ GeV energy range (in accordance with what is expected from diffusive transport).

Ongoing studies of the CR anisotropy in electrons and positrons are also being carried out at the lower part of the spectrum by Fermi [54] and AMS-02. A dedicated study will be discussed in following sections.

1.2 Cosmic Rays in Near Earth Orbit

Cosmic rays at the Earth neighborhood are influenced by two phenomena that produce distortions on the local interstellar spectrum (LIS). The first one is the solar wind, essentially a plasma of protons and electrons which composes the heliosphere and extends up to the boundaries of the solar system. The second is the Earth's geomagnetic field which comprises the Earth's magnetosphere.

1.2.1 Solar Modulation

The solar wind is a magnetized plasma of low energy protons and electrons in hydrodynamic expansion that is ejected from the solar corona to the interplanetary medium. The plasma drives out the magnetic field lines, that in conjunction with the Sun's rotation results in an Archimedian spiral pattern for the large-scale field. On top of this large-scale field, small-scale magnetic field irregularities are also present as a result of the turbulence and instabilities of the solar corona and interplanetary medium.

Charged particles interacting with the solar wind move along the large-scale field lines and are scattered by the small-scale field irregularities resulting in a diffusive regime. This interaction is the solar modulation, and has a major impact in low energy particles ($E \lesssim 10$ GeV).

Particles influenced by the solar modulation undergo diffusion, convection, gradient and curvature drifts and adiabatic energy changes in the same way that the ISM propagation. Current models

are described by a transport equation first formulated by Parker[92]. The equation can be solved numerically, or analytically under simplifying assumptions as in the so-called *force-field approximation* of Gleson and Axford [66]. In this approximation, the solar wind is considered as a radial field with potential ϕ.

The solution of the transport equation connects the local flux $\mathrm{F}_{\odot}$ which has been modulated by the solar wind, with the local interstellar flux $\mathrm{F_{LIS}}$ by $\mathrm{F}_{\odot}(\mathrm{r},\mathrm{E},\mathrm{t}) = \mathrm{p}_{\odot}^2/\mathrm{p}_{\mathrm{LIS}}^2\mathrm{F_{LIS}}(\infty,\mathrm{E}+\Phi(\mathrm{t}))$:

$$\mathrm{F}_{\odot}(\mathrm{E}) = \frac{\mathrm{E}^2 - \mathrm{m}^2\mathrm{c}^4}{(\mathrm{E}+\Phi)^2 - \mathrm{m}^2\mathrm{c}^4}\mathrm{F_{LIS}}(\mathrm{E}+\Phi), \tag{1.5}$$

where E is the energy at the Heliosphere, and Φ is related to the solar modulation parameter ϕ by $\Phi = Ze\phi$. The value of the solar modulation parameter represents the energy loss experienced by a particle of Z=1 approaching the Earth from infinity.

Although it is not considered in the force-field-approximation, the orientation of the solar magnetic field leads to an alternating magnetic field polarity along successive solar cycles (11 yrs). This effect produces a charge sign dependence of the solar modulation [64],[33].

1.2.2 Earth Magnetic Field

The Earth's magnetic field constitutes the last barrier for cosmic rays before being detected at Earth. Particles entering the geomagnetosphere follow spiral trajectories around the field lines and eventually loose their energy. The GeoMagnetic Field (GMF) can be approximated by a tilted dipole field with moment $\mathcal{M} = 8.1 \times 10^{22}\mathrm{Am}^2$ rotated 11° with respect the Earth's rotation axis and displaced $\sim$ 400 Km from the Earth's center. The tilt and offset induce distortions in the GMF, being the most notable located at the South Atlantic. This region, known as the *South Atlantic Anomaly*, is characterized by a very weak field strength. Therefore, particles are allowed to penetrate deeply and enhance the local flux.

An important aspect concerning cosmic rays is the so-called *geomagnetic cutoff*. Particles entering the Earth's magnetic field experience the Lorentz force which curves their trajectories. Hence, cosmic rays may not be able to reach the detector depending on their rigidity (R=pc/|Z|e) and incoming direction.

The minimal rigidity that a particle must have in order to penetrate the magnetic field is called the rigidity cutoff R_c. In the dipole approximation, the rigidity cutoff has been analytically calculated by Störmer [107].

$$R_c = \frac{\mathcal{M}\cos^4\lambda}{\mathcal{R}^2\left[1+(1\pm\cos^3\lambda\cos\phi\sin\xi)^{1/2}\right]^2}, \tag{1.6}$$

where $\mathcal{M}$ is the dipole magnetic moment, $\mathcal{R}$ is the distance from the dipole center and λ is the geomagnetic latitude along the dipole. ξ and ϕ are the polar angle from local zenith and azimuthal angle in the clockwise direction from the local magnetic east. The sign $\pm$ corresponds to different particle's charge sign.

For vertical incidence ($\xi = 0$) there is no dependence on the azimuthal direction, and the rigidity cutoff is reduced to:

$$R_c(\xi = 0) = 14.5GV \frac{\cos^4 \lambda}{\left(\frac{\mathcal{R}}{R_\oplus}\right)^2}, \tag{1.7}$$

where $R_\oplus$ is the Earth's radii.

It is remarkable that the R_c is maximum at the geomagnetic equator with an approximate value of 15GV for vertical incidence, vanishing at the magnetic poles. Taking into account the particle incident angle, values above $\sim$ 10GV are possible for positive charged particles in the magnetic equator approaching from the western horizon, in spite of $\sim$ 50GV from the eastern horizon. This asymmetry has been observed at all latitudes, and is called the East-West effect.
In fact, the field is not a perfect dipole. A more precise description of the GMF and its annual rate of change is given by the International Geomagnetic Reference Field (IGRF) [91], which describes the magnetic field in a more general spherical harmonic expansion with weights determined experimentally [2]. At the first order, the dipole approximation is recovered. This description of the magnetic field is used in conjunction with computational codes that trace the particle trajectories to determine the rigidity cutoff.

A more thorough determination of the cutoff rigidity can be obtained back-tracing individual particles in the geomagnetic field with a given position, time and rigidity. This is done integrating the Lorentz equation to see if the particle escapes to the outer space. However, the trajectories determination is not straightforward as trajectories that would otherwise be allowed, are forbidden due to the presence of a solid object, the Earth. As rigidity decreases, more complex orbits may be allowed and forbidden at each point.

For each point, a cone of allowed and forbidden trajectories may be built, with the edges corresponding to the upper and lower limit of the rigidity cutoff. Intermediate states correspond to unstable solutions of the equation, effect called *penumbra*.

1.3 Antimatter in Cosmic Rays

Several probes at galactic and cosmological scales suggest that the Universe is CP asymmetric, containing negligible amounts of antimatter. For what concerns our Galaxy, a small fraction of the observed cosmic rays is antimatter, positrons and antiprotons which are attributed to a secondary origin (product of the spallation of primaries). Provided a secondary origin, the fluxes can be computed in a relative robust way given an appropriate knowledge of the $\bar{p}, e^+$ production cross sections in pp(nuclei) collisions, and because the average *thickness* primary cosmic rays go through can be estimated accurately from measurements of secondary-to-primary ratios such as the B/C.

[2] On top of this, a more accurate determination of the GMF should take into account its interactions with the solar wind which produce additional distortions.

The origin of antimatter in CRs has been a matter of debate for a long time ago. While light particles, $e^+, \bar{p}, \overline{D}$ are products of the cosmic ray collisions, heavier antinuclei such as $\overline{\mathrm{He}}$ are not expected to be produced by the CR spallation. Hence, the observation of heavy antimatter nuclei would suggest the existence of antimatter domains.

Antimatter channels are well suited for searches of exotic primary sources, indeed, positrons constitute about $\mathcal{O}(10\%)$ of the electrons and $\bar{p}/p$ is just 10^{-4} (Figs. 1.4 and 1.5) owing to their secondary origin. This means that these channels are more sensitive to contributions from primary sources of matter and antimatter. In short, antimatter production mechanisms in CR are fairly well understood and the absence of primary sources provides a *preferred* channel in searches for signatures of exotic sources. In particular in many DM scenarios, large amounts of e^+, $\bar{p}$, $\bar{D}$ can be produced and be observed from Earth. In spite of the effort put into this direction, no consensus has been reached weather signals of DM have been already spotted in these channels or not.

Observations of $\bar{p}$ (Figs. 1.4 and 1.5) and low energy e^+ are remarkably well reproduced by numerical simulations describing their secondary production and propagation in the Galaxy, such as GALPROP [108], DRAGON [19] and USINE [84], hence supporting the secondary origin hypothesis.

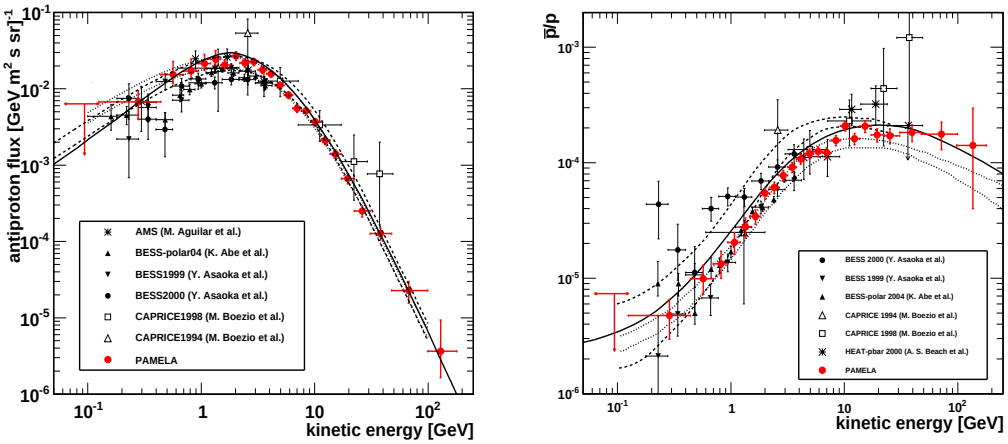

Figure 1.4: Antiproton flux with a model describing secondary production of $\bar{p}$ (Left). Antiproton to proton ratio (Right). [4]

High energy e^+ observations have been nevertheless difficult to explain from a purely secondary production. This proves the study of CR e^+ a promising window to search for signatures of new phenomena. We will devote the next section to this point.

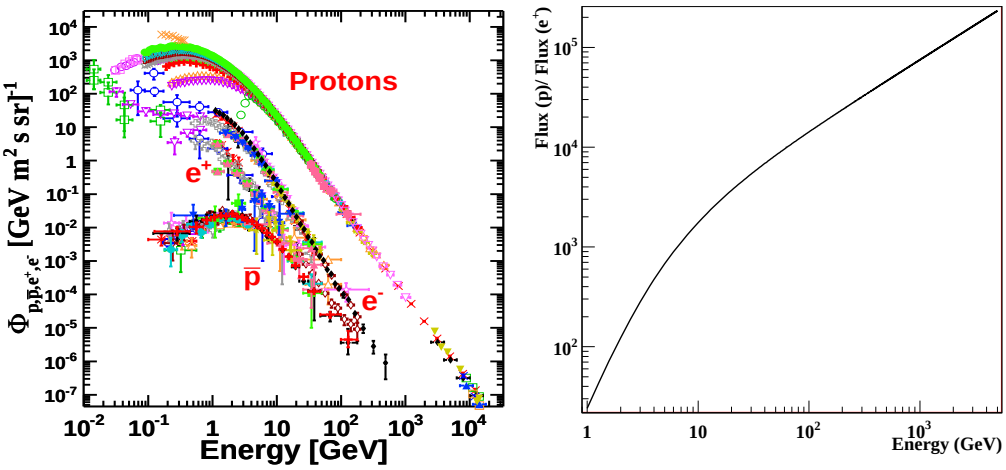

Figure 1.5: Absolute proton (upper), electron (intermediate), positron (lower) and antiproton (bottom) measured fluxes (Left). Ratio of the proton to e^+ parametrized flux (Right). As can be seen, the proton flux is $\mathcal{O}(10^3 - 10^4)$ larger that the e^+ flux. This presents a challenge to searches in the positron spectrum as detectors with a high proton rejection power are required.

1.3.1 The Positron Fraction

Positrons are believed to have a secondary origin, product of the interaction of primary protons with protons of the rarefied ISM. The products of these interactions include charged pions and kaons (π^+, K^+), which eventually decay producing equal number of positrons and electrons with a soft spectrum [89].

There are however, a number of models that provide primary sources for CR $e^{\pm}$. In particular, astrophysical sources (Pulsars, SNRs) and WIMPs annihilation in the galactic halo have been extensively studied.

To investigate the positron spectrum, it is convenient to introduce the positron fraction. The positron fraction is defined as the ratio of the positron flux ϕ_{e^+} to the electron plus positron flux $\phi_{e^+} + \phi_{e^-}$.

$$\text{Positron Fraction} \equiv \text{PF} = \frac{\phi_{\mathrm{e}^+}}{\phi_{\mathrm{e}^+} + \phi_{\mathrm{e}^-}}. \tag{1.8}$$

If we assume positrons are produced as secondaries from spallation of primary protons and nuclei, then the spectral index must be softer compared to primaries. As electrons are produced in primary sources and secondary as well, it is expected that the positron fraction decreases with the energy [101], and in fact, this is what computational models such as GALPROP reproduce. The reason behind it lies on the primary and secondary fluxes dependence on energy after propagation:

$$\begin{aligned} Q^p_{prim}(E) \propto E^{-\alpha_p} \quad &\Rightarrow \quad \phi^p_{prim}(E) \propto E^{-\alpha_p-\delta} \sim E^{-2.81} \\ Q_{sec}(E) \propto \phi_{prim}(E) \quad &\Rightarrow \quad \phi_{sec}(E) \propto \sigma \cdot \phi_{prim}(E) \cdot E^{-\delta}, \end{aligned} \tag{1.9}$$

where Q^p_{prim} is a proton primary source term, ϕ are the observed fluxes [57],[56], δ is the spectral index of the diffusion coefficient[3] (which will be introduced in chapter 2), and σ is the production cross section for secondary particles.

For primary electrons and secondary positrons we have:

$$\begin{aligned} Q_{e^-}(E) \propto E^{-\alpha_e} \quad &\Rightarrow \quad \phi_{e^-}(E) \propto E^{-\alpha_e-\ell(E)} \sim E^{-3.18} \\ Q_{e^+}(E) \propto \phi^p_{prim}(E) \quad &\Rightarrow \quad \phi_{e^+}(E) \propto E^{-\alpha_p-\delta-\ell(E)}, \end{aligned} \tag{1.10}$$

where α_p,α_e are the spectral indexes for proton and electron primary sources, and $\ell(E)$ is due to diffusive propagation with energy loses which can be roughly estimated to be between δ and 1 [101]. Then, the positron fraction:

$$\mathrm{PF} = \frac{1}{1+\phi_{\mathrm{e}^-}/\phi_{\mathrm{e}^+}} \simeq \frac{1}{1+\mathrm{kE}^{\rho}}, \tag{1.11}$$

where $\rho = \delta + \alpha_p - \alpha_e$, should decrease with the energy.

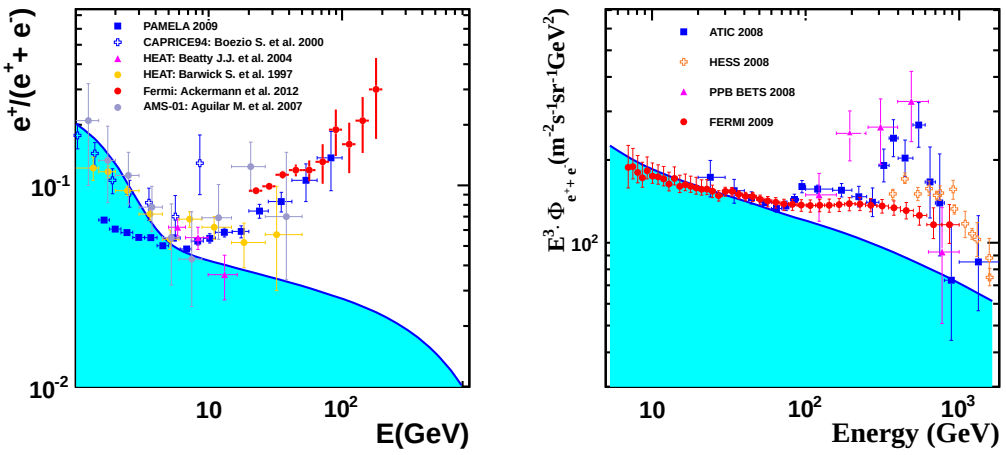

Figure 1.6: Left:Positron fraction $e^+/(e^+ + e^-)$ measurements referenced in the figure. In red, the latest data from Fermi. The blue line is from GALPROP standard diffusion model. Right: Electron + Positron Flux, scaled by E^3. The blue line is from GALPROP standard diffusion model.

However, since the very beginning of measurements of the positron fraction (Agrinier et al. 1969; Buffington, Orth, & Smoot 1975; Muller & Tang 1987; Golden et al. 1987, 1994), it became

[3]Thereby the ratio of secondaries to primaries such as B/C provides an estimate of $\delta \sim 0.5$

apparent a rise with the energy above a few tens of GeV that suggested either the existence of a new source of positrons, or a depletion of primary electrons. By the mid-90's, a confirmation came from the balloon-borne experiment HEAT [17] and later on, in 1998 a CRs precision measurement era was born with AMS-01 observation of the positron fraction [5].

More recently, a number of experiments, Pamela[3], Atic[29], PPBets[110], Hess[58] and Fermi[53],[55] have raised a lot of controversial over the observation of a significant increase with energy of, on the one hand the individual spectra of e^+e^- and the total one, and on the other hand, the positron fraction as well (Fig. 1.6). This distinctive feature has been hailed as a signature of DM annihilation or decay, however, in order to reconcile the different observations ($\gamma, \bar{p}$...), the DM explanation turns out to be tightly constrained and even ruled out for conventional models. Moreover, the limited knowledge of the CR production mechanisms and the uncertainties in the parameters governing the CR propagation makes even harder to come to a verdict.

A dedicated study will be discussed in the following chapter, however, and putting aside the theoretical issues that may dominate the uncertainties of the study, we should emphasize that in order to be able to specify the nature of this excess, more statistics, a higher background rejection, a larger dynamical range and a better energy resolution are required, purposes for which AMS-02 has been designed.

1.3.2 Dark Matter Source of Cosmic Ray $e^{\pm}$

The possibility that a significant amount of the matter content of the Universe could be explained by a new type of elementary particle is well motivated both from the cosmological and particle physics point of view.

First of all, it should be noticed that among the SM particles, there are not feasible candidates to account for the missing mass. SM neutrinos may indeed contribute to the Ω_{DM} but cannot be a sizable part of it, as neutrinos are relativistic, thus behave as hot DM which is not endorsed by observations.

There are a number of reasons to believe that the Standard Model (SM) is not a fundamental theory but rather an effective field theory valid up to a few TeV. Many extensions to the SM have been introduced to provide answers to some open questions, such as the origin of the three families of fermions and the hierarchical spectrum of their masses, the gauge coupling unification, the baryon asymmetry and for our purposes, Dark Matter (DM). The fact is that many of these theories provide in a natural way particles that could play the role of DM.

From the cosmological perspective, a generic class of weakly interacting massive particles (WIMPs) also provides excellent candidates to account for cold non-baryonic Dark Matter. The reason behind it is that any viable production process of a particle candidate for DM must satisfy the observed relic abundance. The situation for WIMPs is rather optimistic in this regard as stable particles with weak-scale masses M_{weak} that interact with weak interactions and were produced thermally in the early universe, automatically reproduce the right abundance.

In a standard picture, WIMPs production and annihilation processes occurred copiously in the early universe as a result of the collisions between particles of the thermal plasma during the radiation-dominated epoch.

$$\chi\overline{\chi} \leftrightarrow l^+l^-, \mathrm{q\overline{q}}, \mathrm{W^+W^-}, \mathrm{Z^+Z^-}... \tag{1.12}$$

With temperatures $\mathrm{T} \gg \mathrm{m}_\chi$ the production and annihilation process were very efficient and were in equilibrium with a common annihilation rate of $\Gamma = \langle\sigma\mathrm{v}\rangle\mathrm{n_{eq}}$, where $\langle\sigma\mathrm{v}\rangle$ is the thermally averaged annihilation cross section and n_{eq} the number density at equilibrium. As the Universe expanded and cooled below the WIMP mass, the WIMP particles decoupled and the number of WIMPs decreased exponentially as $e^{-(m_\chi/T)}$ due to a Boltzmann-suppression since only particles with energies in the tail of the Boltzmann distribution had enough energy to produce WIMP pairs.

At the same time, as the Universe expanded and cooled, the self-annihilation processes become more inefficient and when the annihilation rate becomes smaller than the Hubble expansion rate, then the co-moving number density of WIMPs is not altered and becomes frozen at the thermal relic abundance, producing the so called freezeout or decoupling. From this time, the decoupled particles no longer interact with the cosmic soup and just expand freely, with a number density that scales inversely proportional to the scale factor a as $n \sim 1/a^3$.

The number density n(t) for a decoupled specie then evolves obeying a Boltzmann equation where two processes take part, annihilation and evolution due to the Hubble expansion

$$\frac{dn}{dt} + 3Hn = \langle\sigma\mathrm{v}\rangle(\mathrm{n}^2 - \mathrm{n}_{\mathrm{eq}}^2), \tag{1.13}$$

where H is the Hubble rate. This equation can be solved numerically to yield a value for the present relic density as a function of the annihilation cross section

$$\Omega\mathrm{h}^2 \approx \frac{3 \times 10^{-27}\mathrm{cm}^3\mathrm{s}^{-1}}{\langle\sigma\mathrm{v}\rangle}. \tag{1.14}$$

Although in this expression the DM particle mass is not involved, the relic density depends on it through the annihilation cross section. The S-wave annihilation cross section reads

$$\langle\sigma\mathrm{v}\rangle \approx \frac{g^4}{16\pi^2 M_\chi^2}, \tag{1.15}$$

where if the coupling $g = g_{weak} \approx 0.65$ and $M_\chi \sim M_{weak},\ \mathcal{O}(100\mathrm{GeV})$ then it just matches the required abundance, fact that has been often referred as the *"WIMP miracle"*.

However, WIMPs are not the only solution to the Dark Matter problem, e.g. axions or unstable DM have been suggested in the literature. In fact, a huge number of candidates have been introduced, mainly from extensions of the SM to solve the DM problem. A detailed compilation of the proposed candidates is out of the scope of this work and good references covering this topic can be found for instance in [61], [20] and references therein.

The Distribution of Dark Matter

Dark Matter distribution is presently not very well determined. In particular for our Galaxy, the Dark Matter content can be estimated, but the specific distribution is far beyond current surveys. This problem is typically addressed with numerical simulations, given the complexity of the highly non-linear interaction processes involved in the evolution of DM structures. In particular, N-body simulations have been so far well suited for the analysis of the gravitational collapse of a system of collisionless particles, and thus extensively used in the modelization of CDM structures.

Dark Matter hierarchically clusters in the so-called DM Halos, which ranges in mass and size from the tiniest substructures, to galactic sized halos and beyond (Fig.1.7). In particular, at the galactic scale, galaxies are embedded in halos that extend far beyond the galaxy visible edges and dominate the total mass as evidenced by galactic rotational curves.

CDM halo clustering is characterized by self-similar spherical structures at different scales with common density profiles, that are nearly isothermal ($\rho \sim r^{-2}$).

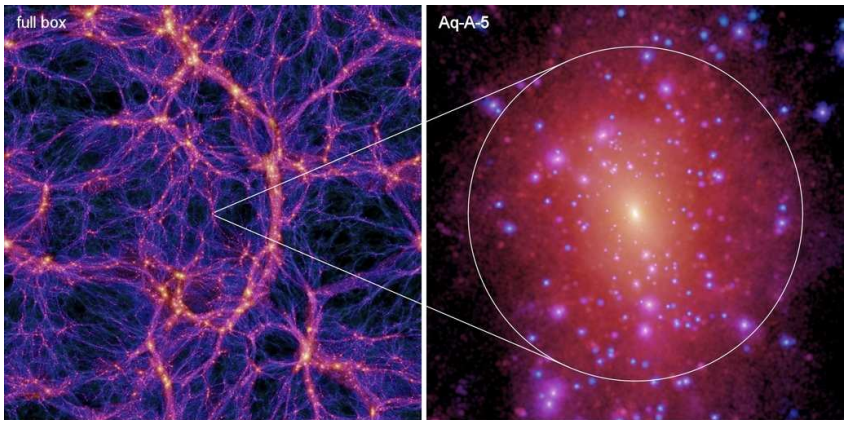

`Figure 1.7:` Aquarius Simulation. Projected Halo squared DM density at $z = 0$ (Left). Re-simulation of a selected Halo from the simulation at higher numerical resolution [106]

A common density profile that has been found to reproduce remarkably well halos in the simulations over a mass range spanning 20 decades, from micro-halos, to galaxy cluster scale ones, is the Navarro-Frenk-White profile (NFW) [90]

$$\rho(r) = \frac{\rho_s}{(r/r_s)^{\gamma}(1 + r/r_s)^{3-\gamma}}, \tag{1.16}$$

where $\gamma = 1$ and the scale radius r_s and ρ_s are parameters that vary from halo to halo, but are related trough the concentration parameter c by:

$$r_{vir} = cr_s, \tag{1.17}$$

where the virial radius r_{vir} is useful to estimate the extent of the halo and it is often defined as the

radius at which the density is 200 times the critical density. With this definition the mass of the halo, and thus the normalization factor for each subhalo can be calculated as follows:

$$M_{halo} = \int_0^{r_{vir}} 4\pi r^2 \rho(r) dr = 4\pi \rho_s r_s^3 \left[\ln(1+c) - \frac{c}{1+c} \right]. \tag{1.18}$$

The concentration parameter c, can be generically defined as $c = \frac{\overline{\rho}(r_{vmax})}{\rho_{crit,0}}$ and varies from halo to halo, but can routinely be calculated from the halo fitting procedure in the simulations.

As computational power has been growing, the resolution of simulations has been increasing, and it has been found that smaller structures are best fitted by the same NFW profile letting the inner slope γ become a free parameter. Yet another profile has been found to reproduce well the smaller scales, the Einasto profile:

$$\rho(r) = \rho_s \exp^{-\frac{2}{\alpha}[(r/r_s)^\alpha - 1]}. \tag{1.19}$$

As far as our Galaxy is concerned however, the different Dark Matter density profiles at the solar neighborhood do not differ substantially, showing more prominent deviations near the galactic center. Actually, it is a matter of debate the exact distribution in the inner parts of the host Halo, as simulations including baryons produce profiles that are in general steeper at the core than those which only include Dark Matter. Moreover, the *cuspiness* of the core is still an open problem [47],[75], but for antimatter searches, the impact of these issues is minute as we will see in the next chapter.

One of the major contributions from simulations is the demonstration of the existence of substructure after the hierarchical merging, both gravitationally bounded (subhalos) and unbounded (streams). For Milky Way (MW) sized halos, simulations are currently able to resolve subhalos of $10^4 - 10^5 M_\odot$ within the main halo, and to characterize their inner structure and spatial distribution. In particular, it has been found that subhalo mass abundance proportional to $M^{-\alpha}$ with $\alpha = [1.9, 2]$.

A word of caution must be casted in any case, for the resolution of simulations is still far from the size of the smallest substructures, and the extrapolations along decades of halo masses that must be performed certainly introduce additional theoretical uncertainties.

Dark Matter Indirect Detection

Dark Matter indirect detection is based on the idea of detecting signatures of the annihilation or decay of DM particles in the cosmic radiation, photons and neutrinos. The idea was born on the realization that the same process that led WIMPs to fit the required DM relic density (Eqn. 1.12), may produce sizable distortions on the cosmic ray spectra that we can measure.

A simple estimate of the annihilation rate per volume :

$$\frac{1}{2}\langle \sigma \mathrm{v} \rangle \frac{\rho_\odot^2}{\mathrm{m}^2} \simeq 1.4 \times 10^{-31} \mathrm{cm}^{-3}\mathrm{s}^{-1} \left(\frac{\rho_\odot}{0.3 \mathrm{GeV cm}^{-3}} \right)^2 \left(\frac{\mathrm{m}}{100 \mathrm{GeV}} \right)^{-2} \left(\frac{\langle \sigma \mathrm{v} \rangle}{3 \times 10^{-26} \mathrm{cm}^3 \mathrm{s}^{-1}} \right), \tag{1.20}$$

gives a rate of $1.6 \times 10^{34}\mathrm{s}^{-1}$ for a 1Kpc sphere surrounding the Earth, assuming a local density of $0.3\mathrm{GeVcm}^{-3}$. If the branching ratio for annihilation into leptons is significant, then we expect a sizable contribution from DM annihilation to the positron flux.

1.3.3 Astrophysical Sources of Cosmic Ray $e^{\pm}$

Among the astrophysical objects that populate our Galaxy, many can contribute to the positron abundance in cosmic rays, but the required energy excludes a large part of them. Following a Hillas-like argument, the astrophysical sources able to inject the required order of energy most widely accepted are SNRs and pulsars (Fig. 1.8)[4].

In fact, recent surveys indicate that there is a large number of sources which emit γ-rays in the GeV region. In particular, more than 500 sources have been identified with energies above 10 GeV [1].

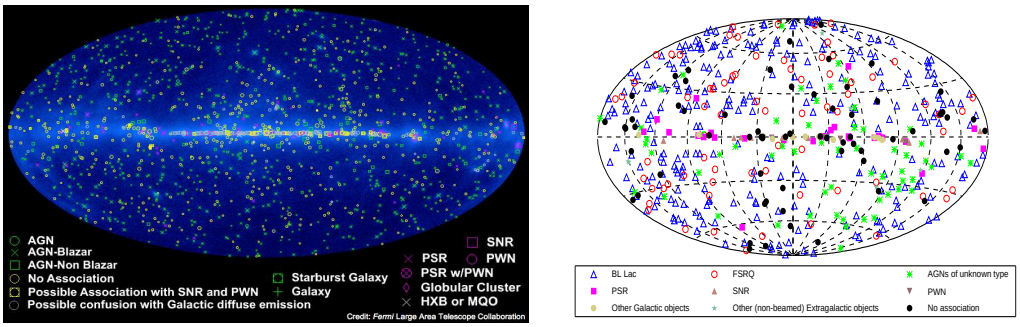

Figure 1.8: The Fermi LAT catalog of γ-ray sources (Left). Fermi LAT catalog of sources with energies above 10 GeV from [1]. Most galactic sources of GeV γ-rays are SNR and PSR/PWN.

Supernova Remnants

If secondary $e^{\pm}$ are produced by the spallation of primaries in the propagation in the ISM, then it is conceivable that those primaries may produce also secondaries in the interactions in the sources prior propagation, in particular by the hadronic interaction of primaries with the expanding gas in SNRs.

The argument to disregard this component so far has been that the average residence time of primaries in SNRs, which should be inferior to the SNR lifetime $\mathcal{O}(10^4)\mathrm{yrs})$, is much shorter than the average residence time of CRs in the Galaxy $\mathcal{O}(10^6 - 10^7\mathrm{yrs})$. Even considering the density in the source $\sim 10\mathrm{cm}^{-3}$ is higher than the ISM gas $\sim 0.1\mathrm{cm}^{-3}$ due to the gas compression by the shock, the grammage estimated inside the SNR is much smaller ($\sim 0.2\mathrm{gcm}^{-2}$) that the average

[4] Although other possibilities have been investigated such as production in giant molecular clouds[46], microquasars[71] or gamma-ray bursts[77],[76].

grammage of the ISM (a few gcm^{-2}). Therefore, the production of secondaries in the sources should be negligible compared to production during propagation in the ISM.

However, this argument neglects that these secondaries produced in the sources may be also accelerated along with primary electrons, yielding a significantly harder spectrum [21]. If this were the case, the raising positron fraction can be explained without resorting to new additional sources, in a pure illustration of the *Occam Razor's* principle.

This mechanism would further imply an increase on the $\bar{p}/p$ above 100 GeV [22], and on heavier nuclei secondary to primary ratios (B/C, Ti/Fe) [87], [6], which future observations will test.

Pulsars

Another popular primary source for positrons are pulsars and their associated nebula, the pulsar wind nebulae (PWN). Pulsars are rapidly spinning magnetized neutron stars that transfer part of their rotational energy into a magnetized wind. The large electric fields induced by the rotating neutron star, strip electrons from the star surface to such extent that the pulsar is surrounded by a co-moving plasma called the *pulsar magnetosphere* which extends up to a distance known as light cylinder $R_L = c/\Omega$.

These electrons in turn emit synchrotron and/or curvature radiation while drifting far from the star along the magnetic field lines. The photons energy is large enough to produce electron-positron pairs in the strong magnetic field of the pulsar magnetosphere by magnetic conversion, and/or through photon-photon pair production with photons from the local radiation fields such as thermal X-rays from the neutron star surface. Thus, pulsars are expected to produce pairs of electrons and positrons as a result of electromagnetic cascades induced by the acceleration of electrons in their magnetosphere.

It is then reasonable to think that the physical process that produces e^+e^- in the pulsar magnetosphere is presumably the same that produces the Gamma-Ray emission [70], although additional processes such as re-acceleration in the pulsar wind nebula should be taken into account.

It is worth stressing that a pulsar source of $e^{\pm}$ does not produce in a natural way antiprotons, in accordance with $\bar{p}/p$ observations.

2

Signatures in the Electron and Positron Spectra

RECENT measurements of the $e^{\pm}$ spectra extend the energy range up to unexplored energies in the hundreds of GeV range confirming the excess starting at about 10 GeV already suggested by HEAT [17] and AMS-01 data [5]. This excess can be explained by the annihilation of Dark Matter in the context of exotic physics, or by nearby astrophysical sources such as pulsars. In order to discriminate between the competing models for primary positron production, we investigate the role of cosmic ray electron anisotropies as potential signatures to probe an exotic explanation to the positron excess.

This chapter is based on the related works [28],[27] where we calculate the contribution to the electron flux due to both the collection of all known Gamma-Ray pulsars (as listed in the ATNF catalog) and by the annihilation of Dark Matter. We address the problem of the electron anisotropy in both scenarios and estimate the prospect that a small dipole anisotropy might be found by future observations. In particular, the sensitivity in the positron and $e^+ + e^-$ spectra is discussed.

2.1 Introduction

The recent claims from the PAMELA [3], ATIC [29], PPB BETS [110] and Fermi [62] collaborations of an excess in the ratio of positrons to electrons plus positrons (positron fraction) and the $e^+ + e^-$ flux, seems to support what HEAT and AMS-01 data suggested regarding the existence of a possible primary cosmic ray electrons source.

A large number of candidates have been suggested to reproduce the observed positron fraction. Among the exotic ones, the annihilation of Dark Matter may be the most widely studied.

If Dark Matter annihilates in the galactic halo, its annihilation products can be measurable from Earth. As it has been pointed out in previous works (e.g. [32]), PAMELA data seems to accommodate preferably leptonic channels rather than Dark Matter annihilating to quark pairs, but typically large boost factors are required to adjust the shape to the data. These boost factors reflect the increase of the expected annihilation rate and originate for instance if we consider a new light force carrier into which the DM particle annihilates, leading to a Sommerfeld enhancement at low velocities, annihilation of a non thermal WIMP, or from inhomogeneities in the Dark Matter halo (clumps, Dark Matter mini spikes etc).

More conventional scenarios such as pair production in nearby astrophysical objects can also reproduce the spectral shape. Specifically in this chapter, we analyze the possible contribution of pulsars and leptophilic Dark Matter. For the former one we consider all gamma ray pulsars listed in the ATNF pulsar catalog. For the latter one, we rely on the latest simulations of MW sized DM halos, allowing for leptons in the DM annihilation final states. Finally, we calculate the predicted dipole anisotropy produced in both scenarios, i.e., Dark Matter annihilation and nearby pulsars, and assess the detection capability of such signature by future observations.

2.2 Cosmic Ray Electron and Positron Propagation

Cosmic ray propagation is a diffusive process due to the random galactic magnetic fields. If we denote the number of particles of type i per unit volume found at time t at $\vec{x}$ with energy E by $n_i(E,\vec{x},t)$ $[GeV^{-1}cm^{-3}]$, the evolution equation as initially written by *Ginzburg* and *Syrotvatskii* [65] can be expressed as:

$$\begin{aligned}\frac{\partial n_i}{\partial t} &= \nabla(\mathbf{D}\nabla n_i) - \nabla(\vec{v}n_i) - \frac{\partial}{\partial E}(bn_i) \\ &+ \beta cN\sum_{s<i} n_s\sigma_{i,s} - \beta cN\sigma_i n_i - \frac{n_i}{\Gamma\tau_i} + Q_i, \end{aligned} \tag{2.1}$$

where $\nabla(\mathbf{D}\nabla n_i)$ is the diffusion term and $\mathbf{D}(E,\vec{x},t)$ $[\mathrm{cm}^2/\mathrm{s}]$ is the diffusion tensor; $\nabla(\vec{v}n_i)$ is the convection term and $\vec{v}=\vec{v}(\vec{x})$ $[\mathrm{cm}/\mathrm{s}]$ is the velocity of the galactic wind; $\frac{\partial}{\partial E}(bn_i)$ represents the energy loss with $b(E,\vec{x},t)$ $[\mathrm{GeV}/\mathrm{s}]$ being the rate of energy change; $\frac{n_i}{\Gamma\tau_i}$ is the fraction of particles lost by radioactive decay with a characteristic life-time τ_i [s] and $\beta cN\sum_{s<i} n_s\sigma_{i,s} - \beta cN\sigma_i n_i$ is the number density of particles created or destroyed by spallation processes in the propagation due to interactions with the interstellar medium of density N, with a cross section $\sigma_{i,s}$ $[\mathrm{cm}^2]$. Finally, we have the source term $Q_i(E,\vec{x},t)$ $[\mathrm{GeV}^{-1}\mathrm{cm}^{-3}\mathrm{s}^{-1}]$ that describes the injection of particles of type i into the Galaxy.

For electron and positron propagation, the relevant processes are diffusion, convection, energy losses and the source term. Propagation can be approached in two complementary ways. The first one is to solve the transport equation using numerical methods in the same way the *GALPROP* package [11] does. The second one is to obtain an analytical solution to the transport equation with a set of realistic simplifying assumptions. In the following, we use the standard *GALPROP* code to get the positron and electron backgrounds and an analytical solution of the propagation equation for the primary positron flux. For primary positron sources, we have used the Green functions formalism as described in [49] where the two main processes, diffusion and energy losses, are considered. The resulting diffusion-loss equation for this process is given by:

$$\begin{aligned} \frac{\partial}{\partial t} n(E,\vec{x},t) &= D(E)\cdot\nabla^2 n(E,\vec{x},t) \\ &- \frac{\partial}{\partial E}(b(E)n(E,\vec{x},t)) + Q(E,\vec{x},t), \end{aligned} \tag{2.2}$$

where $b(E) = -\frac{dE}{dt} = aE^2 + bE + c \approx aE^2$ codifies the energy losses due to (a) inverse Compton scattering (IC) and synchrotron radiation, (b) bremsstrahlung and (c) ionization. At the energies we are interested in, $\mathrm{E} > 10\,\mathrm{GeV}$, the energy loss is very well approximated by the synchrotron losses in the interstellar (ISM) magnetic fields and inverse Compton scattering off the background radiation (Cosmic Microwave Background radiation (CMB) and starlight at optical and IR frequencies). The energy loss due to these processes is calculated as [65]:

$$\begin{aligned} -\frac{dE}{dt} &= \frac{32\pi}{9} c \left(\frac{e^2}{mc}\right)^2 \left(w_0 + \frac{B^2}{8\pi}\right)\left(\frac{E}{mc^2}\right)^2 \\ &= 8\mathrm{x}10^{-17}\left(\mathrm{w}_0 + 6\mathrm{x}10^{11}\frac{(\mathrm{B}/1\mathrm{G})^2}{8\pi}\right)\mathrm{E}^2 \approx 10^{-16}\mathrm{E}^2[\mathrm{GeVs}^{-1}], \end{aligned} \tag{2.3}$$

where the energy density $w_0 = w_{CMB} + w_{opt-IR}$ is the energy density of the photon background $[eV/cm^3]$ with $w_{CMB} = 0.25\ \mathrm{eV/cm^3}$ and $w_{opt-IR} = 0.5\ \mathrm{eV/cm^3}$. w_B stands for the ISM magnetic field energy density $w_B = \frac{B^2}{8\pi} = 0.6\ \mathrm{eV/cm^3}$ for B=5μG.

For the diffusion coefficient $D(E) = D_0 E^\gamma$, three setups MAX, MED and MIN, which are consistent with measurements of the boron to carbon ratio B/C can be considered [48]. There is an important caveat here as stressed in [48], namely, the possible enhancement of the positron flux due to the relative poor knowledge of the propagation parameters set. For this aspect, future observations such as AMS-02 measurements of stable secondary-to-primary and unstable ratios, will greatly improve our knowledge on CR propagation and reduce the theoretical uncertainties.

We solve the equation for a steady state source (DM positron injection) and for a non-stationary source (SNRs and pulsars).

Table 2.1: Diffusion Setups

	$\mathbf{D_0[cm^2/s]}$	γ
MAX	1.8×10^{27}	0.55
MED	3.4×10^{27}	0.70
MIN	2.3×10^{28}	0.46

2.3 Astrophysical Sources of High Energy Positrons

Gamma-Ray pulsars are expected to produce pairs of electrons and positrons as a result of electromagnetic cascades induced by the acceleration of electrons in their magnetosphere. There are two main mechanisms of pulsar particle acceleration with the subsequent radiation emission and pair production processes, namely the polar cap and the outer gap models. We will not detail these mechanisms here. In short, in both models the electrons can be stripped from the star surface and accelerated to ultrarelativistic energies by electric fields in the magnetosphere of the pulsar. We assume that the positron injection spectrum can be expressed as a power-law with an exponential cutoff at E_c, $\frac{dN_e}{dE} = E^{-\alpha} e^{-E/Ec}$.

Previous works (e.g. [70], [26], [74], [112], [31],[63], [97], [67]) have shown the plausibility of pulsars as sources of primary cosmic ray electrons. In our analysis, we will assume a benchmark model as considered in [97], namely, the "standard model" (ST). Although more refined models for electron production in pulsars can be considered, some of them produce an $e^{\pm}$ output well below the observations (e.g. Harding-Ramaty model [70] or the one devised by Zhang and Cheng [79]) or a comparable one (e.g. Chi et al. [31]). In the latter case, the most outstanding pulsars produce similar patterns to those considered in the ST model, so we will assume the most simple scenario for positron production in pulsars as a benchmark model for the study.

The ST model assumes that all the rotational energy of the pulsar is lost through magnetic dipole radiation. Since the rotational energy is given by $E = I\Omega^2/2$ (where I$\approx 10^{45} gcm^2$ is the moment of inertia and Ω the spin frequency), the spin-down power will be $\dot{E} = I\Omega\dot{\Omega}$. For such a magnetic dipole radiator, the energy loss rate can be written as a function of the neutron star's radius R, and α the angle between the dipole and rotation axes $\dot{E} = -\frac{B^2 R^6 \Omega^4 \sin^2\alpha}{6c^3}$, i.e. $\dot{\Omega} \propto -\Omega^3$. Integrating this expression leads to the solution of the time evolution of the rotational velocity of a pulsar for which the magnetic dipole radiation braking dominates:

$$\Omega(t) = \frac{\Omega_0}{(1 + t/\tau_0)^{1/2}}, \tag{2.4}$$

where Ω_0 is the initial spin frequency and $\tau_0 = \frac{3c^3 I}{B^2 R^6 \Omega_0^2}$ is a characteristic time taken to be around 10^4 years for nominal pulsar parameters. Using Eq. 2.4, we obtain the spin-down power $\dot{E}$ of the pulsar.

$$\dot{E} = I\Omega\dot{\Omega} = \frac{1}{2} I\Omega_0^2 \frac{1}{\tau_0} \frac{1}{(1+t/\tau_0)^2}. \tag{2.5}$$

If we assume that a fraction $f_{e^\pm}$ of the spin-down power $\dot{E}$ is translated into pair production, we can describe the power injected into $e^\pm$ by a luminosity function $\mathcal{L}_{e^\pm}$ as:

$$\mathcal{L}_{e^\pm}(t) = f_{e^\pm}\dot{E} = \frac{\mathcal{L}_0}{(1+t/\tau_0)^2}, \tag{2.6}$$

where $\mathcal{L}_0 = f_{e^\pm}\frac{1}{2\tau_0} I\Omega_0^2$.

Integrating Eq. 2.5 over the pulsar age T, the total energy output can be approximated by $E_{out} = I\int dt\Omega\dot{\Omega} \approx I\Omega_0^2/2$. If $t/\tau_0 \gg 1$ then $\Omega_0^2 \simeq \Omega^2\frac{t}{\tau_0}$ leads to an energy output into electrons of:

$$E_{out}[ST] = f_{e^\pm}\dot{E}\frac{T^2}{\tau_0}, \tag{2.7}$$

where the energy budget is determined by the present spin-down power Ė, the age of the source T and the conversion efficiency into pairs $f_{e^\pm}$ that is assumed to be of a few percent. Thus, the $e^\pm$ source for a single pulsar located at a distance r, injecting positrons at time t and energy E can be expressed as:

$$Q(E,r,t) = Q_0 \cdot \mathcal{L}_{e^\pm}(t) E^{-\alpha} \exp(-E/E_c)\delta(r), \tag{2.8}$$

where Q_0 is the normalization factor taken to satisfy the total energy release constraint $E_{tot} = \int^T d\tau \int_{1GeV}^{E_{max}} EQ(E,\tau)dE$ and $\mathcal{L}_{e^\pm}$ is the luminosity of the source. We have introduced a spectral cutoff at E_c=1TeV motivated by the ATIC and Hess data [58]. This cutoff will only be relevant for young pulsars, as old pulsars have a maximal $e^\pm$ energy below the cutoff due to energy losses. For our purposes, we assume typical pulsar injection for magnetic dipole radiation braking (Eq. 2.5), nonetheless a similar analysis can be conducted for other choices e.g. exponential decay luminosity as it is expected from microquasars or $e^\pm$ release from the nebula surrounding pulsars.

Once we have described the source of electrons from a single pulsar, we proceed to estimate the contribution to the local e^+e^- flux from a realistic collection of Gamma-Ray pulsars. For this purpose we will consider all the Gamma-Ray pulsars listed in the Australian Telescope National Facility (ATNF) [81] pulsar catalog [1]. Young pulsars with typical ages lower than $10^4 - 10^5$ years are considered to be surrounded by a pulsar wind nebula (PWN) or a SNR shell that confines the injected electrons before releasing them to the ISM. This has to be taken into account when we consider the age of the pulsars that can contribute to the electron abundance. In this respect we will consider two collections (BM2,BM1). In the first one we will take a lower bound of 10^4 years constraining our pulsar collection to ages between 10^4 and 10^7 years (Table 2.3). This constraint allows us to accept pulsars like Vela which is still surrounded by a PWN. In this scenario, we assume a low conversion efficiency for the young pulsars ($\mathcal{O}(1\%)$) to take into account the possible

[1] http://www.atnf.csiro.au/research/pulsar/psrcat

confinement of leptons. A larger efficiency would imply a non negligible contribution above the background of secondary electrons around 2 TeV due to the contribution of Vela, which is not endorsed by Hess observations of the $e^+ + e^-$ flux.

In the second one, we will consider that pulsars with ages below $5\text{x}10^4$ years cannot contribute to the bulk of electrons, i.e. we constrain our collection to mature pulsars. This introduces an injection delay Δt between the pulsar's birth and the injection of electrons into the ISM due to their confinement in the PWN. This delay may be relevant for young pulsars for which $T \simeq \Delta t$ but for sufficiently old pulsars we can safely dismiss the delay issue and set the injection time at the pulsar age.

The condition for Gamma-Ray emission as described in [114] is that the fraction size of the outer gap be less than one, $g = 5.5P^{26/21}B_{12}^{-4/7} < 1$ in terms of the pulsar period P and the pulsar surface magnetic field B_{12} (in $10^{12}G$ units) resulting in a collection of more than two hundred pulsars, from which three lie at a distance closer than 1kpc.

Regarding the determination of the injection spectral index α, we have to take into account the constraints that come from observations of synchrotron radiation from SNRs. We can consider, as in the Harding-Ramaty model [97], that the $e^{\pm}$ have the same spectral index as Gamma-Rays emitted by pulsars (which has been measured by EGRET to be around 1.4-2.2 for energies $0.1 < E < 10$ GeV [109]). This is a fairly large range, so for the sake of simplicity we will assume that our collection of pulsars have all the same spectral index $\alpha = 1.7$ provided that with this configuration we get reasonable fit to the data (e.g. [67]).

As an additional simplifying assumption we will take a universal set of parameters for the whole collection unless otherwise specified in the text.

Once we have the positron source we proceed to calculate the number density of positrons by solving the diffusion-loss equation (Eq.2.2) for a non stationary source. The solution of the equation has been previously derived for a burstlike power-law injection source with a cutoff E_c ([14], [67]).

$$\phi(E,r,t) = \frac{\beta c}{4\pi}\frac{Q_0}{\pi^{3/2}r^3}\left(\frac{r}{D_{diff}}\right)^3 (1-atE)^{\alpha-2}E^{-\alpha}e^{-\frac{E}{(1-atE)E_c}}e^{-\left(\frac{r}{D_{diff}}\right)^2}, \tag{2.9}$$

where the distance scale is approximately,

$$D_{diff}(E,t) \simeq 2\sqrt{D(E)t\frac{1-(1-E/E_{max})^{1-\gamma}}{(1-\gamma)E/E_{max}}}, \tag{2.10}$$

as a function of the index of the power-law dependence of the diffusion term on energy, γ, and the maximum energy given by the energy losses: $E_{max} \simeq 1/(at)$ with $a \simeq 10^{-16}$ GeV^{-1}s^{-1}.

Given that the source emits with luminosity $\mathcal{L}_{e^\pm}(t)$, the flux will be given by $\phi(E,r,t) = \int_T^t \mathcal{L}_{e^\pm}(t')\phi(E,r,t')dt'$. We have calculated the pulsar contribution to the local electron flux in the

case of burstlike injection and continuous injection for our collection of young and mature pulsars. Even in the continuous case, the injection is well approximated by a burstlike event as a result of the steepness of the slope of the luminosity function for a braking index due to magnetic dipole radiation. In this case, a broader peak in the spectrum is produced because a significant fraction of the electrons are released recently, thus having a shorter cooling time and reaching Earth with a higher energy [78]. In order to reproduce the spectral features of the Fermi data, we assume a MED diffusion scenario with an overall conversion efficiency of 3%. Due to the relative variability of the collection of pulsars in the age/distance parameter space, we adjust the conversion efficiency for a few number of objects that show prominent features in the spectrum at the considered energies, namely Geminga, Monogem (Fig. 2.1).

Table 2.2: Pulsar Parameters

Pulsar	**d[Kpc]**	**T** $[10^5 \mathrm{years}]$	$E_{out}\mathbf{BM1/BM2}[10^{47}\mathrm{erg}]$	$f_{e^\pm}\mathbf{BM1/BM2}[\%]$
Geminga	0.16	3.42	11.9/7.0	10.0/6.0
Monogem	0.29	1.11	2.7/4.5	18.0/30.0
Vela	0.29	0.11	0.0/0.3	0.0/1.0

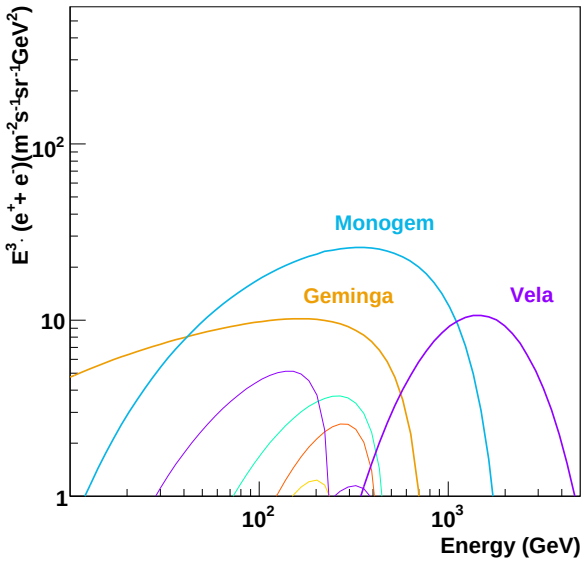

Figure 2.1: Contribution to the electron flux by the collection of pulsars considered in the BM2 setup , Table 2.3.

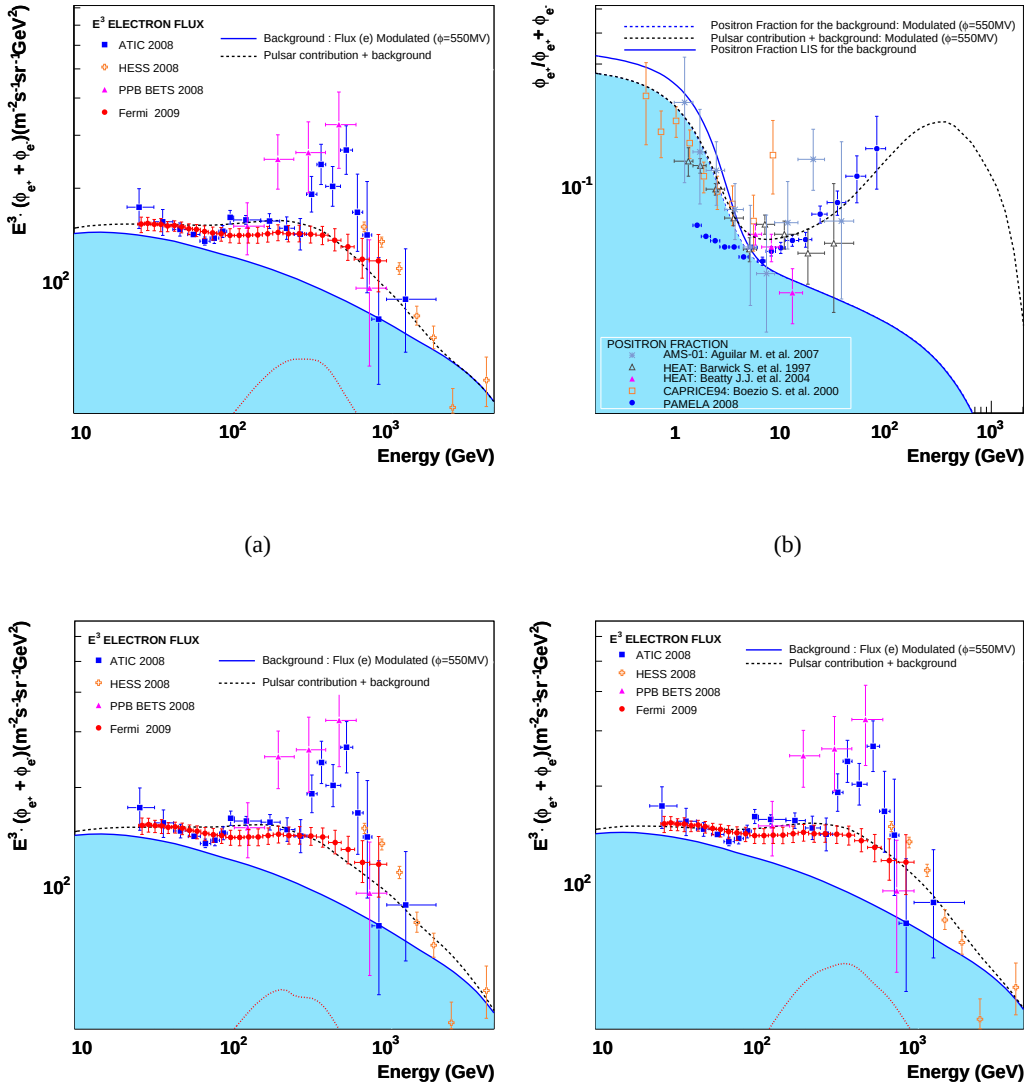

Figure 2.2: (a) and (b): Mature pulsar contribution for a burstlike injection. The efficiencies have been adjusted to $f_{\pm e}^{Monogem} = 18\%$, $f_{\pm e}^{Geminga} = 10\%$, $f_{\pm e}^{J2043+2740} = 0.1\%$. (c): Mature + young pulsar contribution to the $e^+ + e^-$ flux for burstlike injection. The efficiencies have been adjusted to $f_{Monogem}^{\pm e} = 30\%$, $f_{Geminga}^{\pm e} = 6\%$, $f_{J2043+2740}^{\pm e} = 0.1\%$, $f_{Vela}^{\pm e} = 1\%$. (d): Mature pulsar contribution to the $e^+ + e^-$ flux for continuous injection. The efficiencies have been adjusted to $f_{Monogem}^{\pm e} = 15\%$, $f_{Geminga}^{\pm e} = 6\%$, $f_{J2043+2740}^{\pm e} = 0.1\%$.

We introduce a delay Δt between the pulsar birth and the electron release to the interstellar medium for both sets of pulsars. For the BM1 setup $\Delta t \simeq 5\text{x}10^4$ years and $\Delta t \simeq 10^4$ years for the

BM2 setup which correspond to their injection time into the ISM.

The resulting fluxes are shown in Fig. 2.2 for the considered scenarios. In order to account for the experimental data in the hundreds of GeV, the conversion efficiency into pairs of Monogem and Geminga must be above the nominal value of 3% but inside the standard range (1-30%) considered in [80]. This values may change depending on the diffusion setup considered, the PWN $e^{\pm}$ release delay, pulsar cutoff, etc so it should be considered as a single realization of the multiple possibilities that can reproduce the data [67].

Pulsar Name	**d[Kpc]**	**T** $[10^5 \mathrm{years}]$	$\dot{E}[10^{34}\mathrm{erg/s}]$
J0633+1746	0.16	3.42	3.2
B0656+14	0.29	1.11	3.8
B0833-45	0.29	0.11	690.0
B0355+54	1.10	5.64	4.5
J2043+2740	1.13	12	5.6
J1740+1000	1.36	1.14	23.0
J0538+2817	1.39	6.18	4.9
B1055-52	1.53	5.35	3.0
J1549-4848	1.54	3.24	2.3
B1706-44	1.82	0.18	340
B1449-64	1.84	10.40	1.9
B0740-28	1.89	1.57	14.0
B0114+58	2.14	2.75	22.0
J0821-4300	2.20	14.90	3.3
J1046+0304	2.25	4.16	1.4
B1221-63	2.29	6.92	1.9
B2334+61	2.47	0.41	6.2
J1747-2958	2.49	0.26	250.0
B1951+32	2.50	1.07	370.0
B1719-37	2.51	3.45	3.3
J1830-0131	2.68	11.50	2.3
B0136+57	2.70	4.03	2.1
J1028-5819	2.76	0.90	83.0
B1046-58	2.98	0.20	200.0

Table 2.3: Gamma-Ray Pulsars from the ATNF Catalog. A subset from the collection of pulsars in the database is listed with d $<$ 3Kpc and 10^4 years $<$ T $<$ 10^7 years.

2.4 Dark Matter Source of High Energy Positrons

There is strong evidence toward the existence of huge amounts of non-visible matter at galactic scales from studies of the galaxy rotation curves [18]. According to the standard ΛCDM cosmological model, approximately a 22% of the energy content of the universe is in the form of Cold Dark Matter (CDM) [96]. If we consider that the same phenomenon may be taking place at such different scales, then the disc of our Galaxy could be embedded in a Dark Matter halo, as extensively investigated with high-resolution numerical simulations, and the result of the interactions between the halo constituents may produce signatures we can study.

Leading candidates to account for it are weakly interacting particles (WIMPs), with the neutralino and the Kaluza-Klein boson B^1 the most extensively studied ones. The relic density of these particles is determined by their annihilation cross section. Observations of the CMB and large scale structure surveys provide estimates of the relic density constraining the annihilation cross section up to a canonical value of $\langle \sigma v \rangle \approx 3 \times 10^{-26}\ \mathrm{cm}^3\mathrm{s}^{-1}$. This value sets the production rate of standard model particles, e.g. leptons, that can be measured as tracers of Dark Matter annihilation.

The signal that results from DM annihilation, depends on the squared DM density from the astrophysical side, and on the DM particle mass and cross section from the particle physics side. Since the annihilation rate depends on the squared density, the presence of clumpiness or substructure implies an enhancement of the signal compared to a smooth density distribution. The present Dark Matter structure is considered to have its roots in small amplitude quantum fluctuations during inflation. In the accepted "bottom-up" hierarchical structure formation, smaller clumps gather together to form larger systems, completely determined by the initial power spectrum of the primordial fluctuations. Galaxies are thus embedded in large Dark Matter halos that in turn are made up of self-bound substructure or subhalos.

The mass distribution, abundance and internal structure of clumps is determined by means of high-resolution numerical simulations as the Aquarius simulation [106]. In this section, we will model the DM halo as in Pieri et al. [94].

The total density of a DM Halo receives two contributions that can be described with a *smooth* and a *clumpy* components. Regarding the smooth component, it has been found that a Einasto profile provides good fits to the radial density profile:

$$\rho_{sm}(r) = \rho_s \exp\left[-\frac{2}{\alpha}\left(\left(\frac{r}{r_s}\right)^{\alpha} - 1\right)\right], \alpha = 0.17\ . \tag{2.11}$$

Regarding the contribution from the population of subhalos, the spatial and mass distribution of halos are well parametrized by:

$$\frac{d^2N_{sh}}{dMdV}(M,r) = A_{sh}(M/\mathrm{M}_{\odot})^{-1.9} \times \exp\left[-\frac{2}{\alpha}\left(\left(\frac{r}{R_a}\right)^{\alpha} - 1\right)\right], \alpha = 0.678, \tag{2.12}$$

which in terns of the number density $\rho_{\mathrm{sh}} = \frac{dN_{sh}}{dV}$:

$$\begin{aligned}\frac{d\rho_{\rm sh}(M_{\rm sub},R)}{dM_{\rm sub}} &= N_{cl}^{tot}\langle M_{cl}\rangle \frac{d\mathcal{P}_V(R)}{dV}\frac{d\mathcal{P}_m(M_{\rm sub},R)}{dM_{\rm sub}} \\ &= M_{cl}^{tot}\frac{d\mathcal{P}_V(R)}{dV}\frac{d\mathcal{P}_m(M_{\rm sub},R)}{dM_{\rm sub}}\ , \end{aligned} \tag{2.13}$$

where N_{cl}^{tot} is the total number of subhalos and $\langle M_{cl}\rangle$ their mean mass, and the mass and spatial probability distributions are normalized:

$$\int d\mathcal{P}_{\rm tot} = \int_{\rm MW} d^3\vec{x}\,\frac{d\mathcal{P}_V(R)}{dV}\int_{m_{\rm min}}^{m_{\rm max}} dm\,\frac{d\mathcal{P}_m(m,R)}{dm} = 1\ . \tag{2.14}$$

For what concerns the internal structure of the subhalo, it has been found that a Einasto profile with $\alpha = 0.17$ provides a good description of the radial inner profile in the resolved subhalos in the simulation [106]. The concentration parameter is fitted to a double power-law of the mass:

$$c_{200}(M,r) = \left(\frac{r}{R_{vir}}\right)^{-\alpha_R}\times\left(C1\left(\frac{M}{\mathrm{M}_\odot}\right)^{-\alpha_{C1}} + C2\left(\frac{M}{\mathrm{M}_\odot}\right)^{-\alpha_{C2}}\right), \tag{2.15}$$

where M is the mass of the clump and r the galactocentric distance. For Einasto profiles, one has that the scale radius $r_s = r_{200}/c_{200}$ and $\rho_s = M_{200}/\left(\int_0^{r_{200}} dr'\,4\pi r'^2 f(r')\right)$, with r' the clump's inner radial coordinate, $f(r')$ the clump inner density profile and r_{200} the radius which encloses an average density equal to 200 times the critical density of the universe. Once we have the clump mass M and the distance to the galactic center r, the clump inner density profile $\rho_{cl}(M,r,r')$ is defined unequivocally.

Given a subhalo of inner profile ${\rho_{\rm sub}}^{DM}$, the corresponding annihilation rate will be proportional to the *annihilation volume* ξ:

$$\xi_{\rm sub}(M_{\rm sub},R) \equiv 4\pi\int_{V_{\rm sub}} dr\,r^2\left[\frac{{\rho_{\rm sub}}^{DM}(r,M_{\rm sub},R)}{\rho_\odot}\right]^2. \tag{2.16}$$

Table 2.4: Parameters describing the characteristics of the Dark Matter Halo distribution from the Aquarius simulation as in [93],[94]. The three blocks in the table refer to parametrizations of 1) the smooth galactic halo, 2) the concentration parameter and 3) the galactic subhalo population.

R_{vir} [kpc]	433
M_{vir} [$M_\odot$]	$2.50 \cdot 10^{12}$
r_s [kpc]	20
ρ_s [$10^6 M_\odot \mathrm{kpc}^{-3}$]	2.4
$\rho_\odot$ [GeV cm^{-3}]	0.48
α_R	0.237
C1	232.15
C2	-181.74
α_{C1}	0.0146
α_{C2}	0.008
A_{sh} [$M_\odot^{-1}\mathrm{kpc}^{-3}$]	25.86
R_a[kpc]	199
N_{cl}	$1.17 \cdot 10^{15}$
$\frac{dP_V}{dV}(r_\odot)$ [kpc^{-3}]	$8.47 \cdot 10^{-8}$
$\langle\xi\rangle_M$ [kpc^3]	$7.19 \cdot 10^{-10}$
$M_{cl}^{tot}(< R_{vir})$ [$M_\odot$]	$4.33 \cdot 10^{11}$
$f_{cl}^{tot}(< R_{vir})$	0.18
$f_\odot$	$2.7 \cdot 10^{-3}$

With all these ingredients, the source term for the clumpy component can be written as:

$$Q_{sh}(E,R) = \frac{1}{2}\langle\sigma v\rangle \left(\frac{\rho_\odot}{m_{DM}}\right)^2 \mathcal{F}(E) N_{cl} \frac{d\mathcal{P}_V(R)}{dV} \int_{m_{\min}}^{m_{\max}} dm\, \xi_{\mathrm{sub}}(m,R) \frac{d\mathcal{P}_m(m,R)}{dm}, \quad (2.17)$$

and for the smooth component:

$$Q_{sm}(E,R) = \frac{1}{2}\langle\sigma v\rangle \left(\frac{\rho_\odot}{m_{DM}}\right)^2 \mathcal{F}(E) \left(\frac{\rho_{sm}(R)}{\rho_\odot}\right)^2, \quad (2.18)$$

where $\mathcal{F}(E) = \sum_k f_k(E) = \sum_k \frac{dN_k^{e^+}(E)}{dE}$ denotes the number of positrons generated per annihilation and energy interval (for each branching channel k).

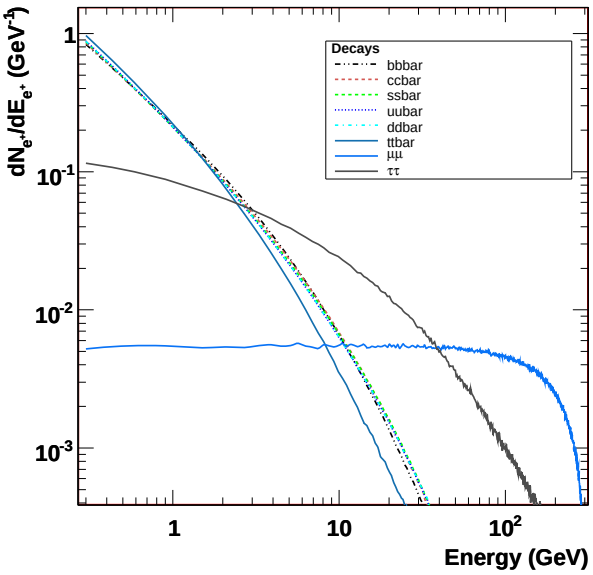

Figure 2.3: Decays spectra $f_k(E) = \frac{dN_k^{e^+}(E)}{dE}$ for some particular channels, calculated with Pythia [103], [104] with a *injection* energy of 300GeV.

Finally, the relative contribution to the total source term Q(E,R), and hence, the local flux, is performed using the local *clump fraction* $f_\odot = \frac{M_{tot}}{\rho_\odot}\frac{d\mathcal{P}_V(odot)}{dV}$ and the total clump fraction $f_{cl}^{tot} = \frac{M_{cl}^{tot}}{M_{vir}}$. For more details we refer the reader to [93] and [94].

Once we have the source term we proceed to calculate the flux at the Earth by solving the steady state ($\frac{\partial}{\partial t}n(E,\vec{x}) = 0$) of Eq.2.2. As already done e.g in [16], the equation can be solved turning the energy evolution into an evolution over a pseudo-time $\tilde{t}$.

$$\tilde{t} = \tau_E \frac{E^{\gamma-1}}{1-\gamma}, \tag{2.19}$$

where $\tau_E \equiv 1/a = 10^{16} GeV s$ and γ is the exponent of the energy dependence of the diffusion index.

The equation then reads:

$$\frac{\partial \psi}{\partial \tilde{t}} - D_0 \Delta\psi = \tilde{Q}(\vec{x},\tilde{t}), \tag{2.20}$$

where $\psi = E^2 n$ and $\tilde{Q} = E^{2-\gamma}Q$. This equation is analogous to the heat equation with positrons evolving with the pseudo-time $\tilde{t}$. The solution of this equation can be obtained in the Green function formalism, where the probability for a positron with monochromatic injection energy E_s initially

located at $\vec{x}_s$ to reach the observer position $\vec{x}$ with energy $E \leq E_s$, is described by the Green function $G(\vec{x}, E \leftarrow \vec{x}_s, E_s)$. The solution is then given by the convolution of the Green function over the sources $Q(\vec{x}_s, E_s)$.

$$n(\vec{x}, E) = \int_E^\infty dE_s \int_{Halo} d^3\vec{x}_s G(\vec{x}, E \leftarrow \vec{x}_s, E_s) Q(\vec{x}_s, E_s). \tag{2.21}$$

We can relate the positron propagator $G(\vec{x}, E \leftarrow \vec{x}_s, E_s)$ with the propagator of the heat equation $\tilde{G}(\vec{x}, \tilde{t} \leftarrow \vec{x}_s, \tilde{t}_s)$

$$G(\vec{x}, E \leftarrow \vec{x}_s, E_s) = \frac{\tau_E}{E^2} \tilde{G}(\vec{x}, \tilde{t} \leftarrow \vec{x}_s, \tilde{t}_s), \tag{2.22}$$

where the propagator of the 3D heat equation is just

$$\tilde{G}(\vec{x}, \tilde{t} \leftarrow \vec{x}_s, \tilde{t}_s) = \left\{ \frac{1}{4\pi D_0 (\tilde{t} - \tilde{t}_s)} \right\}^{3/2} \exp\left\{ -\frac{(\vec{x} - \vec{x}_s)^2}{4 D_0 (\tilde{t} - \tilde{t}_s)} \right\}, \tag{2.23}$$

with a typical diffusion length $D_{diff} = \sqrt{4 D_0 (\tilde{t} - \tilde{t}_s)}$

The positron flux at the Earth is then $\phi_\odot(E) = \frac{\beta c}{4\pi} n(\vec{x}_\odot, E)$

$$\phi_\odot(E) = \frac{\beta c}{4\pi} \frac{\tau_E}{E^2} \int_E^\infty dE_s \int d^3\vec{x}_s \left\{ \frac{\mathcal{A}}{(E^{\gamma-1} - E_s^{\gamma-1})} \right\}^{3/2} \exp\left\{ -\mathcal{A} \frac{(\vec{x}_\odot - \vec{x}_s)^2}{(E^{\gamma-1} - E_s^{\gamma-1})} \right\} Q(\vec{x}_s, E_s), \tag{2.24}$$

where $\mathcal{A} = \frac{1-\gamma}{4\pi D_0 \tau_E}$. As previously stated, PAMELA data favors leptophilic DM, i.e., candidates whose annihilation products are predominantly leptons. The case of direct annihilation into electron and positron pairs can provide good fits to the ATIC data but it must be excluded if we take into account the Fermi results due to a sharp drop at the end-point (see e.g. [85]). Therefore we are left with annihilations into $\mu^\pm$ and $\tau^\pm$ which provide a much softer injection spectrum and can accommodate both PAMELA and Fermi. For such injection spectra, large annihilation rates are required. The astrophysical boost factor, i.e, boost based on the presence of clumpiness, has been proved to be insufficient to account for the required normalization to adjust the data. In this respect, proposals of particle physics boost factors as velocity dependent cross sections, have been recently considered.

For our purpose, which is to evaluate the expected anisotropy resulting from sources that reproduces the observed abundances, we will assume the required normalization to fit the data as a result of any of the considered mechanisms that can boost the annihilation rate. Here, we consider a DM

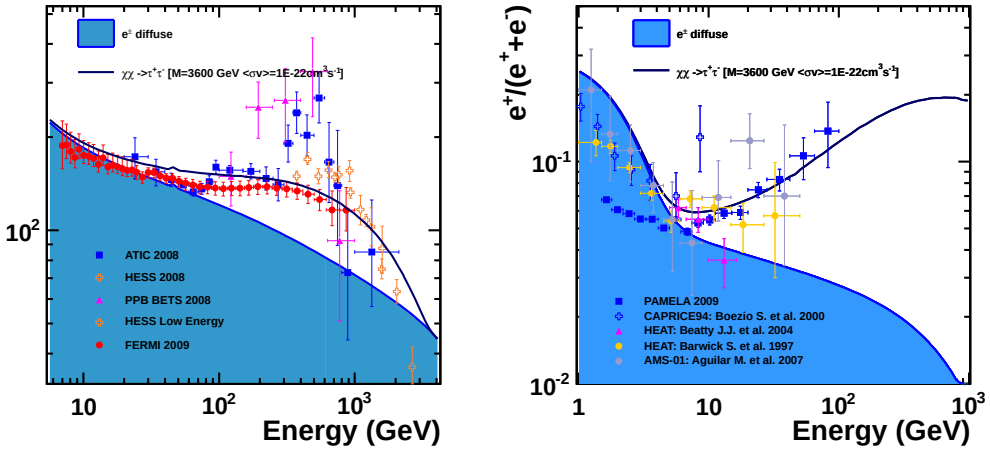

(a) (b)

Figure 2.4: DM halo contribution to the electron spectrum as described in the text. In each figure the blue flooded area denotes the background whereas the blue solid line accounts for the DM contribution over the background. Annihilation into $\tau^+\tau^-$ with a cross section $\langle\sigma v\rangle = 1\text{x}10^{-22}\text{cm}^3/\text{s}$. The considered DM mass $M_{DM} = 3.6$ TeV within MED diffusion setup. (a): $E^3 \cdot (e^+ + e^-)$ (b): Positron Fraction

candidate that annihilates into $\tau^\pm$ with a mass of 3.6 TeV (Fig. 2.4) which has been boosted $\mathcal{O}(10^3)$ with a cross section of $10^{-22} cm^3 s^{-1}$.

We also address the possibility of a nearby DM clump being the responsible of the bulk of positrons found in the Fermi, ATIC and PAMELA data. For this purpose, we treat here the clump as a point-like object at a given distance *d* contributing to the source term with luminosity *L* in the same fashion as already done in [25]. This possibility has been found to be very unlikely unless the Sommerfeld effect is at play, but such a source would imprint a signature in the electron arrival direction that could constitute a signal of Dark Matter annihilation in case of the absence of pulsars in the neighborhood. In this sense, the evaluation of such a signal makes the study meaningful. The expected flux for a clump of DM annihilating into $\tau^\pm$ or $\mu^\pm$ with masses around 3 TeV and 2 TeV respectively can reproduce the Fermi data with the drop observed by Hess, and with slightly different normalizations the PAMELA data. As a possibility, we show the flux produced by the annihilation in the $\tau^\pm$ channel of a DM clump located at 0.9 Kpc with a DM mass of 3.6 TeV. In this case, as in a pulsar scenario, a MED diffusion setup is appropriate, as the MIN and MAX cases show prominent bumps in the spectrum at high and low energies respectively, that are not observed in the Fermi data.

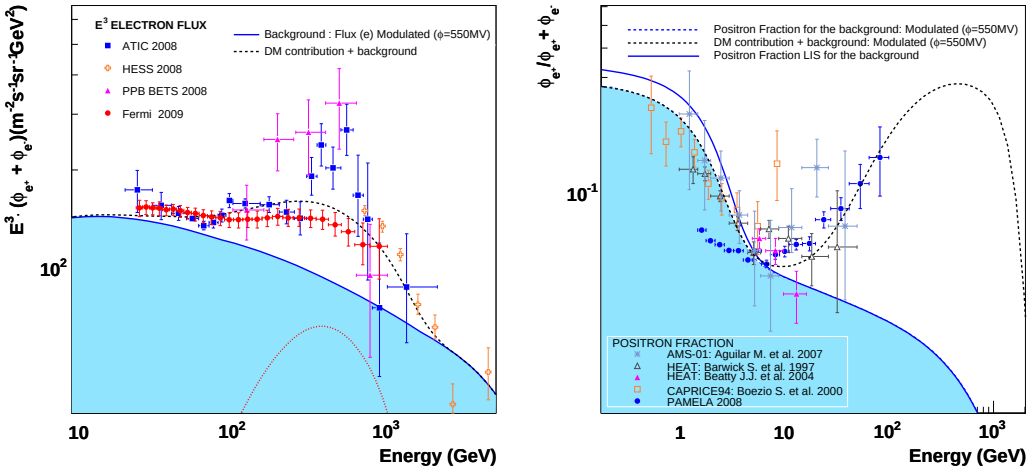

(a) (b)

Figure 2.5: DM point-like source contribution to the electron spectrum. In each figure the blue solid line stands for the background whereas the black dashed line accounts for the DM contribution over the background to the total flux. The red dashed line denotes the DM contribution to the total flux. The blue dashed line that bounds the blue flooded area denotes a modulated positron fraction for the background. DM clump situated at d=0.9Kpc. MED diffusion setup and luminosity $L = 1.0\text{x}10^{9}\text{M}_{\odot}^{2}\text{pc}^{-3}$. We assume a DM candidate of mass 3.6 TeV that annihilates into $\tau^{+}\tau^{-}$ with cross section $\langle\sigma v\rangle = 3\text{x}10^{-25}\text{cm}^{3}/\text{s}$ (a): $E^{3}\cdot(e^{+}+e^{-})$ (b): Positron Fraction

2.5 Anisotropies

So far, large scale anisotropies of CR have been measured to be less than 1% [7], but it is known that if they were produced by sources with some spatial structure, small anisotropies should be present in the arrival directions and could be correlated to the potential sources, whether they be known or not. In the case of high energy electrons, very light charged particles, diffusion competes with large energy losses resulting in relatively short paths $\mathcal{O}$(Kpc), so it is expected that we can use them to sample only sources within a certain distance and age. The cosmic ray intensity can, in general, be expanded over the celestial sphere in spherical harmonics. At first order, when we have a marked directionality, we have a dipole anisotropy as could be the case of a single source dominating the spectrum. In this case, the intensity can be expressed as

$$I(\theta) = \bar{I} + \delta\bar{I}\cos\theta, \tag{2.25}$$

where $\bar{I} = 1/2(I_{max} + I_{min})$ being this maximum and minimum intensities related to a forward-backward measurement[2].

The calculation of the anisotropy produced by a single source in a diffusive process, has been carried out by Mao et al.[82] and is given by:

$$\delta_i = \frac{3D}{c} \frac{\mid \nabla N \mid}{N}, \tag{2.26}$$

where $D(E)$ is the diffusion coefficient and N is the electron number density.

In the search for anisotropies, several channels can be considered. On the one hand, anisotropy can be searched for in the all lepton flux $N = N_{e^+} + N_{e^-}$ à la Fermi. On the other hand, the search can be conducted in separate e^+ and e^- populations, or even in the ratio N_{e^+}/N_{e^-} à la AMS-02.

The sensitivity for every of these searches can be estimated, simply comparing the expected signal, i.e. the degree of dipole anisotropy, with purely statistical fluctuations which are $\propto \sqrt{N_{evts}}$.

We can describe the number density $N_{e^\pm}$ by an isotropic diffuse component $N^d_{e^\pm}$ and a source component that is not isotropic $N^s_{e^\pm}$. The estimation of the anisotropy in the fluxes is straightforward from Eqn. 2.26, as only the anisotropic component of N (that is, the signal) is left in the gradient. If we assume that the primary source (which is anisotropic by definition) produce electrons and positrons in equal numbers ($N^s_{e^+} = N^s_{e^-} = N^s$), then the expected anisotropy will be diluted as in table 2.5:

Table 2.5: Anisotropy dilution factors and expected statistical accuracy for each channel.

Channel	**Anisotropy Intensity**	**Dilution Factor**	**Expected Accuracy**
Positron	N^s	$N^d_{e^+} + N^s$	$\sqrt{N^d_{e^+} + N^s}$
Electron	N^s	$N^d_{e^-} + N^s$	$\sqrt{N^d_{e^-} + N^s}$
Lepton	$2 \cdot N^s$	$N^d_{e^+} + N^d_{e^-} + 2 \cdot N^s$	$\sqrt{N^d_{e^+} + N^d_{e^-} + 2 \cdot N^s}$

Considering that the positron fraction above 10 GeV is $\mathcal{O}(10\%)$, then we expect the positron channel to be the best suited for anisotropy searches, being the least diluted.

In order to illustrate this point, in Fig. 2.6 we show the sensitivity in 5 years to a dipole anisotropy in the three channels listed in table 2.5 for a Fermi-like experiment considering a pulsar source distribution as in section 2.3.

Estimates of the expected anisotropy in the case of a dominant pulsar have been previously shown in e.g. [26],[74] but they fail to take into account the possible effects that could arise from a

[2]The dipole anisotropy parameter $\delta = \frac{I_{max}-I_{min}}{I_{max}+I_{min}}$ where if $I(\theta) = I_0 + I_1 \cdot \cos(\theta)$ then $\delta = \frac{I_1}{I_0}$. The fluctuations $\frac{I(\theta,\phi)-\langle I\rangle}{\langle I\rangle} = \frac{I_1}{I_0}\cos(\theta)$, can be expanded $\frac{I(\theta,\phi)-\langle I\rangle}{\langle I\rangle} = \sum_{\ell=0}^{\infty}\sum_{m=-\ell}^{\ell} a_{\ell m}\, Y_{\ell m}(\theta,\phi)$ yielding $\delta = 3\sqrt{\frac{C_1}{4\pi}}$ where $C_1 = \frac{1}{3}\sum_{m=-1}^{1}(a_{1m})^2$ is the first order term of the angular power spectrum

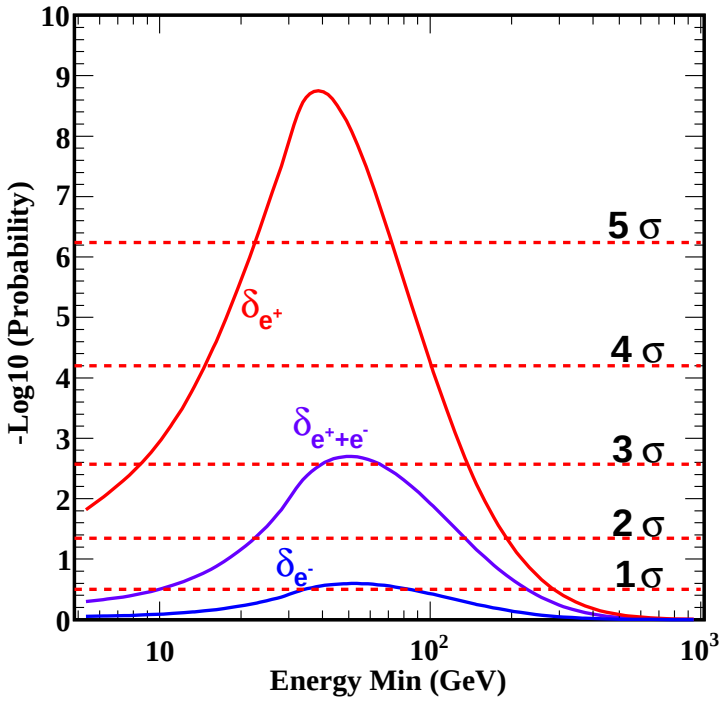

Figure 2.6: Probability that an observed anisotropy δ as expected from a distribution of pulsars as in section 2.3 is due to a fluctuation of an isotropic distribution of events, for the leptonic channels listed in table 2.5.

realistic collection of pulsars; there could be e.g. systematic cancellations. We have calculated the anisotropy in the case of a collection of pulsars taken from the ATNF catalog and in the framework of Dark Matter annihilation of clumps throughout the halo, both in the case of a dominating point-like source or a distribution of clumps. In the presence of an isotropic background plus a number of contributing sources to the total flux, the expected dipole anisotropy is given by :

$$\delta = \frac{\sum \phi_i(E,r,t)\langle \delta_i \hat{r}_i \hat{n}_i \rangle}{\phi_T}, \tag{2.27}$$

where the index i runs over all the discrete sources that contribute to the full dipole. The product $\langle \delta_i \hat{r}_i \hat{n}_i \rangle$ represents the projection of the individual dipole over the direction of maximum intensity that is energy dependent and $\phi_T(E,r,t)$ denotes the total flux observed at Earth. The projection can be easily calculated taking into account the angular separation θ of two sources on the celestial sphere given by:

$$\theta = \arctan\left(\frac{\sqrt{A_1^2 + A_2^2}}{\sin\delta_1 \sin\delta_2 + \cos\delta_1 \cos\delta_1 \cos(\alpha_2 - \alpha_1)}\right), \tag{2.28}$$

where $A_1 = \cos\delta_2 \sin(\alpha_2 - \alpha_1)$, $A_2 = \cos\delta_1 \sin\delta_2 - \sin\delta_1 \cos\delta_2 \cos(\alpha_2 - \alpha_1)$ and the right ascension and declination are denoted by α_i and δ_i.

In our model, we evaluate the anisotropy (Fig. 2.7) produced by the collection of pulsars considered in Fig. 2.2 (a) for a MED diffusion setup. The dipole anisotropy will change direction depending on the energy, but the main contributor to the full dipole is shown to be Monogem above a few tens of GeV up to the TeV and in second place Geminga. A big contribution to the anisotropy (and the positron flux) can be expected also at higher energies by younger objects like Vela or CTA1, although it is still unclear if such an object can produce a sizable amount of electrons due to the PWN confinement.

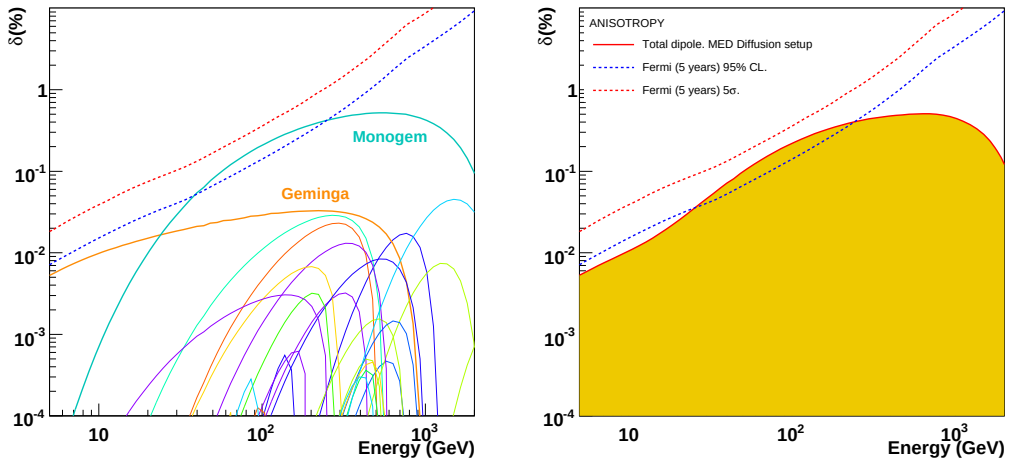

Figure 2.7: Individual (Left) and Full (Right) dipole anisotropy in the electron + positron spectrum for every pulsar considered in Fig. 2.2 and Table 2.3 for a MED diffusion setup. We also show the Fermi sensitivity to such an anisotropy at the 2 (blue dashed) and 5 (red dashed) σ CL in 5 years.

The full dipole (Fig. 2.7) will be given by the projection of the individual anisotropies in the direction of the maximum intensity at each energy, resulting in a clear signal in the direction of Monogem at energies above 20 GeV. The contribution due to Geminga has a stacking effect to the full anisotropy due to the relative position between it and Monogem, so, changes in their individual contributions to the flux, codified for instance in the pair conversion efficiency, should not change the anisotropic pattern. Contributions from other pulsars don't result in a systematic addition of their signal to the full anisotropy into a particular direction due to their spatial distribution, so they constitute a kind of isotropic background. In this scenario, measurements of a possible privileged in-

coming direction should point out an excess in the Monogem/Geminga direction, roughly opposite to the direction of the Milky Way (MW) center.

It is possible however that we could be observing the contribution of some yet undiscovered pulsars that could show up in a potential study of anisotropies. In this respect, searches for Gamma-Ray sources as the one conducted by Fermi will help to support or disfavor the test. In any case it is expected for an astrophysical source that the dipole anisotropy should be relatively constrained to the galactic plane, tracing the distribution of visible matter.

In the case of a DM Halo contributing to the full dipole, as in the case of the Aquarius simulation, due to the symmetry of the clump distribution we would expect a dipole anisotropy in the direction of the MW center. The expected dipole anisotropy [28] will be given by:

$$\delta = \frac{1}{\phi_T} \int \phi(E, \mathbf{r}) \langle \delta_{clump}(\mathbf{r}) \mathbf{n} \rangle d^3\mathbf{r}, \tag{2.29}$$

where $\langle \delta_{clump}(r) n \rangle = \frac{6D(E)}{cD^2_{diff}}(r_\odot - r\cos\varphi)$ is the projection of the clump contribution to the full dipole in the direction of the MW center and r,φ are the cylindrical coordinates of the clump distribution.

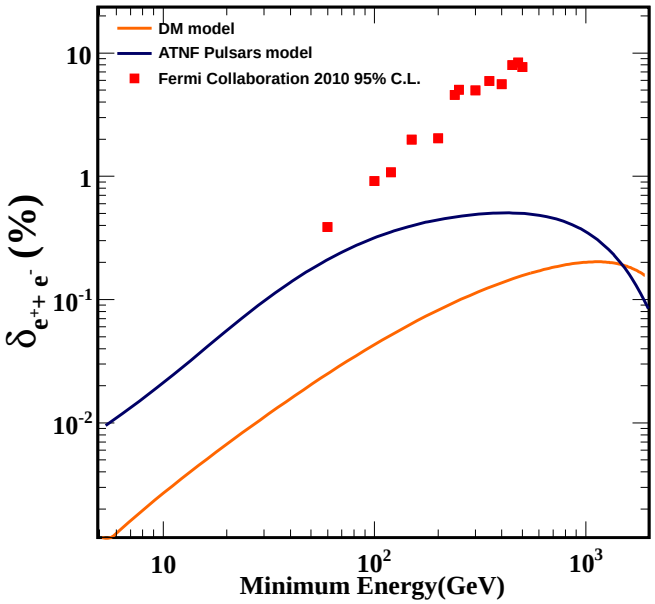

Figure 2.8: Dipole anisotropy in the electron + positron spectrum produced by the population of pulsars (Blue) in comparison with a distributed DM source considered in Fig. 2.4 (Orange). We also show the Fermi current upper limits on $e^+ + e^-$ dipole anisotropy [54].

Then the expected dipole anisotropy in the $e^+ + e^-$ flux for the pulsar and DM scenarios can be computed. For the sake of simplicity, we will derive the dipole anisotropy for the parametrizations used in the previous sections. In figure 2.9 the expected anisotropy for both $e^{\pm}$ sources is shown together with current limits from the Fermi collaboration [54]. We expect anisotropies at the few *permil* level at intermediates energies for a pulsar source, and about 10 to 5 weaker in a general DM scenario.

We can also consider a DM point source as responsible of the bulk of PAMELA and Fermi electrons as could be the case of a large DM clump [25] or minispikes around an intermediate mass black hole [24]. This scenario allows a more unconstrained anisotropy not restricted to the galactic plane, as we are tracing the DM halo. In this case the expected anisotropy is reduced to $\delta = \frac{\phi(E,r)\delta_{pointsource}}{\phi_T}$ where $\delta_{pointsource} = \frac{6D(E)d}{cD^2_{diff}}$ being d the distance to the source (Fig. 2.9).

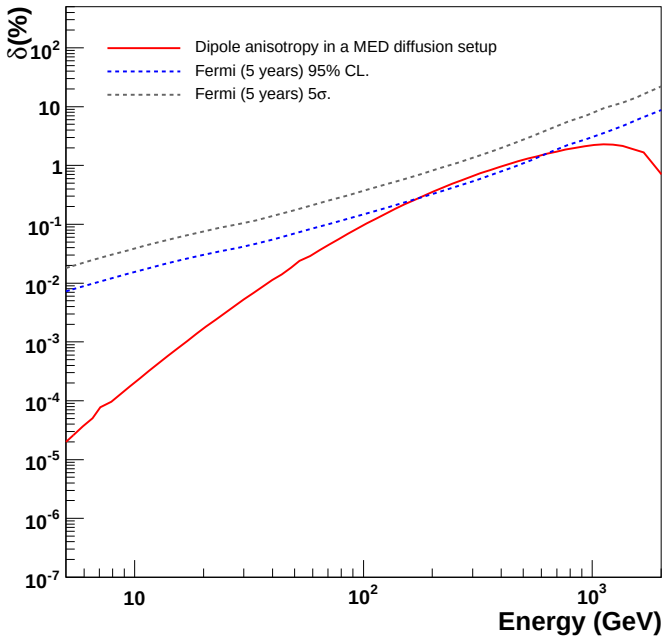

Figure 2.9: Dipole anisotropy in the electron + positron spectrum from the DM point-like source as considered in Fig. 2.5. We also show the Fermi sensitivity to such an anisotropy at the 2 and 5 σ CL in 5 years.

Although the probability of finding such a bright clump in our neighborhood is rather small, there are some scenarios, with the Sommerfeld effect at play, where this probability can be boosted up to 15%. In this case, the anisotropy would exceed the 2σ level pointing toward the existence of a dominant source. This measurement should also be complemented with searches for Gamma-Ray emission to achieve a consistent prediction.

2.6 Conclusions

A number of possibilities have been proposed as potential candidates to account for the positron excess. From the standard astrophysical point of view, pulsars seem to be the most promising candidates. Just considering the already known Gamma-Ray pulsars is enough to explain the spectrum for reasonable model assumptions. In particular, two nearby pulsars, Geminga and Monogem, provide good fits to the data with conversion efficiencies of $\eta \sim 10 - 20\%$.

For a DM scenario, the contribution from the annihilation in the halo can reproduce the observed patterns once we have solved the required normalization issue by means of particle physics boosts on the thermal averaged cross section. To do this, annihilation through leptonic channels is mandatory in order to satisfy the antiprotons constraints.

In these models, the measured spectrum can be reproduced and no clear signatures can be found to distinguish between a Dark Matter scenario and pulsars, as the spectral shape seems to lack information of the origin of the $e^{\pm}$. In order to distinguish between the proposed candidates the study of anisotropies is proposed. Different channels can be used in the anisotropies search: $e^+ + e^-, e^+, e^-, e^+/e^-$, being the positron channel the most interesting due to lower isotropic backgrounds.

We have analyzed the expected anisotropy from a configuration of pulsars selected from the ATNF catalog and also derived the anisotropy in a general Dark Matter scenario, both in the case of a very bright point source and in the case of a clumpy distribution as illustrated by N-body simulations. For the DM point-like source and the pulsar scenarios, future observations should be able to detect a dipole anisotropy at 2σ CL in five years at least. On the other hand, we would expect an excess toward the MW center in the case of a clumpy halo as the main contributor to the primary positron flux, however, the degree of anisotropy would be well below the expected sensitivity of current observations.

In summary, we expect a sizable anisotropy in a pulsar scenario towards the galactic anticenter, roughly in the Geminga and Monogem direction. A tiny anisotropy may be also present in a DM halo scenario toward the galactic center. If we consider a large contribution from a clumpy-like source, the anisotropy may be enhanced and be directed in general out of the galactic plane.

Anisotropies have been shown to be a valuable tool to disentangle the positron excess problem, nonetheless there are still many of theoretical uncertainties (e.g. the Dark Matter halo distribution or the mechanism of pair production in pulsars). It must be borne in mind that we have not taken into account the proper motion of the pulsars or even that of the Dark Matter clumps, which could result in an enhancement or suppression of the anisotropy. Moreover, the case of a dipole anisotropy toward a pulsar cannot exclude a Dark Matter scenario, as it is possible to have a large Dark Matter cloud in the same direction masking the signal. In any case, the precise study of $e^{\pm}$ anisotropies should be conducted together with pulsar surveys to help to discriminate between astrophysical and more exotic sources.

II

THE AMS EXPERIMENT

3

The AMS Experiment

THE Alpha Magnetic Spectrometer (AMS) is a general-purpose high energy particle detector which aims for high precision studies of cosmic rays. From its privileged location on the ISS (International Space Station), it takes advantage of the virtually background free environment that characterizes experimentation in space to address some of the open fundamental questions in modern particle physics such as the asymmetry of matter-antimatter and the nature of the Dark Matter content in the universe.

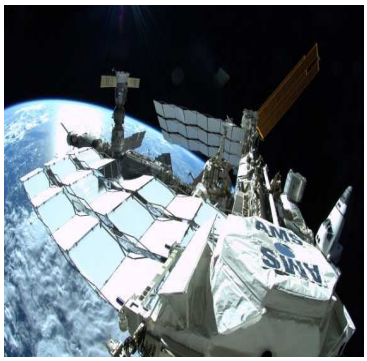

3.1 Introduction

The AMS experiment is an international collaboration which involves 64 institutions from 16 countries across Europe, America and Asia. The AMS scientific goals include the search for primordial antimatter, the pursuit of the nature of Dark Matter, and precision measurements of the composition of cosmic rays which will contribute to the understanding of their origin and propagation in the Galaxy, but first and foremost, AMS will search for new physics phenomena that could not be reached from ground-based experiments.

AMS was first proposed by MIT physicist Nobel laureate Samuel Ting, and approved by the U.S. Department of Energy (DOE) in 1995. The goal of the project was to install a magnetic spectrometer in space, which followed an agreement between NASA, responsible of the space transportation,

installation, and supervision of all safety critical issues, and the AMS collaboration, in charge of the detector design, operation, and the scientific exploitation of the results. For these purposes, the experimental programme was originally scheduled in two phases: a precursor flight on the space shuttle and a long exposure period on the ISS.

In June 1998, a prototype to study the feasibility of the project, AMS-01, was flown on board the space shuttle Discovery for a 10-day mission which validated the overall design. After completion of the first stage of the experiment, the tragic loss of Space Shuttle Columbia in 2003 put into severe restrictions the future orbital missions and thus the continuation of the second phase of the project, AMS-02. Finally, in January 2009, NASA restored AMS-02 to the shuttle manifest and on May 16th 2011 AMS-02 was flown on board the Space Shuttle Endeavour, mission STS-134, to the International Space Station and was deployed on May 19th at the upper Payload Attach Point on the S3 Truss of the International Space Station (ISS) (Fig.3.1). Shortly after deployment, AMS started data taking. Since then, AMS has been continuously collecting science data at the ISS in a low Earth orbit (altitude $\sim$ 360Km) with a full sky coverage, at an average rate of 500 Hz [1] (Fig 3.2) that are already providing unprecedented statistics in the field of high energy cosmic ray physics.

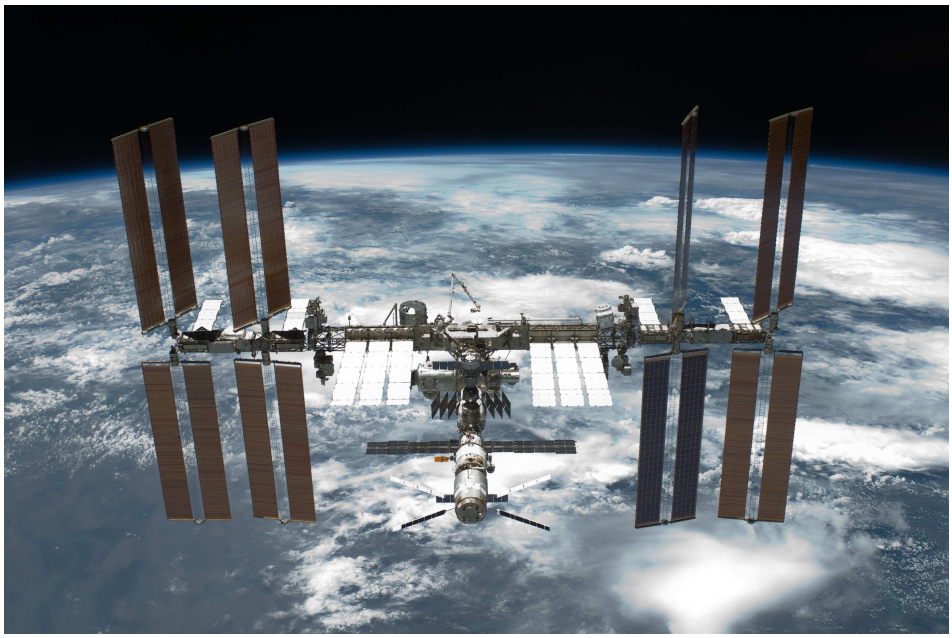

Figure 3.1: AMS-02 Detector Installed in the ISS Truss.

AMS main goal is the study of Antimatter, for which it has been specifically designed.

On the one hand, AMS-02 particle identification capabilities allows for precise determination of the spectra of rare CR components (e^+,$\bar{p}$,$\bar{D}$,γ). Distortions on the spectra of these faint signals can arise from the annihilation or decay of Dark Matter particles, thus providing evidence of their

[1] In the first 5 weeks, it had already collected 1.5 $\times 10^9$ triggers from cosmic-rays

existence and clues to their properties. On the other hand, AMS will search for Antimatter of primordial origin, looking for the presence of anti-nuclei such as $\overline{\mathrm{He}}$ in cosmic-rays. The measurement of an anti-helium nuclei could be a direct proof of the existence of antimatter domains, due to the extremely low probability of $\overline{\mathrm{He}}$ production by spallation [30].

Finally, AMS will perform high statistic measurements of charged cosmic rays with isotopic separation which will help to greatly improve our understanding of CR propagation. The current modelization of the origin and propagation of CR in our Galaxy aims to describe all primary and secondary component fluxes and diffuse γ-ray spectra within a single model with a number of free parameters (Galactic disk and Halo size properties, injection spectra etc...) that can be constrained with measurements of the elemental and isotopic spectra in a wide energy range.

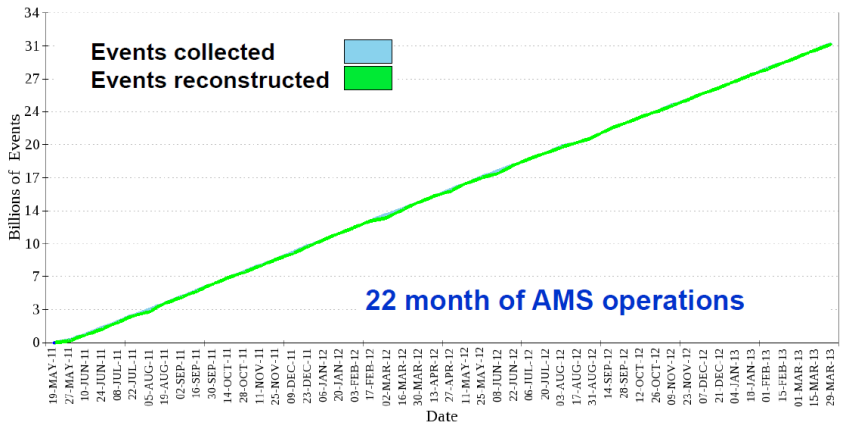

Figure 3.2: AMS-02 Number of events reconstructed (green) and transferred (blue): 31×10^9 events collected from 19th May to 29th March, 2013.

3.2 The Precursor Flight

The AMS detector prototype, AMS-01, was flown for a 10-day mission on the Space Shuttle Discovery, STS-91. The primary goals of the mission were testing the spectrometer design principles and gaining experience on its operation in space.

AMS-01 was composed of:

- **A Silicon Detector** to measure the sign of the charge and the momentum of the charged particles.
- **A Permanent Magnet** to provide the trajectory bending of charged particles needed for the momentum determination.

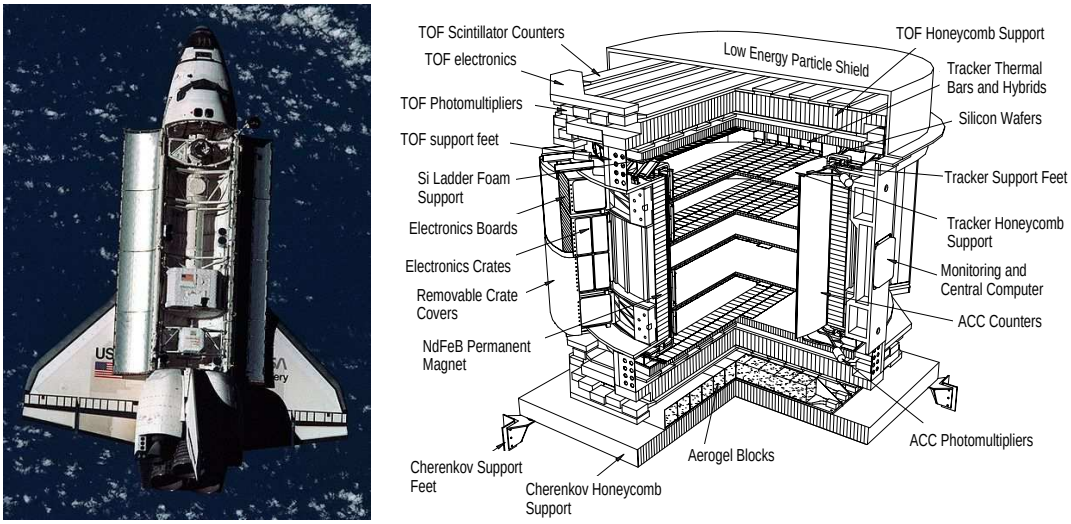

Figure 3.3: Left: AMS-01 on board the NASA Space Shuttle Discovery. Right: Schematic view of the components of the AMS-01 detector.

- **A Time of Flight** to measure the velocity of the charged particles and to provide the trigger of the experiment.
- **An Anticounter system** to veto particles out of the fiducidal volume of the spectrometer.
- **A threshold Cerenkov detector** to separate low velocity from high velocity particles.

The highly successful AMS-01 flight fulfilled the original goals and collected over 80 million events which rendered significant scientific results .

- Cosmic-ray positron fraction measurement from 1 to 30-GeV with AMS-01 [42] (Fig 3.4): The success of the measurement of the positron fraction in space set the benchmark for future experiments in space such as PAMELA, and laid the ground for the second part of the project, AMS-02.
- Search for Antihelium in Cosmic Rays [34]: A total of 2.86×10^6 Helium nuclei were observed with no anti-helium candidate found. This measurement set the upper limit of the the ratio of the $\overline{\mathrm{He}}$/He relative fluxes of 1.1×10^{-6} at 95% C.L. (Fig 3.5), where the same spectra for both species was assumed.
- Protons in Near Earth Orbit [38].
- Leptons in Near Earth Orbit [37].
- Cosmic Protons [35].

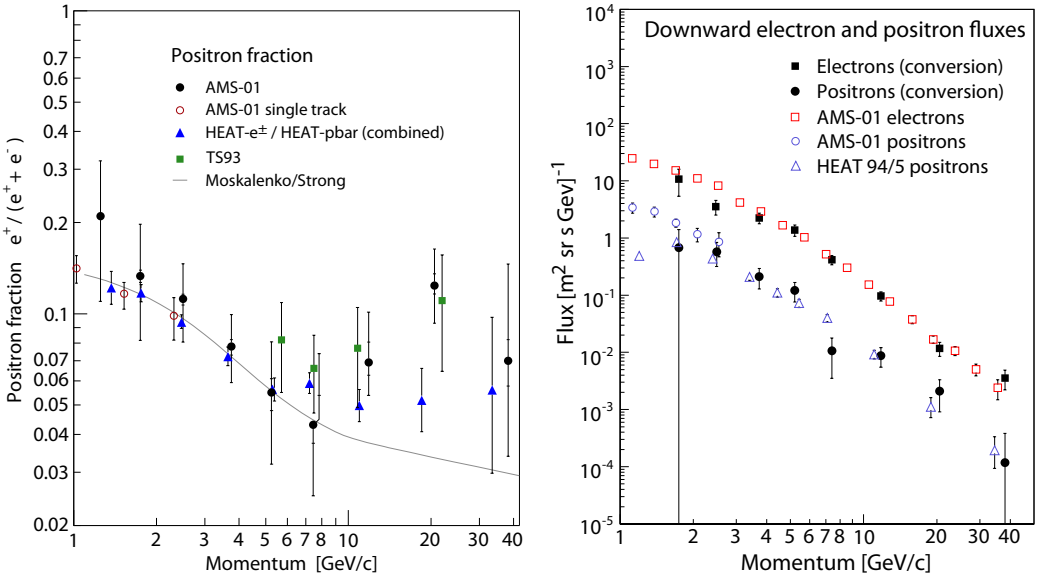

Figure 3.4: Left: Positron fraction measured by AMS-01 compared to earlier results. Right: Electron and Positron absolute fluxes measured by AMS-01 compared to earlier results.

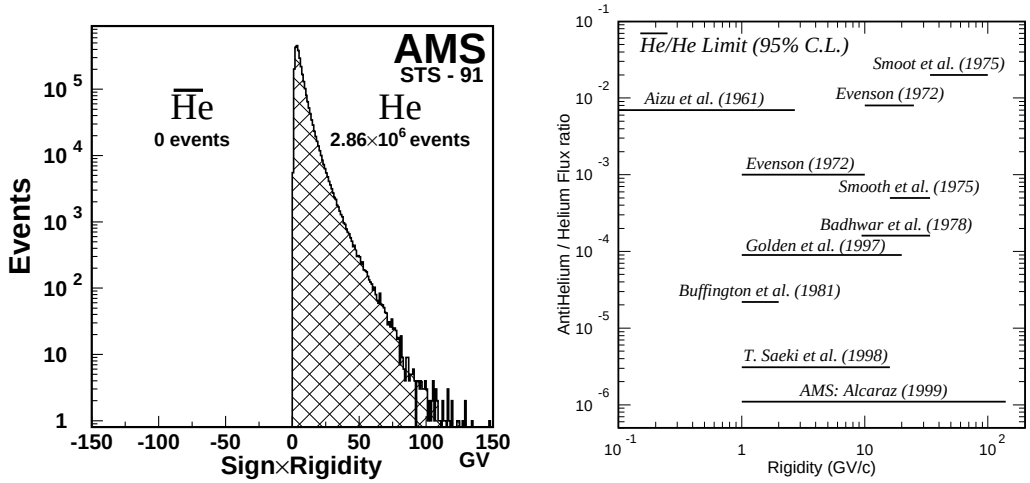

Figure 3.5: Left: Rigidity × Charge sign for Z=2 events for anti-helium searches with AMS-01. Right: Upper limit at 95% C.L. for the $\bar{He}/He$ ratio set by AMS-01.

- Helium in Near Earth Orbit [36].
- A study of cosmic ray secondaries induced by the Mir space station using AMS-01 [39].
- Isotopic Composition of Light Nuclei in Cosmic Rays [41].

- Relative Composition and Energy Spectra of Light Nuclei in Cosmic Rays [40].

3.3 Second Phase: The AMS-02 Detector

The AMS-02 detector is a large acceptance magnetic spectrometer designed to perform precision measurements of charged cosmic-rays in space (Fig. 3.6).

Figure 3.6: AMS-02 Zoom-In View at the ISS Truss.

The detector has been designed for a long duration mission on the ISS, with a lifetime matching that of the International Space Station (until 2020 or longer). In addition to the intrinsic constraints of space-born detectors, AMS has to deal with weight and power supply budgets from the shuttle transportation and ISS boarding limitations. Specifically, the detector dimensions are 5x4x3 m^3 with a total weight of 7500 kg. The allocated power is 2 kW and the data down-link rate to ground is in average 10Mbps.

The potential of the detector's particle identification capabilities relies on the redundancy in the measurement of the particle properties with the different sub-detectors. The main components of the spectrometer as displayed in Fig. 3.7, are:

- **Permanent Magnet**: The particle bending in the magnetic field is provided by a permanent magnet generating a field $\sim 0.15\mathrm{T}$ at the center of the system.

- **Silicon Tracker (STD)**: A set of nine planes of silicon detectors which determine the coordinates of the points used to reconstruct the tracks.

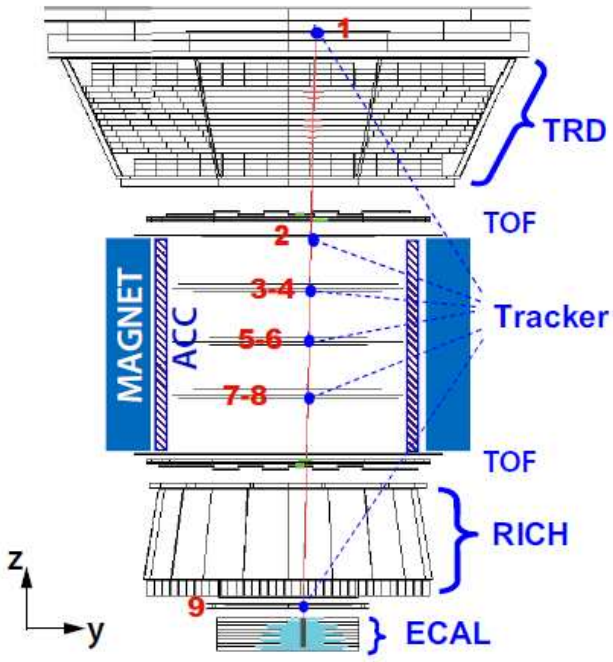

Figure 3.7: AMS-02 Schematic Layout

- **Anti-Coincidence Counters (ACC)**: An array of anticoincidence counters covering the inner part of the magnet provides the veto for the non fiducidal trajectories in AMS.

- **Time of Flight (TOF)**: The time of flight is measured by a hodoscope of Time of Flight scintillation counters (TOF) which also provides a measurement of the particle's velocity. The TOF is also providing the trigger of the detector.

- **Transition Radiation Detector (TRD)**: Designed to distinguish between light and heavy particles of the same charge and momentum, and in particular, between positrons and protons.

- **Ring Imaging Cerenkov Detector (RICH)**: Provides a measurement of the particle velocity with a precision of 10^{-3} allowing for isotope identification.

- **Electromagnetic Calorimeter (ECAL)**: Allows for an accurate distinction between leptons and hadrons and energy determination of electromagnetic particles up to $\sim$TeV.

The electronics contain 650 microprocessors for data reduction which scales down the raw-data volume, by a factor 1000 without science information loss, and thus allows its direct down-link to ground.

3.3.1 The Permanent Magnet

The AMS Permanent Magnet (PM) has the shape of a cylinder like vessel 80cm height, with an inner radius of 111.5cm and an outer radius of 129.9cm.(Fig 3.8).

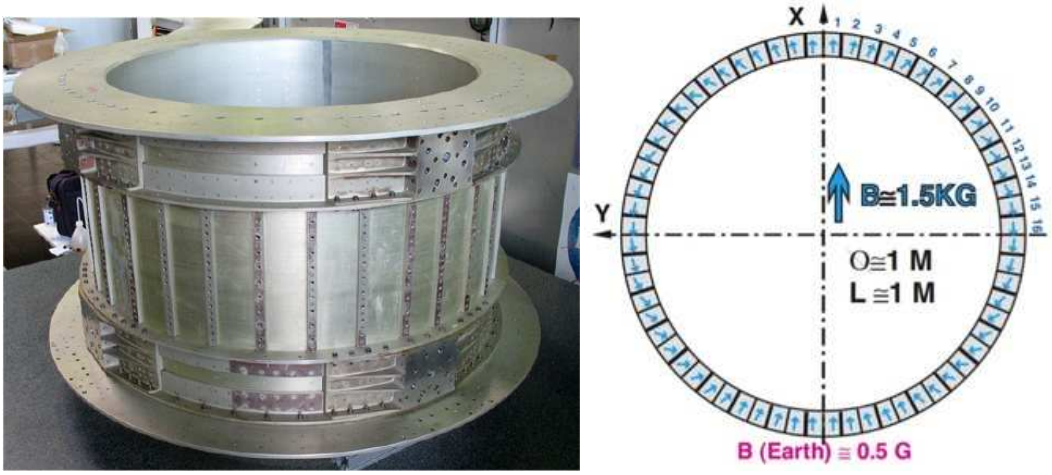

Figure 3.8: Left: AMS-02 permanent magnet. Right: PM Magnetic Field orientation. The detector coordinate system has been chosen according to the magnetic field.

It is composed of 64 high-grade Nd-Fe-B sectors. Each sector is composed of 100 blocks of $5.08 \times 5.08 \times 2.54\mathrm{cm}^3$ which are glued together with epoxy. The Nd-Fe-B magnets are among the strongest permanent magnets, and the AMS Permanent Magnet is able to develop a dipole magnetic field of 0.15 T with a negligible dipole moment [2]. In addition, the field outside the magnet is small enough to comply with the strict NASA safety regulations concerning fringe magnetic field on the ISS. [3].

The Permanent Magnet provides also the reference frame for AMS as depicted in figure 3.8. The X coordinate is parallel to the magnetic field, the Y coordinate runs in the bending direction and the Z direction goes along the cylinder axis.

3.3.2 The Silicon Tracker Detector (STD)

The AMS-02 tracking system is composed by silicon sensors covering an effective area of $6.4m^2$ which allows for a particle track trajectory determination with an accuracy better than $10\mu m$ in the bending direction (Y), and $30\mu m$ in the non-bending one (X).

The silicon tracker is able to precisely measure the curvature of particles in the magnetic field hence providing a rigidity measurement $R = pc/|Z|e$. It is composed of 2264, $41 \times 72 \times 0.3\mathrm{mm}^3$,

[2] A non negligible dipole moment could result in a significant force on the apparatus.

[3] The magnetic field has been measured to be <3G at 2 meters distance from the center of the magnet.

double-sided silicon microstrip sensors grouped in 192 double-sided *ladders*, the basic unit which contains read-out electronics and mechanical support.

On opposite sides of the silicon sensors, strips p^+ (junction) and n^+ (ohmic) strips are deployed along orthogonal directions. The p side runs along the ladder length and are daisy chained up to the ladder end, where are connected to the read-out chips. The n side strips are also encroached to the ladder end by means of a kapton cable, which covers the signal from the sensors to the same readout channel. P-side strips provide the measurement in the bending coordinate and the n-side strips measure the non-bending coordinate, thus, each silicon sensor measures the coordinate of a particle in two orthogonal directions simultaneously.

Each of these ladders is ensembled in a total of 9 layers which contains ~ 200000 read-out channels. Layers 3-8 in figure 3.7 are supported by three planes of low density aluminum honeycomb covered with carbon fiber skins that match the cylindrical shape inside the magnetic field. Each of these planes is equipped with two layers of silicon ladders.

The other three planes, numbered 1, 2 and 9 in figure 3.7 are equipped with one layer of silicon ladders and are located respectively on top of the TRD, on the top of the magnet and in-between the RICH and the ECAL separated by a distance of about 3m. Planes from 2-8 in figure 3.7 constitute the *Inner* tracker and are enclosed with a thermally stable carbon fiber structure.

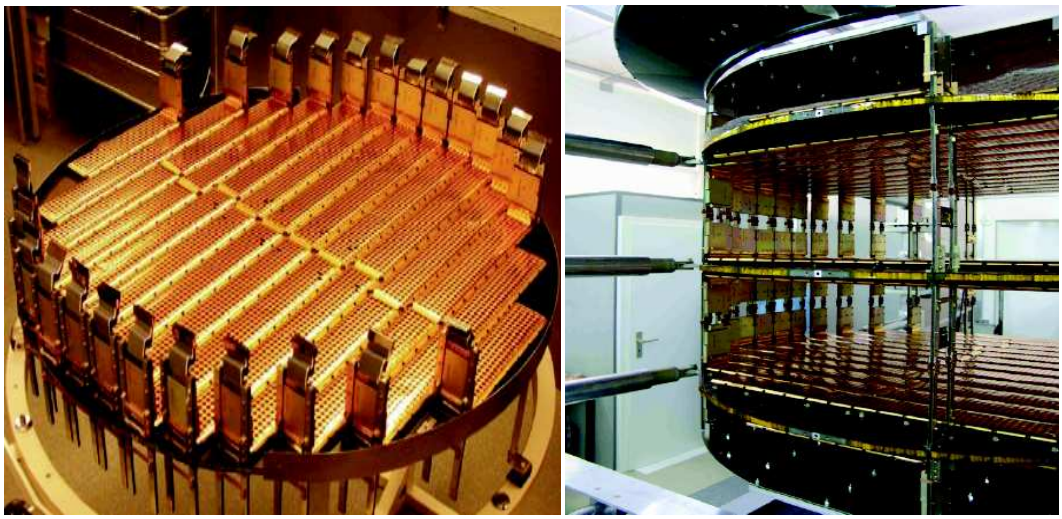

Figure 3.9: Left: Tracker silicon ladders in a single plane. Right: Three inner planes consisting on double-sided layers equipped with silicon-detectors

The mechanical stability of the seven layers in the inner tracker is critical to maintain the required resolution of the silicon tracker. The stability is monitored using an optical laser system, the tracker alignment system (TAS) which is mounted outside the inner tracker volume, and allows for the determination of module displacements with an accuracy better than $5\mu\mathrm{m}$. Finally, the tracker layers are dynamically aligned using cosmic-ray protons to an accuracy of $3\mu\mathrm{m}$.

The Tracker rigidity resolution has been estimated with MC simulation. In particular, the 100% relative error[4] is reached for protons and Helium at 2000GV and 2700GV respectively for a Tracker configuration including layers 1 and 9.

3.3.3 The Transition Radiation Detector (TRD)

The AMS-02 TRD is located above the upper Time-of-Flight and it is attached to the support structure of AMS on top of the magnet vacuum case.

The sub-detector is composed on a fleece radiator and straw tube proportional wire chambers which efficiently captures the transition radiation produced in the radiator. It consists on 5428 straw tubes of 6mm diameter which are arranged in 328 modules of sixteen straws and mounted on 20 layers, interleaved with a 20mm fiber fleece radiator material. All the structure is supported in a conical shaped octagon structure, built out of a carbon fiber/aluminum honeycomb sandwich.

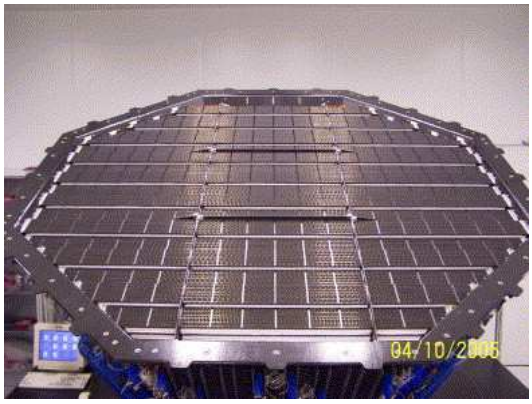

Figure 3.10: TRD: Octagon structure with all 328 straw modules integrated.

The upper and lower 4 layers run parallel to the magnetic field direction (X view) while the central 12 layers run in the orthogonal direction (Y view), thus providing a 3D tracking capability.

The fleece radiator is built with 10μm thick propylene fibers (LTP 375 BK) with a density of 0.06g/cm^3, which provides a 50% photon emmision probability in the X-ray region. The straw tubes are filled with a Xenon/CO_2 gas mixture which collects the X-ray photons and the ionization radiation as well.

Two vessels storing the mixture that fill the gas circuit, hold a total of 48 kg of Xe and 5Kg of CO_2. This, in addition to the measured leak rate of the gas filling the tubes of 6μg/s, mainly due to diffusion of the CO_2 through the tube walls, ensures an effective lifetime of more than 20 years in space.

The TRD provides an independent proton rejection capability of 100-1000 for a 90% efficiency in order to separate positrons from hadrons in the 1.5-300 GeV energy range.

[4]This rigidity value is often referred as maximum detectable rigidity (MDR)

3.3.4 The Time of Flight (TOF)

The Time of Flight system consists of four layers of fast plastic scintillator counters, arranged in two planes which covers the full AMS-02 acceptance. Given its large acceptance, it is in charge of the fast trigger (FT) of the detector, which is the first level of the data acquisition chain. Additionally, it provides an independent measurement of the particle β in the low energy region ($\sigma \sim 4\%$), and an independent measurement of the absolute value of the particle charge up to Z=20.

Figure 3.11: TOF system of AMS-02. UTOF and LTOF are separated by a distance of 1.2m

The TOF has a characteristic time resolution $\sim$ 160ps which is good enough to separate downward and upward particles at the 10^{-9} level. Finally, the TOF system also flags cosmic-rays with Q>1, rejecting protons at the trigger level without interfering the measurement of the high charge component of CR.

The two planes of TOF are situated at the top of the magnet bore (Upper TOF: UTOF) and at the exit (Lower TOF: LTOF). Each plane consists of two scintillator layers built of 8-10 paddles of 1cm thickness, 12cm wide and variable length (117-134 cm), which are partially overlapped to avoid geometrical inefficiencies.

The four layers of scintillation paddles are oriented in orthogonal directions in order to guarantee a granularity of 12x12cm^2.

The light produced when a particle crosses a paddle is collected at both ends of the counter. Each paddle is optically coupled with 2 to 3 photomultiplier tubes on each side for redundancy. The PMTs have been chosen with a high magnetic field tolerance to minimize the effect of the strong magnetic field generated by the magnet. The scintillators are coupled at both ends via plexiglass

light guides to the photomultipliers.

3.3.5 The Ring Imaging Cherenkov (RICH)

The Ring Imaging Cherenkov detector is designed to separate charged isotopes in cosmic rays by measuring their velocity β with a precision of $\Delta\beta/\beta = 0.1\%$. It is also targeted to measure the particle absolute charge up to Z<26.

The RICH consists of a layer of radiator material, a conical reflector and a detection plane. When charged particles cross the radiator at a velocity greater than the Cherenkov threshold, a cone of Cherenkov radiation is emitted. The emitted photons are detected by an array of PMTs which covers a detector plane after an expansion length of 46.8 cm. To increase the reconstructed efficiency, a truncated conical mirror covering the lateral structure is used to collect the emitted photons that otherwise would escape its acceptance, and direct them to the detector plane. With this addition, the reconstruction efficiency is increased as $\sim$ 30% of the photons are reflected on it and re-directed towards the detector plane. The reflective material is a mixture of 100nm aluminum and 300nm of $\mathrm{SiO_2}$ with a reflectivity of 85% at $\lambda = 420$nm.

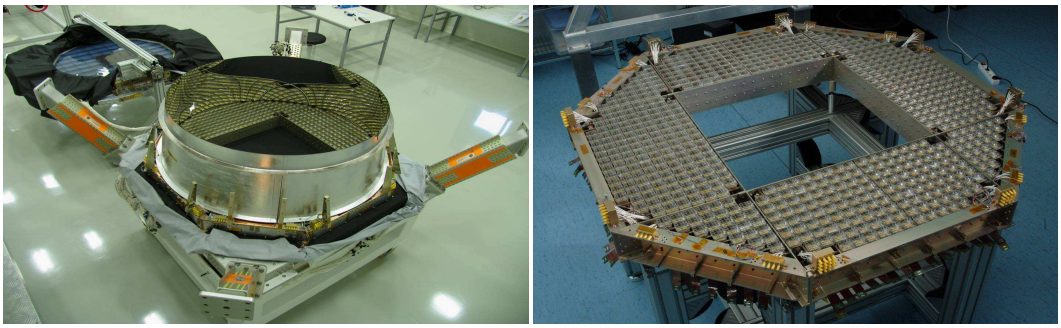

Figure 3.12: Left: RICH conical mirror Right: PMT detection plane

The radiator holds 92, 2.5-thick tiles of Aerogel (n = 1.05) and a central square built of 16, 0.5cm-thick tiles of NaF (n = 1.334). The central section boosts the photon detection efficiency due to the higher emission angle of the Cherenkov cone of the NaF. It also serves to increase the detector dynamical range as a result of a threshold velocity of $\beta = 0.75$.

At the lower part of the RICH, the detector plane supports a set of 680 4x4 multi-anode PMTs equipped with independent light-guides, adding up to a total of 10880 channels with a section of 4x4 mm^2 each. The central part of the detector plane, is not instrumented to reduce the interaction length of particles in the ECAL geometrical acceptance.

3.3.6 The Anti Coincidence Counter (ACC)

The Anti Coincidence Counter is composed by an array of 16 paddles arranged in a cylindrical shell surrounding the silicon tracker within the magnet bore. The main tasks of the ACC are to exclude tracks outside the AMS-02 geometrical acceptance, to suppress triggers originating from secondary particles produced by the interaction of primary particles with the detector structure, and to reduce the trigger rate in periods of high flux, e.g. the South Atlantic Anomaly.

The ACC paddles are composed of scintillator plastic (Bicron BC-414) of 826 x 826 x 8mm arranged in order to form a cylinder of a diameter of 1.1 m. Photons produced in the scintillator are collected in wavelength shifter fibers of 1mm diameter, which are embedded in grooves milled into the scintillation panels. At both ends of each paddle, the wavelength shifter fibers are grouped into two bundles of 37 fibers each, that drive the scintillation light to the PMT photocathodes.

The ACC is instrumented with 16 PMTs, 8 at the top and 8 at the bottom. These PMTs are very similar to the ones used in the TOF in order to minimize the effect of the strong magnetic field on the photomultiplier. The very high efficiency and a high degree of homogeneity of the scintillating fibers ensure a reliable and fast ACC veto trigger for high inclination particles.

Figure 3.13: Left: ACC panel production Right: The Anti-Coincidence Counter integration in the Vacuum Case.

3.3.7 The Electromagnetic Calorimeter (ECAL)

The AMS-02 Electromagnetic Calorimeter is a fine grained sampling calorimeter built out of lead and scintillating fiber which allows a precise tracking capability and a 3D imaging of the longitudinal and transverse components of development of electromagnetic showers.

The main task of the ECAL is to provide an accurate measurement of the particles energy, and to reject hadrons from electromagnetic particles. In addition, the ECAL also provides a stand-alone gamma trigger which efficiently [5] identifies gamma-rays. The ECAL is composed of lead foils of 1mm thick and scintillator fibers of 1mm diameter glued together with epoxy in a sandwich-like

[5] 90% at 2GeV and above 99% for energies greater than 10GeV

shape with an average density of 6.83 $\mathrm{g/cm^3}$ and a total weight of 487 kg. The lead-scintillator pancake has an active area of 638x648 $\mathrm{mm^2}$ and a thickness of 166.5 mm ($\sim 16.7\mathrm{X_0}$) and its arranged in 9 superlayers of 18 mm thick. The imaging capability is obtained by stacking the superlayers with fibers running along orthogonal views : X axis (5 layers) and Y axis (4 layers).

Each superlayer is read out by 36 2x2 multianode Hamamatsu PMTs arranged at both opposite ECAL edges. Each PMT channel covers an area of 9x9 $\mathrm{mm^2}$ corresponding to $\sim$35 fibers, defined as cell. This unit divides ECAL into 18 layers with a total of 1296 cells (324 PMTs), allowing for a precise sampling of the shower profile with 18 independent measurements. The AMS-02 calorimeter structure has been developed to achieve a high λ/X_0 ratio (the radiation length X_0 $\sim$1cm and the nuclear interaction length λ $\sim$26cm). This ratio is proportional to $Z^{4/3}$ being this, one of the reasons to use Pb in the construction of the ECAL.

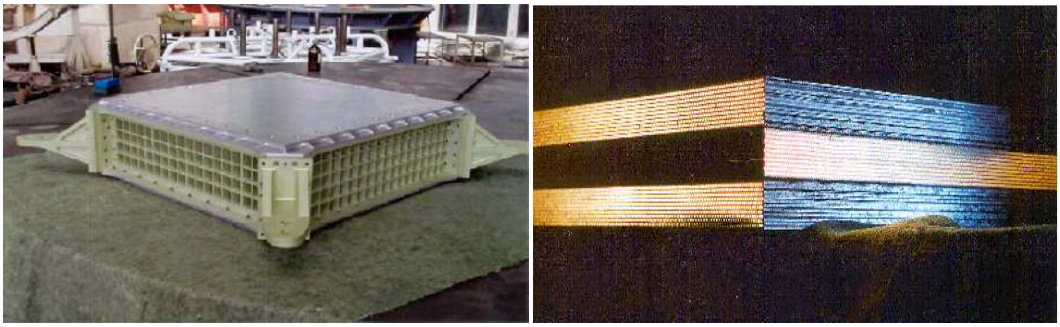

Figure 3.14: Left: Ecal Structure Right: Ecal superlayers.

With this design, an almost complete containment of electromagnetic showers is ensured. On the other hand, about $\sim$ 50% of the protons escape the calorimeter without interact (MIPs) while the remaining ones develop hadronic showers which are only partially contained. The hadronic interaction probability P in the ECAL:

$$\mathrm{P} = 1 - \mathrm{e}^{-\mathrm{T}/\lambda} \sim 0.4, \tag{3.1}$$

where T is the absorber depth. With this design, the rejection factor for hadrons up to the TeV is $\sim 10^4$.

Additionally, the ECAL also provides tracking capabilities with an angular resolution that has been measured to be $\sim 1^\circ$ for electromagnetic showers.

The ECAL energy resolution for high energy electrons has been measured in TB conditions and is well parametrized by:

$$\sigma(E)/E = \sqrt{(0.104)^2/E + (0.014)^2}. \tag{3.2}$$

For the estimation of the energy, the signals are processed over a wide dynamical range that goes from the very small energy deposition of MIPs (with $\sim$ 8 photoelectrons), to the TeV scale (with $\sim 10^5$ photoelectrons). To achieve this performance, the calorimeter front end electronics has

been designed in two gain modes: High gain for low energy measurements and low gain for highest ones. The ratio of high to low gain is HG/LG$\sim$33.

Finally, the ECAL can also be used as a standalone photon detector.

4

Performances of AMS-02 Detector for e/p Rejection

THE measurement of cosmic ray positrons has to deal with a proton background that is $10^3 - 10^4$ times larger than the e^+ signal.
This chapter describes the analysis performance for e/p separation and how the main background can be suppressed with the electromagnetic calorimeter, the transition radiation detector and the silicon tracker. The selection introduced in this chapter will be used in the positron fraction analysis that will be presented in chapter 5.

✧ ✧ ✧

4.1 Introduction

The dominant backgrounds for the positron selection are on the one hand protons, which constitute the bulk of the Cosmic Rays, and on the other hand charge confused electrons. In this chapter we will describe the selection that deals with the former one and introduce the sub-detectors involved in the positron fraction analysis. The latter one will be addressed in chapter 5. We present the performances of the TRD, ECAL and Tracker to suppress the proton component, the major source of background contamination to the positron signal. We begin by introducing the preselection that will be used throughout all the analysis stages. The classifiers used in the analysis are also described, and their performances are evaluated on signal and background flight data samples.

We take advantage of AMS-02 redundancy for e/p discrimination to obtain clean control samples from flight data for the evaluation of the sub-detectors performances. In particular, a clean sample with high statistics for the signal (positrons) can be obtained from electrons, which we assume to be identical to positrons aside from the charge sign. These samples in turn allow us to

evaluate the sub-detectors selection efficiencies for signal and background.

At high energies, the electron sample, selected as Rigidity < 0, is not a pure sample as a result of the proton contamination due to charge sign confusion (CC) in the Tracker. Clean samples and in particular clean reference distributions of the ECAL for the signal can be obtained though with tight cuts on the TRD, and conversely, reference distributions of the TRD can be obtained with tight cuts on the ECAL. With this procedure it is possible to study the subdetectors performances using flight data.

Finally, a clean sample of protons selected as Rigidity > 0 can be obtained easily using the same strategy, as protons are at least 10 times more abundant than any other CR component.

4.2 Data Sample

AMS-02 data taking started on 2011 May 19 at 9:30 CDT. Since then, AMS has been continuously recording data, collecting in the first 22 months over $31{\cdot}10^9$ events. Reported results are based on the data collected from 2011 May 19 to 2012 December 10, for a period of nearly 18 months. In order to use the AMS-02 full discrimination capabilities, we select events inside the ECAL geometrical acceptance (which represents $\sim 10\%$ of the full acceptance [98]).

4.3 Data Preselection

A common preselection is used in all the positron fraction study as well as to estimate the sub-detector performances in the analysis. The aim is to use a reduced tractable volume of AMS data with a very high efficiency on the signal, reducing the background as much as possible.

Throughout this analysis, we require a cluster of hits in the ECAL, and a track in the TRD and Tracker. We also accept only particles transversing the detector from the top of AMS. This is performed demanding a measured velocity $\beta \sim 1$ with the TOF consistent with a downward particle.

Along the orbit, AMS effective time of data acquisition (DAQ), *livetime*, varies as a result of the input rate (fig. 4.1), and the operating conditions. We apply a cut on the livetime, which ensures us to be under nominal operation conditions. Furthermore, it is an effective way to avoid the South Atlantic Anomaly (SAA), an anomalous geomagnetic location with a very high rate of low energy particles which are not representative of the LIS positrons and would spoil the measurement of the positron fraction.

In addition, low energy secondary particles are produced by the collision of cosmic rays in the atmosphere. To study this contribution, the Earth geomagnetic field plays a major role, as only particles above a threshold rigidity can go through it. This rigidity has been introduced in chapter 1 is called the geomagnetic cutoff and depends on the location of the orbit and the particle's incidence

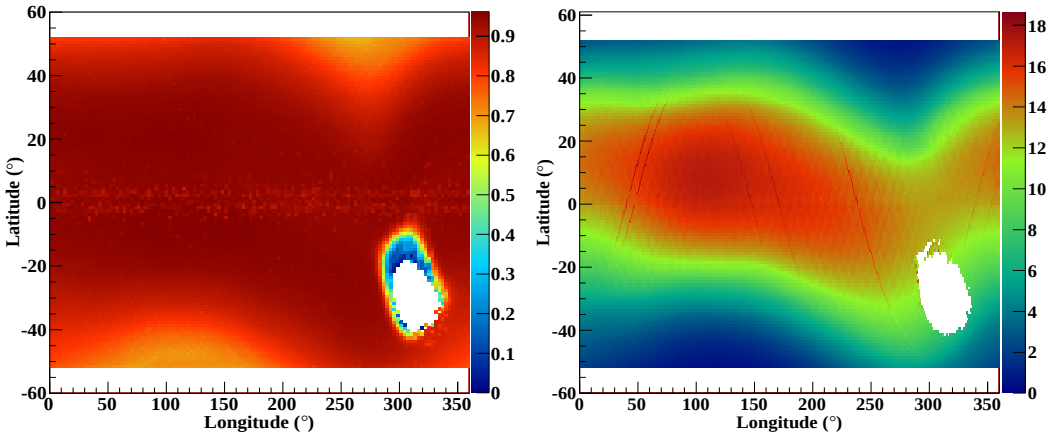

Figure 4.1: Left: AMS-02 Livetime (Left) and Maximum IGRF cutoff rigidity (Right) upper limits for positive and negative charged particles as a function of the geographical longitude and latitude. The SAA can be clearly spotted with a low livetime and the geomagnetic poles as well.

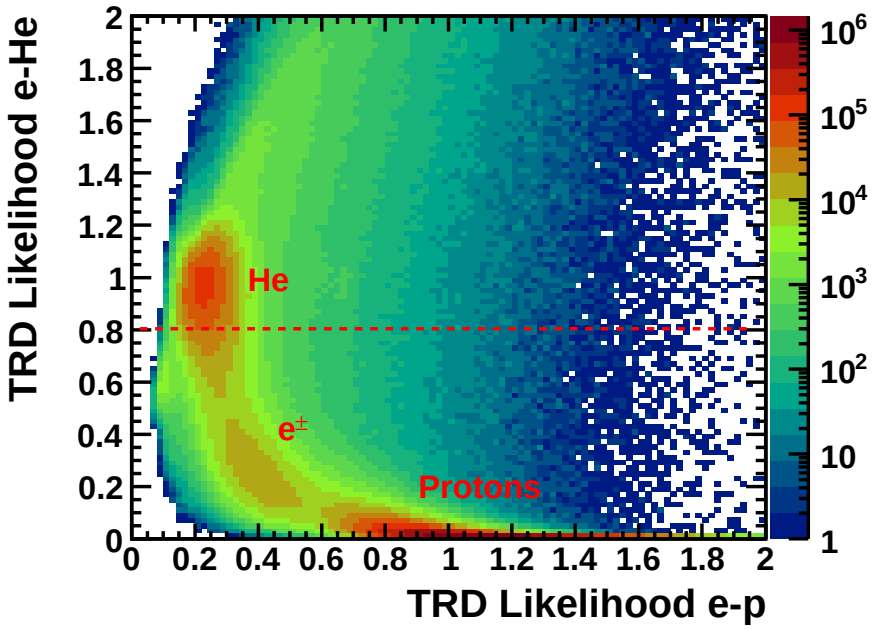

Figure 4.2: Protons, Helium and $e^{\pm}$ in the TRD Likelihoods map. A cut on TRD Likelihood e-He is used to clean the sample from Helium.

Table 4.1: Preselection cut statistics and cumulative events fractions I.

Total	**Minimum Energy**	**Beta**	**Livetime**
2200013703	460647890	351580036	348672087
(%)	(%)	(%)	(%)
100.0	20.9	16.0	15.6

angle. A cut on the geomagnetic cutoff rigidity [1] has been included to avoid under-cutoff particle contamination in the sample. To further ensure no contamination of under-cutoff particles is present in the sample, a safety factor of 30% above the considered cutoff rigidity has been applied. This factor has been validated by back-tracing a reduced sample of the selected events in the Earth's magnetic field. This cut will be used in the positron fraction analysis, nonetheless we avoid it for e/p rejection studies, as it correlates the reconstructed energy in the ECAL and the rigidity in the Tracker.

Table 4.2: Preselection cut statistics and events fractions II calculated respect Preselection I.

Cut	**Events** $(\times \mathbf{10^6})$	**First cut Ev. Frac. (%)**	**Cumulative Ev. Frac.(%)**	**Relative Ev. Frac.(%)**
Preselection I	348.7	100.0	100.0	100.0
Energy > $1.3 \cdot \mathrm{R_{Cutoff}}$	134.8	38.6	38.6	38.6
Number of Tracker tracks = 1	110.1	88.4	31.6	81.7
Tracker track χ^2_X < 10	106.1	88.6	30.4	96.3
Tracker track χ^2_Y < 20	104.0	89.8	29.8	98.1
Inner Tracker charge < 1.5	79.3	80.6	22.8	76.3
ECAL Fid. Volume $\mathrm{X_{ecal}} < 31\mathrm{cm}$	75.0	88.6	21.5	95.2
ECAL Fid. Volume $\mathrm{Y_{ecal}} < 31\mathrm{cm}$	71.6	88.8	20.5	95.5
Tracker - ECAL Matching X < 3cm	55.6	40.8	15.9	77.6
Tracker - ECAL Matching Y < 10cm	54.9	46.2	15.7	98.8
TRD track nHits > 8	54.6	86.6	15.7	99.4
TRD Likelihood e-He < 0.8	54.5	83.7	15.6	99.8

The main backgrounds that can be suppressed at preselection level are non-interacting protons and CR helium. For the former one, we impose the reconstructed energy at the ECAL to be $E > 2\mathrm{GeV}$ [2]. For the latter one, we request the charge measured by the inner Tracker to be compatible with 1 and the TRD Likelihood e-He less than 0.8 (Fig.4.2).

[1] The cutoff considered here is the *worst* case i.e. the larger of the two IGRF cutoffs upper limits calculated for a negative and positive particle

[2] This cut will no be applied in the sample used for the efficiencies determination and performances evaluation.

A good TRD track can be obtained requesting a minimum of eight TRD hits. Besides it, additional requests on the Tracker are required, namely, only particles with a single Tracker track are accepted. We also require for this track a good χ^2 in X and Y directions to provide a clean particle tracking which in turn, has an impact on the accuracy in the determination of the charge sign.

Finally a loose spatial matching between the extrapolation of the Tracker track at the ECAL and the ECAL shower is used.

The events fraction of the cuts as a first cut, the cumulative events fraction in the sequence and the relative events fraction with respect to the previous cut are displayed in tables 4.1 and 4.2. Starting from a sample of 2.2×10^9 events entering the ECAL with reconstructed shower, Tracker track and TRD track we get a final 55 million events after preselection cuts.

4.4 The Electromagnetic Calorimeter

4.4.1 Introduction

Electromagnetic and hadronic particles differ substantially in the way they interact with matter. When an electromagnetic particle enters a thick absorber medium, it initiates a particle shower where pair production and bremsstrahlung (the dominant processes for high energy electrons and photons) generate more electrons and photons with lower energy.

The typical length scale of these processes in which electrons transfer a fraction of their energy into γ by bremsstrahlung, and photons are converted by pair production, is the radiation length X_0, which is defined as the mean distance over which a high energy electron losses all but 1/e of its energy by bremsstrahlung, and $\frac{7}{9}$ of the mean free path for pair production by a high energy photon.

This cascade process continues with further particle multiplication, and eventually reaches a phase when bremsstrahlung is no longer the dominant energy loss process, and ionization and dissipation start to take over. At this point, the shower is at the critical energy $\mathrm{E_c}$, defined as the energy at which bremsstrahlung energy loss rate equals the ionization one. At this stage, the shower reaches its maximum, characterized by the largest particle multiplicity. Beyond this point, the average particle energy is not large enough to support further particle multiplication, and the shower declines.

The longitudinal development (Fig. 4.3) has been found to scale logarithmically with the radiation length X_0 of the medium. The mean longitudinal profile of the shower energy deposition is usually parametrized by a gamma distribution:

$$\frac{dE}{dt} = E_0 b \frac{(bt)^{a-1}}{\Gamma(a)} e^{-bt}, \tag{4.1}$$

where $t = x/X_0$ is the longitudinal depth in units of X_0, E_0 is the energy of the incident particle, and a and b are model parameters.

In this description, the maximum of the shower is reached at

$$t_{max} = \frac{a-1}{b} = \log\left(\frac{E_0}{E_c}\right) + C_{\gamma e}, \tag{4.2}$$

where $C_{\gamma e} = 0.5$ for a γ inducing the shower, $C_{\gamma e} = -0.5$ for an electron starting the shower and $b \sim 0.5$ with a weak dependence on Z. These values reflect that for a longitudinal containment of a 98% of the energy of the shower it is necessary a depth of material of $\sim 2.5\mathrm{t}_{\max}$.

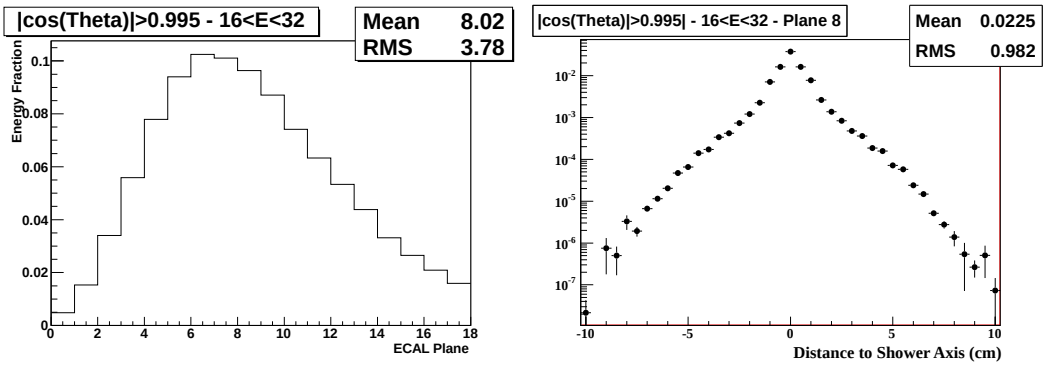

Figure 4.3: Left: Longitudinal profile of the shower. ISS data normal incidence 16-32 GeV e^-. Right: Transverse profile of the shower on ECAL layer 8. ISS data normal incidence 16-32 GeV e^-.

The lateral dispersion of the shower is the result of the particle opening angle produced at each step of particle production by bremsstrahlung and pair production, $\theta_{pair,brems} \sim m_e^2 c/E$, and the multiple scattering of the $e^{\pm}$ in the medium. The transverse development of electromagnetic showers scales to a good approximation with the *Moliere* radius $R_M = X_0 E_s/E_c$, where $E_s \simeq 21$MeV. On average, a 90% of the shower is contained laterally on a R_M and 99% of the shower is contained in a cylinder of $3.5R_M$.

The transverse development of the shower (Fig. 4.3) is characterized by a narrow core with some tails that broaden as the shower develops. It can be parametrized as the sum of two components, one for the core and other for the tails[69]:

$$\begin{aligned} f(r) &= p \cdot f_C(r) + (1-p) \cdot f_T(r) \\ &= p \cdot \frac{2rR_C^2}{(r^2+R_C^2)^2} + (1-p) \cdot \frac{2rR_T^2}{(r^2+R_T^2)^2}, \end{aligned} \tag{4.3}$$

where p is a probability giving the relative weight of the core component and $R_{C,T}$ is a phenomenological function of x/X_0 and $\log E$.

In contrast to electromagnetic showers, hadronic showers are the result of hadronic interactions and are not well described by analytical models. Protons lose their energy by ionization and by scattering off the matter nuclei. In a similar way to the radiation length, the hadronic interaction is characterized by a nuclear length λ that is essentially energy independent. The maximum of the hadronic shower can be parametrized in terms of λ as:

$$\lambda_{max} \sim [0.6 \times log(E) - 0.2]\lambda. \tag{4.4}$$

Since λ is much larger than X_0, hadronic showers need a much larger absorber material to be contained than electromagnetic ones.

On the lateral development, hadronic showers are generally speaking broader than their counterpart in electromagnetic ones. For a radial containment of 95%, it is necessary aproximately a $R_{95\%} \sim \lambda$.

At high energy, hadronic showers are characterized by multiparticle production and particle emission originating from nuclear decay of excited nuclei. Primary protons interact inelastically producing secondary pions, nucleons and low energetic photons. These secondaries may lose part of their energy by ionization, or undergo yet another hadronic interaction, thus, giving rise to the development of the hadronic shower.

Pions produced in hadronic showers decay rapidly through $\pi^0 \rightarrow \gamma\gamma$ into two energetic photons that subsequently develop an electromagnetic shower which can fake a signal in the ECAL. These kind of interacting protons, protons that interact in the first layers of the ECAL, producing π^0 that decays into highly colimated photons, constitute the hardest background to reduce (at some point it becomes an irreducible background). The fraction of π° produced has a weak dependence on E:

$$\pi^\circ/\mathrm{all} \propto \log(\mathrm{E}). \tag{4.5}$$

Finally, in the case of a full containment of the hadronic shower, for an equivalent energy of the incident particle, a different deposited energy can be expected from electromagnetic and hadronic showers, as the latter ones include processes that may result in energy leakages such as leakage due to μ, ν escaping the ECAL carrying away energy, nuclear excitation, breakup and evaporation.

In order to exploit all these differences for hadron discrimination with the ECAL, a set of variables are used. These variables make use of topological information of the shower, multiplicity of the sub-components of the shower (hits) and energy distribution in the longitudinal and transverse components. In the following section, we will introduce these variables for $e^\pm$ selection with the ECAL standalone.

4.4.2 Selection

In this section, a description of the selection strategy and the cuts used to obtain a clean $e^\pm$ sample will be introduced. For this purpose, many possible approaches can be used, each of them providing advantages and disadvantages from the others. The next items are intended to summarize the approaches that have been considered in the analysis.

- Multivariate methods: These methods (Boosted Decision Trees, Neural Networks...) can be used to extract the most of the ECAL imaging capabilities to separate $e^\pm$ from protons. The methods try to exploit non-linear correlations between variables that are used to separate two

different populations (signal and background) in a given data sample. To build the classifier, it is necessary to perform a training with a test sample, using signal and background tagged populations, that must be statistically independent from the analysis data-set. A check between both populations is necessary for instance to avoid the so-called *over-training*, situation in which the decision boundaries are too close to the training sample and do not trace the underlying distribution, but instead are adapted to the noise. This kind of procedure may be problematic in energy regions with low statistics where the training cannot be performed with flight data, and the analysis must rely on MC. In the case of AMS-02 ECAL, different approaches using multivariate methods have been used, in particular, Boosted Decision Trees (BDT) have been adopted to perform $e^{\pm}$ and proton separation.

- Rectangular Cut methods: This method is founded on the different behavior of the species we want to separate for a set of physical variables. Typically, the variables used have a weak dependence on the energy that is previously known, and the cut applied can be extrapolated to high energies with a source of systematic errors very low. The main advantage of this kind of selection procedure is that it relies exclusively on data, however, it does not make optimal use of the information available, as the correlation between variables in the n-dimensional hyperplanes are not fully taken into account.

Apart from these methods, other alternatives can be considered such as Likelihood-Probability methods. In particular, likelihood - χ^2 based methods can be used to maximize e-p rejection potential using the 3-D information of the hits that build the shower.

In this section we will introduce the two ECAL methods that will be used in the positron fraction analysis, namely, the boosted decision tree (BDT), and a rectangular cut method, the shower shape selection.

Tagged Samples

To study the performances of these classifiers, and in general in the study of the positron fraction, it is mandatory to obtain clean samples both for the background (protons) and signal (positrons). Owing to the AMS-02 sub-detectors redundancy, the samples can be constructed with flight data. These samples in turn will allow us to have a data-driven control of the background in the measurement.

For the construction of the tagged samples, we rely on the independence of the calorimeter and the TRD. This uncorrelation is based on the different sub-detectors operating principles, and the fact that both sub-detectors are separated by the magnet, allowing for secondary particles produced in the upper TOF and TRD to be swept away before reaching the ECAL.

In the following, the signal and background control data samples will be built with flight data electrons and protons respectively. The electron sample is initially proton contaminated due to charge confusion of protons, however, for the study of the ECAL, pure reference distributions of the ECAL can be constructed with a tight cut on the TRD Likelihood e-p (which will be introduced

later in the chapter) in the electron sample. The set of cuts used for the tagging are listed in table 5.1 in chapter 5.

In Fig. 4.4 we show the ratio E/P of the reconstructed energy and the signed momentum for the preselected sample (blue) and TRD tagged sample (red) for energies $\sim 110\mathrm{GeV}$ measured in the ECAL. In the following, the tagged electrons (E/P<0) will be used as a control sample to estimate the performances of the ECAL.

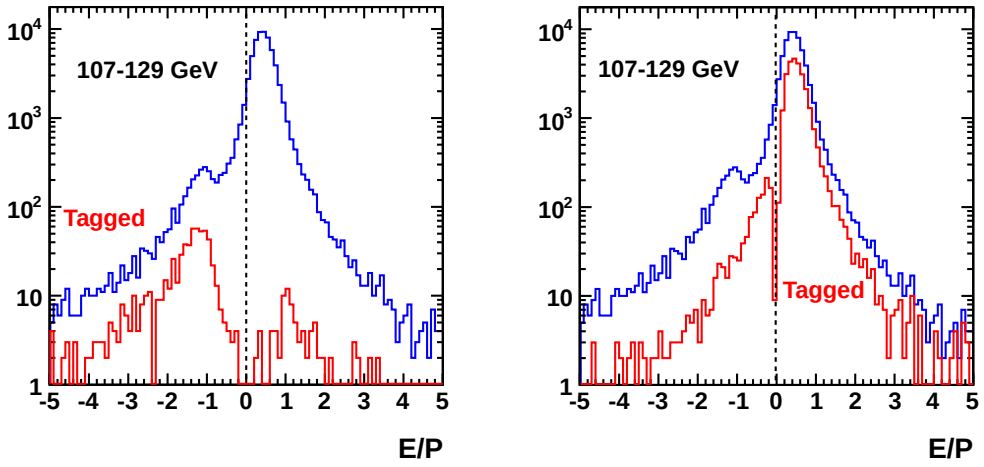

Figure 4.4: TRD tagged samples for the signal (Left) and background (Right). For the signal, we use tagged electrons (E/P<0) and for the background we select protons (E/P>0).

Shower Shape Selection

In this classifier, a parametrization on the energy of a number of variables that are used to discriminate between flight data electrons and protons is worked out for the signal. The variables used in the selection are the following:

1. Mip-Finder
2. Shower Maximum
3. Longitudinal leakage
4. Average hit energy
5. Moliere Radius
6. Shower Longitudinal Dispersion
7. Shower FootPrint
8. Energy deposited in the first two layers
9. Energy fraction $\mathrm{E_{CoG\pm 2cell}/E_{tot}}$

Although a complete description of the cuts is covered in appendix A, an illustrative cut is shown in figure 4.5. The Moliere Radius cut (Distribution of the fraction of energy in a $\pm 3\mathrm{cm}$ around the

shower axis), is shown for flight data electrons (R<0) and protons (R>0) as a function of the inverse rigidity, with the projections in X and Y.

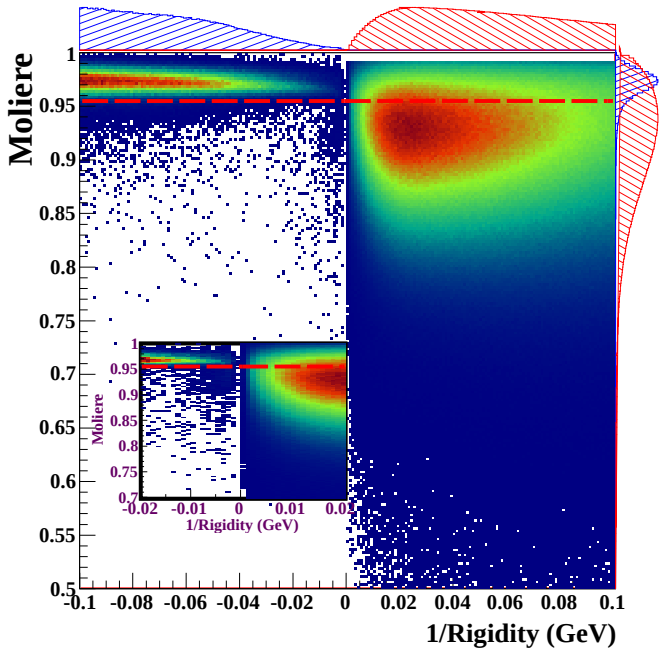

Figure 4.5: Ecal Selection: Distribution of the fraction of energy in a $\pm 3\mathrm{cm}$ around the shower axis (Moliere radius cut) for flight data electrons (Rigidity<0 and blue in projections) and protons (Rigidity>0 and red in projections), with a zoom-in to the high-rigidity spectra.

The Boosted Decision Tree

A set of 19 variables describing the 3D shower shape have been combined to build the AMS-02 BDT algorithm [99]. The resulting classifier is shown in Fig. 4.6 for tagged flight data electrons and protons, where signal and background are clearly separated.

In order to accumulate significant statistics, the training has been performed using flight-data samples over nine energy intervals (0.5-2), (2-5), (5-10), (10-20), (20-40), (40-70), (70-120), (120-200), (200-∞) with the Multi Variate Analysis Tool TMVA [73].

The ECAL-Tracker Compatibility.

As stated in the previous section, electromagnetic cascades are almost fully contained in the ECAL, while hadronic ones are much more spread. This means that unlike electrons and positrons, protons do not deposit most of their energy in the detector. For this reason, the study of the compatibility of the Tracker momentum and the ECAL energy is a powerful tool to perform e/p separation.

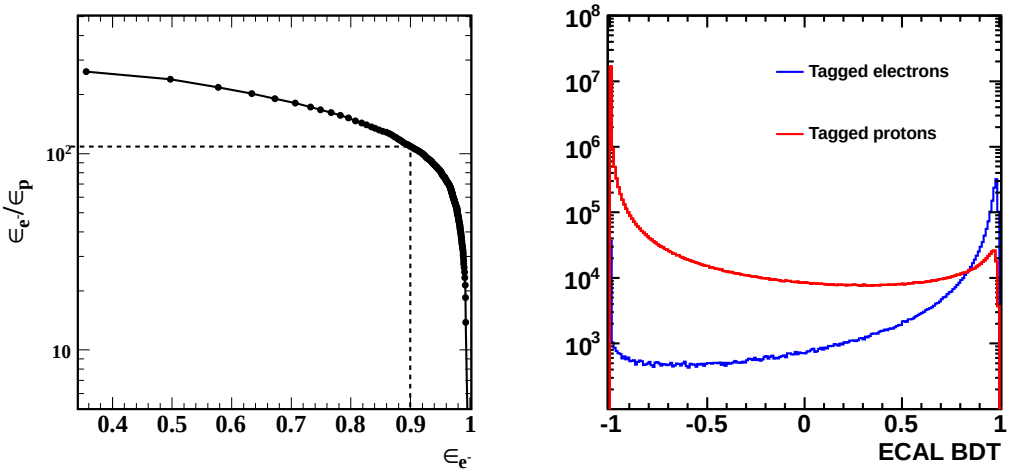

Figure 4.6: Left: BDT ROC curve (signal efficiency vs ratio of signal and background efficiency). Right: BDT distributions for flight data tagged electrons and protons with energies 2-100 GeV.

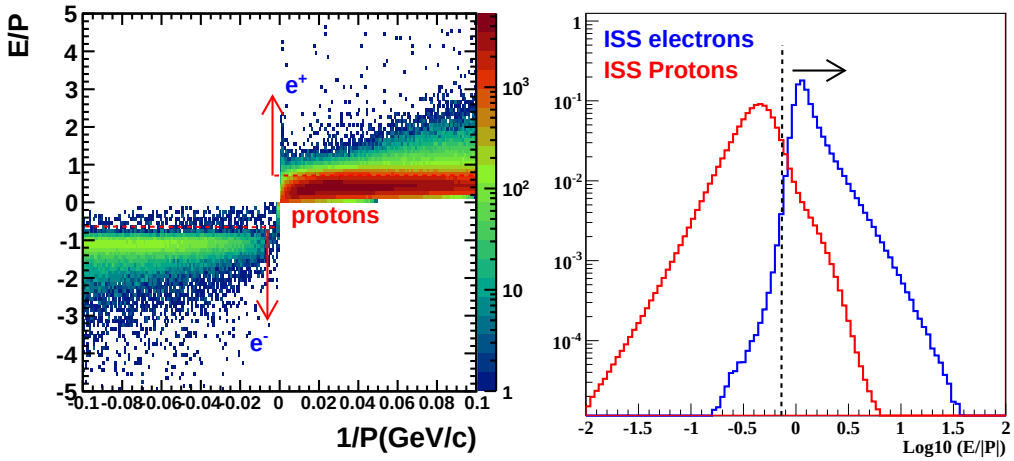

Figure 4.7: E/P distribution for preselected ISS electrons and protons (E/|P|<5 excluded). A cut in E/|P| > 0.75 is shown.

The compatibility of the particle energy with the Tracker and the ECAL is performed with the ratio of the reconstructed energy in the ECAL and the measured momentum $E/|P|$ (Fig. 4.7). For protons, the deposited energy is not compatible with the momentum as protons do not deposit all the energy in the calorimeter. In fact, in average protons energy deposition in the AMS-02 calorimeter is roughly half their true energy, as inferred from Eq. 3.1, resulting in a peaked proton distribution in ~ 0.5. Electrons however, do deposit almost all their energy in the calorimeter, and leakages are

well estimated. This is the reason behind electron sample peaking in $E/|P| \sim 1$. Long tails toward large values of $E/|P|$ are the result of low momentum reconstructions, due interactions in/or before the tracker that produce delta rays, which is larger in the case of electrons than protons. This will be investigated in the next chapter.

The ECAL-Tracker compatibility cut is correlated with the calorimeter cuts and cannot be disentangled from them. For this reason, the performance of the cut is shown for each ECAL selection, in figure 4.8. The cut applied $0.75 < \mathrm{E}/|\mathrm{P}| < 5$, has a negligible effect on the signal efficiency. The rejection is enhanced by a factor 10 (Fig. 4.8).

Signal and Background Efficiencies

The shower shape selection presents an efficiency between 80-90% on the tagged signal sample, with a background efficiency at the 2-3% level (Fig. 4.8) for energies measured in the calorimeter between 2-350 GeV. The background efficiency for this selection is at the 1% level for a measured momentum with the tracker between 2-350 GeV/c (Fig. 4.8). When compatibility between the momentum and energy is required, the background efficiency is at the 3×10^{-4} level for a measured momentum with the tracker between 2-350 GeV/c (Fig. 4.8) with an efficiency between 80-90% on the tagged signal sample.

The BDT classifier has an efficiency of 90% on the signal and presents a background efficiency of 1% for energies measured in the calorimeter between 2-350 GeV. The background efficiency for a measured momentum with the tracker between 2-350 GeV/c is 5×10^{-3} (Fig. 4.9). The cut applied is BDT > 0.5. When compatibility between the momentum and energy is required, the background efficiency is at the 10^{-4} level for a measured momentum with the tracker between 2-350 GeV/c (Fig. 4.9) with an efficiency of 90% on the tagged signal sample.

Regarding the compatibility of the performances in measured energy and momentum, it is worth to notice that as a proton reconstructed energy in the calorimeter is in average one half of the original proton energy, the proton background at a given reconstructed energy is that of a higher momentum, which is considerably lower as a result of the steepness of the spectrum. This means that the proton background we expect at a given energy measured in the ECAL is much lower than the background we expect at a given momentum.

On the other hand, we expect also a higher rejection power[3] in momentum with respect reconstructed energy in the ECAL, as protons with a low energy deposition with respect their momentum can be easily identified with the calorimeter for instance considering the energy deposition along the ECAL depth. A limit case are the minimum ionizing particles, which constitute a large fraction $\mathcal{O}(50\%)$ of the total proton sample for all the momentum range considered. Nevertheless, it should be kept in mind that the rejection power should decrease with increasing energy, as the fraction of pions in hadronic showers scale logarithmically with the energy, and this is the hardest component to suppress.

[3] Where it is customary to define the rejection as the ratio of the signal and background efficiencies.

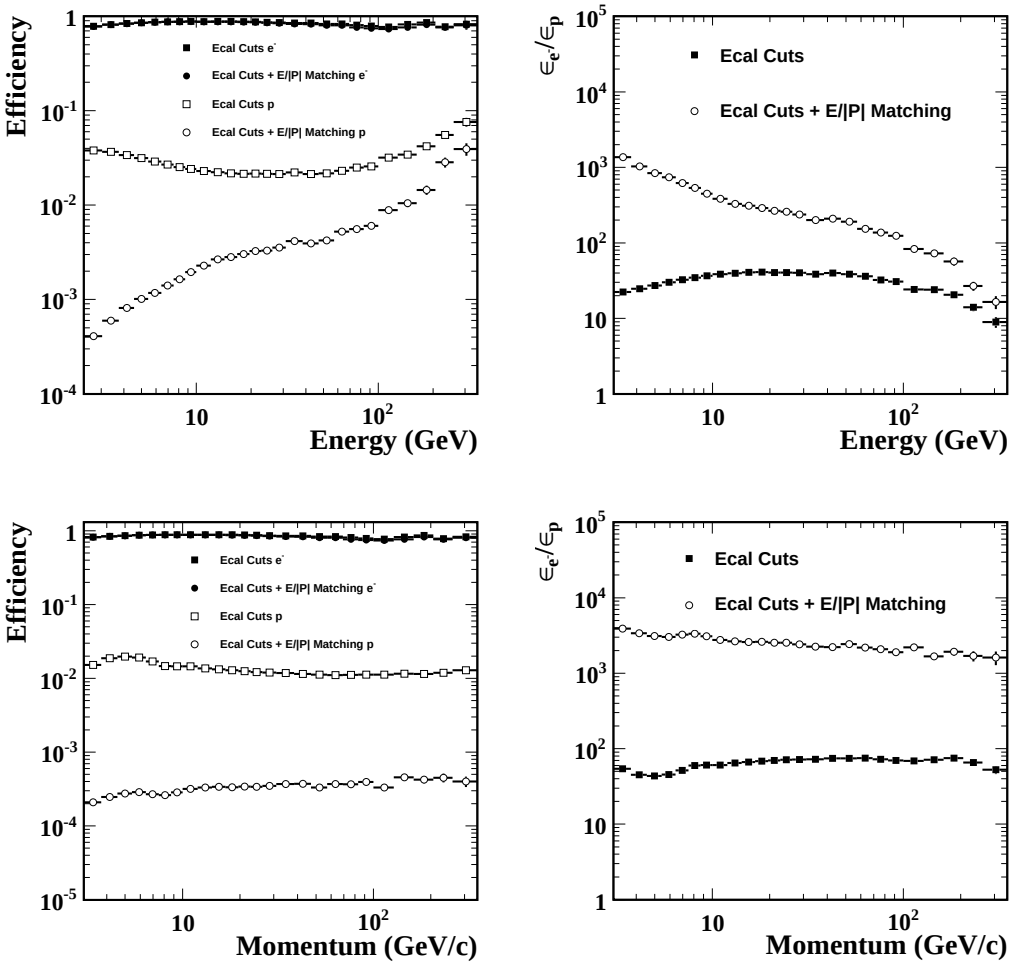

Figure 4.8: Shower shape selection. Upper plots in reconstructed energy. Lower plots in momentum. Left: Signal and background efficiencies. Right: Efficiencies ratio.

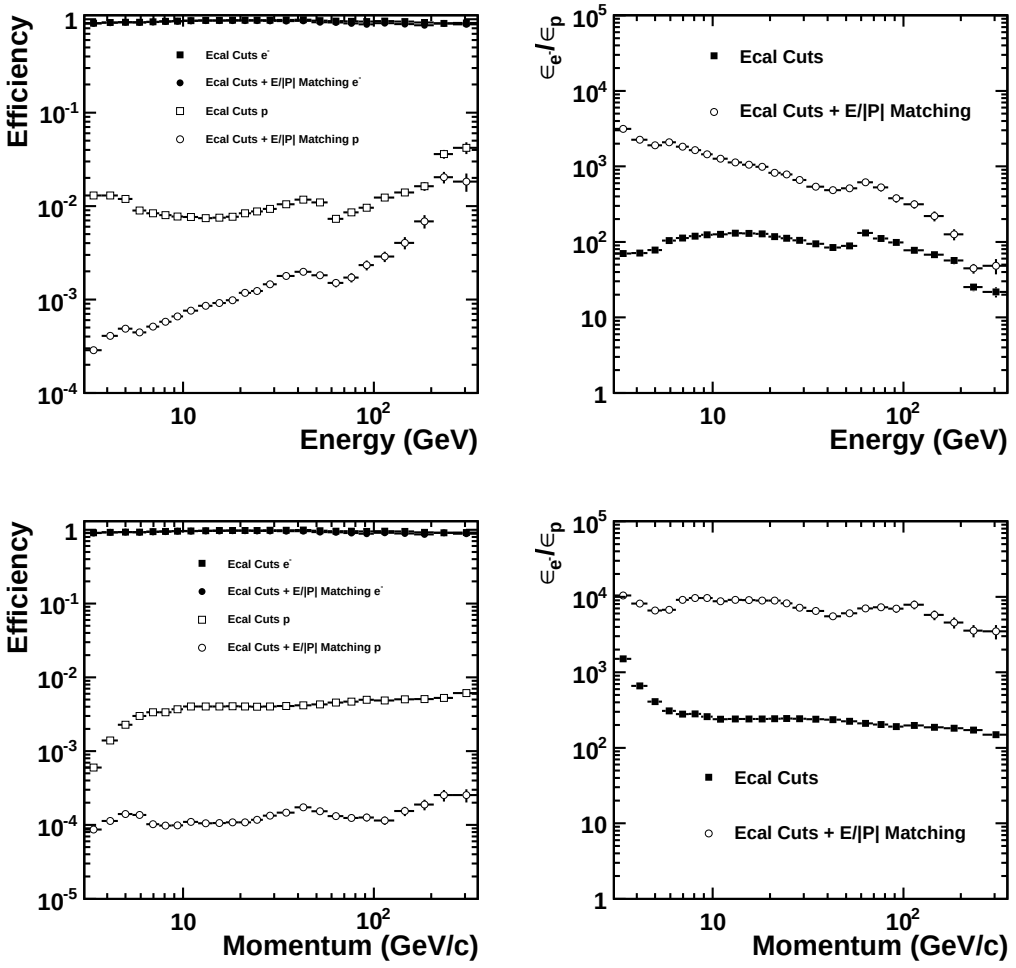

Figure 4.9: BDT selection. Upper plots in reconstructed energy. Lower plots in momentum. Left: Signal and background efficiencies. Right: $e^-\mathrm{eff}/\mathrm{p}\ \mathrm{eff}$ Efficiencies ratio.

4.5 The Transition Radiation Detector

The transition radiation is emitted when a charged particle crosses an inhomogeneous medium such as the interface of two media with different dielectric constants [51]. The energy radiated for a particle with charge ze crossing a single boundary from vacuum to a medium with plasma frequency ω_p is [59]

$$I = \alpha z^2 \gamma \hbar \omega_p / 3, \tag{4.6}$$

and the number of emitted photons with energy $\hbar\omega$ above a threshold $\hbar\omega_0$ is given by [51]

$$N_\gamma(\omega > \omega_0) \simeq \frac{\alpha z^2}{\pi} \left[\left(\ln \frac{\gamma \omega_p}{\omega_0} - 1 \right)^2 + \frac{\pi^2}{12} \right]. \tag{4.7}$$

About half of the energy is emitted in the range $0.1 \leq \hbar\omega/\gamma\hbar\omega_p \leq 1$. For a particle with $\gamma = 10^3$, the radiated photons lie in the soft X-ray range. Since the single boundary x-ray yield is low ($N \simeq \alpha$, $\alpha \simeq 1/137$), a stack of consecutive interfaces in the radiator is in practice used to enhance the signal.

The TRD e/p separation is established on the dependence of the deposited energy in the TRD tubes with the Lorentz factor γ.

4.5.1 Selection

A likelihood method has been used to perform the selection with the TRD in the positron fraction analysis. Other methods may also be considered such as the *cluster counting* method [98], which relies in the number of clusters above a threshold energy, however, it has been shown to have inferior performances [98].

Likelihood e-p

The likelihood method is based on the likelihood ratio test, which evaluates the relative probability of two hypothesis. In this case, the proton and the electron assumption. The likelihood is defined as:

$$\mathcal{L}_{e-p} = \frac{W_e}{W_e + W_p} \qquad ; \qquad \mathrm{W_{e,p}} = \sqrt[n]{\prod_i^n P^i_{e,p}(E_i)}, \tag{4.8}$$

where $P^i_{e,p}(E_i)$ are the probability density functions for electrons (e), protons(p) and E_i the cluster deposited energy for every cluster i of the event (Fig. 4.10).

The TRD estimator is then defined as : $-ln\mathcal{L}_{e-p}$. This estimator will be in the following, generally denominated as TRD Likelihood.

The likelihood is built taking into account the energy deposition along the path-length in the tube. The path-length is calculated using an extrapolation of the tracker track. A refit of the TRD track is performed to identify misreconstructed events due to large angle scattering within TRD or Upper TOF.

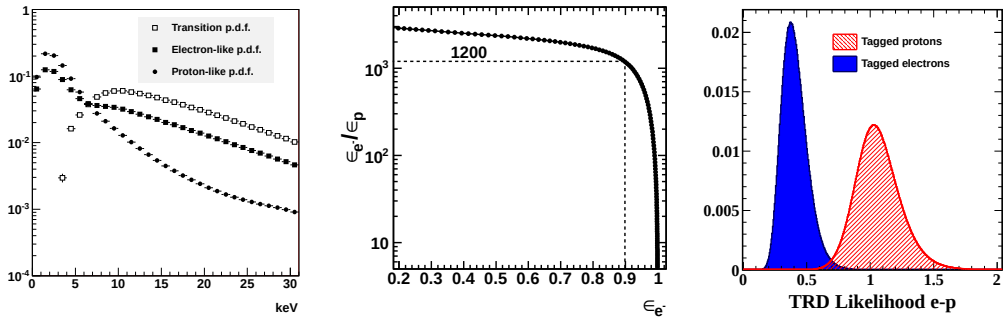

Figure 4.10: Left: Typical Electron-like, Proton-like and transition p.d.f. from TB data, used to build the likelihood as in Eqn. 4.8. Center: ROC curve. Right: TRD Likelihood e-p distributions for flight data tagged electrons and protons.

A time-dependent alignment and calibration are also performed as TRD movements has an impact on the TRD track fitting, and path-length calculation, and therefore, have considerable effect on the performances for e/p separation. Gain calibrations are performed every 30 minutes for every tube in the TRD, including gas refilling periods.

Signal and Background efficiencies

The efficiency of the likelihood has been determined on flight data using tagged electron and proton samples (Fig. 4.11). Clean samples can be obtained using a tight ECAL selection similar to the one described in the previous section.

The cut applied on the TRD Likelihood e-p is: $-ln\mathcal{L}_{e-p} < 0.55$ which results in a 90% signal efficiency with a proton efficiency at the *permil* level (Fig. 4.11). The calculation of the proton efficiency, can be performed in energy or rigidity intervals. Considering that the TRD has an optimal operational range up to $\sim$ 250 GeV, proton efficiency will be higher if we measure it in reconstructed energy in spite of the momentum, starting from about reconstructed energies higher than $\sim$ 100 GeV.

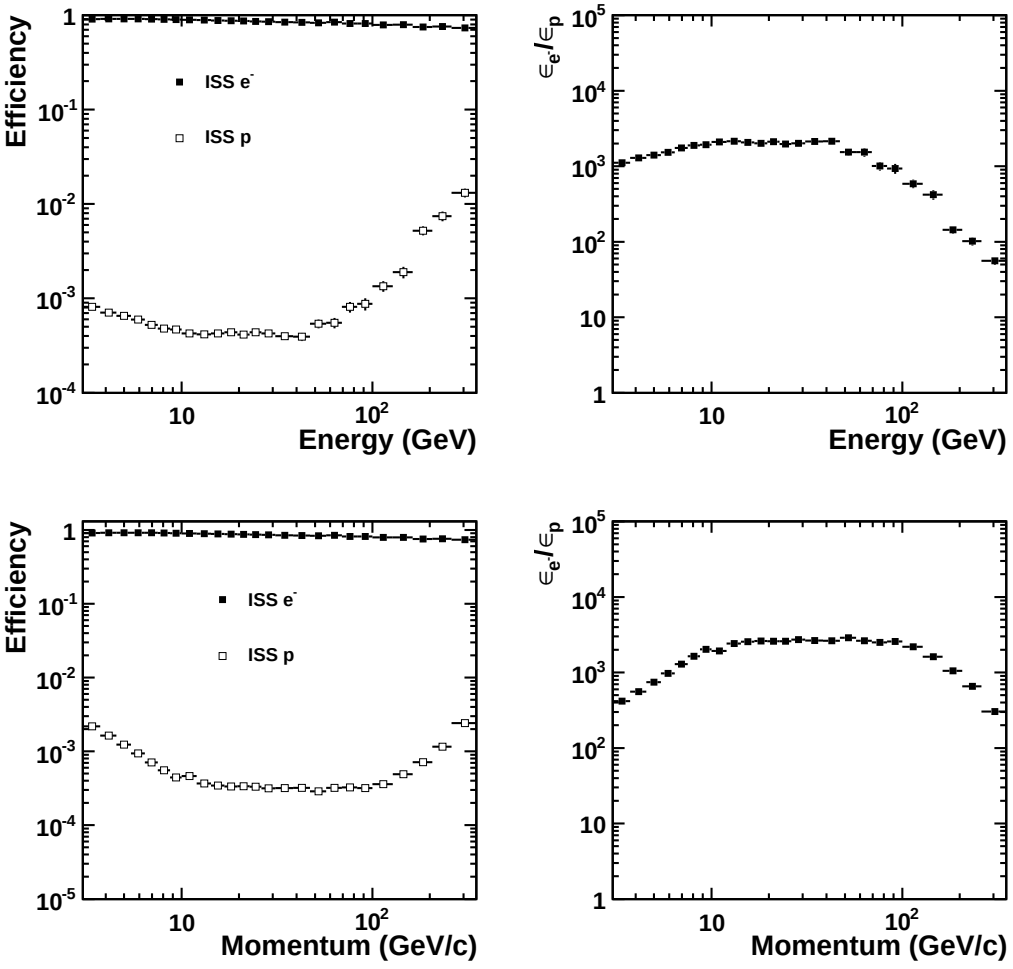

Figure 4.11: TRD Electron and Proton efficiencies. Upper plots in reconstructed energy. Lower plots in momentum. Right: TRD $e^-\mathrm{eff}/\mathrm{peff}$ Efficiencies Ratio

4.6 Combined performances for e-p rejection

The dominant sources of contamination in the positive rigidity sample are protons and charge confused electrons. In this chapter we have studied the rejection of the proton component with the TRD, ECAL and Tracker standalone. The AMS-02 redundancy for e-p rejection and the individual capabilities of the TRD and ECAL allows to obtain flight data clean samples of electrons and protons up to hundreds of GeV energy range, that otherwise would not be accessible from ground-based facilities such as CERN test-beam facilities.

The redundancy is complemented with the independence of the TRD and ECAL (+Tracker) which is based on the different operating principles of the subdetectors and the fact that they

are separated by the permanent magnet, thus allowing secondary particles to be swept away before reaching the ECAL. The uncorrelation of the TRD and ECAL allows to determine the full proton discrimination power of the selection. If we define the rejection of the subdetectors as $\mathcal{R}_{ECAL,TRD} = \epsilon_{e^-}^{ECAL,TRD}/\epsilon_p^{ECAL,TRD}$, then the combined rejection is just:

$$\mathcal{R} = \mathcal{R}_{ECAL+Tracker} \times \mathcal{R}_{TRD} = \frac{\epsilon_{e^-}^{ECAL+Tracker}}{\epsilon_p^{ECAL+Tracker}} \times \frac{\epsilon_{e^-}^{TRD}}{\epsilon_p^{TRD}}. \tag{4.9}$$

This rejection can be used to estimate the proton background we expect in the positron fraction analysis once the proton and positron fluxes are known. To make an estimation it suffices to use the proton and positron parametrizations of the flux ($\phi_p^{param}, \phi_{e^+}^{param}$) in Fig. 1.5. Then, a rough estimation of the proton background can be obtained assuming a good momentum measurement, that is, that the matrix $\mathcal{M}(P \to (P_{meas}, P_{meas} + \Delta P_{meas}))$ which describes the probability of a particle with momentum P being reconstructed with a momentum within the range $(P_{meas}, P_{meas} + \Delta P_{meas})$ is in good approximation diagonal. The fraction of protons with respect protons and positrons is:

$$\frac{\phi_p^{meas}}{\phi_p^{meas} + \phi_{e^+}^{meas}} \simeq \frac{\epsilon_p \cdot \phi_p^{param}}{\epsilon_p \cdot \phi_p^{param} + \epsilon_{e^+} \cdot \phi_{e^+}^{param}} \simeq \frac{\phi_p^{param}}{\mathcal{R} \cdot \phi_{e^+}^{param}}. \tag{4.10}$$

From this equation, the full rejection power using the BDT selection is $\mathcal{O}(10^6 - 10^7)$ up to 350 GeV/c and $\mathcal{O}(10^6)$ for the shower shape selection (Fig. 4.12). This rejection power ensures an almost proton background free analysis (Fig. 4.12) up to at least 100 GeV/c, and a contamination at the level of $\mathcal{O}(5 - 10\%)$ at the highest momentum range (Fig. 4.12).

A similar estimation can be performed for the electron sample. Naively, if we assume a charge confusion level of $\sim 10\%$ for protons at the highest energies, and that electrons are roughly 10 times more abundant than positrons, then, the proton contamination in the electron sample after the selection will be $\sim 10^{-2}$ inferior than in the positron sample. Therefore, the negative rigidity sample contains a negligible amount of residual protons after selection cuts. In fact, as we have shown in figure 4.4, it is even possible to obtain a clean sample of electrons with just one subdetector. This possibility will be exploited in the next chapter to minimize the statistical error of the positron fraction analysis.

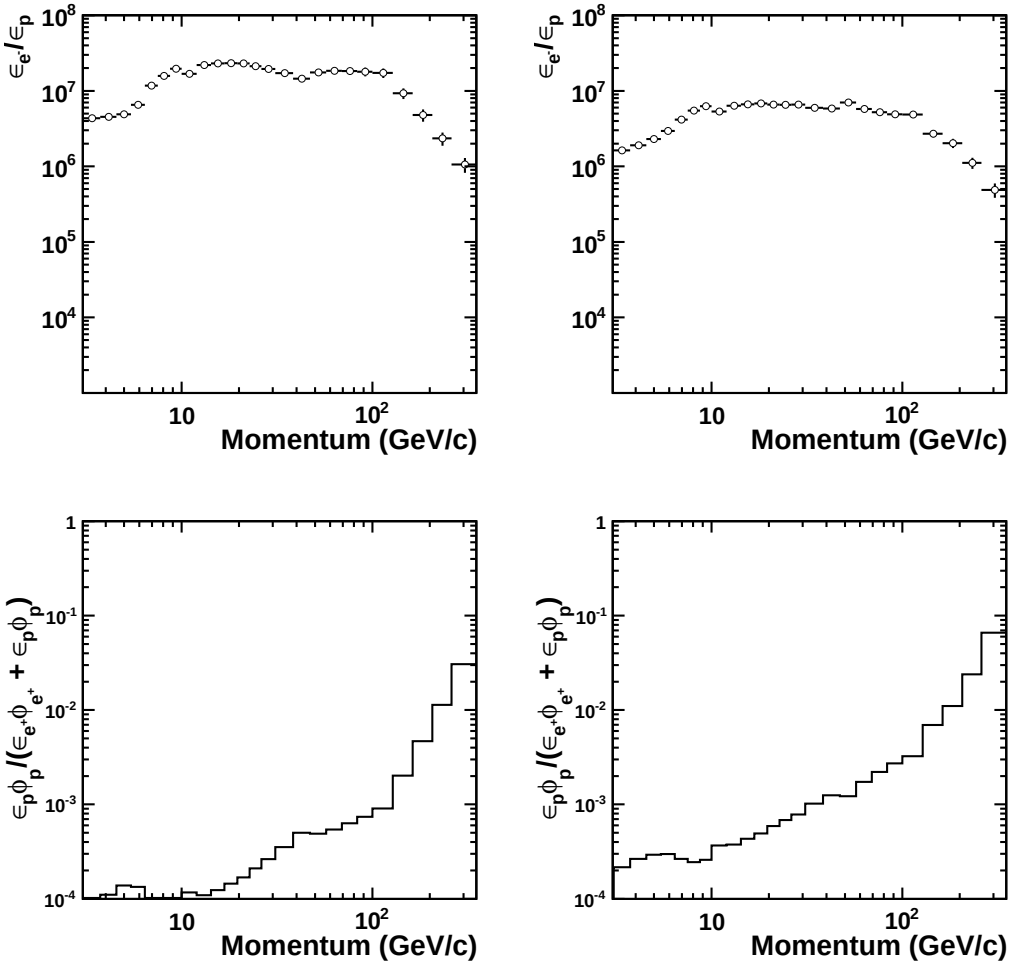

Figure 4.12: Rejection power of ECAL + Tracker + TRD (Upper plots) and proton contamination estimation (Lower plots) for the BDT (Left) and shower shape (Right) selections.

5

Determination of the Positron Fraction

THE measurement of the positron fraction is one of the main goals of the experiment. We will devote this chapter to the analysis of the $e^+/(e^+ + e^-)$ and we will do it from two perspectives: On the one hand, we will introduce the analysis using cut-based methods for two alternative set of classifiers. On the other hand, we will use data-driven techniques to obtain the $e^+/(e^+ + e^-)$ from a complementary view. This in turn will enable us to optimize the statistical error and study a potential systematic error of the method.
We will conclude the chapter with the estimation of the systematic errors.

5.1 Introduction

In this chapter, a detailed calculation of the positron fraction with the methods introduced in the previous chapter will be described. The data set used in the analysis will consist on the preselected sample presented in chapter 4. We will use the selection already sketched in the previous chapter to obtain clean samples of electrons and positrons. Next we will introduce the strategy for the analysis, which basically consists on two separate methods based on an event-counting and template-fitting procedures for the two ECAL selections already described. A comprehensive description of the corrections needed to address the backgrounds present in the sample follows. This accounts for protons and charge confused electrons backgrounds. In particular, the latter source of contamination will be investigated.

To conclude the chapter, many sources of systematic errors are studied, concerning the selection, dependence on the geometrical acceptance, bin-to-bin migrations and analysis methods.

5.2 Positron Fraction Determination

The study of the positron fraction is fairly simple. Electrons and positrons must be selected in the R<0 and R>0 samples respectively to build the ratio $e^+/(e^+ + e^-)$.

We define the positron fraction as:

$$\frac{e^+}{(e^+ + e^-)} = \frac{\phi_{e^+}}{(\phi_{e^+} + \phi_{e^-})}, \tag{5.1}$$

where the fluxes $\phi_{e^\pm}(E)$ and the number of events $N_{e^\pm}(E)$ at an energy E are related by:

$$N_{e^\pm}(E) = A_{e^\pm}(E) \cdot \phi_{e^\pm}(E) \cdot \Delta E \cdot \Delta t, \tag{5.2}$$

where $A_{e^\pm}(E)$ is the acceptance, which essentially comprises the geometric acceptance, the trigger efficiency and the preselection and selection efficiencies [98].

The advantage of using the ratio in spite of other observables is that under the assumption of equality between electrons and positrons, many of the systematic effects cancel. Moreover, the acceptances and in particular the efficiencies, are the same for electrons and positrons ($A_{e^+}(E) = A_{e^-}(E)$) and consequently cancel in the ratio. Hence, the ratio of fluxes is reduced to the ratio of the number of measured $N_{e^\pm}$.

$$\frac{e^+}{(e^+ + e^-)} = \frac{N_{e^+}}{(N_{e^+} + N_{e^-})}. \tag{5.3}$$

Therefore, the determination of the positron fraction is merely the determination of the number of positrons and electrons in a sample of observed $e^\pm$ that may contain some residual background.

The R<0 preselected sample comprises a nearly pure component of electrons with a small fraction $\mathcal{O}(1\%)$ of $\bar{p}$. In addition to these species, at high energies an additional component of charge confused protons may be present. The R>0 preselected sample is composed essentially of protons and positrons with a relative abundance of $\sim 10^4$. At high energies, however, an additional component may contribute, namely, charge confused electrons.

We can use the selection methods described in chapter 4 to obtain a high purity sample of $e^\pm$. As we have seen in the previous chapter, the selection provides a sample of electrons with a negligible proton background, and a sample of positrons with some degree of purity. Although it has not been addressed yet, the positive rigidity has also another source of background namely, charge confused electrons. Therefore, the number of observed positrons after selection have a small contribution from the electron and proton backgrounds.

If we denote as $\mathcal{P}$ the purity of the sample which is defined as the fraction of $e^\pm$ events in the sample, and $\mathcal{C}$ the charge confusion level which is defined as the fraction of events with a wrong assignment of the rigidity sign, then, the following equalities hold:

$$\begin{aligned} (\mathrm{R} > 0:) \qquad \mathcal{P} \cdot \mathrm{N}^{\mathrm{obs}}_{\mathrm{e}^+} &= \mathrm{N}_{\mathrm{e}^+} \cdot (1 - \mathcal{C}) + \mathrm{N}_{\mathrm{e}^-} \cdot \mathcal{C} \\ (\mathrm{R} < 0:) \qquad \mathrm{N}^{\mathrm{obs}}_{\mathrm{e}^-} &= \mathrm{N}_{\mathrm{e}^+} \cdot \mathcal{C} + \mathrm{N}_{\mathrm{e}^-} \cdot (1 - \mathcal{C}), \end{aligned} \tag{5.4}$$

where $N_{e^-}^{obs}$ and $N_{e^+}^{obs}$ are the number of observed electrons and positrons, and N_{e^+} is the number of positrons after charge confusion and proton subtraction corrections.

From equations 5.4, we derive the number of positrons after charge confusion and proton subtraction corrections:

$$N_{e^+} = \mathcal{P} \cdot \frac{1-\mathcal{C}}{1-2\mathcal{C}} N_{e^+}^{obs} - \frac{\mathcal{C}}{1-2\mathcal{C}} N_{e^-}^{obs}. \tag{5.5}$$

Then, the positron fraction, $\frac{e^+}{e^+ + e^-} = \frac{N_{e^+}}{(N_{e^+} + N_{e^-})}$ can then be expressed as:

$$\frac{e^+}{e^+ + e^-} = \frac{(1/(1-2\mathcal{C}))(\mathcal{P}(1-\mathcal{C}))N_{e^+}^{obs} - \mathcal{C}N_{e^-}^{obs}}{\mathcal{P}N_{e^+}^{obs} + N_{e^-}^{obs}}. \tag{5.6}$$

5.3 Strategy of the Analysis

We have followed two different strategies for the determination of the positron fraction. An event-counting method and a template-fitting analysis.

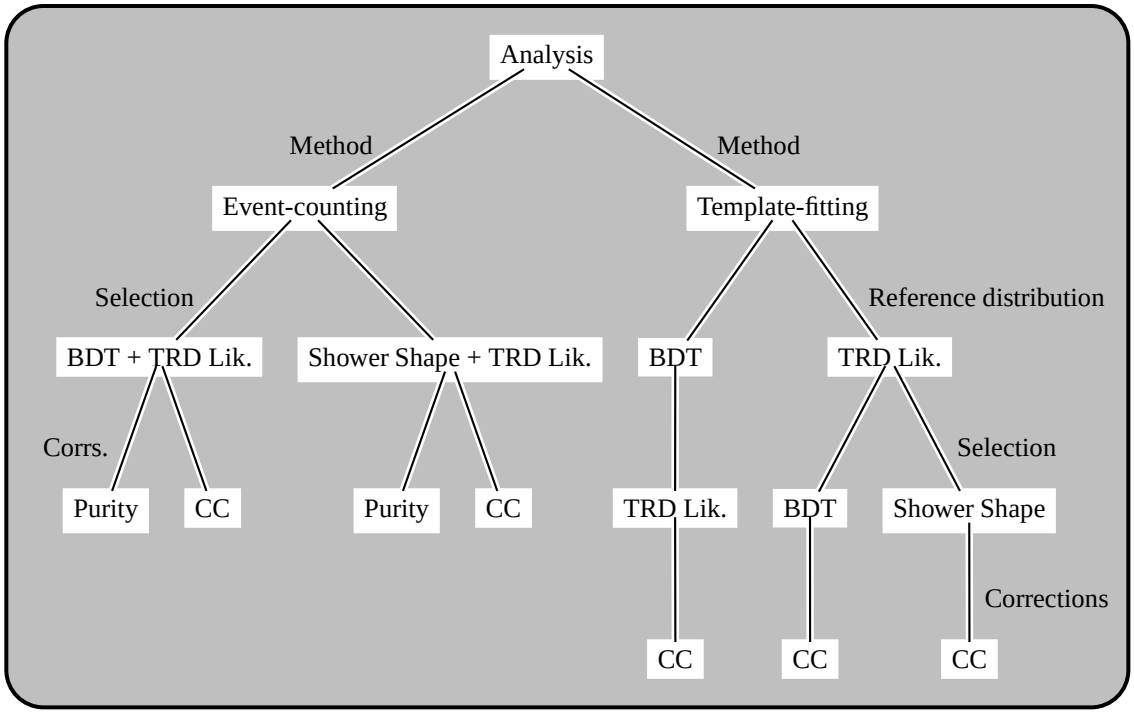

Each of the considered analysis has its own selection and corrections as depicted in the diagram. In all the analysis considered, the selection includes the same E/|P| matching selection that has been described in chapter 4.

5.3.1 Event-Counting Method

We use the selection of the TRD, ECAL and Tracker described in chapter 4 to obtain a high purity sample of electrons and positrons. This is done simply counting events passing a given criteria, in our case, satisfying a set of cuts devised to suppress the proton background.
We have two different ECAL classifiers, therefore, the analysis is performed in a twofold way, one for each ECAL classifier. The following selections are used:

$$-ln\mathcal{L}_{e-p} < 0.55 \;\;\&\;\; 0.75 < \mathrm{E}/|\mathrm{P}| < 5 \;\;\&\;\; \begin{cases} \mathrm{BDT} > 0.5 \\ \text{Shower Shape Selection} \end{cases}$$

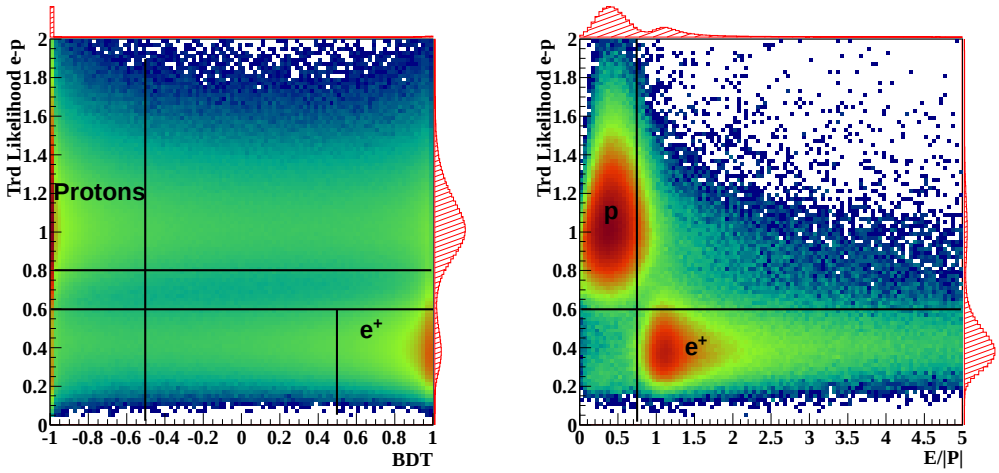

Figure 5.1: Preselected sample with R>0 and E/|P| matching (Left) and BDT>0 (Right). The different species are clearly separated in the upper-left (high purity protons) and lower-right(high purity positrons).

In figure 5.1 the R>0 sample is displayed as a function of the BDT,TRD-Likelihood and E/|P|. The Signal and Background regions are clearly separated allowing us to obtain a high purity sample of positrons and electrons.

Once the positron and electron samples are selected, the next step is to estimate the residual backgrounds. For an event-counting analysis, these backgrounds are protons and charge confused electrons, which will be evaluated in the next section.

5.3.2 Template-Fitting Method

An alternative approach to determine the positron fraction is to use a template-fitting technique to evaluate the abundances of the species present in the data sample. In this case, reference distributions (templates) are used to estimate the contribution from signal (e^+) and background (protons) to

a sample that has been originally depleted of proton and electron background with a set of selection cuts. These cuts are performed on distributions that are not correlated to the templates used in the fit.

Two different template distributions have been used in the fit. A TRD distribution, and an ECAL distribution. If we use a TRD template, the selection can be performed for the two ECAL classifiers, whereas if we use an ECAL template, the selection will be carried out with the TRD. The selection/templates combinations used for this analysis are summarized as in the previous diagram. In addition to these selections, compatibility between the momentum and energy is required.

With this procedure, the number of protons is obtained as a by-product of the fit procedure, so no correction for proton contamination is required. In spite of this, a correction for charge confusion of electrons is necessary, and will be described in the following section. Finally, the selection cut or working point used in this analysis is selected according to the criteria minimizing the overall error.

5.4 Corrections

The samples selected by the previous procedures are not 100% pure, and need to be corrected for the residual background. In particular, two types of background may be present in the positron sample, namely, protons and charge confused electrons. For the former one it is interesting to estimate the purity of the sample, while for the latter, the characteristic variable is the level of charge confusion.

The electron sample has a negligible contamination of charge confused protons and positrons and is to good aproximation 100% pure.

5.4.1 Sample Purity

The purity of the sample is defined as:

$$\mathrm{Purity} \equiv \mathcal{P} = 1 - \mathrm{Contamination} \quad ; \quad \mathrm{Contamination} = \frac{\mathrm{N_p}}{\mathrm{N_{R>0}}}. \tag{5.7}$$

To estimate the sample purity, the number of positrons and protons has been obtained at each energy bin from a fit to the relevant variables. Control data samples for signal and background are selected at each energy interval, with a negligible contamination, and are used as input distributions (templates) to the fit. The template construction for the signal is obtained from a pure sample of e^-. The background template has been built with an independent sample of protons selected according to table 5.1.

The estimation of the relative abundances of protons and positrons on the sample has been calculated varying the templates relative contributions to the data, performing a likelihood fit. The templates have been varied within statistics to take into account fluctuations in the input distributions. Finally, the purity is obtained from the TRD(BDT) distribution, calculating the relative abundances

of $e^{\pm}$ and protons below (above) a particular cut. Examples of fits for a particular set of cuts in the TRD,ECAL and Tracker, are displayed in figs 5.2 for the BDT and TRD likelihood templates.

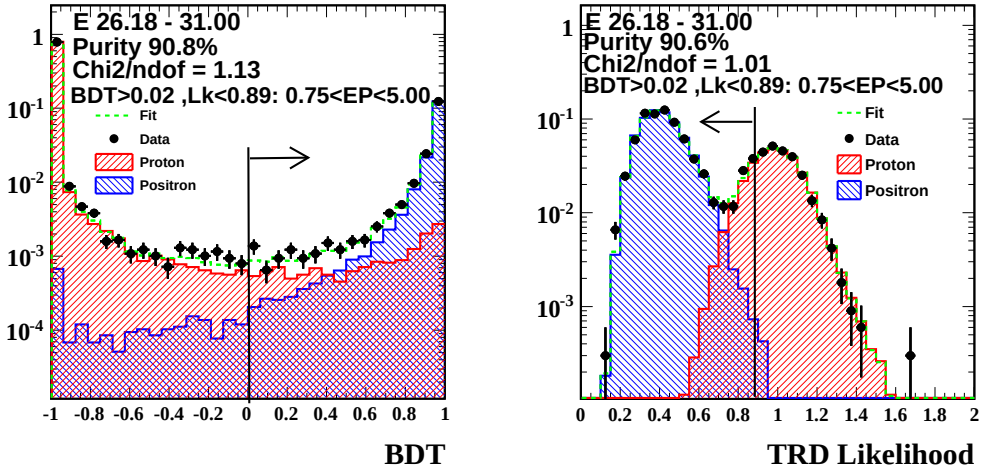

Figure 5.2: Example of the template fit used to compute the sample purity in the E: 26-31 GeV. Fits to the BDT template (Left) and TRD template (Right) with e^+ template in blue, proton template in red and in green the fit result to the the data distribution (black points). The selection is $\mathrm{BDT} > 0.02 + \mathrm{TRDLik.} < 0.89 + \mathrm{E}/|\mathrm{P}|\mathrm{Matching}$

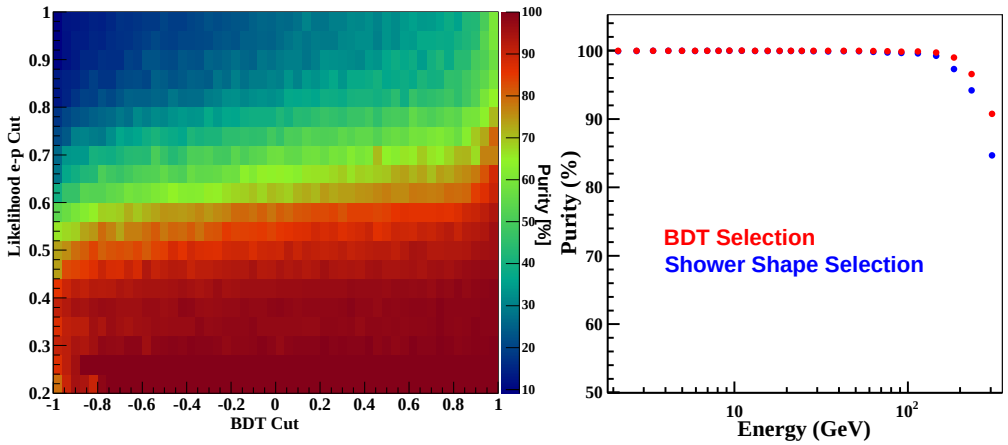

Figure 5.3: Left: R>0 && 0.75 < E/|P| < 5 sample purity for E: 260-350 GeV. Right: R>0 sample purity for BDT and shower shape selection.

This method allows us to obtain the purity of the R>0 sample for any set of cuts. In particular, a scan on the BDT-TRD Likelihood map for each energy bin has been carried out. The result for the last energy bin is displayed in figure 5.3.

Taking this into account, the purity of the positron sample has been calculated for the Shower Shape selection and the BDT selection (Fig. 5.3), where the selection cuts have been summarized in section 5.3.1. The positron sample purity for the BDT selection is above 95% and above 90% for the Shower Shape selection up to 250 GeV. These measurements are compatible with the estimations described in chapter 4.

Table 5.1: Cuts and samples used for the template construction.

Template Distribution	Selection Cut	Sample
Signal		
BDT	Likelihood < 0.55	R<0
Likelihood	BDT > 0.85	R<0
Background		
BDT	Likelihood > 0.8	R>0
Likelihood	BDT < -0.5	R>0

5.4.2 Charge Confusion

Besides the proton background, a major source of contamination are electrons that mimic a positron signal as a result of a misreconstrution of the sign of the rigidity. The charge confusion is defined as the fraction of events with a wrong assignment of the rigidity sign:

$$\mathcal{C} = \frac{\mathrm{N}(\mathrm{Sign}[\mathrm{R}^{\mathrm{rec}} \cdot \mathrm{R}^{\mathrm{true}}] = -1)}{\mathrm{N}_{\mathrm{tot}}}. \tag{5.8}$$

We have studied this effect both in MC samples and TB data, where two sources of charge confusion have been identified:

1. Spillover: It is directly related to the finite resolution of the tracker rigidity and multiple scattering. The tracker rigidity resolution steadily worsens with energy as it approaches the MDR. These processes are characterized by high rigidities resulting in $\mathrm{E}/|\mathrm{P}| \leq 1$. At some point, this effect becomes irreducible as the MDR is intrinsic to the magnet and tracker capabilities. In figure 5.4 it is shown the spillover contribution ($|P| \geq E$) to the CC for energies between 65-100 GeV.

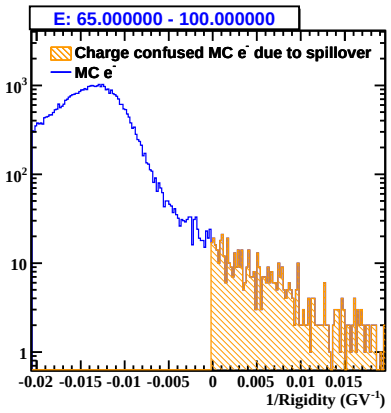

Figure 5.4: Spillover MC electrons

2. Secondary tracks: The existence of multiple hits in the tracker layers, which results in a high multiplicity of reconstructed tracks and in wrong hit associations to a particular track, is another source of charge confusion. Physical processes involved in these effects produce secondary particles created in the upper part of AMS. In particular, for electrons, delta rays originated in the TRD and upper TOF are the main source for secondary tracks in the Tracker. Typically, these wrong hit associations result in low rigidity measurements, hence, contributing in the high E/|P| tails ($|P| \ll E$).

These mechanisms of charge confusion can be distinguished in figure 5.5 where the lower TOF measured charge $\mathrm{TofQ_{low}}$-E/|P| scatter plot is shown for 100 GeV TB electrons with reconstructed rigidity R > 0.

Two regions are clearly apparent. The first one, $\mathrm{TofQ_{low}} \sim 1$ is characterized by a high rigidity clean track. This corresponds with a flip of the charge sign due to the tracker resolution. The second region, characterized by a $\mathrm{TofQ_{low}} > 1$ is attributed to multiple hits in the Tracker layers, which produce a bad hit association in the track. A consequence of it are low rigidity track reconstructions which in turn feed the E/|P| distribution at $\mathrm{E/|P|} \gg 1$. For this reason the suppression of these tails in the E/|P| distribution reduces the charge confusion due to secondary tracks.

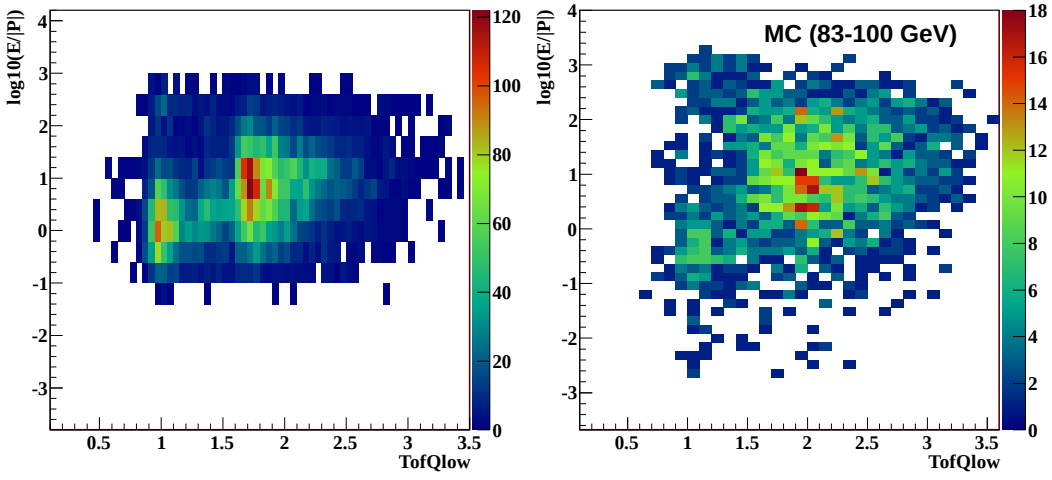

Figure 5.5: E/|P| vs Charge measured in the lower TOF for charge confused 100 GeV TB electrons (Left) and 83-100 GeV MC sample. Two regions can be clearly spotted, corresponding with the two mechanisms of C.C. described in the text, that are reproduced in MC as well.

Layers	In P1 Acc.	Out of P1 Acc.
Inner	2.9%	9.3%
Inner + P1	10.1%	-
Inner + P9	9.2%	34.0%
Inner + P1 + P9	34.5%	-

Table 5.2: Fraction of events for the different Tracker patterns used in the analysis.

The level of charge confusion is directly related to the combination of the Tracker layers (Tracker patterns) used in the reconstruction of the Tracker track. This is mainly attributable to the distinctive lever arm associated whenever an external layer (Layer 1 or 9) is present. Conversely, as a result of the geometrical acceptance (and efficiency) of the different Tracker layers, a particle reconstructed rigidity can be classified according to the Tracker pattern. These patterns present different track qualities and therefore a characteristic rigidity resolution and charge sign determination power.

In view of this, the sample has been split into six mutually exclusive track patterns, as in Table 5.2. This allows us to evaluate a potential systematic effect related to the subtraction of the electron background. From table 5.2, one third of the analyzed sample has both external Tracker layers P1 and P9, and about 90% of the events have at least one external layer for the rigidity reconstruction.

In order to reduce the charge confusion in the sample, two variables are used that are very sensitive to the charge confusion processes, the E/|P| and the χ^2 of the track in the non-bending plane (χ^2_x). In figure 5.6 the distributions are shown for the one particular Tracker pattern from a sample of 100 GeV and 180 GeV TB electrons with reconstructed rigidity R<0 and wrong charge sign assignment (R>0). We have performed a scan on these variables and estimated the amount of charge confusion for each tracker pattern and TB energy-point. In figure 5.6 the level of charge confusion for each pair of cuts is shown where we have combined the results for the different tracker patterns by means of a weighted mean.

The following cuts have been used in order to suppress the electron background due to charge confusion:

- $0.75 < E/|P| < 5$
- $\chi^2_x < 10$

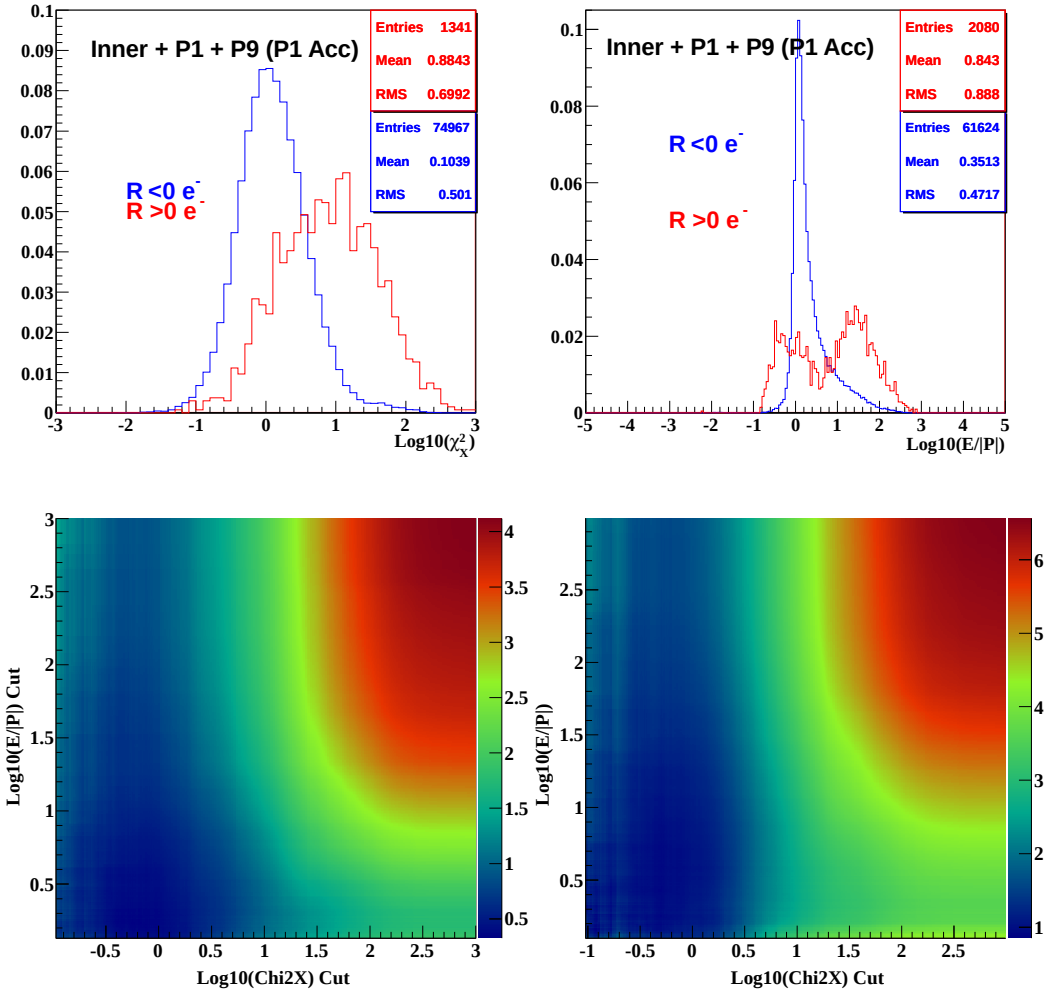

Figure 5.6: Upper plots: Test Beam 100 GeV electrons. The χ^2 of the track in the non-bending plane for R<0 electrons (blue) and R>0 electrons (red) in a full span Tracker configuration (left). Test Beam 180 GeV electrons. The E/|P| distribution R<0 electrons (blue) and R>0 electrons (ref) in a full span Tracker configuration (right). Lower Plots: Charge confusion (%) for 100 GeV (left) and 180 GeV (right) MC electrons for a wide range of χ^2_x and upper limit on E/|P| cuts. A lower threshold $\mathrm{E}/|\mathrm{P}| > 0.75$ is included.

This charge confusion applies to both analysis methods, namely, the event-counting and the template-fitting analysis. Different corrections are also calculated for each ECAL selection. We have evaluated the charge confusion for each tracker pattern using MC and TB data. In figure 5.7, we show the level of charge confusion for each Tracker pattern. Good agreement is found between TB data and the simulation.

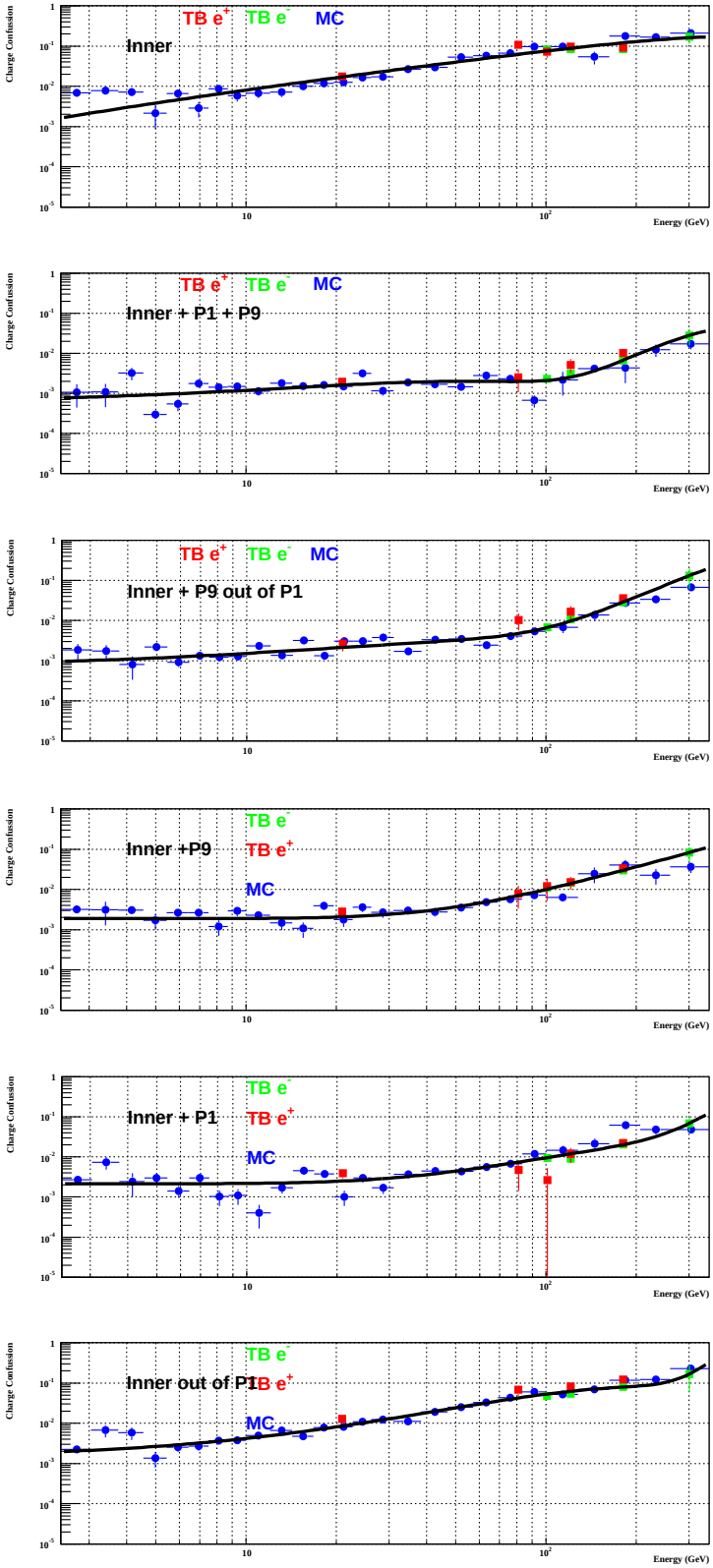

Figure 5.7: Charge Confusion parametrization (black line) from TB data and MC for each of the Tracker patterns for a BDT selection.

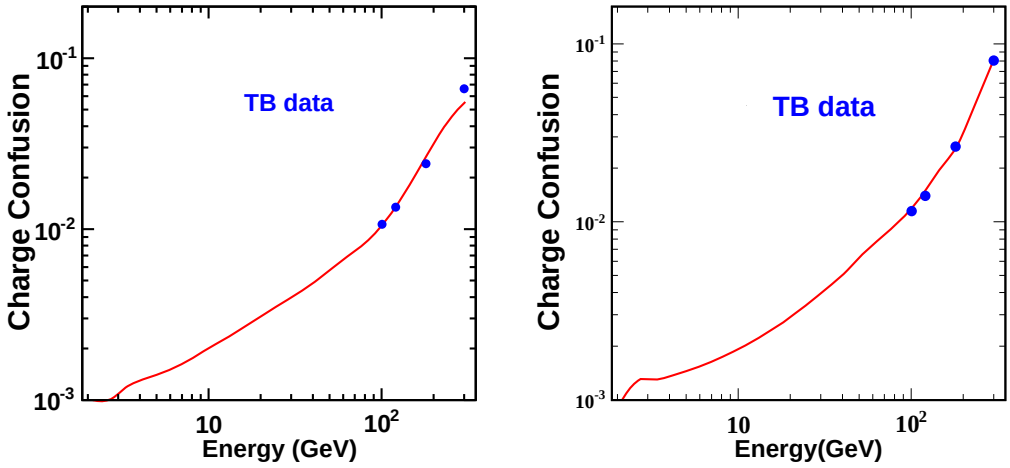

Figure 5.8: Average charge confusion parametrization from TB data and MC using the Shower Shape selection (left) and BDT Ecal selection (right).

In the following, a parametrization for each pattern will be used to evaluate the level of charge confusion in the data. We use these parametrizations to estimate the electron background due to CC, where the different patterns have been combined by means of a weighted mean. To account for the steepness of the electron spectrum, we weight the charge confusion in every energy bin with the e^- spectrum. The resulting charge confusion for each ECAL selection ranges from the permil level to the percent level at energies above 100GeV (Fig. 5.8).

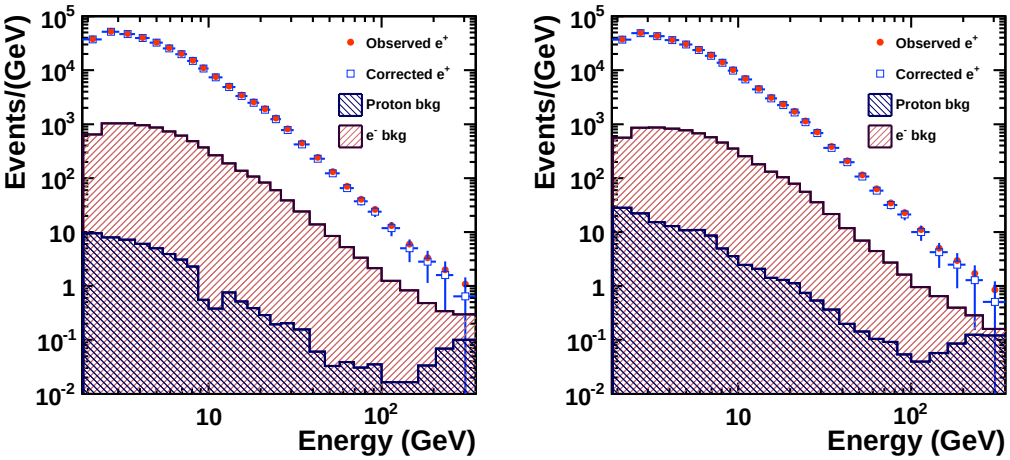

Figure 5.9: Number of observed and corrected positrons with an estimation of the electron and proton backgrounds for the event-counting analysis, BDT selection (Left) and Shower Shape selection (Right).

Charge confusion is at $\sim 1\%$ at 100 GeV and 5-10% at the highest energies. Small differences in the level of charge confusion are observed between the different ECAL selections, mainly due to the requirement of specific shower shapes in the Shower Shape selection which results in the supression of multiple track events such as brehmsstrahlung events.

Finally in figure 5.9 we show the number of observed positrons per GeV, the number of corrected positrons for charge confusion and protons using Eq. 5.5 and the estimation of the proton and electron backgrounds. The backgrounds are estimated simply as $N^{p}_{bkg} = (1 - \mathcal{P}) \cdot \mathrm{N}^{\mathrm{obs}}_{\mathrm{e}^+}$ for the former, and $N^{ele}_{bkg} = \mathcal{C} \cdot \mathrm{N}^{\mathrm{obs}}_{\mathrm{e}^-}$ for the latter. From these estimations, we can observe that the dominant background after selection cuts are charge confused electrons, however, at energies, the proton background starts grow as a result of the TRD reaching its optimal operational regime.

5.5 Positron Fraction Determination with the Event Counting Method

The measured positron fraction can be calculated counting events, before and after subtracting the proton and electron contamination calculated in the previous section. The number of positrons and electrons surviving the selection cuts for the two ECAL selections, in addition to the residual proton background estimated at each energy bin, are listed in table D.1.

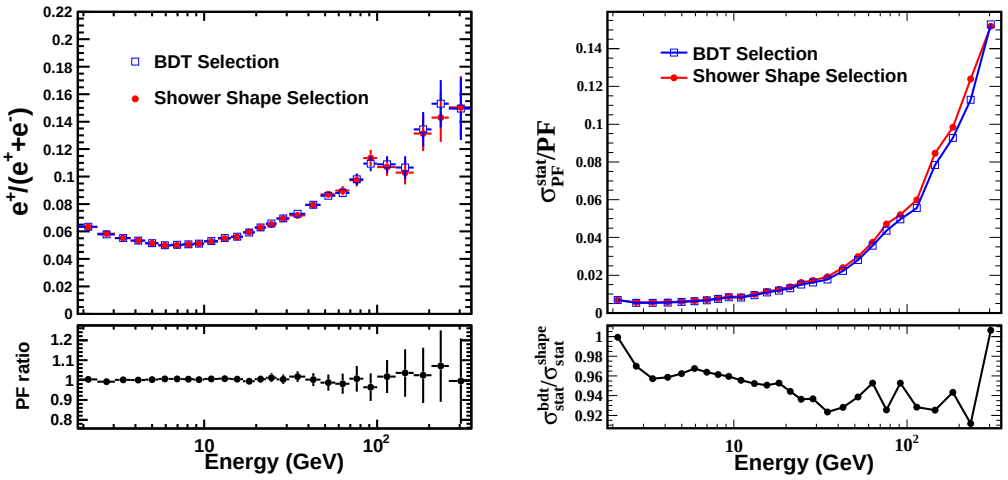

Figure 5.10: Left: Positron fraction reference analysis as detailed in tables D.2, D.3. Right: Relative statistical error and ratio of the σ^{stat} in the event counting analysis for the BDT and Shower Shape selections

The positron fraction is evaluated for each tracker pattern. The number of positrons and electrons, and the resulting positron fraction for each tracker pattern are listed in the tables of appendix B. The most relevant patterns are shown in Figure 5.11.

The calculation of the positron fraction is done for the two ECAL selections using a weighted mean of every Tracker pattern result. The results using both ECAL selections (Figure 5.10) are statistically compatible with a $e^{\pm}$ sample overlap of 80% of common events.

The statistical error (Fig. 5.10) is in average 5%-10% larger for the Shower Shape selection reaching a 15% relative error for both analysis at the highest energy interval. In tables D.2,D.3 we present the results of the cut-based analysis with all Tracker spans combined for the two ECAL selections. In this case, the number of positrons, which is taken as $\mathrm{Ne}^{+} = \sum_{\mathrm{i}=0}^{\mathrm{npatterns}} \mathrm{Ne}_{\mathrm{i}}^{+}$ is only indicative.

We have searched for evidences of systematic contributions to the systematic error due to charge confusion which may be revealed in different Tracker configurations.

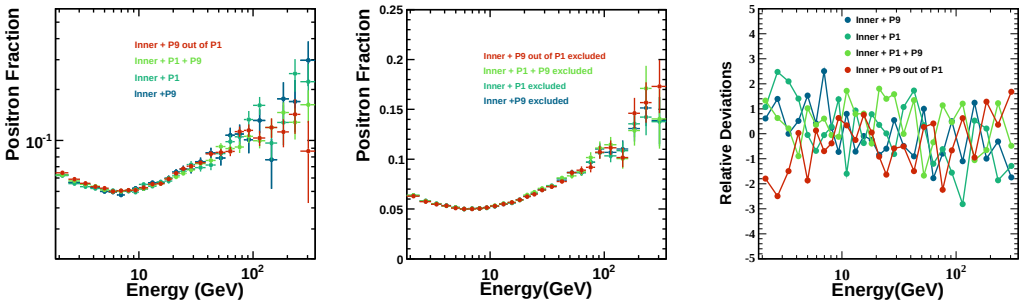

Figure 5.11: Left: Positron Fraction for the most relevant Tracker patterns. Center: Positron fraction with a Tracker pattern removed. Right: Relative deviations of the positron fraction for each tracker pattern with respect the mean positron fraction when the same tracker category is removed, normalized to the positron fraction errors added in quadrature.

In Figure 5.11 the positron fraction (BDT selection) for each Tracker pattern and the positron fraction when one of the Tracker categories is removed from the final calculation is shown. The deviation of the positron fraction for each tracker pattern from the analysis when one of the Tracker categories is removed for each Tracker pattern is shown (Fig. 5.11), which is compatible with statistical fluctuations.

5.5.1 Stability of the Result

The procedure used in the estimation of the proton background may introduce a source of indetermination in the measurement. Another possible source of indetermination related with the selection and proton background subtraction may arise since the selection cuts used in the analysis are just one realization of the many possible combinations that may be used to determine the positron fraction with different samples purities.

In order to evaluate the impact of these effects on the positron fraction, a scan (Fig. 5.13) has

been carried out in the BDT-TRD Likelihood cuts parameter space[1]. In figure 5.12, the positron fraction before and after correction for background contamination is shown with a wide range of positron sample purities. No substantial features are found in the scan (Fig. 5.13), and the scatter of the different realizations corresponds to uncertainties in the fit procedure and due to the proton background subtraction method. In addition to this, statistical fluctuations may be present and contribute to the dispersion of the positron fraction distribution due to the different selection efficiency of the cuts in the scan. For each realization, a fraction p of the events, which can be evaluated from the electrons sample, will be shared for all the combinations of cuts, and a fraction $(1-p)$ will be allowed to fluctuate between realizations.

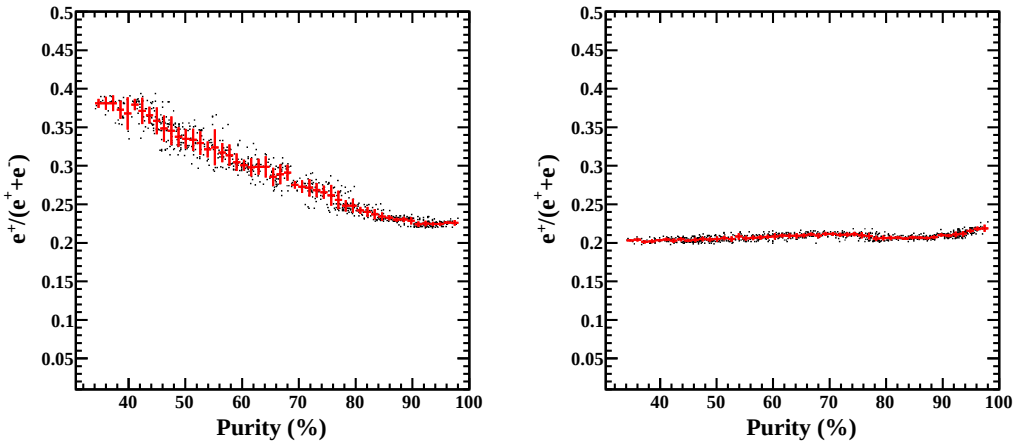

Figure 5.12: Left: Positron fraction before proton contamination correction in the last energy bin. Right: Positron fraction after proton contamination correction in the last energy bin.Each black point represents a single realization in the scan. The red points represent the averaged results in the bin.

To estimate the systematic contribution from purely statistical fluctuations, a toy MC has been devised and a bootstrapping technique has been adopted (Fig. 5.14). For each point of the BDT-TRD Likelihood cuts parameter space, we have evaluated the expected number of positrons N_{e^+} from observed N_{e^-} and mean positron fraction f as $N_{e^+} = N_{e^-} f/(1-f)$. We have generated a Poisson distributed $N_{e^+}^{pois}$ with expected value N_{e^+} which accounts for the fraction of events that are allowed to fluctuate. The positron fraction is then built from two positron components, one with probability p and one with probability $1-p$.

The total number of positrons is: $N_{e^+}^{*} = p \cdot N_{e^+} + (1-p) \cdot N_{e^+}^{pois}$ which yields for each point of the BDT-TRD map a new fraction f^*. The dispersion in the full map f^* provides an estimate of the fraction statistical uncertainty.

[1] TRD cut for the Shower Shape Selection.

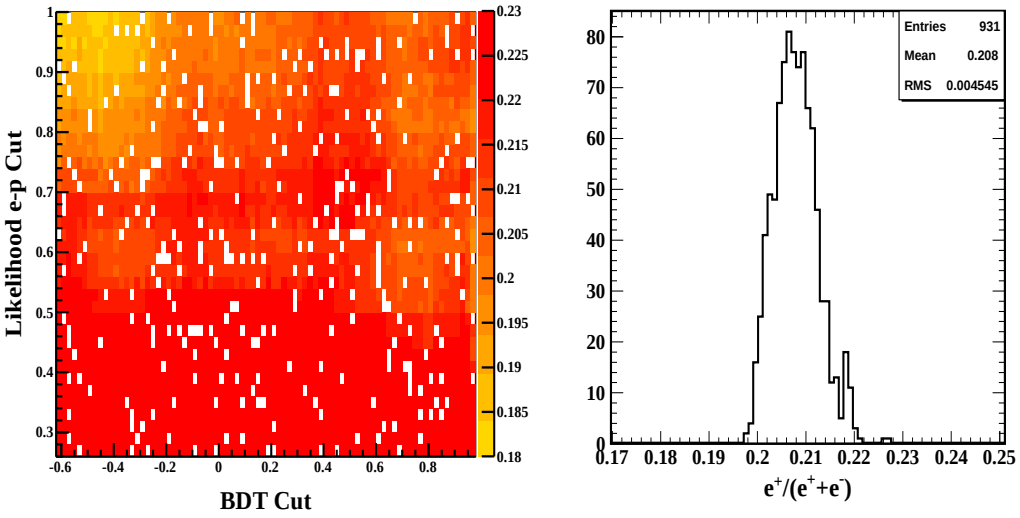

Figure 5.13: Left: Positron fraction after proton correction in the last energy bin for a wide range of cuts. Right: Positron Fraction distribution in the scan for the last energy bin.

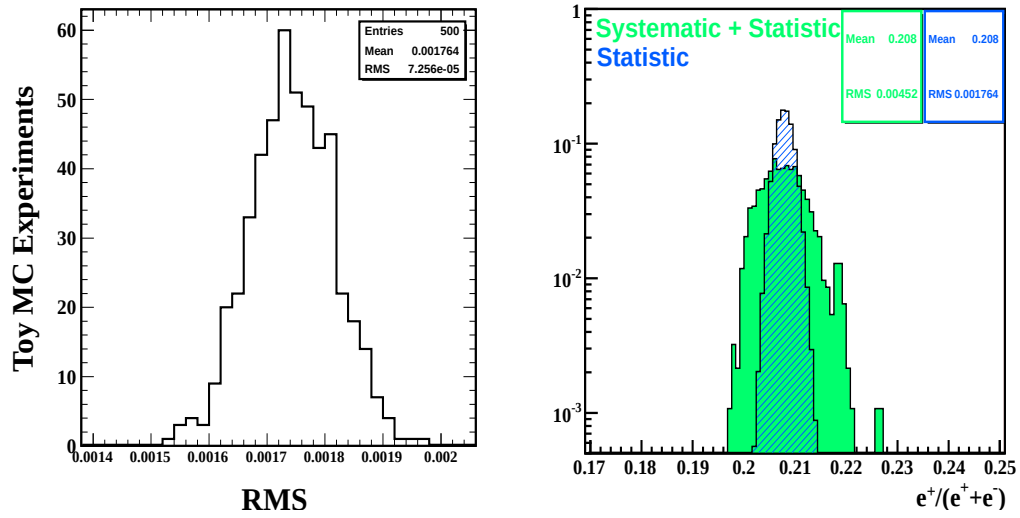

Figure 5.14: Left: Statistical fluctuations of 500 toy mc simulations of the positron fraction in the last energy bin. Right: Positron Fraction distribution in the scan (statistical + systematic) and expected positron fraction distribution due to fluctuation of the non-overlapping fraction of events. The quadratic difference of the distributions dispersions represents a measure of the systematic uncertainty.

We have repeated this sampling 500 times and have obtained the distribution for each energy bin

of the positron fraction RMS (Fig. 5.14). The mean value of this distribution is to good approximation the statistical fluctuations contribution to the reported width. We estimate then the contribution to the systematic error due to proton subtraction as the quadratic difference of the reported width and this estimation of the statistical contribution.

The systematic error due to the selection and background subtraction for both ECAL selections is shown in figure 5.15. This source of systematic error is small compared to the statistical error and at the highest energies is inferior to a 4%.

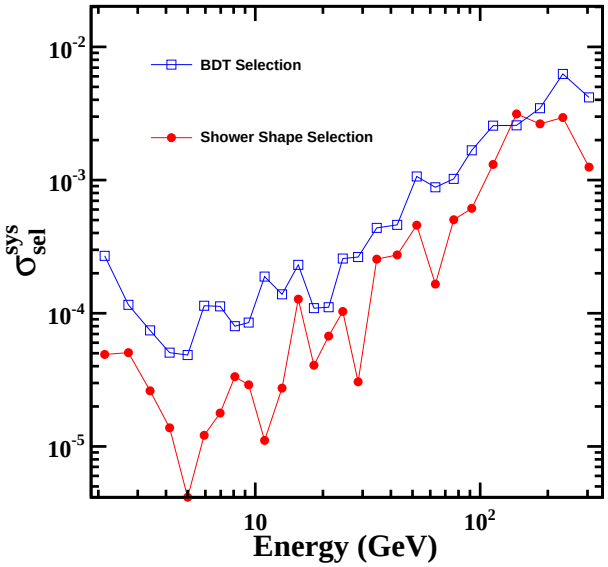

Figure 5.15: Systematic error due to the selection and background subtraction for both ECAL selections.

5.6 Positron Fraction Determination with the Template Fitting Method

In this section, an optimization of the positron fraction analysis is presented. In the event counting analysis it has been shown that the determination of the positron fraction is stable for a broad range of sample purities. This is a consequence of the data-driven estimation of the proton background which is feasible due to the ECAL and TRD redundancy that allows to determine signal and background reference distributions from flight data.

The upshot is that the positron fraction analysis is determined by maximizing the statistics rather than optimizing the systematic errors, therefore the best way to improve the analysis is to improve statistics by means of relaxing the selection cuts. In addition to this, this method will serve as a a cross-check to the event counting analysis.

To select positrons, the sample is initially depleted of protons using a selection on the ECAL or TRD, depending on the analysis, and an E/|P| matching, as described in the diagram in section 5.3. A fit is then carried out in the data sample using a distribution (BDT or TRD Likelihood), in which positrons, electrons and protons abundances are simultaneously measured for the positive and negative rigidity samples.

The relative contribution of signal and background in the data sample at every energy bin is obtained varying the normalization of reference distributions for each component (Figure 5.16).

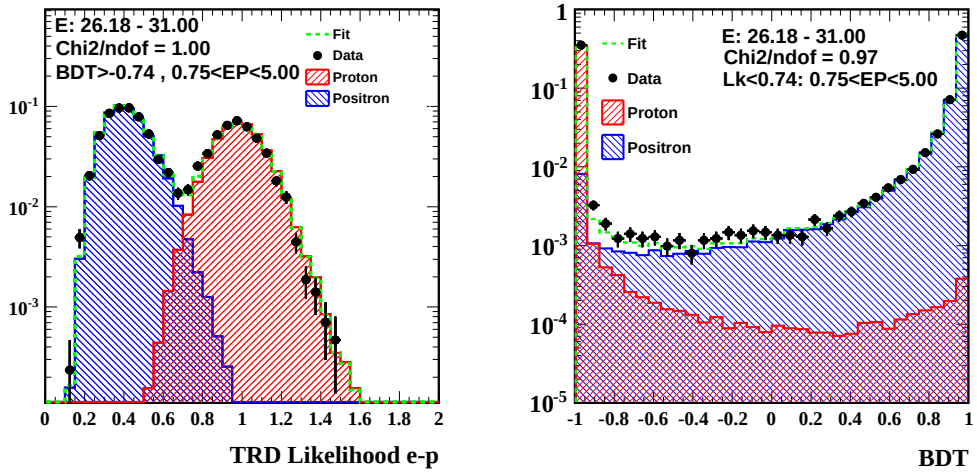

Figure 5.16: Left: Example of the fit procedure using the TRD Likelihood template with selection cuts in the free variables E/|P| and BDT. Right: Example of the fit procedure using the BDT template with selection cuts in the free variables E/|P| and TRD Likelihood.

Clean reference distributions for signal and background are selected with either the TRD Like-

lihood or BDT, and the E/|P| matching, using electrons and protons respectively. The combination of cuts and reference distributions depends on the analysis, and are listed in Table 5.1. With these control samples, we build the PDFs for signal (positrons) and background (protons) in one of the variables (TRD Likelihood,BDT) which are used as templates in the fit.

To take into account the finite statistics of the control data sample, the template is allowed to fluctuate within Poisson statistical errors in the fit. Finally, a correction for charge confusion is applied with the average charge confusion (Fig. 5.8) estimated in section 5.4 for both ECAL selections.

We choose an unbiased signature of the goodness of the method from the χ^2 of the fit. The χ^2 per degree of freedom of the fit does not show a trend with energy and is compatible with one (Fig. 5.17), indication that the proton background is under control.

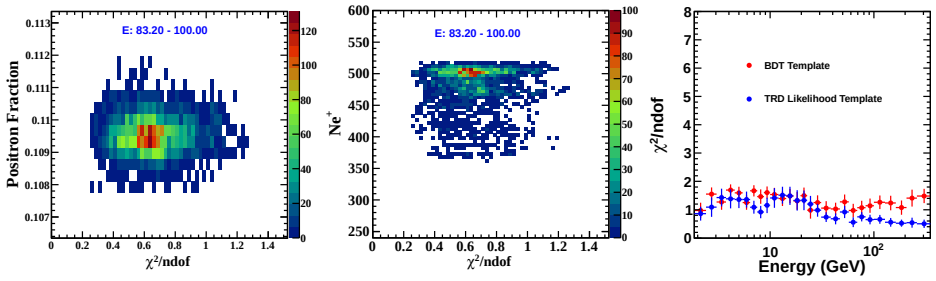

Figure 5.17: Positron fraction (left) and number of positrons (center) with energies in (83.20-100.00) [GeV] using the TRD template-fitting technique and varying the BDT selection, vs the χ^2 per degree of freedom of the fit. Average $\chi^2/ndof$ for each energy bin using TRD likelihood or ECAL BDT template for the fit (right).

In order to summarize the results, the analysis will be conducted using the TRD likelihood template. As shown in figure 5.18, the resulting positron fraction after electron subtraction is stable for wide range of cuts in the BDT.

To validate that the proton background is well determined, a scan has been carried out in the cutting variables (BDT for the TRD-likelihood template analysis) with an broad range of sample purities (Figures 5.18 and 5.19), in order to estimate a potential systematic error. In this scan, the input control data sample has been varied in order to reveal contributions to the systematic uncertainty related to the input templates and the fit procedure.

No correlation is observed between the positron fraction and the number of positrons and reduced χ^2 of the fit, as shown in figures 5.19 and 5.17 which serves as an additional validation of the method.

To check that the positron fraction result is not in the tail of the positron fraction distribution, the mean value in the scan is used. Results after electron background subtraction are shown in figure 5.20 for both ECAL selections, using the TRD template in the fit. The results are listed

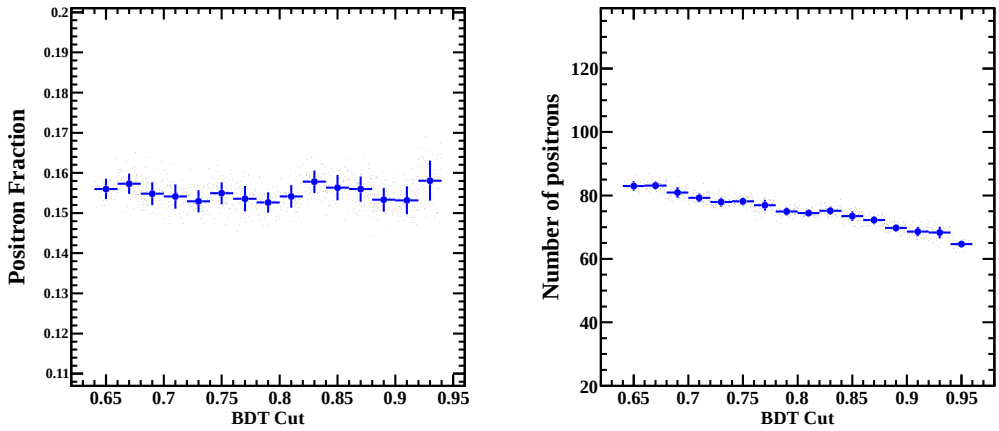

Figure 5.18: Positron fraction and number of positrons obtained with the TRD Template-fitting method for the BDT selection when the BDT cut is varied in the last energy interval around the working point.

in tables D.5,D.4. The positron fraction results for both ECAL selections are compatible, and the statistical error is in average 3-5% larger in the shower shape selection as a result of a lower selection

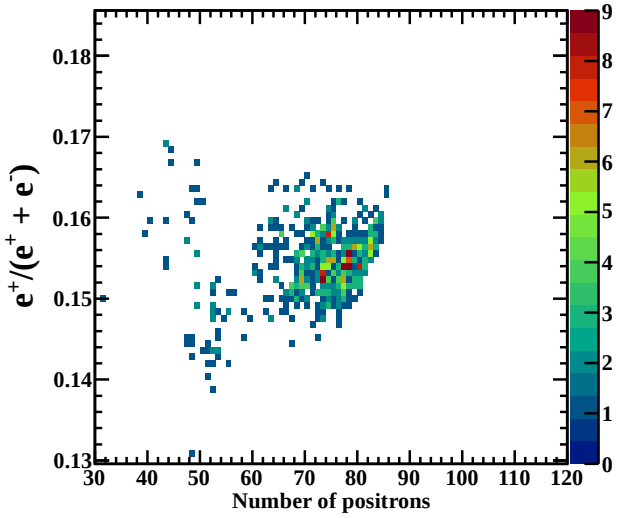

Figure 5.19: Positron Fraction and number of positrons in E (260,350)[GeV] estimated from the TRD template-fitting for the BDT selection, around the working point (varying the BDT cut between $0.6 < \mathrm{BDT} < 1.0$). No correlation is observed.

efficiency. In the highest energy bin, the statistical error has a significant contribution from the charge confused electron substraction, which is the reason for the shower shape selection showing a smaller σ^{stat}.

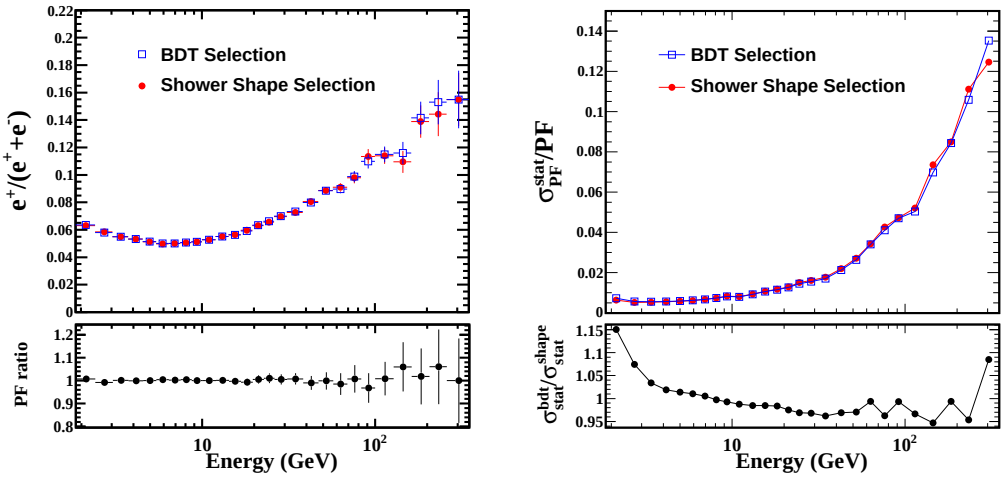

Figure 5.20: Left: Positron fraction reference analysis for the two ECAL selections, using TRD Likelihood template fitting as detailed in tables D.4,D.5. Right: Relative statistical error and ratio of the σ^{stat} in the template fitting for the BDT and Shower Shape selections

The stability of the analysis is studied in a similar way as in the event counting analysis. The statistical contribution to the dispersion of the positron fraction distribution when varying the selection cuts is obtained from 500 toy MC experiments following the approach described in the previous section. Results for the last energy interval are displayed in figure 5.21.

The dispersion of the positron fraction have two contributions, a systematic one due to the selection and fitting process, and a statistical one due to the fluctuations of the non-shared events. The systematic contribution is estimated as the quadratic difference of the positron fraction dispersion and the statistical contribution. The systematic error due to the selection and fit procedure is added to the full systematic error in quadrature.

The systematic error due to the fit procedure and selection cuts for each energy interval is shown in figure 5.22 for both ECAL selections. The systematic error quoted for the shower shape selection has been estimated varying the input templates in the fit. The dispersion of the positron fraction at each energy represents an upper limit of the systematic uncertainty of the fit procedure.

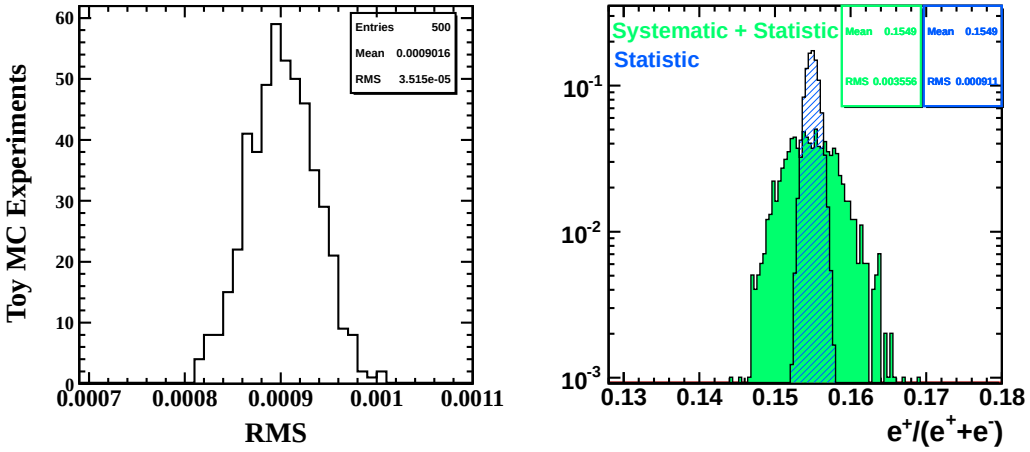

Figure 5.21: Statistical fluctuations of 500 toy mc simulations of the positron fraction in the last energy bin. The mean value of the RMS of the 500 toy mc simulations at every energy bin provides the expected dispersion due to the statistical fluctuations of the non-shared events (left). Positron Fraction distribution for the BDT selection (right) and positron fraction estimation of the dispersion due to the statistical fluctuations of the non-shared events.

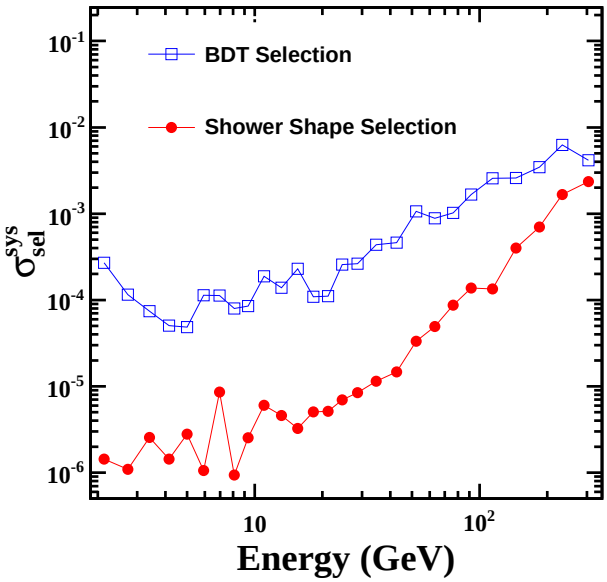

Figure 5.22: Systematic error for the BDT and shower shape selections due to selection and fit procedure.

5.7 Additional Systematic Uncertainties

In this section we will study additional systematic effects not covered in the previous sections. In particular, throughout all this work, it has been assumed that the detector acceptance is identical for electrons and positrons, aside from a conceivable effect derived from the charge sign measurement. This assumption is fairly true, but in the presence of the AMS-02 magnetic field, asymmetries in the detector acceptance could show up as a systematical effect that should addressed.

Another source of systematic effect that must be studied is related to the Earth's geomagnetic field. Specifically, due to the geomagnetic cutoff, low rigidity particles entering the Earth's magnetic field are not allowed to penetrate, depending on the geomagnetic latitude and longitude. However, high energy protons and electrons interacting with the atmosphere produce low energy secondary particles that are below the rigidity cutoff, and can be detected. A dedicated cut on the cutoff has been applied to reject this component, however, a significant deviation along the ISS orbit from the mean value of the positron fraction should evidence a source of systematic effect that again, should be addressed.

Finally, the energy bin width of the measurement has been chosen according to the ECAL energy resolution. A systematic associated to bin-to-bin migrations is also evaluated.

Other sources of systematic uncertainties have been studied, such as the contribution from variations in the reference templates. Their contribution to the overall systematic is negligible.

5.7.1 Charge Confusion

Charge confused electrons constitute, along with protons, a major background of the positron fraction analysis. In this section we study the stability of the result for different charge confusion corrections.

We have used different tracker patterns with different MDRs and levels of charge confusion in the estimation of the positron fraction, to study the systematic uncertainty due to the charge confusion correction. The results from these mutually exclusive subsamples are compatible within their statistical errors as shown in figure 5.11. Likewise, the positron fraction evaluated with the shower shape and BDT selections have been calculated with different charge confusion corrections and their results are compatible.

Charge confusion has been obtained from MC samples and TB data. A parametrization with the energy for each tracker pattern has been used to evaluate the electron background. We have used the uncertainties associated to these parametrizations (Fig. 5.23) which account for discrepancies between TB and MC estimations of the charge confusion, to evaluate the systematic error.

In table D.6 we list the systematic uncertainty due to charge confusion for both selections, which is obtained from each tracker pattern and ECAL selection. The final value is the weighted mean of the combination of the uncertainty for all the tracker patterns. The systematic error for both ECAL selections is shown in figure 5.24 and is $\sim 5\%$ at the highest energies.

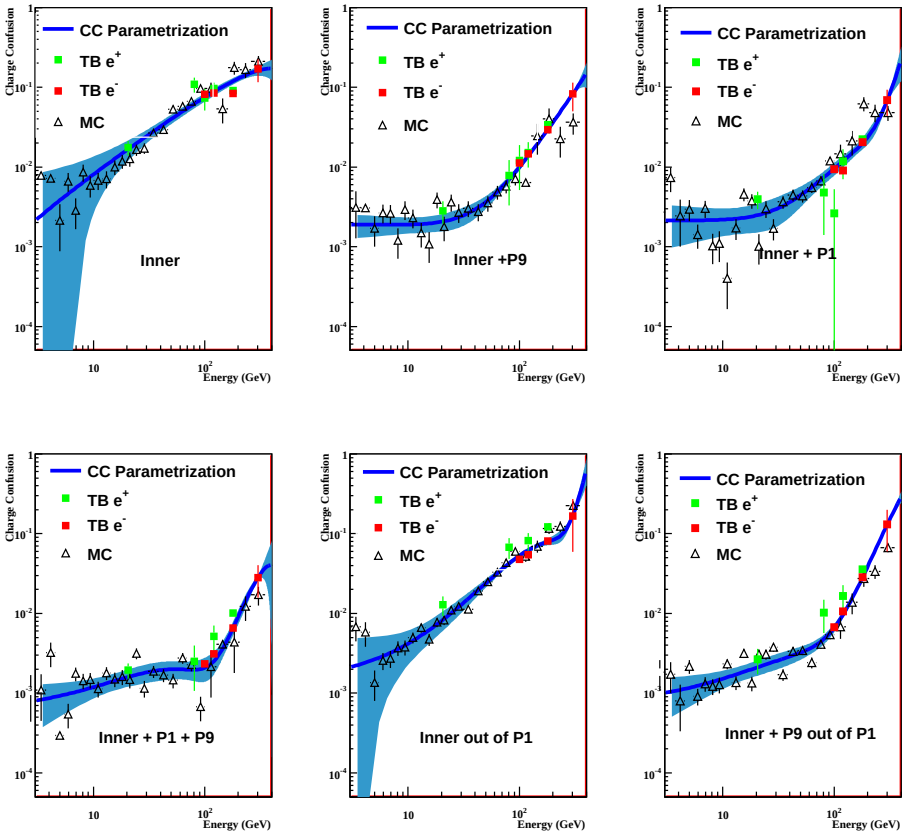

Figure 5.23: Charge Confusion estimation uncertainty used for the systematic error evaluation for each tracker pattern for the BDT selection.

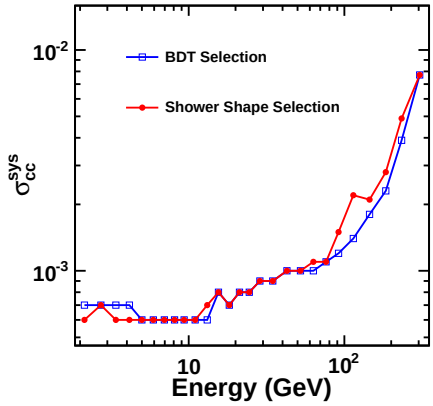

Figure 5.24: Charge Confusion systematic error for the BDT and shower shape selections.

5.7.2 Detector Acceptance

One major assumption in the positron fraction study is the identity between electrons and positrons except for the charge sign. To put it in another way, we have assumed that the acceptance for electrons and positrons is the same, however we are dealing with a *real* detector, and small discrepancies may be possible. In particular, we will inspect potential systematics arising from deviations in the geometrical acceptance of electrons and positrons.

To study these effects, we use electron and positron flight data and MC simulation samples. In particular, the dependence of the positron ratio with the local particle incident angle is inspected. The θ and ϕ dependence for flight data positrons and electrons is shown in figure 5.25.

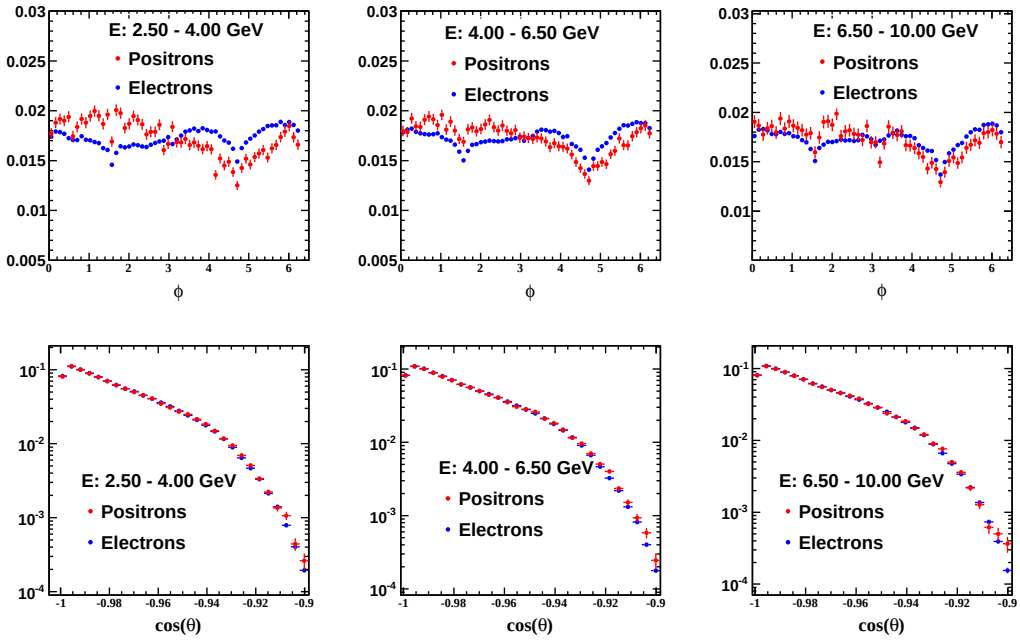

Figure 5.25: Electron and positron dependence on ϕ (Left) and θ (Right) local coordinates.

From these figures, there is an apparent departure from azimuthal symmetry in the local ϕ angle. Electrons and positrons dependence in the local ϕ angle differ at low energies, which introduces a dependence in ϕ for the ratio. On the contrary, electrons and positrons relative dependence on the polar angle is constant. We have checked this behavior in the MC simulation for which we find a good agreement. This behavior is a purely geometrical effect of the detector, which in conjunction with the AMS-02 magnetic field, produces a small dependence of the ratio with ϕ at low energies (Figure: 5.26). In case of symmetry in the ϕ coordinate, excess and deficit of electrons and positrons for different ϕ should balance and the mean ratio would yield the correct ratio. However, the detector is not completely symmetric as a result of different efficiencies for a few ladders of the tracker. This

asymmetry causes that at low rigidities electron and positron acceptances do not cancel out along different ϕ angles, hence, introducing a small systematic effect. Furthermore, no relation with cutoff East-West effect has been found by tightening the cutoff cut, which further supports the previous statement.

In order to estimate the impact on the positron fraction measurement, different fiducidal volumes have been selected restricting the full analysis chain to polar angles from $\theta = 180°$ up to the full acceptance at every energy. A fit is performed to validate the compatibility of the positron fraction dependence with ϕ with a constant, for each fiducidal volume in $\cos\theta$. The different positron fractions in the ϕ angle for different polar angles are shown in figure 5.26. The reduced χ^2 of the fit as a function of $\cos\theta$ for different energy intervals (Figure 5.26) shows that the azimuthal dependence of the ratio vanishes for vertical incident particles (Fig. 5.26). In addition, at energies above 15 GeV, the azimuthal dependence of the ratio vanishes at all incident angles.

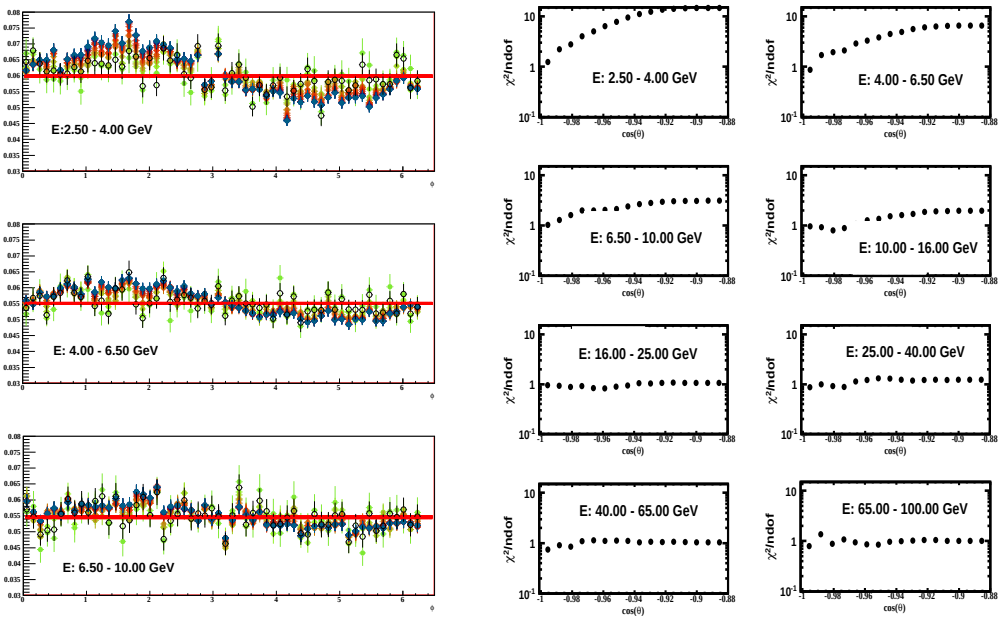

Figure 5.26: Left: e^+/e^- dependence on the ϕ local coordinate for different particle incidence angles (labeled with different colors in the figure). The dependence of the ratio on ϕ changes for different fiducidal volumes when the polar angle is restricted (Left). Right: Reduced χ^2 of the fit for different polar angle thresholds at different energy intervals. For vertical incident particles no dependence on ϕ is observed in the ratio. For E>10GeV no dependence on ϕ is observed in the ratio.

However, in spite of the positron fraction dependence with the azimuthal angle, the mean value of the positron fraction is compatible with the positron fraction of vertical incident particles, that we have shown does not depend on ϕ. In figure 5.27 we show the positron fraction for vertical

incidence particles ($\cos\theta < -0.99$) in blue, the positron fraction for particles with polar angles $\cos\theta \geq -0.99$ in green, and the positron fraction for the full geometrical acceptance in red. The difference between the mutually exclusive subsamples ($\cos\theta < -0.99$ and $\cos\theta \geq -0.99$) is compatible with statistical fluctuations. Therefore, the impact of the asymmetry in the acceptance is minute.

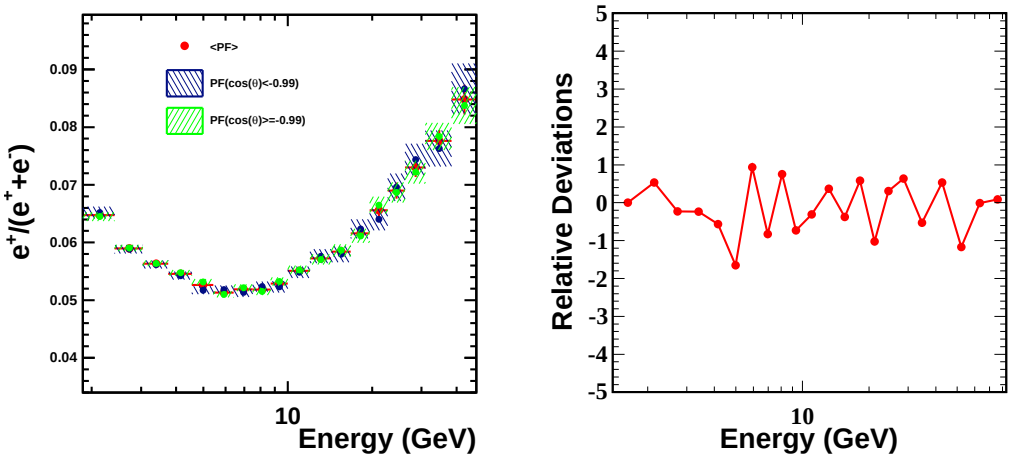

Figure 5.27: Left: Mean positron fraction using all geometrical acceptance (red), restricting to vertical incidence particles with $cos\theta < -0.99$ (blue dashed squared) and particles with $cos\theta \geq -0.99$ (green dashed squared). Right: Compatibility between the positron fraction for vertical incident particles and particles with $cos\theta \geq -0.99$. Their relative deviations normalized to their statistical errors added in quadrature are compatible with statistical fluctuations.

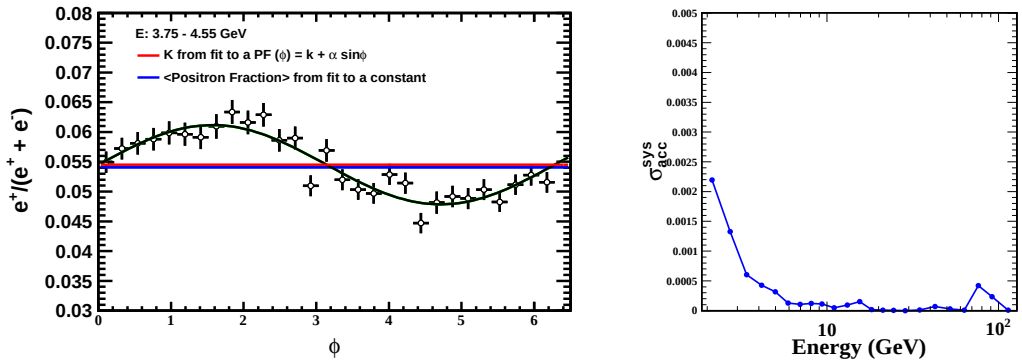

Figure 5.28: Left: Differential ratio in the ϕ coordinate. Mean ratio in the symmetric acceptance (red) case and measured ratio (blue). The offset between both values represent a systematic uncertainty in the measurement. Right: Systematic error due to an asymmetry in the acceptance.

In order to estimate the systematic uncertainty, we have compared the measured positron fraction with the mean positron fraction that would result in case of electron and positron acceptance being equally weighted. The latter one has been calculated assuming that in case of symmetry, the ratio should show a sinusoidal shape $PF(\phi) = K + \alpha \cdot \sin\phi$ with mean value K which is the correct ratio (Figure 5.28). The offset between the mean ratio (red line in figure 5.28) and the measured ratio (blue line in figure 5.28) is taken as a systematic uncertainty due to an asymmetry in the acceptance. The systematic error,which is shown in figure 5.28, is relevant at the lowest energies and negligible for energies greater than 10 GeV.

5.7.3 Rigidity Cutoff

Under cutoff particles may be a source of systematic errors. In the analysis, a dedicated cut has been applied to reject this component, namely, the particles energy must exceed the cutoff rigidity by a 30% at least at every orbit location. The 30% of safety factor is an estimation which has been validated by backtracing a fraction of the events in the magnetic field, however, it is plausible there is some residual contamination.

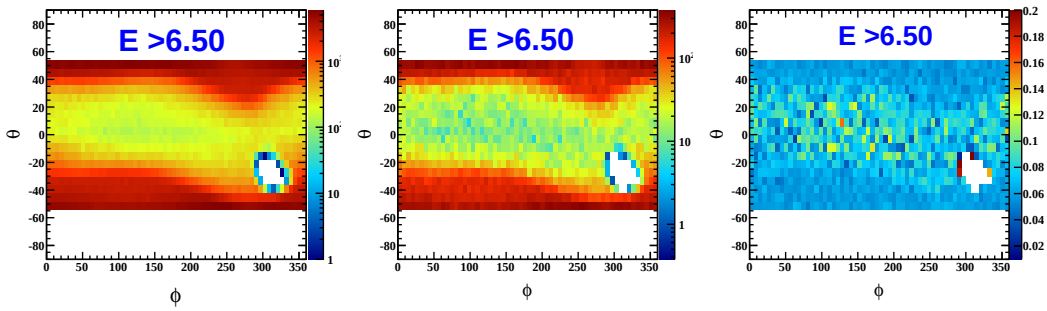

Figure 5.29: Integrated number of electrons (left), positrons (center) in geographical coordinates, and positron to electron ratio (right) for energies above 6.5 GeV.

To study a systematic effect related to the cutoff, the positron fraction has been calculated at different geomagnetic field locations with different cutoff rigidities. In figure 5.29 the electron and positron occupancy map in geographical coordinates, is shown for energies above 6.5 GeV for events that satisfy the cutoff condition.

The integrated positron to electron ratio (Fig. 5.29) shows an appreciable trend in geographical coordinates, where the apparent S-wave-like band is due a region with a higher cutoff rigidity and thus, displays a ratio corresponding to a higher energy. If we restrict the ratio to an energy interval and compute the mean positron fraction and the fraction for a coordinate pair (θ, ϕ) we find that deviations from the mean value at any energy are within statistical fluctuations (Fig. 5.30). A check has been performed repeating this procedure loosening and tightening the rigidity cutoff, proving the residual undercutoff background negligible.

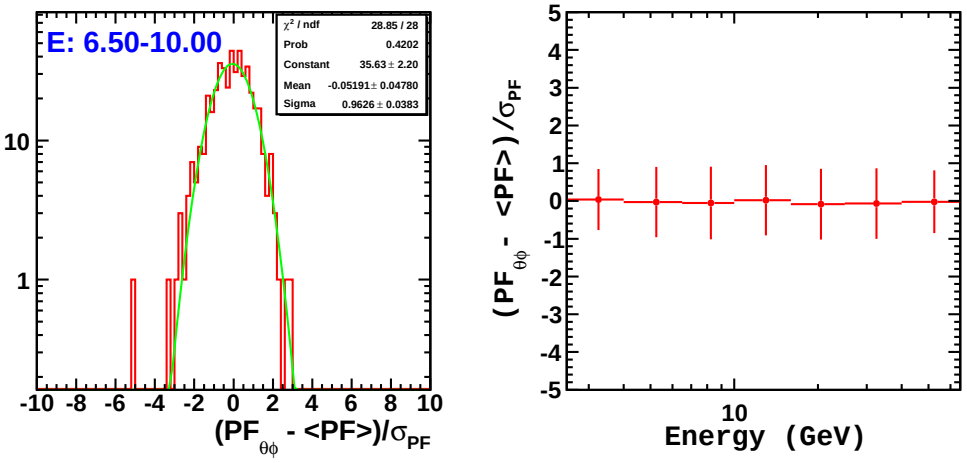

Figure 5.30: Pulls: Deviations from mean positron fraction $(PF_{\theta\phi} - \langle PF\rangle)/\sigma_{PF}$ for energies between 6.5-10 GeV (Left). The mean and σ at every energy interval of the pulls (right)

5.7.4 Bin to Bin Migration

In this section, the energy bin to bin migration is considered. The ECAL energy resolution has been measured in TB conditions. For vertical tracks has been found to be:

$$\frac{\sigma(E)}{E} = \frac{10.4\%}{\sqrt{E(GeV)}} \oplus 1.4\%. \tag{5.9}$$

For inclined tracks, a safety margin of $\oplus 2\%$ has been chosen for the constant term in accordance to TB measurements.

The steepness of the $e^{\pm}$ spectra suggest a wide binning to minimize potential bin migrations and to avoid unfolding procedures. In addition to this, a compromise must be made to accumulate statistics in the highest energy bins.

Taking all these ingredients into account, for the lower part of the spectrum where the number of $e^{\pm}$ flattens, a bin width of 4-5σ has been chosen . For intermediate energies, a bin width greater than 5σ is used in order to minimize bin to bin migrations. Finally for energies above 100 GeV, a bin width greater than 10σ has been adopted to get a sizable number of positrons.

With this sharing, we assure the bin-to-bin migration in negligible.

5.8 Summary and Results

In this section the positron fraction results are summarized for the four analysis described in this chapter. A comparison of these results with the published measurement is covered in appendix C.

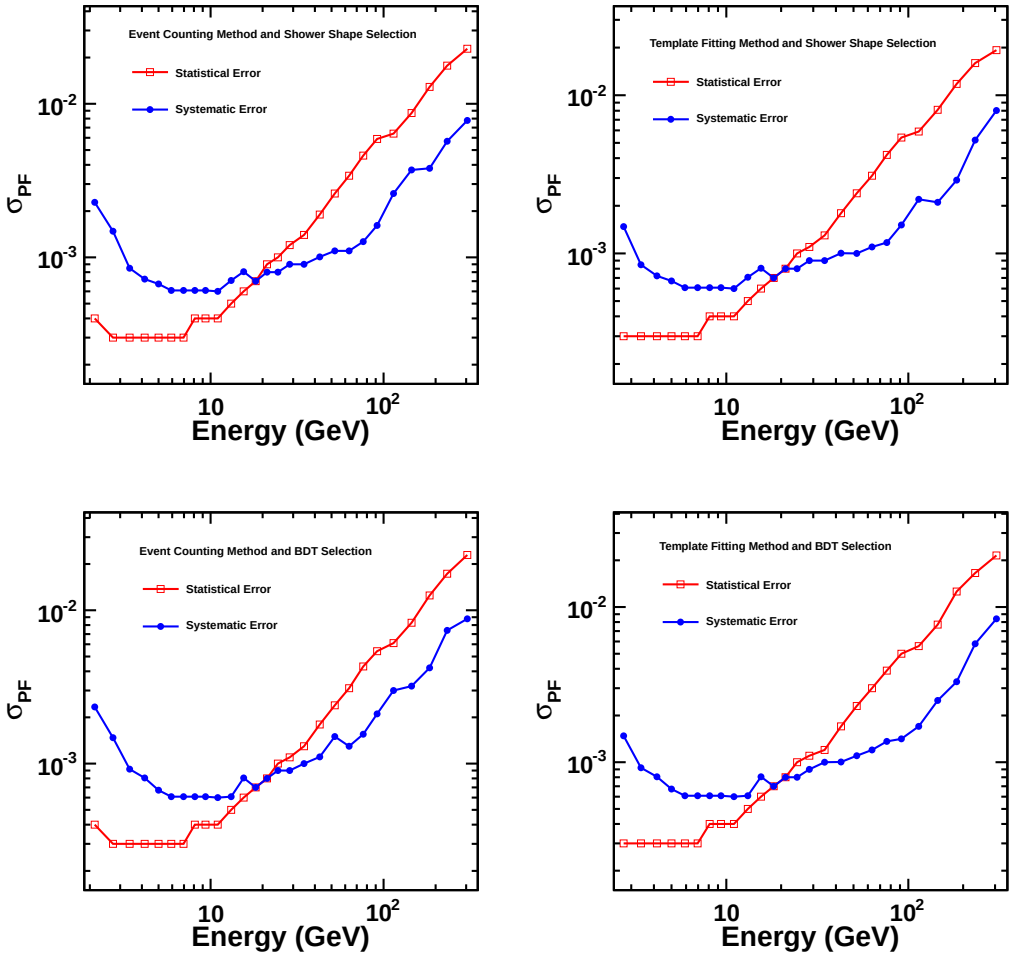

Figure 5.31: Positron fraction systematic and statistical errors for the four analysis studied in the chapter.

The measured positron fraction is presented in tables 5.3,5.4,5.5 and 5.6, where the number of positrons Ne^{+}, fraction, statistical error $\sigma_{stat.}$, and systematic error $\sigma_{sys.}$ are introduced.

In figure 5.31 the statistical and total systematic errors are shown for the four analysis. The statistical error dominates in all the analysis for energies above 20 GeV.

The systematic error, which is split into several contributions that have been described earlier in this chapter, is the result of all these individual contributions added in quadrature. From them, the most relevant at the highest energies are those related to the estimation of the charge confusion $\sigma_{c.c.}$ and the selection and fit procedure $\sigma_{sel.}$. At the very low energies, the systematic error related to the asymmetry in the acceptance $\sigma_{acc.}$ dominates the overall error.

The results of the four analysis are compatible within their statistical errors and sample overlap. The most accurate analysis, which we estimate with the inferior overall error, is the analysis with

the template fitting method using the BDT selection. The reason is that the positron fraction analysis larger contribution to the overall error is the statistical one, and the template fitting method maximizes the statistics owing to the separation power of the TRD and ECAL which allows to accurately determine the positron and electron abundances with a sizable fraction of proton background.

In figure 5.32 we show the total error, estimated as the statistical and systematic errors added in quadrature, and the optimal analysis, which is provided with the BDT selection.

The positron fraction shows a steady increase for energies above 10 GeV, up to 250 GeV. This increase is not expected from purely secondary production and will be further investigated in the next chapter.

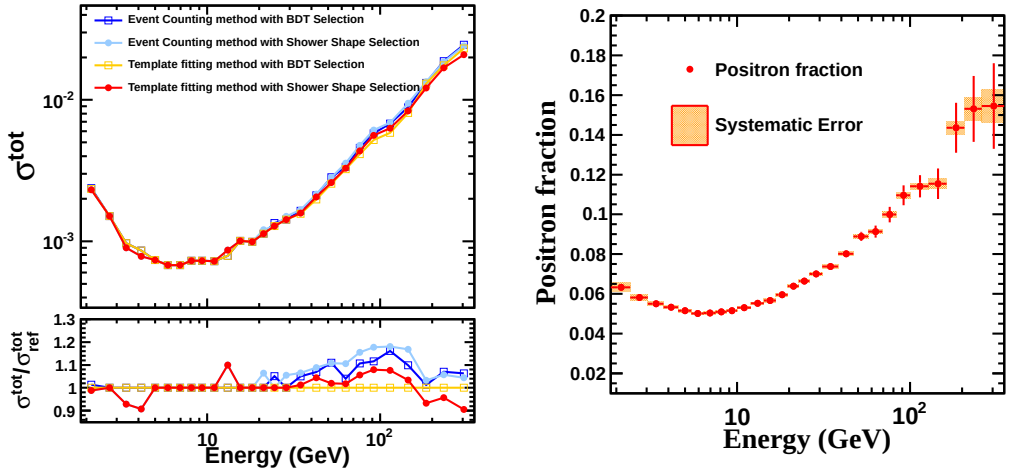

Figure 5.32: Positron fraction statistical + systematic errors added in quadrature for the four analysis. The reference PF fraction used in the ratio of errors is the one determined with the template fitting method with BDT selection (left). Optimal positron fraction result (right).

At energies above 350 GeV, the proton background becomes harder to reject, on the one hand, because the TRD enters a different regime, and on the other hand, because proton showers in the ECAL become more electromagnetic-like. To sort these issues, the selection with the ECAL must be maximized, which at the highest energies will imply to use MC simulations to train the selection classifiers. This will enable to use the TRD and ECAL redundancy even with samples with low purities. Reference distributions from MC simulation can be used then for a template fitting analysis at the highest energies.

In addition to this, at some point charge confusion background becomes an issue as we approach the MDR of the Tracker. To go to higher energies it will be compelling to use Tracker patterns with a large lever arm, which in turn will restrict the overall acceptance and enlarge the statistical error. Taking this into account, it is necessary to collect more data to go to higher energies.

Table 5.3: Positron fraction using the BDT Selection with an event-counting analysis.

Energy (GeV)	$\mathbf{Ne}^{+}$	**Fraction**	$\boldsymbol{\sigma_{stat.}}$	$\sigma_{sel.}$	$\sigma_{acc.}$	$\sigma_{c.c.}$	$\boldsymbol{\sigma_{sys.}}$
2.00 - 2.41	20517.40	0.0634	0.0004	0.0003	0.0022	0.0007	0.0023
2.41 - 3.04	32722.13	0.0579	0.0003	0.0001	0.0013	0.0007	0.0015
3.04 - 3.75	33326.54	0.0552	0.0003	0.0001	0.0006	0.0007	0.0009
3.75 - 4.55	31650.53	0.0533	0.0003	0.0001	0.0004	0.0007	0.0008
4.55 - 5.43	28591.03	0.0514	0.0003	0.0000	0.0003	0.0006	0.0007
5.43 - 6.42	25082.86	0.0500	0.0003	0.0001	0.0001	0.0006	0.0006
6.42 - 7.50	21525.33	0.0502	0.0003	0.0001	0.0001	0.0006	0.0006
7.50 - 8.69	17666.16	0.0506	0.0004	0.0001	0.0001	0.0006	0.0006
8.69 - 10.00	14054.21	0.0512	0.0004	0.0001	0.0001	0.0006	0.0006
10.00 - 12.01	14846.30	0.0529	0.0004	0.0002	0.0000	0.0006	0.0006
12.01 - 14.26	10998.70	0.0551	0.0005	0.0001	0.0001	0.0006	0.0006
14.26 - 16.78	8377.33	0.0562	0.0006	0.0002	0.0001	0.0008	0.0008
16.78 - 19.59	6981.02	0.0592	0.0007	0.0001	0.0000	0.0007	0.0007
19.59 - 22.71	5766.20	0.0630	0.0008	0.0001	0.0000	0.0008	0.0008
22.71 - 26.18	4310.11	0.0658	0.0010	0.0003	0.0000	0.0008	0.0009
26.18 - 31.00	3733.90	0.0695	0.0011	0.0003	0.0000	0.0009	0.0009
31.00 - 38.36	3119.73	0.0729	0.0013	0.0004	0.0000	0.0009	0.0010
38.36 - 47.03	1988.58	0.0795	0.0018	0.0005	0.0001	0.0010	0.0011
47.03 - 57.22	1248.73	0.0860	0.0024	0.0011	0.0000	0.0010	0.0015
57.22 - 69.18	783.82	0.0881	0.0031	0.0009	0.0000	0.0010	0.0013
69.18 - 83.20	523.06	0.0980	0.0043	0.0010	0.0004	0.0011	0.0016
83.20 - 100.00	401.25	0.1094	0.0054	0.0017	0.0002	0.0012	0.0021
100.00 - 127.90	329.49	0.1088	0.0061	0.0026	0.0000	0.0014	0.0030
127.90 - 162.60	174.06	0.1065	0.0083	0.0026	0.0001	0.0018	0.0032
162.60 - 206.00	122.54	0.1344	0.0125	0.0035	0.0002	0.0023	0.0042
206.00 - 260.00	86.15	0.1530	0.0173	0.0063	0.0002	0.0039	0.0074
260.00 - 350.00	57.85	0.1495	0.0229	0.0042	0.0002	0.0077	0.0088

Table 5.4: Positron fraction using the Shower Shape Selection with an event-counting analysis.

Energy (GeV)	$\mathbf{Ne^{+}}$	**Fraction**	$\boldsymbol{\sigma_{stat.}}$	$\sigma_{sel.}$	$\sigma_{acc.}$	$\sigma_{c.c.}$	$\boldsymbol{\sigma_{sys.}}$
2.00 - 2.41	20433.77	0.0632	0.0004	0.0000	0.0022	0.0006	0.0023
2.41 - 3.04	30689.98	0.0584	0.0003	0.0001	0.0013	0.0007	0.0015
3.04 - 3.75	30473.32	0.0551	0.0003	0.0000	0.0006	0.0006	0.0008
3.75 - 4.55	29036.82	0.0534	0.0003	0.0000	0.0004	0.0006	0.0007
4.55 - 5.43	26450.76	0.0513	0.0003	0.0000	0.0003	0.0006	0.0007
5.43 - 6.42	23474.68	0.0497	0.0003	0.0000	0.0001	0.0006	0.0006
6.42 - 7.50	19996.10	0.0500	0.0003	0.0000	0.0001	0.0006	0.0006
7.50 - 8.69	16341.51	0.0504	0.0004	0.0000	0.0001	0.0006	0.0006
8.69 - 10.00	12954.00	0.0511	0.0004	0.0000	0.0001	0.0006	0.0006
10.00 - 12.01	13580.77	0.0527	0.0004	0.0000	0.0000	0.0006	0.0006
12.01 - 14.26	10000.00	0.0548	0.0005	0.0000	0.0001	0.0007	0.0007
14.26 - 16.78	7594.09	0.0560	0.0006	0.0001	0.0001	0.0008	0.0008
16.78 - 19.59	6348.75	0.0596	0.0007	0.0000	0.0000	0.0007	0.0007
19.59 - 22.71	5154.91	0.0628	0.0009	0.0001	0.0000	0.0008	0.0008
22.71 - 26.18	3789.62	0.0651	0.0010	0.0001	0.0000	0.0008	0.0008
26.18 - 31.00	3285.42	0.0693	0.0012	0.0000	0.0000	0.0009	0.0009
31.00 - 38.36	2668.51	0.0717	0.0014	0.0003	0.0000	0.0009	0.0009
38.36 - 47.03	1708.17	0.0793	0.0019	0.0003	0.0001	0.0010	0.0010
47.03 - 57.22	1094.23	0.0871	0.0026	0.0005	0.0000	0.0010	0.0011
57.22 - 69.18	703.59	0.0897	0.0034	0.0002	0.0000	0.0011	0.0011
69.18 - 83.20	447.07	0.0974	0.0046	0.0005	0.0004	0.0011	0.0013
83.20 - 100.00	356.01	0.1134	0.0059	0.0006	0.0002	0.0015	0.0016
100.00 - 127.90	279.50	0.1070	0.0064	0.0013	0.0000	0.0022	0.0026
127.90 - 162.60	146.83	0.1029	0.0087	0.0031	0.0001	0.0021	0.0037
162.60 - 206.00	107.99	0.1314	0.0129	0.0026	0.0002	0.0028	0.0038
206.00 - 260.00	69.46	0.1430	0.0177	0.0029	0.0002	0.0049	0.0057
260.00 - 350.00	45.78	0.1503	0.0228	0.0012	0.0002	0.0077	0.0078

Table 5.5: Positron fraction using the Shower Shape Selection with a Template-Fitting analysis.

Energy (GeV)	$\mathbf{Ne^+}$	**Fraction**	$\boldsymbol{\sigma_{stat.}}$	$\sigma_{sel.}$	$\sigma_{acc.}$	$\sigma_{c.c.}$	$\boldsymbol{\sigma_{sys.}}$
2.00 - 2.41	23522.78	0.0630	0.0004	0.0000	0.0022	0.0006	0.0023
2.41 - 3.04	34287.72	0.0585	0.0003	0.0000	0.0013	0.0007	0.0015
3.04 - 3.75	33159.15	0.0549	0.0003	0.0000	0.0006	0.0006	0.0008
3.75 - 4.55	31374.35	0.0533	0.0003	0.0000	0.0004	0.0006	0.0007
4.55 - 5.43	28528.09	0.0513	0.0003	0.0000	0.0003	0.0006	0.0007
5.43 - 6.42	25373.33	0.0498	0.0003	0.0000	0.0001	0.0006	0.0006
6.42 - 7.50	21615.76	0.0500	0.0003	0.0000	0.0001	0.0006	0.0006
7.50 - 8.69	17827.25	0.0506	0.0004	0.0000	0.0001	0.0006	0.0006
8.69 - 10.00	14181.49	0.0512	0.0004	0.0000	0.0001	0.0006	0.0006
10.00 - 12.01	14919.04	0.0527	0.0004	0.0000	0.0000	0.0006	0.0006
12.01 - 14.26	11129.37	0.0550	0.0005	0.0000	0.0001	0.0007	0.0007
14.26 - 16.78	8518.86	0.0565	0.0006	0.0000	0.0001	0.0008	0.0008
16.78 - 19.59	7129.81	0.0596	0.0007	0.0000	0.0000	0.0007	0.0007
19.59 - 22.71	5829.95	0.0630	0.0008	0.0000	0.0000	0.0008	0.0008
22.71 - 26.18	4334.37	0.0655	0.0010	0.0000	0.0000	0.0008	0.0008
26.18 - 31.00	3775.15	0.0696	0.0011	0.0000	0.0000	0.0009	0.0009
31.00 - 38.36	3128.75	0.0727	0.0013	0.0000	0.0000	0.0009	0.0009
38.36 - 47.03	2015.95	0.0806	0.0018	0.0000	0.0001	0.0010	0.0010
47.03 - 57.22	1311.14	0.0886	0.0024	0.0000	0.0000	0.0010	0.0010
57.22 - 69.18	833.73	0.0910	0.0031	0.0000	0.0000	0.0011	0.0011
69.18 - 83.20	538.41	0.0980	0.0042	0.0001	0.0004	0.0011	0.0012
83.20 - 100.00	428.40	0.1135	0.0054	0.0001	0.0002	0.0015	0.0015
100.00 - 127.90	358.17	0.1140	0.0059	0.0001	0.0000	0.0022	0.0022
127.90 - 162.60	189.83	0.1095	0.0081	0.0004	0.0001	0.0021	0.0021
162.60 - 206.00	140.34	0.1389	0.0118	0.0007	0.0002	0.0028	0.0029
206.00 - 260.00	88.31	0.1443	0.0160	0.0017	0.0002	0.0049	0.0052
260.00 - 350.00	73.00	0.1550	0.0193	0.0023	0.0002	0.0077	0.0080

Table 5.6: Positron fraction using the BDT Selection with a Template-Fitting analysis.

Energy (GeV)	$\mathbf{Ne^{+}}$	**Fraction**	$\boldsymbol{\sigma_{stat.}}$	$\sigma_{sel.}$	$\sigma_{acc.}$	$\sigma_{c.c.}$	$\boldsymbol{\sigma_{sys.}}$
2.00 - 2.41	23975.49	0.0632	0.0004	0.0002	0.0022	0.0007	0.0023
2.41 - 3.04	35341.47	0.0581	0.0003	0.0001	0.0013	0.0007	0.0015
3.04 - 3.75	35778.52	0.0550	0.0003	0.0001	0.0006	0.0007	0.0009
3.75 - 4.55	33668.72	0.0533	0.0003	0.0000	0.0004	0.0007	0.0008
4.55 - 5.43	30427.74	0.0515	0.0003	0.0000	0.0003	0.0006	0.0007
5.43 - 6.42	27001.13	0.0501	0.0003	0.0001	0.0001	0.0006	0.0006
6.42 - 7.50	23068.01	0.0503	0.0003	0.0001	0.0001	0.0006	0.0006
7.50 - 8.69	19042.28	0.0509	0.0004	0.0000	0.0001	0.0006	0.0006
8.69 - 10.00	15261.85	0.0515	0.0004	0.0001	0.0001	0.0006	0.0006
10.00 - 12.01	16099.99	0.0530	0.0004	0.0002	0.0000	0.0006	0.0006
12.01 - 14.26	12070.44	0.0552	0.0005	0.0001	0.0001	0.0006	0.0006
14.26 - 16.78	9260.46	0.0566	0.0006	0.0002	0.0001	0.0008	0.0008
16.78 - 19.59	7764.11	0.0595	0.0007	0.0000	0.0000	0.0007	0.0007
19.59 - 22.71	6480.85	0.0638	0.0008	0.0001	0.0000	0.0008	0.0008
22.71 - 26.18	4875.28	0.0664	0.0010	0.0001	0.0000	0.0008	0.0008
26.18 - 31.00	4245.56	0.0700	0.0011	0.0002	0.0000	0.0009	0.0009
31.00 - 38.36	3587.61	0.0737	0.0012	0.0004	0.0000	0.0009	0.0010
38.36 - 47.03	2288.92	0.0801	0.0017	0.0003	0.0001	0.0010	0.0010
47.03 - 57.22	1508.81	0.0889	0.0023	0.0004	0.0000	0.0010	0.0011
57.22 - 69.18	947.28	0.0913	0.0030	0.0006	0.0000	0.0010	0.0012
69.18 - 83.20	639.15	0.0999	0.0039	0.0006	0.0004	0.0011	0.0014
83.20 - 100.00	479.53	0.1096	0.0050	0.0007	0.0002	0.0012	0.0014
100.00 - 127.90	414.50	0.1141	0.0056	0.0010	0.0000	0.0014	0.0017
127.90 - 162.60	232.44	0.1154	0.0077	0.0017	0.0001	0.0018	0.0025
162.60 - 206.00	136.75	0.1436	0.0126	0.0024	0.0002	0.0023	0.0033
206.00 - 260.00	93.00	0.1531	0.0166	0.0043	0.0002	0.0039	0.0058
260.00 - 350.00	72.07	0.1545	0.0215	0.0034	0.0002	0.0077	0.0084

III

Diagnosis Of An Excess

6

Characterization of the Positron Excess

In chapter 5 we have described the analysis that establishes the observation of a rising positron fraction with the energy. In this chapter we characterize the positron excess from three perspectives: It's dependence with time, direction and energy. We also address the possibility that the excess requires the inclusion of primary sources, whether from a particle physics or an astrophysical origin. Some physics models are used to illustrate this point.

6.1 Positron Fraction Stability in Time

We have searched for temporal variations of the positron fraction for different time spans and energy ranges (Fig. 6.1).

The sample is folded in time at every energy interval. For each folding we evaluate the positron ratio, resulting in a distribution of e^+/e^- for different time spans, which we normalize to the mean value $< e^+/e^- >$ at that energy.

Finally, we fit the resulting distributions to a constant value which yields the following probability map (Fig. 6.2) for each folding and energy bin.

At high energies, $E > 20$ GeV, the variation in time is compatible with purely statistical fluctuations and no indication of either a systematic effect or temporal structures are found. At low energies, deviations are observed for time intervals above approximately 10 days, fact that is consistent with variations in the solar activity.

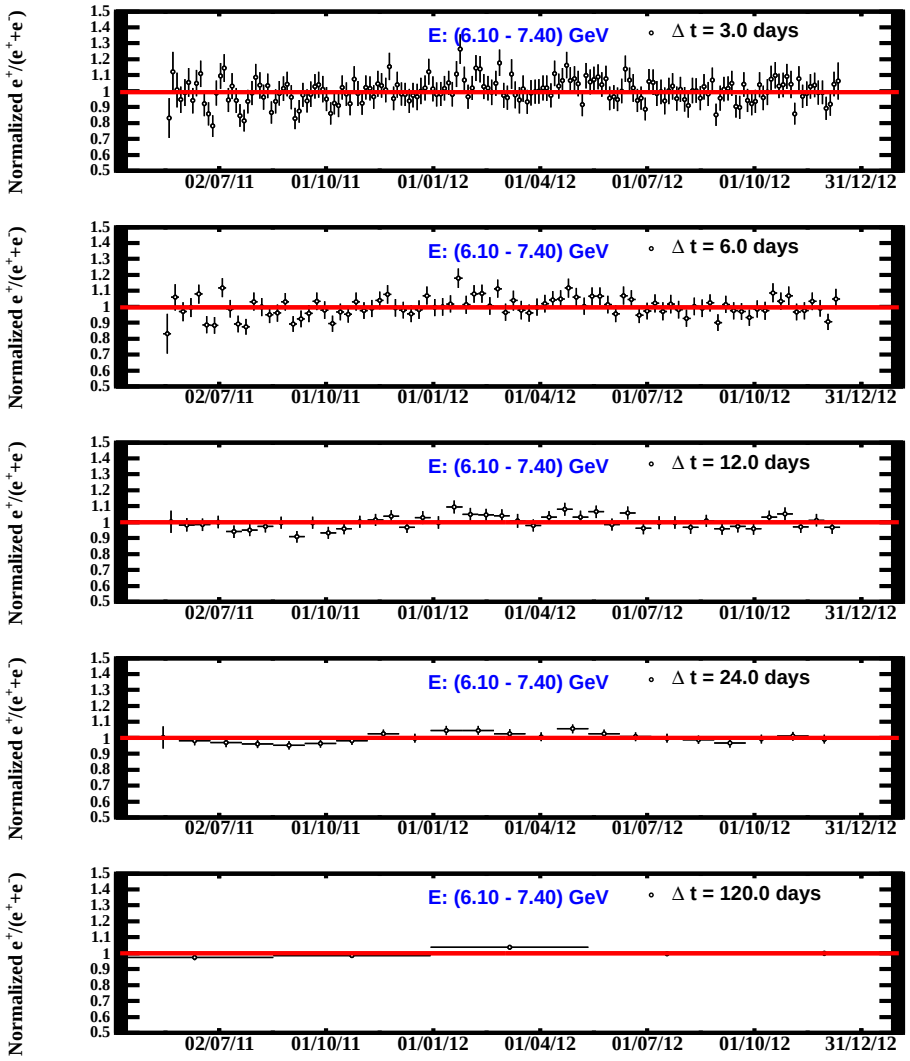

Figure 6.1: Positron fraction temporal variation: Normalized positron fraction evolution with time, for different time intervals in an illustrative energy bin.

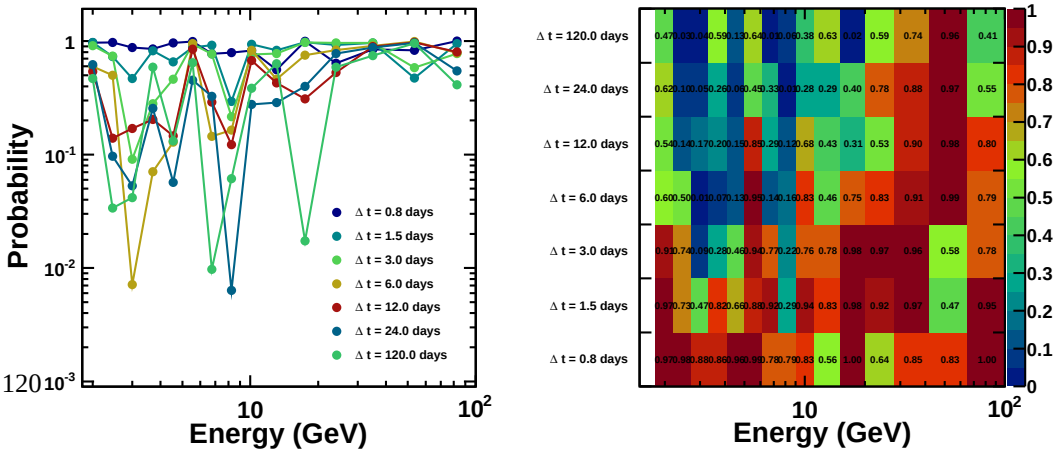

Figure 6.2: Fit χ^2 probability for each folding and energy point.

6.2 Spectral Structures

A search for spectral structures in the positron fraction data has been conducted. Fine structures at ECAL energy resolution scales are studied by means of a simple model in which the fluxes are assumed to be the combination of two contributions: a diffuse power law spectrum of e^+, e^- and a common single source of e^+, e^-:

$$\Phi_{e^+} = K_{e^+}\mathrm{E}^{-\gamma_{e^+}} + \mathrm{K_s E}^{-\gamma_s}\exp^{-\mathrm{E/E_c}} \tag{6.1}$$

$$\Phi_{e^-} = K_{e^-}\mathrm{E}^{-\gamma_{e^-}} + \mathrm{K_s E}^{-\gamma_s}\exp^{-\mathrm{E/E_c}}, \tag{6.2}$$

where $K_{e^\pm}$ and K_s are the relative contributions from the diffuse and single source spectra. The diffuse spectra are assumed to follow a power law with spectral index $\gamma_{e^\pm}$ and the single source is described as a single power law with spectral index γ_s and an exponential cut-off energy of $\mathrm{E_c}$.

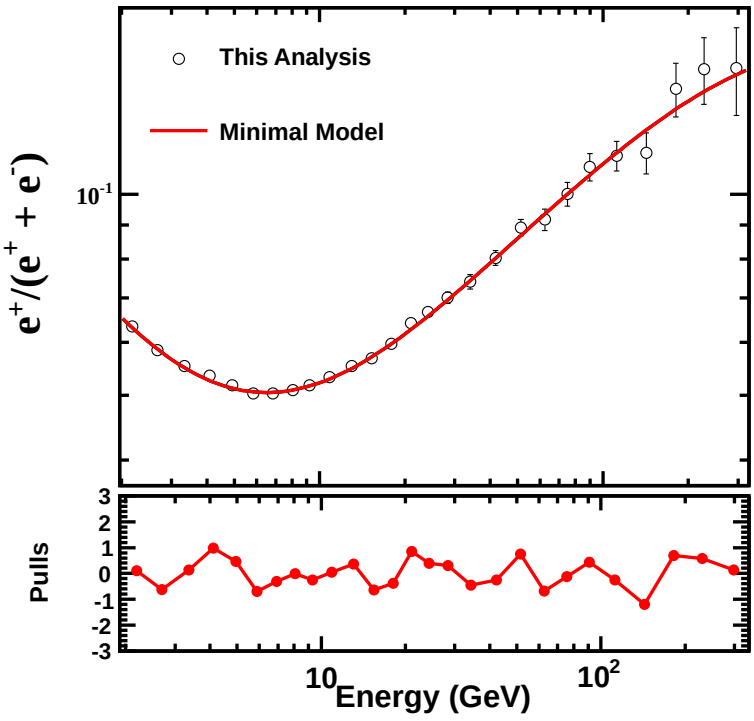

Figure 6.3: Search for structures with a minimal model for the flux.

This construction yields a 5 parameter model for the positron fraction which remarkably fits the data (Fig. 6.3). From this model that there is no evidence of significant spectral structures at energy

scales at the level of the ECAL energy resolution.

In addition, a search for spectral structures at larger scales has been performed. The approach followed to disentangle structures in the positron fraction from a continuous background with statistical fluctuations is based on an implementation [88] of the Mariscotti method as described in [83], [102]. Still, no indications of significant small to intermediate energy scale features in the positron fraction have been found.

6.3 Anisotropy

Primary sources of cosmic ray positrons and electrons may induce some degree of anisotropy on the measured positron and electron fluxes [26],[28] . Previous searches have been carried out on the flux of electrons and positrons [43],[54]. In AMS, a systematic search for anisotropies on the positron ratio, that is, the ratio of the positron flux to the electron flux is performed using 500,000 positrons and electrons in the energy range from 16 to 350 GeV collected during the initial 21 months of operations on the ISS, from 19 May 2011 to 10 March 2013.

The positron ratio is computed for different energy ranges and arrival directions in galactic coordinates. The fluctuations of the resulting sky maps are evaluated at several angular scales and upper limits to their amplitude are obtained.

In some models [100], a relative excess of positrons towards the Sun direction is expected. In AMS, this is searched on sky maps constructed in geocentric solar ecliptic coordinates or, likewise, looking for a seasonal excess of the dipole anisotropy in galactic coordinates.

In order to exclude the effect of a supposed anisotropy of the reference electron flux, the analysis has been repeated on the positron to proton ratio [1].

Finally, the influence of geomagnetic effects is estimated by evaluating the sensitivity to a dipole contribution using the directions obtained after back-tracing in the geomagnetic field.

The overall selection efficiency for positrons and electrons is estimated to be above 80% in the acceptance of the ECAL. The remaining sample contains 35,000 primary positrons, 460,000 electrons and a negligible amount of protons.

The selected events are grouped into 5 cumulative energy ranges from 16 to 350 GeV according to their measured energy in the ECAL. The minimum energy for each range is 16, 25, 40, 65 and 100 GeV.

6.3.1 Anisotropy on e^+/e^-

The arrival directions of electrons and positrons are used to build sky maps in galactic coordinates, (b, l), containing the number of observed positrons and electrons. The maps corresponding to electrons and positrons in the energy range from 16 to 350 GeV are displayed in Fig. 6.4. The spread

[1] Procc. of the ICRC Brazil 2013. Determination of the positron anisotropy with AMS. To be published

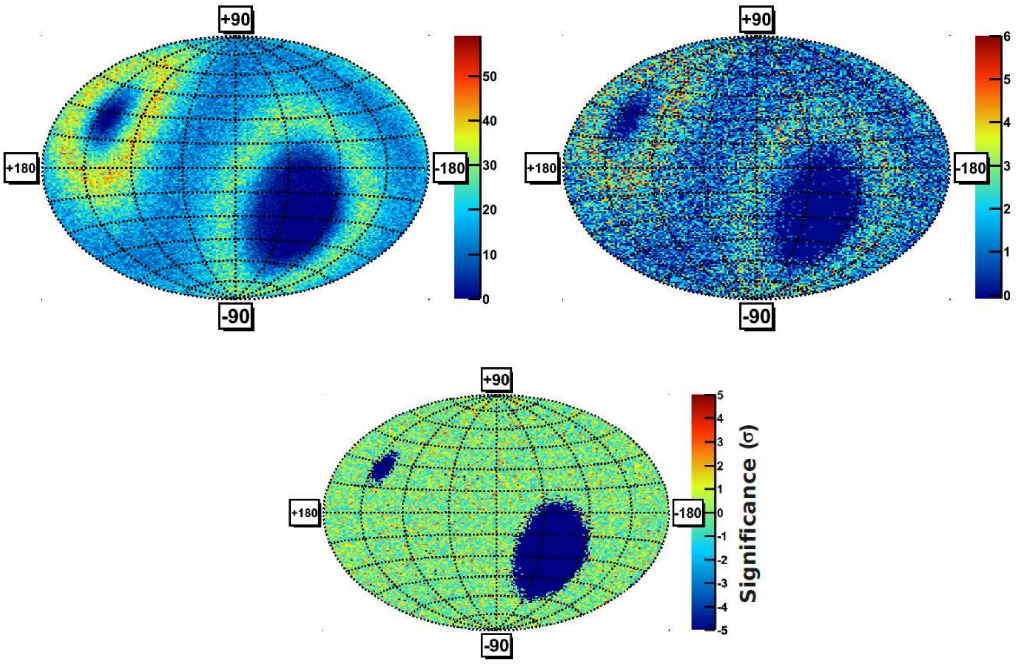

Figure 6.4: Sky maps showing the arrival directions of selected 16–350 GeV electrons (left) and positrons (center) in galactic coordinates using a Hammer-Aitoff projection. The color code reflects the number of events per bin. Relative fluctuations of the positron ratio e^+/e^- in galactic coordinates.

of the number of events collected on different directions is a consequence of the non uniform sky coverage of the AMS exposure.

Different approaches have been followed to define the binning on the sky maps. First, same area rectangular bins are defined on the $(\sin(b), l)$ plane and regions with low exposure are excluded from the analysis. Second, rectangular bins mapping similar exposure, that is, containing same number of electrons, are defined. The comparison of the results obtained on different binning is used to estimate the stability of the analysis.

For a given energy range, the positron to electron ratio is computed on each galactic coordinate bin. The consistency of the set of bin-to-bin ratios to a common value is estimated using a χ^2 test. A good agreement is found for all energy ranges. Moreover, no structure is observed on the projections along galactic latitude or longitude (Fig. 6.4).

A general description of the relative fluctuations on the observed positron ratio is obtained by means of a spherical harmonic expansion

$$\frac{r_e(b,l) - \langle r_e \rangle}{\langle r_e \rangle} = \sum_{\ell=0}^{\infty} \sum_{m=-\ell}^{\ell} a_{\ell m}\, Y_{\ell m}(\pi/2 - b, l),$$

where $r_e(b,l)$ denotes the positron ratio at (b,l), $\langle r_e \rangle$ is the average ratio over the sky map, $Y_{\ell m}$ are the real spherical harmonic functions, and a_{lm} are their corresponding amplitudes.

The amplitudes of spherical harmonic contributions at fixed angular scale, ℓ, are fit to the data for dipole ($\ell = 1$), quadrupole ($\ell = 2$) and octopole ($\ell = 3$) contributions with a χ^2 minimization. No significant a_{lm} is found at any angular scale ($\ell = 1, 2, 3$) and energy range. As an example, in Fig. 6.5 the results corresponding to a dipole contribution perpendicular to the galactic plane, a_{10}, are displayed together with the 1, 2 and 3σ contours as a function of the minimum energy. Similar sensitivity is obtained on the amplitudes of the other spherical harmonic contributions.

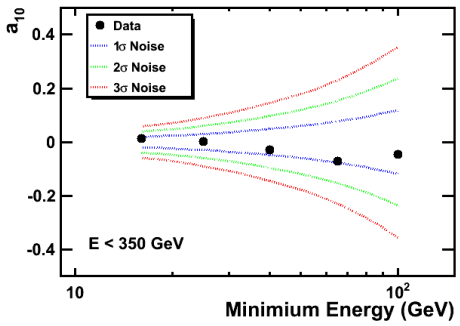

Figure 6.5: Amplitudes a_{10} obtained from fits of a dipole contribution to the data on different energy ranges. The dashed lines correspond to the 1, 2 and 3σ contours.

The intensity of the fluctuations on the studied angular scales is quantified with the coefficients of the angular power spectrum defined as

$$C_\ell = \frac{1}{2\ell + 1} \sum_{m=-\ell}^{\ell} a_{\ell m}^2.$$

The values of the coefficients C_1, C_2 and C_3 obtained from the fits are consistent with the expectations from pure statistical fluctuations on all energy ranges. The results for the dipole coefficient C_1 are shown in Fig. 6.6 along with expected level for random noise and its 68% CL band.

6.3.2 Dipole Anisotropy

The anisotropy induced by primary sources is expected to follow a dipole pattern with the maximum pointing towards the source and the minimum to the opposite direction. It is then customary to define the dipole anisotropy parameter, δ, as the relative difference between maximum and minimum amplitudes. Therefore, δ can be derived from the coefficient C_1 with the expression $\delta = 3\sqrt{C_1/4\pi}$.

Since the coefficients of the multipole expansion are consistent with the expectations from isotropy, limits on the coefficients of the angular power spectrum, C_l, can be obtained for all energy ranges. In particular, limits on the dipole anisotropy parameter δ are derived for any axis in galactic

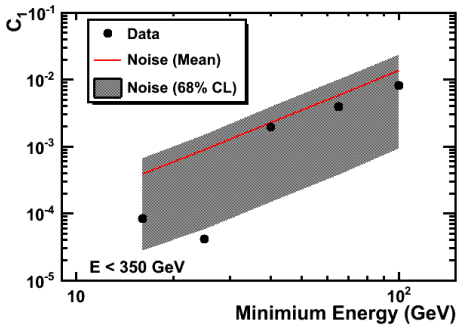

Figure 6.6: Results for the dipole coefficient C_1 obtained from the fits to the data on different energy ranges. The expected level for random noise together with its 68% CL band is also displayed.

coordinates. The upper limits at the 95% confidence level for the 5 cumulative energy ranges are shown in Fig 6.7 and Table 6.1. The limit obtained for the energy range from 16 to 350 GeV is $\delta < 0.030$.

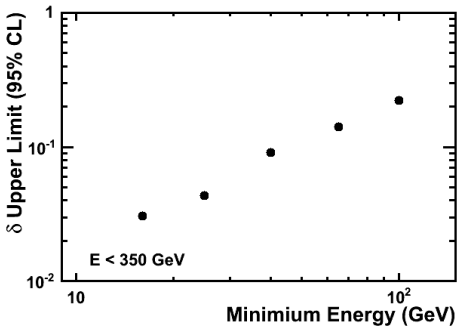

Figure 6.7: AMS upper limits on the dipole anisotropy parameter δ at the 95% confidence level on different energy ranges.

Table 6.1: AMS upper limits on the dipole anisotropy parameter δ (95% C.L.) from Min. Energy up to 350 GeV.

Min. Energy (GeV)	**δ Upper Limit (95% C.L.)**
16	0.030
25	0.044
40	0.090
65	0.142
100	0.222

This value corresponds to the fit of the sky map with 20x20 bins where only bins with at least 50 electrons are considered. The fraction of masked channels is 3.5% and the χ^2 of the fit to a dipole contribution is 390.3 for 382 degrees of freedom.

The stability of the results is verified by repeating the analysis on sky maps constructed with different binning. First, the number of bins in the regular binning is changed in a wide range, namely from 4x4 bins to 40x40 bins. Second, the same analysis is carried out using adaptive bins mapping the AMS exposure. In all cases, negligible differences are found.

The influence of the masked bins in the sky maps is also explored by changing the requirement on the minimum number of electrons from 25 to 200 events per bin, which modifies the number of bins participating in the fit in about 10%. Again, no significant difference is found.

6.3.3 Seasonal Excess

Dark matter annihilation in the Sun vicinity could generate a relative positron excess towards the Sun direction. When integrated over a complete year, the dominant dipole contribution would effectively cancel on the sky maps computed in galactic coordinates. However, seasonal effects may be observed.

The data is divided into 8 seasons covering the whole data taking period and the analysis is repeated on the individual samples. No significant deviation from isotropy is found. As an example, in Fig. 6.8 the values obtained for the dipole coefficient C_1 on the different samples for the energy range 16 to 350 GeV are displayed relative to the expected noise level. Data is consistent with the expectations from pure statistical fluctuations.

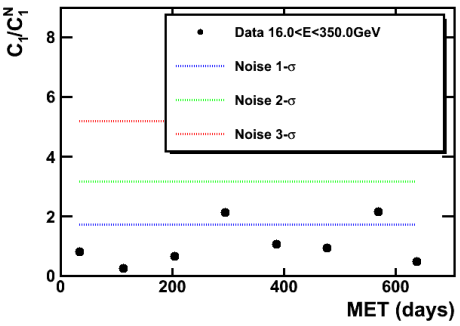

Figure 6.8: Dipole coefficients C_1 obtained from the fit to the data in the energy range 16 to 350 GeV corresponding to the 8 seasons covering the whole data taking period. The values are displayed relative to the expected noise level for random fluctuations. The dashed lines correspond to the 1, 2 and 3σ upper contours.

The effect of an excess towards the Sun direction is enhanced on the appropriate reference system. A complementary analysis is performed using sky maps built in geocentric solar ecliptic

coordinates, where the Earth-Sun axis defines its primary direction and its equatorial plane lies on the ecliptic. No significant deviation from isotropy is found and similar limits on a dipole anisotropy as those obtained in Sec. 6.3.2 are derived.

6.4 Physics Models

The accuracy of this measurement allows to study different models for the positron excess. A minimal model will be used to address the existence of primary sources of positrons. This in turn will provide a model for the diffuse background that we will use as a reference in the following sections.

Within this framework, the AMS-02 measurement of the positron fraction and the $e^+ + e^-$ flux provide an absolute measurement of the source component which will be used to evaluate the most relevant candidates to explain the positron fraction raise with the energy, i.e. Dark Matter and ordinary astrophysical sources. For the positron fraction data, we will use the BDT selection and template fitting analysis (which provides the most accurate measurement), using an energy binning matching that of the positron fraction published result [9]. For the $e^+ + e^-$ absolute flux, we will use AMS published results [15].

6.4.1 Minimal Model

The minimal model is based on a parametrization of the fluxes which are assumed to be the combination of two contributions: a diffuse power law spectra and a common single source of e^+, e^-, as described in section 6.2. Details on the resulting parametrization are presented in table 6.2.

Table 6.2: Minimal model parameters for the positron fraction with the BDT selection and template fitting analysis.

$\gamma_{e^-} - \gamma_{e^+}$	K_{e^+}/K_{e^-}	$\gamma_{e^-} - \gamma_s$	K_s/K_{e^-}	$1/\mathrm{E_c}$	$\chi^2/ndof$
-0.66 ± 0.05	0.090 ± 0.002	0.63 ± 0.05	0.0089 ± 0.0015	$1/0.0015 \pm 1/0.0008$	40.9/53

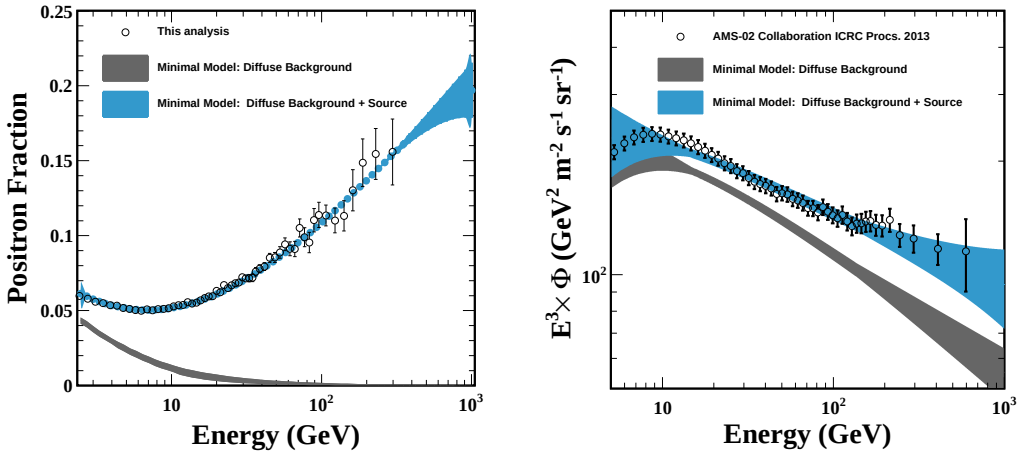

Figure 6.9: Minimal model as described in the text. Electron plus positron flux from [15]

We use these contributions to fit the positron fraction, which yields the relative spectral indexes

and normalizations of electrons and positrons, and the AMS-02 $e^+ + e^-$ absolute flux measurement [15]. The latter provides the absolute spectral index for electrons and positrons, and in particular, the expectations for the electron and positron diffuse background. We will use the diffuse background resulting from this model as the reference background for the physics models presented hereafter.

In figure 6.9 the minimal model results are shown for the positron fraction and $e^+ + e^-$ flux. In this figure the fit minimum energy and solar modulation parameter have been varied to study the stability of the model. The resulting diffuse background (gray band in figure 6.9) from the scan is stable.

This background evaluation is used alternatively to the conventional GALPROP computation of the diffuse $e^{\pm}$ components, which are considerably harder and provide a larger contribution to the overall flux. On the other hand, public codes for CR propagation are tuned to reproduce the measured fluxes and the very precise measurements of the $e^{\pm}$, proton and high Z nuclei performed by AMS will likely become the reference data in the future. Therefore, the background estimation within the minimal model, which is consistent with the AMS data presented here, can be considered a reliable description of the diffuse component.

The most straightforward interpretation of this minimal model implies that the positron fraction is not consistent with a purely diffuse component of electrons and positrons and requires a *primary* source which we shall investigate. An appealing implication of this model is that the source is constrained within the model uncertainties, namely, the spectral index of the primary source flux is determined. Hereafter we will examine some illustrative physical models that may account for these sources.

6.4.2 Dark Matter Source Scenario

Dark matter annihilation or decay can produce a large amount of positrons and electrons, hence, it constitutes a very attractive candidate to explain the reported excesses. Nevertheless, conventional WIMPs annihilation rates with canonical cross sections $\langle \sigma v \rangle = 3\text{x}10^{-26}\text{cm}^3/\text{s}$ are too small to make up the observed abundances. Moreover, the absence of an excess in antiprotons indicates that the annihilation through hadronic channels must be strongly suppressed.

In this chapter we consider the model-independent Dark Matter scenario described in chapter 2. We assume DM particles to annihilate into leptonic final states to satisfy $\bar{p}$ bounds. In particular $\mu\bar{\mu}$ and $\tau\bar{\tau}$ channels are most favored. We will assume the required normalization by means of any of the mechanisms considered in e.g. [13].

The signal that results from DM annihilation, depends essentially on the squared DM density from the astrophysics point of view, and the annihilation cross section from the particle physics side:

$$Q(E,\vec{r}) = \frac{1}{2}\frac{\rho^2(\vec{r})}{M_{DM}^2}\sum_i \langle \sigma v \rangle_i \frac{dN_i(E)}{dE}.$$

We have scanned the $M_{DM} - \langle\sigma v\rangle$ parameter space. The resulting fluxes has been used to perform a joint fit to the AMS-02 positron fraction data and absolute flux data for energies above 30 GeV where solar modulation can be regarded as negligible.

In figure 6.12 we show that in order to reproduce the AMS-02 positron fraction and all-lepton-flux data, the annihilation cross section must be the order of $\sim 10^{-23} cm^3/s$ for TeV DM mass candidates. Similar results are obtained in $\mu\bar{\mu}$ channel but with a slightly worse fit quality.

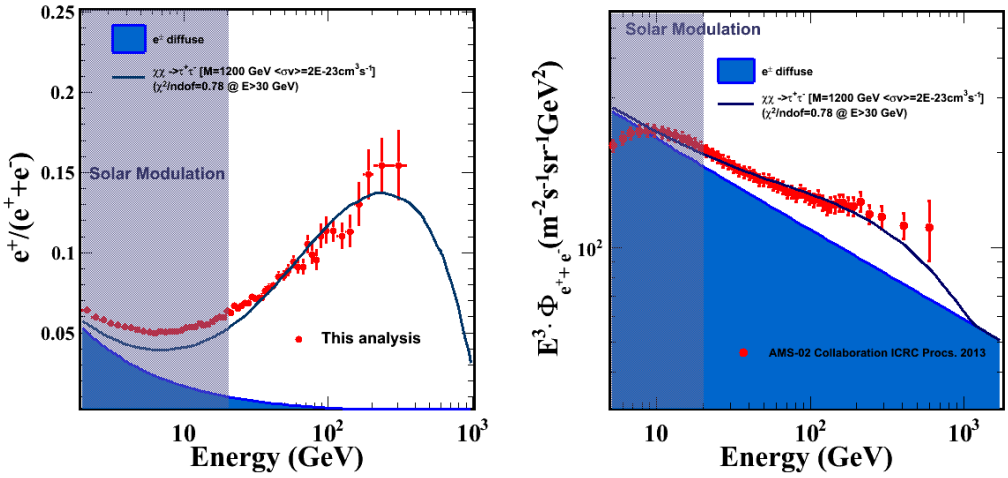

Figure 6.10: Sample fit to the AMS-02 data for a DM candidate in the $\tau\bar{\tau}$ channel with a mass of 1.2TeV and $\langle\sigma v\rangle \sim 2\times10^{-23}$. The background has been obtained from the minimal model described in the text.

A sample fit is shown in Figure 6.10, for a 1.2 TeV DM particle annihilating to $\tau\bar{\tau}$ with a cross section $\langle\sigma v\rangle = 2 \times 10^{-23} cm^3/s$.

6.4.3 Pulsar Source Scenario

In this section, a pulsar model is used to illustrate contribution from purely astrophysical sources.

We calculate the contribution from all gamma ray pulsars listed in the ATNF pulsar catalog to the positron flux as described in chapter 2.

A global χ^2 is performed using AMS-02 positron fraction data and all-lepton-flux data for energies above 30 GeV where solar modulation can be regarded as negligible, scanning the contribution from the individual sources codified in the conversion efficiency $\eta_{e^\pm}$ of the total spin-down power into $e^\pm$. The pulsars that contribute most to the positron flux are Geminga and Monogem, due to their distance and age. For them, best fits are attained with $\eta_{e^\pm} \sim 16\%$ and $\eta_{e^\pm} \sim 4\%$ respectively with a neglible contribution from other pulsars.

In figure 6.12 we show the global fit reduced χ^2 as a function of the contribution of a few

representative pulsars in terms of their conversion efficiency. Some sample fits to data are shown with the contributions from Geminga and Monogem in figure 6.11. Grey band represents part of the sampling with a global $\chi^2/ndof < 2$.

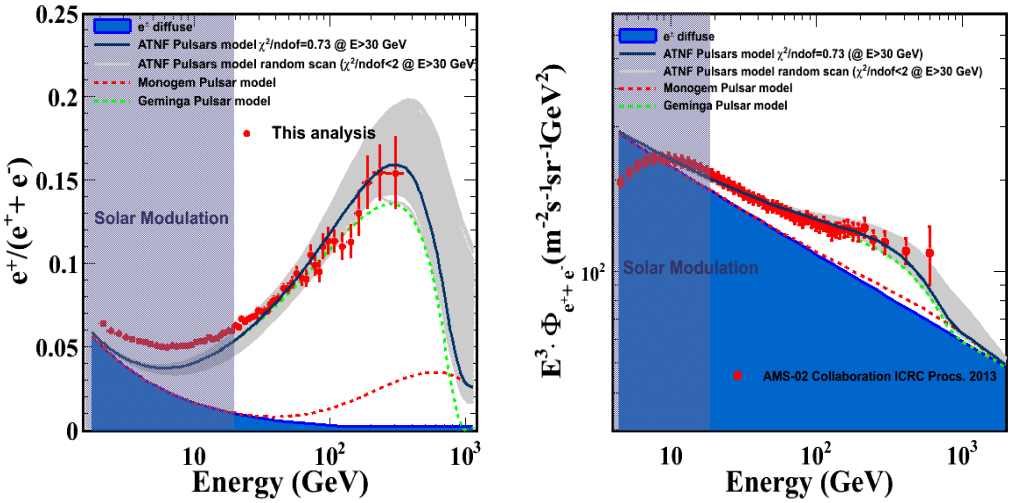

Figure 6.11: Sample fit to the AMS-02 data for a pulsar scenario. The background has been obtained from the minimal model described in the text.

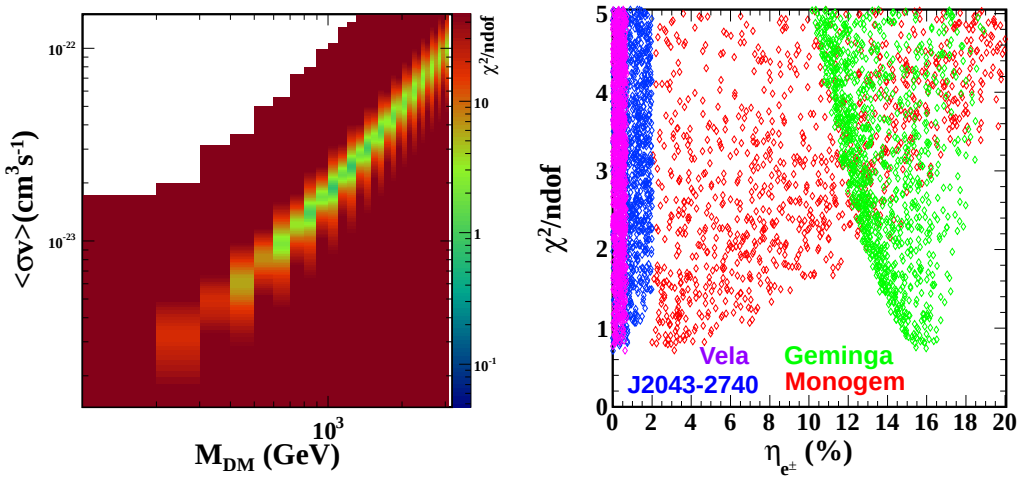

Figure 6.12: Right: $\chi^2/ndof$ of fit for different DM mass and annihilation cross section in the $\tau\bar{\tau}$ channel. Left:$\chi^2/ndof$ of fit for the conversion efficiency sampling for some of the most contributing pulsars.

6.4.4 Anisotropy Expectations

In the previous section we have determined the level of dipole anisotropy present in the positron ratio. In particular, above 16 GeV we estimate an upper limit of 0.03 at 95% C.L. . It is then reasonable to evaluate what level of anisotropy we do expect from the sources considered in section 6.4.

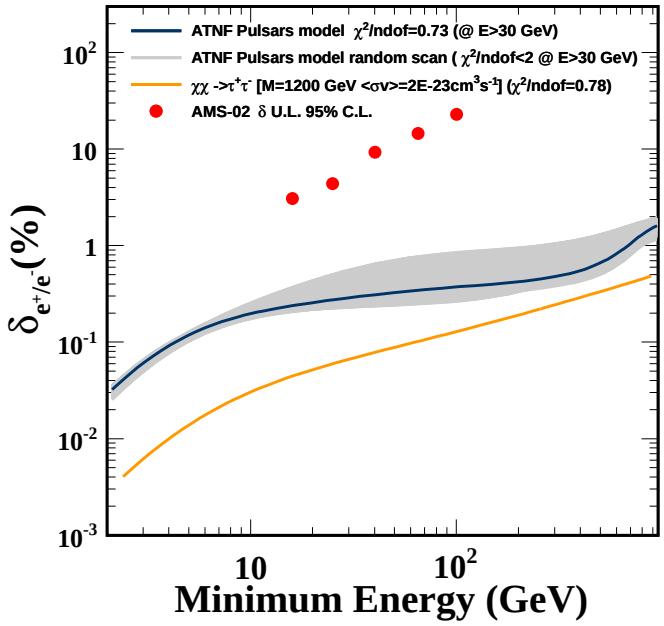

Figure 6.13: Anisotropy produced in the models considered in the text, compared to current AMS-02 U.L. at 95% C.L.

We have presented in chapter 2 estimates of the dipole anisotropy for the individual fluxes. To estimate the degree of anisotropy in the ratio e^+/e^-, we can describe the electron number density $N_\pm$ by an isotropic component $N^d_\pm$ and a source component that is not isotropic $N^s_\pm$:

$$N_\pm = N^d_\pm + N^s_\pm = N^d_\pm \cdot (1 + \frac{N^s_\pm}{N^d_\pm}) \quad ; \quad N^s_\pm = N^0_\pm \cdot (1 + \delta \cdot cos(\theta)), \tag{6.3}$$

where δ is the degree of dipole anisotropy of the source. Under the assumption that the source term is the same for e^+ and e^- then:

$$N_\pm = N^d_\pm + N^0 \cdot (1 + \delta \cdot cos(\theta)) = (N^d_\pm + N^0)(1 + \frac{N^0}{N^d_\pm + N^0}\delta \cdot cos(\theta)). \tag{6.4}$$

The degree of anisotropy in the positron and electron fluxes taking into account that we have an isotropic background are then scaled:

$$\delta_+ = \frac{N^0}{N^d_+ + N^0} \cdot \delta \quad ; \qquad \delta_- = \frac{N^0}{N^d_- + N^0} \cdot \delta = r \cdot \delta_+, \tag{6.5}$$

where $r = \frac{N^d_+ + N^0}{N^d_- + N^0}$ Then, if we assume $\delta_+ \ll 1$ the ratio

$$\frac{N_+}{N_-} = r \cdot \frac{1 + \delta_+ \cdot cos(\theta)}{1 + r \cdot \delta_+ \cdot cos(\theta)} = r \cdot (1 + (1 - r) \cdot \delta_+ cos(\theta)). \tag{6.6}$$

Therefore, the effective dipole anisotropy on the ratio of positrons to electrons:

$$\delta_{ratio} \simeq (1 - r) \cdot \delta_+. \tag{6.7}$$

Using this approximation, we can estimate the dipole anisotropy as in chapter 2 for the sources considered in section 6.4. In figure 6.13 we show the predicted dipole anisotropy for the models considered in this chapter, together with the upper limits derived in this analysis.

We find that the current upper limits are well above theoretical expectations, thus allowing for both production mechanisms.

In spite of this, AMS is a long term experiment that will be collecting data for more than 10 years. In this timescale, we expect to extend current sensitivity on the dipole anisotropy at the level of 1% that can be further improved with a data sample not constrained to the calorimeter acceptance.

6.4.5 Physics Interpretation within the Minimal Model

The minimal model presents a framework where diffuse and primary source $e^{\pm}$ fluxes are determined in a phenomenological way. This provides a powerful test for any physical explanation of the positron excess as the contribution to the total flux of any proposed primary source must be compatible with the minimal model estimations.

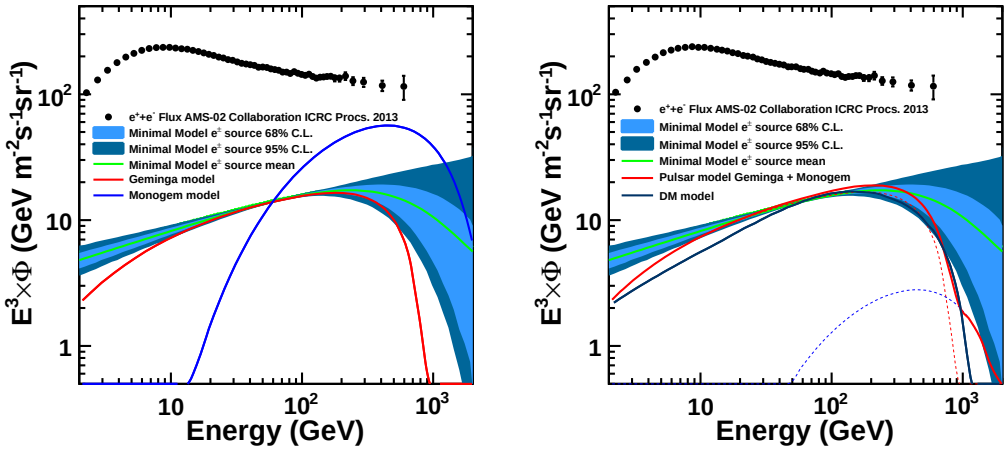

Figure 6.14: Left: Minimal model primary sources with some illustrative pulsar sources described in the text, normalized at 60 GeV. Right: Minimal model primary sources with some reference Physical sources described in the text.

In figure 6.14 we show the fluxes of the primary source contribution from the Minimal Model at one and two sigma C.L. and the reference physics models described in this chapter. The sole contribution of two of the most relevant pulsars, normalized at 60 GeV (Fig. 6.14) is compared with the Minimal Model prediction for the source. From this figure it is remarkable that among already known pulsars, Geminga may provide the Minimal Model primary source in the energy range of the AMS measurement. This is not the case for instance for the Monogem pulsar standalone. In spite of this, a contribution from Monogem to the overall flux can not be ruled out, as its contribution is more relevant at the highest energies where the Minimal Model uncertainties are large.

The primary sources of positrons from physics models investigated in this chapter are compared with the Minimal Model in figure 6.14 (right). In this figure the pair conversion efficiencies of Monogem (4%) and Geminga (16%) in the pulsar scenario, and the annihilation cross section in the Dark Matter scenario, have been tuned to fit the data. We find good agreement for the pulsar and Dark Matter models in the energy range of the AMS measurement where the minimal model uncertainty is small. Nevertheless small differences are apparent in regions where the Minimal Model presents large uncertainties. At low energies, a systematic undershoot in the physics models is observed, that could be an indication of a incomplete description of the diffusion setup, solar modulation effects, or could point out the presence of additional sources such as distant sources contributing to the low energy range. At very high energies near the source cutoff energy, the Dark Matter and pulsar models underestimate the source contribution to the total flux, which could reflect the presence of unaccounted young pulsars in a pulsar scenario, or a larger DM mass in a Dark Matter scenario.

Conclusions and Outlook

The positron channel provides a privileged window to search for new phenomena. This is possible because in the standard picture of cosmic rays, there are no primary sources of cosmic ray antimatter and the observed abundances of positrons are attributed to a secondary origin. In the study of the positron channel, it is convenient to introduce the positron fraction, which is the ratio of the positron to electron plus positron fluxes. The positron fraction determination has the advantage that under the assumption of equal acceptance for positrons and electrons, the computation of the ratio of the fluxes is simplified to the calculation of the ratio of the observed number of events. Moreover, many of the systematic effects cancel out hence providing a robust measurement.

This work has been focused on the measurement of the positron fraction in the 2-350 GeV energy range along with a study of the physical implications of the so-called positron excess. Two complementary approaches have been used for these purposes: On the one hand, the measurement of the positron fraction is performed for a comprehensive number of analyses, using the data collected by the AMS-02 detector at the ISS. On the other hand, a phenomenological study of the positron excess is presented, including some reference physics models.

Experiments prior to AMS have already pointed out the observation of a raise with the energy of the positron fraction that can not be explained in a conventional picture of cosmic ray production and propagation. AMS-02 is thus a long awaited program that is already providing with unprecedented statistics, the most accurate measurement to date of the positron abundance in cosmic rays.

The basis of the determination of the positron fraction is to count positrons and electrons. The negative rigidity sample, is a nearly background free sample of electrons, and the positive rigidity sample yields the positron component with a small contamination of protons (which amounts for the 88% of the cosmic ray abundance), and electrons reconstructed with a positive rigidity. The former one is handled with three subdetectors, the ECAL, the Tracker, and the TRD. The latter is constrained demanding a good track reconstruction in the Tracker.

The ECAL and TRD are designed to reject protons from $e^{\pm}$ independently. In conjunction with the Tracker, they provide a rejection power of $\mathcal{O}(10^7)$, which ensures a nearly background free

sample of positrons at intermediate energies and proton contamination at the highest energies at the percent level with a very high signal efficiency. The individual separation power of the subdetectors and their mutual independece, allows to maximize the statistical error even in conditions of low purity, carrying out a template-based analysis. In this way, the analysis is optimized as the statistical error dominates the overall error.

Two calorimeter selections are used to suppress the hadronic background, a boosted decision tree, and a shower shape cut-based selection which in conjunction with the Tracker, provide a rejection power $\mathcal{O}(10^3 - 10^4)$. The TRD selection is performed using a likelihood estimator which provides a rejection power $\mathcal{O}(10^3)$ up to 300 GeV. The performances of these classifiers are studied with flight data, using control data samples. The control data samples can be obtained from flight data electrons and protons using the redundancy for e-p separation of the ECAL and TRD. In turn, these control data samples can be used as reference distributions in a template-fitting analysis of the positron fraction.

The determination of the positron fraction is performed with four different analysis. We use the two ECAL classifiers described in chapter 4 and two procedures to evaluate the positron fraction: an event-counting method and a template-fitting method.

The purity of the sample in the event counting analysis is estimated from flight data, which we evaluate to be above 90% at the highest energies, taking advantage of AMS-02 redundancy for hadron rejection. The charge confusion is calculated from a Monte Carlo simulation, which has been validated with Test Beam data. In addition, the analyses have been performed on individual Tracker patterns, each one with very different level of charge confusion, thus allowing for the identification of pathological configurations. We find good agreement between the four analysis, which are consistent with a steady rise of the positron fraction starting from about 10 GeV up to 300 GeV.

Several effects have been considered in the estimation of systematic errors. Uncertainty on the input spectra for the template building, uncertainty on the charge confusion estimation, the selection and fit procedure, bin to bin migrations, asymmetry in the detector acceptance and geomagnetic cutoff. Among them, the uncertainty on the charge confusion and in the selection procedure have been found to be the dominant sources of systematic uncertainty at high energies. At low energies, asymmetry in the detector acceptance is the major source of systematic error.

The systematic error dominates at the very low energies, up to 10GeV. At higher energies the statistical error dominates the overall error. The analysis which provides the most accurate measurement is the template-fitting analysis using the BDT selection with the ECAL.

The positron fraction shows a steady raise with the energy from 2GeV up to 300 GeV. We take a deeper insight into the positron fraction and the implications of the rise with the energy. A search for temporal variations and spectral structures has been carried out, showing no evidences of spectral nor temporal structures at any temporal or energy scale.

In addition, a study of the positron incoming directions and searches for anisotropies has been performed. From this study, upper limits on the e^+/e^- dipole anisotropy are obtained ($\delta < 0.03$

95% C.L. for energies above 16 GeV).

All these features together show the existence of new physical phenomena. Some physics models have been used to investigate it.

We find that the positron fraction is consistent with a very simple model of a diffuse $e^{\pm}$ spectrum plus an additional *primary* component which produces electrons and positrons in equal numbers. This simple model provides a phenomenological description of the $e^{\pm}$ spectrum which can be used to obtain a data-driven estimation of the diffuse background and sets a fairly stringent benchmark for any appointed primary source to explain the positron excess. To validate the hypothesis of $e^{\pm}$ primary sources some realistic models are used. In particular, a Dark Matter and an astrophysical interpretation have been considered.

We illustrate the complexity to disentangle both scenarios by just looking at the spectra. In addition to multi-wavelength and multi-channel studies, we show the necessity of high precision measurements with a larger kinematical range.

Likewise, the use of anisotropies in the cosmic ray $e^{\pm}$ spectra is proposed as a new tool to pinpoint the sources of the positron excess. A new calculation of the predicted anisotropy is described for the pulsar and Dark matter sources.

For the pulsar scenario we consider all the gamma-ray pulsars collected in the ATNF catalog. We find that contribution to the local $e^{\pm}$ flux is dominated by nearby young pulsars, Geminga and Monogem, which should have spin-down conversion efficiencies at the 10% level in order to contribute substantially to the reported excess.

Interestingly enough, both pulsars lie roughly in the same direction, which is opposite to the galactic center, providing a *stacking* effect in the expected anisotropy. This has been estimated to be at the few *per-mil* level in the $e^+ + e^-$ spectra and at the *per-cent* level in the e^+ spectra.

For the Dark Matter scenario, we consider a model-independent Dark Matter candidate annihilating in leptonic channels as a result of the tight constraints already present in $\bar{p}$. Best fits to the data are obtained for Dark Matter mass in the TeV range with annihilating cross sections $\langle \sigma v \rangle \sim 10^{-23} cm^3/s$ which are 2-3 order magnitude larger than what it is expected from a thermal relic. There are a number of mechanisms that may provide these large enhancements, however, although not ruled out yet, a Dark Matter signature in these channels is being tightly constrained by γ ray measurements.

The degree of dipole anisotropy produced by a Dark Matter source is estimated, which is almost one order magnitude inferior to the pulsar scenario. Thus, the measurement of an anisotropy could be an indication that an astrophysical object may be the responsible of the e^+ anomalies. Many channels can be used to search for anisotropies i.e. $e^+ + e^-, e^-, e^+, e^+/e^-$. From them, the most sensibles are positrons as a result of lower isotropic backgrounds. We evaluate the potential imprint in the incoming directions from these scenarios in the e^+/e^- which we find compatible with the current limits on δ.

Regarding these physics models, the pulsar and Dark Matter scenarios are found to be compati-

ble with the Minimal Model description of the source. In particular in the energy range of interest, the Geminga pulsar shows a remarkable good agreement with the Minimal Model prediction. Small differences appear at low and high energies where the minimal model uncertainties are large. At low energies, these differences can be explained by an incomplete description of the diffusion setup, solar modulation effects or by the presence of additional sources such as distant pulsars. At high energies the discrepancies can be explained if we take into consideration contributions from additional pulsars such as Monogem or a non negligible contribution from younger pulsars feeding the high energy region.

AMS-02 measurement of the positron fraction constitutes a new paradigm for precision measurements in space. While dark matter interpretations of a positron fraction raise with the energy becomes more and more tightly constrained, an astrophysical explanation turns to be pretty likely. Potential signatures are at hand however. AMS will extend the positron fraction measurement approaching the TeV energy range. Weather a drop in the positron fraction will be observed or not will constitute a very powerful test favoring a Dark Matter interpretation.

In order to move to higher energies, it is necessary to collect more data. The main concerns to extend the energy range are the control of the proton and electron backgrounds. On the one hand, the change of the TRD operation regime can be partially overcome by fully exploiting the calorimeter performances, however, at the highest energies where statistics are limiting, the analysis will rely on Monte Carlo simulation, both for the classifiers training as construction of the reference template for a template-fitting analysis. On the other hand, while charge confusion due to secondary tracks can be constrained, charge confusion due to spillover is intrinsic to the Tracker resolution and the only way to deal with it will be to restrict the acceptance using Tracker patterns with a high MDR, however, this will further reduce the available statistics.

Additional information may be provided by studying the positrons arrival directions. AMS will be collecting data for the ISS lifetime, time enough to enhance the sensitivity towards the percent level, thus being in the regime to discriminate between the models.

Acknowledgments

If I have seen further it is only by standing on the shoulders of giants.

– Sir Isaac Newton

This work is framed within the AMS experiment, and some of the results obtained have been rendered for the collaboration's profit and conversely the author has benefited from the work of the members of the collaboration. A great deal of work has been put into the AMS-02 detector's construction, operation and software development. Therefore, I would like to express my gratitude to all members of the collaboration who took part on it, since this work is also a result of their efforts.

A lo largo de estos años he adquirido muchas deudas que no podré devolver. Es mi intención dar reconocimiento, aun sabiendo que no será de forma exhaustiva, a toda la gente que de una manera u otra ha contribuido a que esta tesis fuera posible.

Me gustaría expresar mi gratitud a mi director de tesis, del que tanto he aprendido, por su continuo consejo y apoyo. Su dedicación ha hecho posible este trabajo. Gracias Jorge, siempre es un placer trabajar y discutir contigo.

Quiero agradecir a Marcos Cerrada y a todos los miembros del departamento de Investigación Básica del CIEMAT por el buen trato recibido a lo largo de estos años.

Me gustaría también agradecer su buena disposición y confianza a Manuel Aguilar, quien no solo me permitió iniciar mi etapa predoctoral en el CIEMAT, pero también sentó las bases de mi futuro investigador.

Este trabajo ha sido también posible gracias al magnífico grupo de AMS en el CIEMAT. En particular me gustaría agradecer a Javier Berdugo y a Carlos Mañá su paciencia y apoyo prestado en el análisis y escritura de este documento. Gracias Javier por aportar sentido común al grupo y ocuparte de los asuntos burocráticos que no siempre son valorados como se debiera. Gracias Carlos,

por la confianza e independencia dadas en los comienzos de esta tesis, las cuales me permitieron crecer. Muchas gracias también a Carlos Delgado, que siempre ha estado dispuesto a echar una mano cuando ha sido necesario, a Carlos Díaz, Carmen Palomares, Jesús Marín, Francesca y Alberto. Un especial reconocimiento a mis compañeros, Cristina y David, con quienes he pasado los buenos y malos momentos y que me han ayudado siempre que lo he necesitado. También gracias a nuestros *pichones*, Bruno, Isabel, Miguel Angel y nuestra adoptada Rosa. I would also like to thank the magnificent Pisa group for their hospitality.

Gracias a Antonio, Carlos y tantos otros, con los que indagamos tantas formas de hacernos ricos, quizá sin darnos cuenta de lo mucho que nos estabamos enriqueciendo. Si alguna vez me hago rico, sin duda estaréis en los agradecimientos.

Muchas gracias a Javier Calonge, Juanjo y Antonio por el trato cordial y por no permitir que los problemas técnicos fueran un obstáculo.

Aun sin estar involucrados en mi trabajo directamente, me gustaría recordar a quienes han compartido conmigo muchos de estos dias: María Aldaya, Jorge, Julia, Miguel, Aurelio, María Cepeda, Jose, María de Prado, Antonio, Carlos, Carmen, Dani, Alberto, Mariano, Bárbara, Manu, Edu, Rafa, Adrián, Juanjo, Javier Sánchez y Javier Santaolalla.

También me gustaría agradecer a Nacho Sevilla, Eusebio e Ignacio Redondo por algunas conversaciones interesantes, y a Jesús Puerta y Mara por ser unos magníficos compañeros de pasillo y tener tan buen gusto con el café.

No hubiera llegado hasta aqui sin amigos como Shu, Cristina y Diego, y todo Nam-Ban, quienes siempre confiaron en que llegaría a buen puerto.

Esta tesis está dedicada a mis padres, Manuel y Reina y a Jaime, Miriam y Silvia.

Para concluir, esta tesis también está dedicada a Junko y a Nico, a quienes es imposible agradecer todo lo que me aportan.

Appendices

A

The Shower Shape Selection

The shower shape selection represents a physical approach to the ECAL selection for e/p separation. A description of the cuts and its parametrization with the energy is presented.

1. Mip-Finder
2. Shower Maximum
3. Longitudinal Leakage
4. Average Hit Energy
5. Moliere Radius
6. Shower Longitudinal Dispersion
7. Shower FootPrint
8. Energy Deposited in the First Two Layers
9. Energy Fraction $\mathrm{E_{CoG\pm 2cell}/E_{tot}}$

The cuts are applied sequentially, thus, the efficiencies quoted correspond to the efficiency of the cut following the sequence. The parametrization on the energy has been tuned to produce an overall efficiency $\simeq 90\%$ and to produce the maximum rejection to protons. An example of the efficiency tunning can be seen in figure A.1.

A.1 Mip-Finder

Cosmic ray protons may be classified in terms of their interaction in the Ecal into 3 general types:

1. Protons that promptly produce an electromagnetic shower through the decay of a π^0.
2. Protons that develops an hadronic shower
3. Protons that do not interact with the ECAL (mips)

This last category includes protons with a energy deposit compatible with the ionization loss rate described by the Bethe-Bloch equation at some of the Ecal planes.

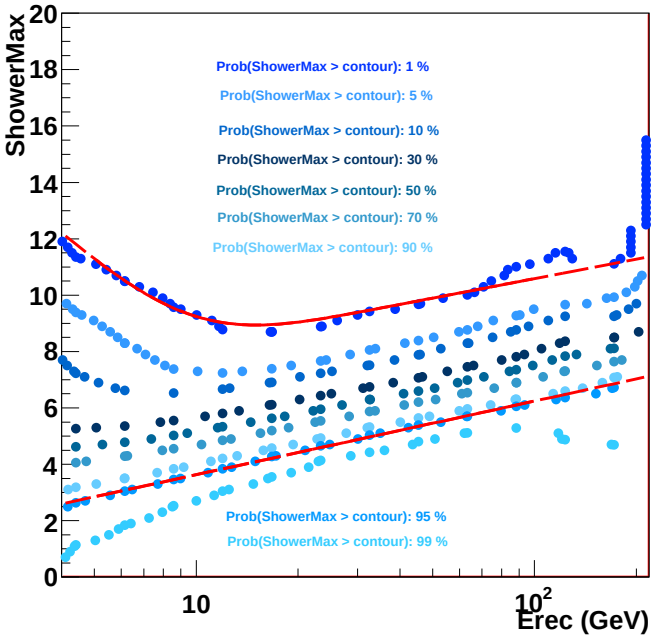

`Figure A.1:` Optimization sample for the Shower Max cut.

Minimum ionizing particles constitute a large fraction of the cosmic-ray protons which are the main background for the positron signal, and thus it is essential to remove them effectively. The typical mip energy scale is $E_{hit} \sim 10$MeV, and they are characterized by a very low hits multiplicity and thus low lateral energy dispersion. With these distinctive properties, a *Mip-Finder* selection rule has been devised in order to efficiently remove mips from the sample.
The criterion adopted is:

- $\mathrm{E_{layer}} < 20\mathrm{MeV}$ if $\mathrm{z_{layer}} < \mathrm{z_{ShowerMaximum}}$

- $\langle \#\mathrm{Hit} \rangle / \mathrm{plane} < 3$ & $\mathrm{E_{\pm 3cm}/E} < 0.999$

With this cut, not only pure mips are removed but also protons not interacting in the first layers that develop a late shower, releasing sizable energy in the calorimeter. For instance, in fig A.2 a 63 GeV proton releases energy at the mip scale (red dashed) in the first layers, and starts a late shower (with a shower maximum mapped from the black dashed slices).

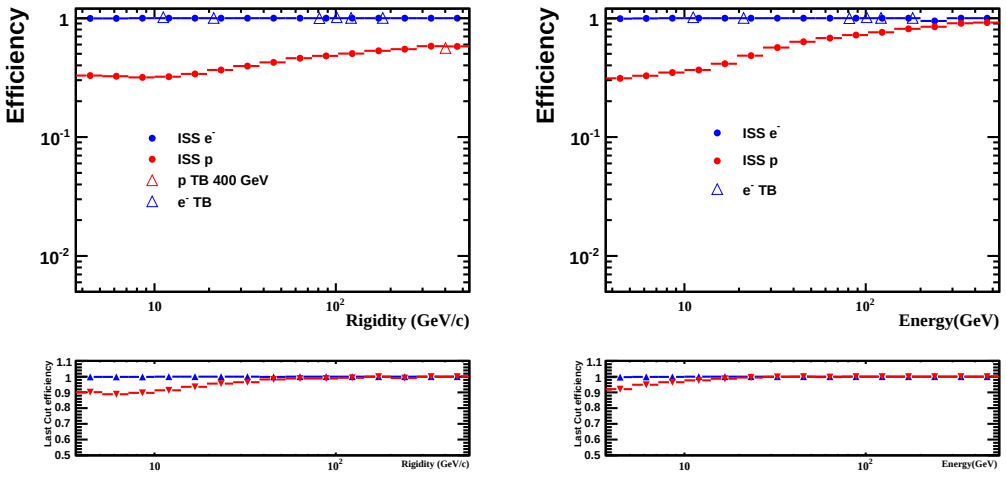

Figure A.3: Mip cut efficiency in Rigidity for flight data and TB (Left) and the cut parametrization with the energy for a pure sample of flight e^- (Right)

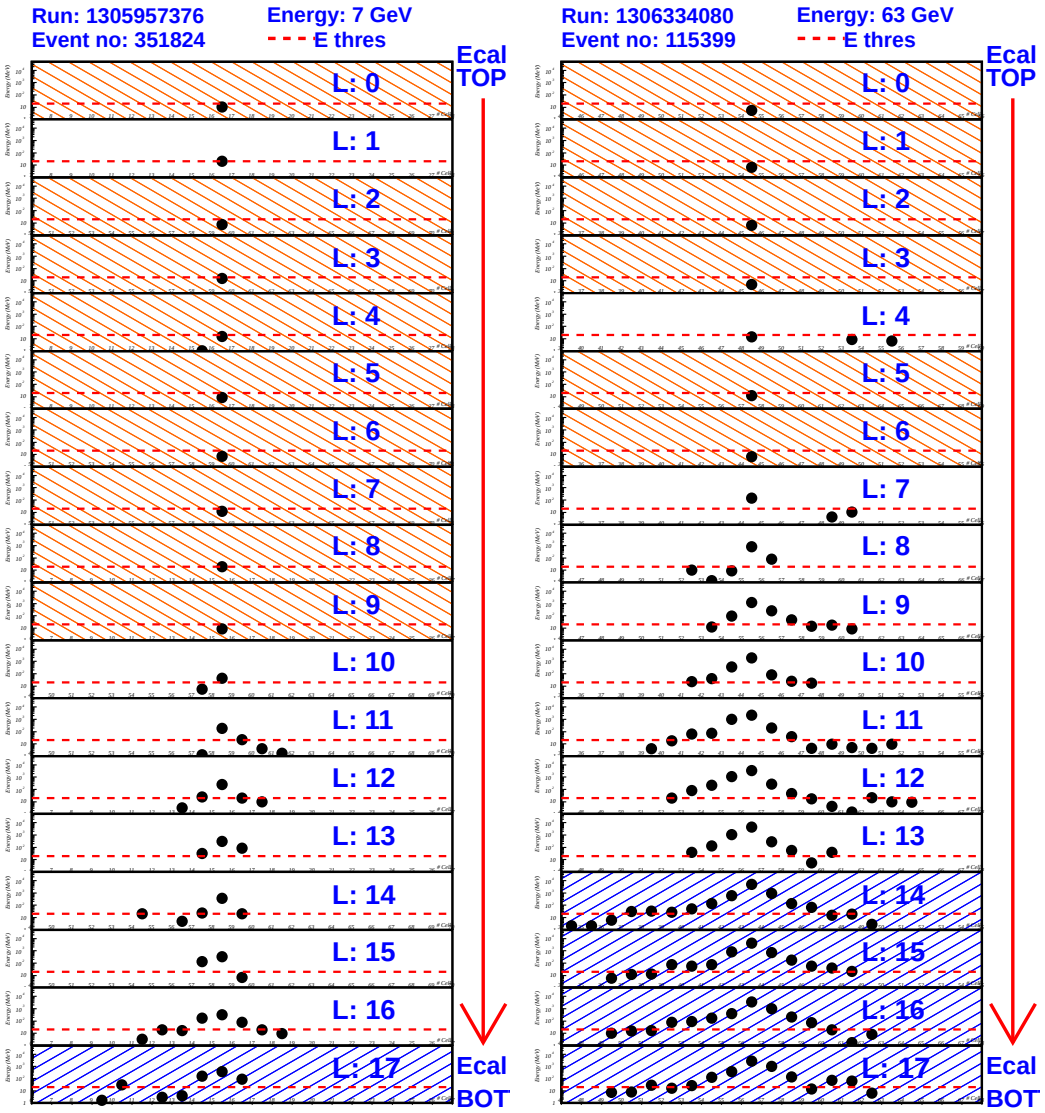

Figure A.2: Hits energy in each cell (black dots) with the layer energy threshold (red dashed line) of the Mip-Finder for each ECAL layer. Layers with energy below the threshold (MIP-like) are filled with red lines. Layers beyond the maximum of the shower are filled with blue lines. Left: Energy deposit of a 7GeV ISS proton tagged by the Mip-Finder, along the 18 planes of the ECAL. Right: Energy deposit of a 63GeV ISS proton tagged by the Mip-Finder, along the 18 planes of the ECAL.

A.2 Shower Maximum

As we have seen in the previous section, the depth of the maximum of the shower in the ECAL has a logarithmic dependence on the energy (Eqn. 4.2) for electromagnetic showers, with a characteristic longitudinal length of $X_0 \sim 1\mathrm{cm}$. On the contrary, protons longitudinal development in the ECAL is quite different, being characterized by the nuclear interaction length $\lambda > 20\mathrm{cm}$. These differences can be exploited to separate hadrons from $e^{\pm}$. In particular, the z position of the Shower Maximum is a powerful estimator that can be used for this purpose.
The following parametrization has been used:

$$\mathrm{Show.Maximum} \quad > \quad \log\left(\frac{|\mathrm{E}|}{184.6}\right) + 7.5(1 - 0.67\,|\mathrm{E}|^{-0.71}) \tag{A.1}$$

$$\mathrm{Show.Maximum} \quad < \quad \log\left(\frac{|\mathrm{E}|}{177.5}\right) + 12.0, \tag{A.2}$$

where the location of the shower maximum is obtained through a fit of the longitudinal profile to a gamma function (en.4.2).

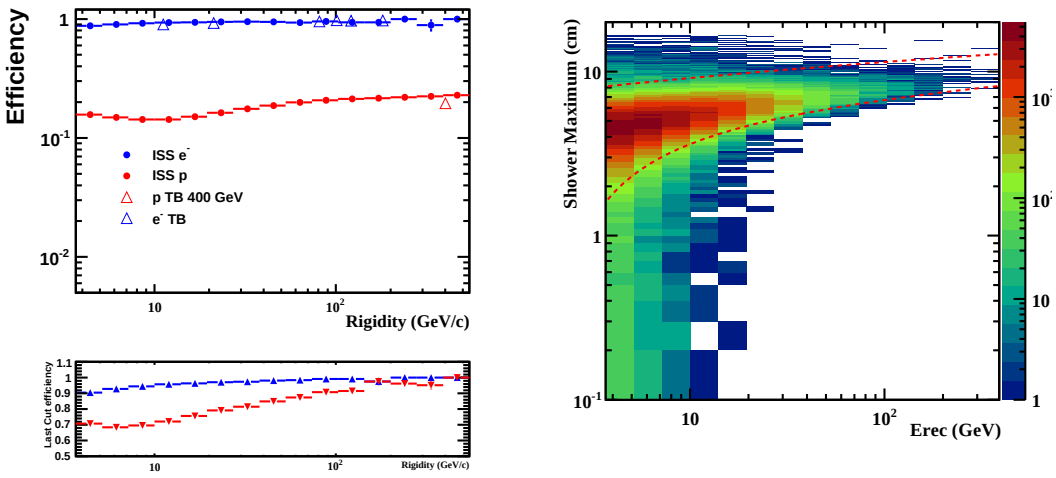

Figure A.4: Shower Maximum cut efficiency in Rigidity for flight data and TB (Left) and the cut parametrization with the energy for a pure sample of flight e^- (Right)

A.3 Longitudinal Leakage

Electromagnetic Showers are not fully contained in the calorimeter, and the longitudinal leakage must be estimated. One way to perform this estimation is by means of the dependence of the missing energy with the fraction of the energy deposited in the last ECAL layer. This can be expressed as:

$$E_{true} - E_{dep} = \alpha \frac{E_{last}}{E_{dep}}, \tag{A.3}$$

where E_{true} is the energy of the incident particle, E_{dep} is the deposited energy in the ECAL, and E_{last} is the energy deposited in the last layer.

Electrons and protons longitudinal energy deposition differ substantially as explained earlier in this chapter. For this reason, the rear leak can be used to further separate the $e^{\pm}$ signal from the proton background. The cut applied is:

$$\text{Rearleak} < 9.76 \times 10^{-2} + 6.26 \times 10^{-4} \cdot \text{E} \tag{A.4}$$

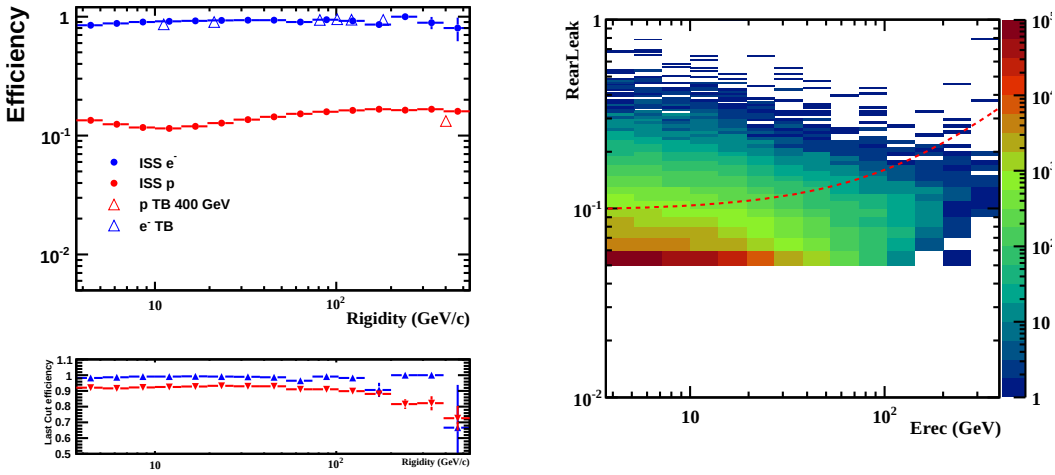

Figure A.5: RearLeak cut efficiency in Rigidity for flight data and TB (Left) and the cut parametrization with the energy for a pure sample of flight e^{-} (Right)

A.4 Average Hit Energy

The partition of the deposited energy among the shower hits has a linear dependence with the energy [98]. A logarithmic dependence has been included in order to maintain a global cut efficiency above 90% at low energies.

$$\frac{\langle \mathrm{E} \rangle}{\#\mathrm{hit}} > 1.17 \times 10^{-3} + 2.76 \times 10^{-2} \cdot Log10(E) + 2.10 \times 10^{-3} \cdot \mathrm{E} \tag{A.5}$$

$$\frac{\langle \mathrm{E} \rangle}{\#\mathrm{hit}} < 2.60 \times 10^{-2} + 2.54 \times 10^{-2} \cdot Log10(E) + 6.56 \times 10^{-3} \cdot \mathrm{E} \tag{A.6}$$

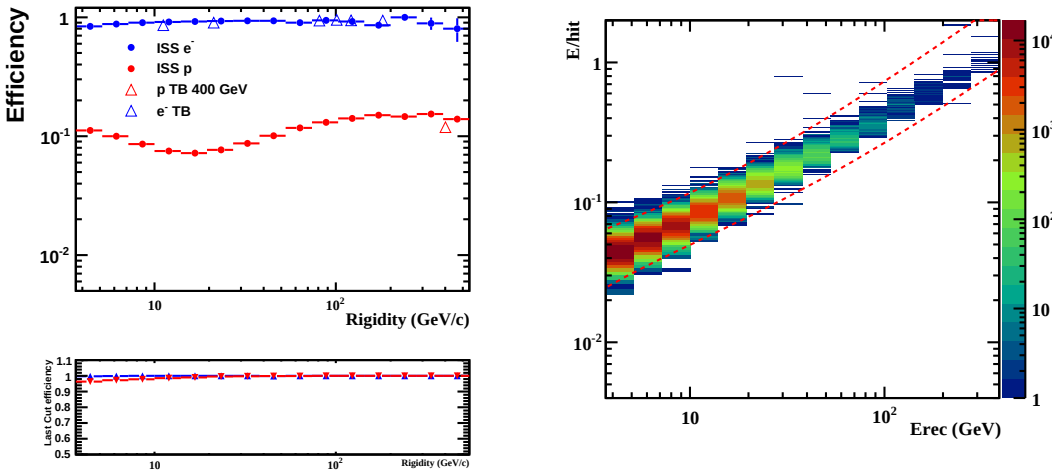

Figure A.6: Average hit energy cut efficiency in Rigidity for flight data and TB (Left) and the cut parametrization with the energy for a pure sample of flight e^- (Right)

A.5 Moliere Radius

The Moliere radius is the characteristic lateral size of an electromagnetic shower, and can be used to separate electrons from hadrons. In AMS ECAL, the Moliere radius is $R_M = 1.8\mathrm{cm}$ corresponding approximately to 2 cells. In average, a 90% of the shower is expected to be contained inside a cylinder of 1Moliere radius, but the same does not apply in general for hadronic showers. For this reason, this quantity can be used to separate both species.
The criterion adopted is:

$$\frac{\mathrm{E}_{\pm 3\mathrm{cm}}}{\mathrm{E}} > 0.96 - 0.6 \cdot \frac{Log10(E+0.74)}{E+0.74} \tag{A.7}$$

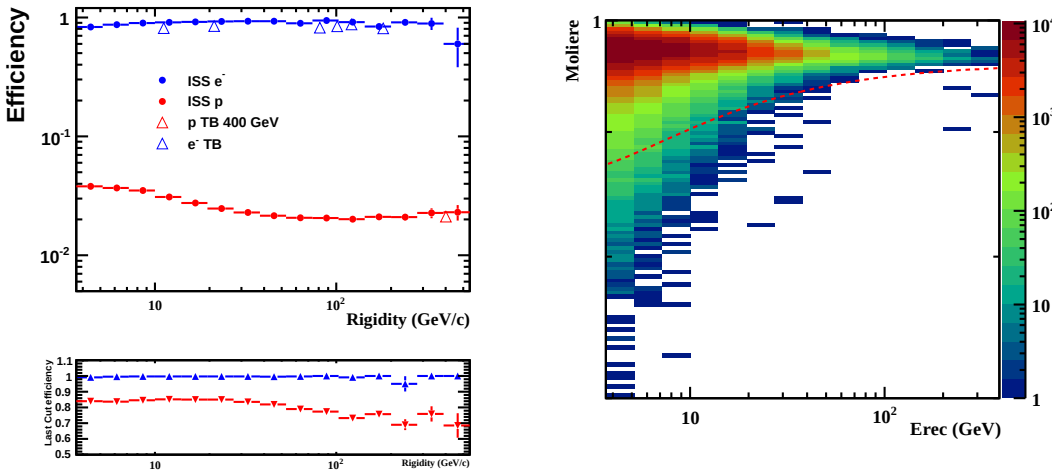

Figure A.7: Moliere cut efficiency in Rigidity for flight data and TB (Left) and the cut parametrization with the energy for a pure sample of flight e^- (Right)

A.6 Shower Longitudinal Dispersion

Defined as the Shower Center of Gravity(CofG) variance along Z:

$$\mathrm{ShowerLongitudinalDispersion} = \frac{\sum_{\mathrm{lay}=0}^{\mathrm{nlayers}} (\mathrm{Z_{lay}} - \mathrm{Z_{CofG}})^2 \cdot \mathrm{E_{lay}}}{\mathrm{E_{tot}}}. \tag{A.8}$$

This variable can be used to reduce the proton contamination. The cut applied, tested on MC is the following:

$$\mathrm{ShowerLongitudinalDispersion} > 9 \tag{A.9}$$

$$\mathrm{ShowerLongitudinalDispersion} < 17 \tag{A.10}$$

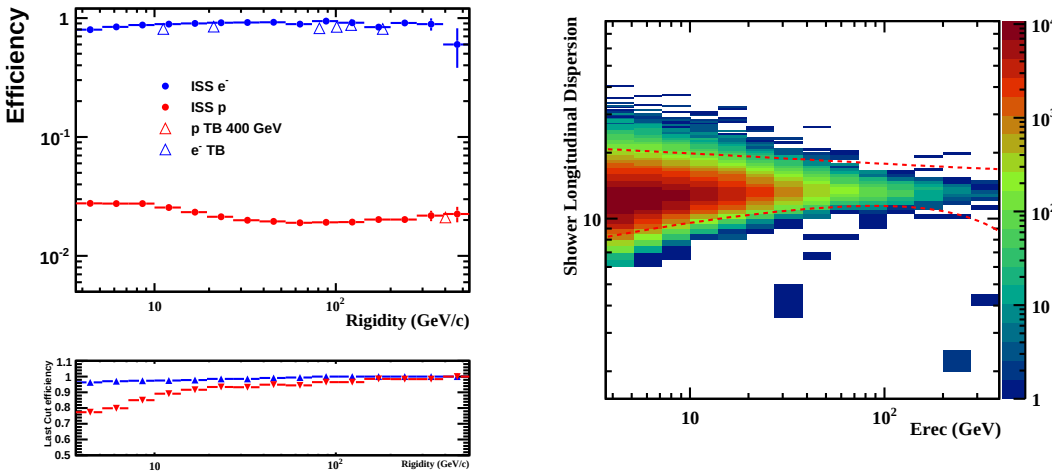

Figure A.8: Shower longitudinal dispersion cut efficiency in Rigidity for flight data and TB (Left) and the cut parametrization with the energy for a pure sample of flight e^- (Right)

A.7 Shower FootPrint

The Shower Footprint is a measure of the shower plane dispersion in two projections. It can be used to estimate the shower transverse component surface. It is defined as follows:

$$\mathrm{FootPrint} = \sum_{\mathrm{i}=1}^{2} \sqrt{\det(\mathrm{I_i})} \qquad ; \qquad \mathrm{I_i} = \begin{pmatrix} \sigma_i^2 & \sigma_{iz} \\ \sigma_{iz} & \sigma_z^2 \end{pmatrix}, \tag{A.11}$$

where the index i runs over the x and y directions and the variance is defined:

$$\sigma_x^2 = \sum_{l=0}^{nlayers} \sum_{c=0}^{ncell} W_{cl} \cdot (X_c - CofGx)^2 \tag{A.12}$$

$$\sigma_{xz} = \sum_{l=0}^{nlayers} \sum_{c=0}^{ncell} W_{cl} \cdot (X_c - CofGx) \cdot (Z_l - CofGz) \tag{A.13}$$

$$\sigma_z^2 = \sum_{l=0}^{nlayers} \sum_{c=0}^{ncell} W_{cl} \cdot (Z_l - CofGz)^2, \tag{A.14}$$

where W_{cl} is defined as

$$W_{cl} = \frac{E_{cl}}{\sum\limits_{lay=0}^{nlayers} \sum\limits_{cell=0}^{ncell} E[cell][lay]}, \tag{A.15}$$

where E_{cl} is the energy deposited in cell c and layer l.

The y projections: σ_y, σ_{yz} are obtained from σ_x, σ_{xz} exchanging $x \leftrightarrow y$.

The cut applied is parametrized with the energy:

$$\mathrm{ShowerFootPrint} > 4.6 + 1.59 \cdot Log10(E) - 0.0081 \cdot E \tag{A.16}$$

$$\mathrm{ShowerFootPrint} < 25.5 - 9.75 \cdot Log10(E) + 0.058 \cdot E \tag{A.17}$$

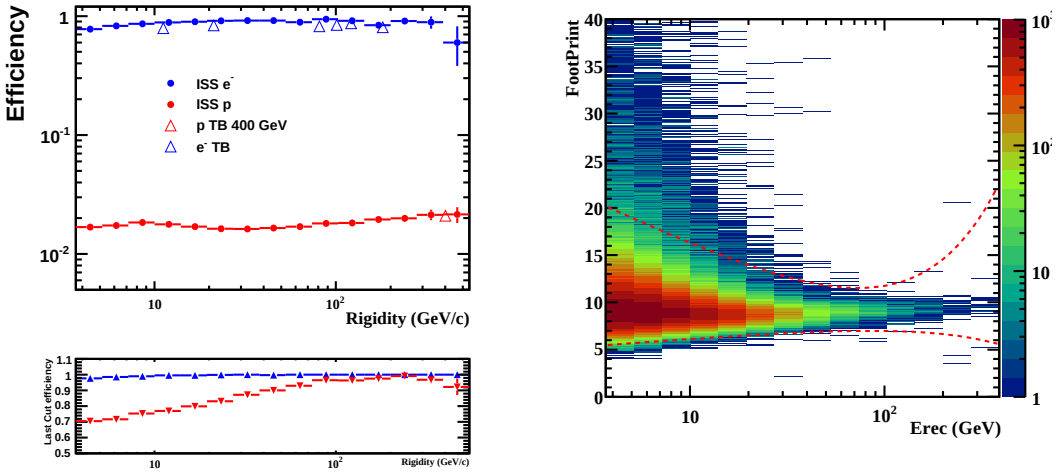

Figure A.9: Shower FootPrint cut efficiency in Rigidity for flight data and TB (Left) and the cut parametrization with the energy for a pure sample of flight e^- (Right)

A.8 Energy Deposited in First 2 Layers

Electrons have a very high probability to develop an electromagnetic shower in a few cm depth of the ECAL. Thus, a cut on the deposited energy in the first two layers has been found to be a good discriminating variable for e/p separation.

$$S5 \quad < \quad 0.90 \cdot Log10(E + 1.5) \tag{A.18}$$

$$S5 \quad > \quad 0.08 \cdot Log10(E + 1.5) \tag{A.19}$$

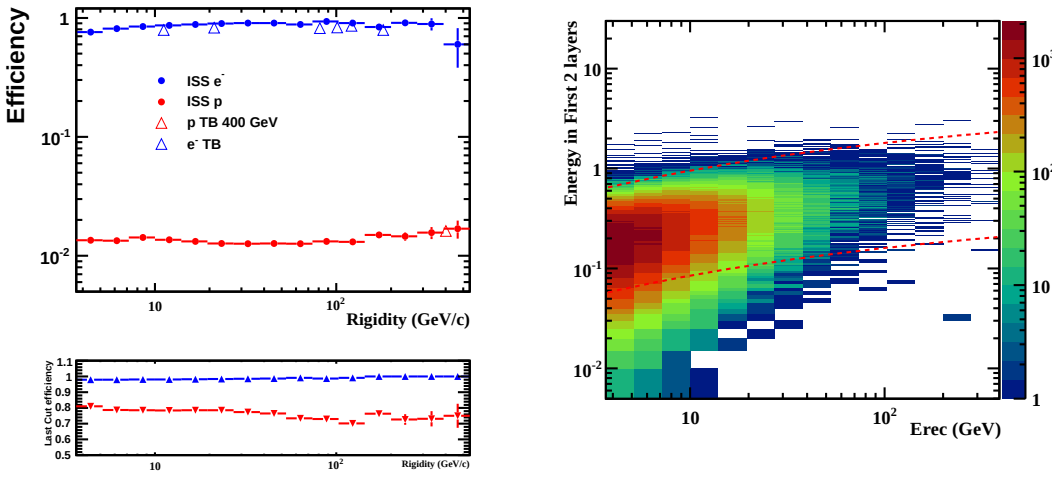

Figure A.10: Energy deposition in the first two layers cut efficiency in Rigidity for flight data and TB (Left) and the cut parametrization with the energy for a pure sample of flight e^- (Right)

A.9 Energy Fraction in 2 Cells around Shower Center of Gravity

The energy fraction in two adjacent cells around the shower center of gravity has proved to be also a powerful measurement to reject hadrons. It is defined as follows:

$$\mathrm{S5} = \frac{\sum_{\mathrm{l=0}}^{\mathrm{nlayers}} \sum_{\mathrm{c=CofGcell-2}}^{\mathrm{CofGcell+2}} \mathrm{E_{cl}}}{\mathrm{E_{tot}}}, \tag{A.20}$$

where E_{cl} is the energy deposition in (l, c) layer and cell.

The cut is parametrized as follows:

$$\mathrm{S5} \;>\; 0.94 + 0.6 \cdot Log10(E+20)/(E+20) \tag{A.21}$$

$$\mathrm{S5} \;<\; 0.96 - 0.6 \cdot Log10(E+20)/(E+20) \tag{A.22}$$

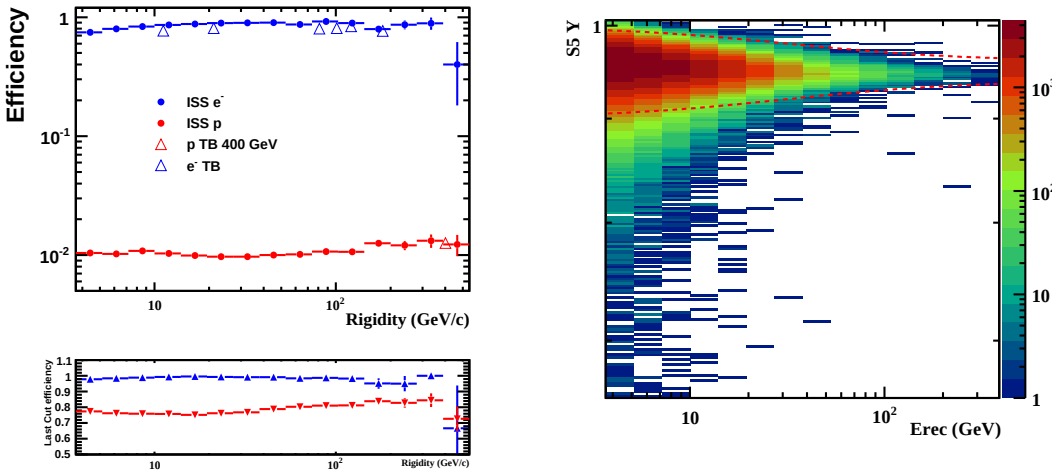

Figure A.11: Energy fraction in 2 cells cut efficiency in Rigidity for flight data and TB (Left) and the cut parametrization with the energy for a pure sample of flight e^- (Right)

B

Positron Fraction by Track Patterns

Table B.1 BDT Selection. Tracker Pattern: Inner Tracker within P1 Acceptance

Emin	Emax	Ne^+	Ne^-	$e^+/(e^+ + e^-)$	C.C.	Purity(%)	N$^{\mathrm{true}}$e$^+$	$e^+/(e^+ + e^-)Corr.$	σ^{stat}
2.00	2.41	576.00	8064.00	0.0667	0.0014	99.9750	565.25	0.0654	0.0027
2.41	3.04	914.00	14230.00	0.0604	0.0019	99.9850	888.57	0.0587	0.0019
3.04	3.75	957.00	15585.00	0.0579	0.0025	99.9850	920.80	0.0557	0.0018
3.75	4.55	941.00	15422.00	0.0575	0.0031	99.9850	895.80	0.0547	0.0018
4.55	5.43	892.00	14855.00	0.0566	0.0038	99.9850	838.35	0.0532	0.0018
5.43	6.42	805.00	13557.00	0.0561	0.0046	99.9850	745.78	0.0519	0.0019
6.42	7.50	675.00	11747.00	0.0543	0.0055	99.9850	613.75	0.0494	0.0020
7.50	8.69	583.00	9575.00	0.0574	0.0064	99.9850	524.48	0.0516	0.0023
8.69	10.00	481.00	7788.00	0.0582	0.0075	99.9950	425.54	0.0515	0.0026
10.00	12.01	526.00	8002.00	0.0617	0.0089	99.9950	458.57	0.0538	0.0026
12.01	14.26	376.00	5848.00	0.0604	0.0106	99.9850	316.67	0.0509	0.0031
14.26	16.78	309.00	4579.00	0.0632	0.0126	99.9850	253.85	0.0519	0.0035
16.78	19.59	267.00	3583.00	0.0694	0.0148	99.9850	216.48	0.0562	0.0042
19.59	22.71	233.00	2911.00	0.0741	0.0172	99.9850	185.30	0.0589	0.0048
22.71	26.18	173.00	2108.00	0.0758	0.0199	99.9850	132.97	0.0583	0.0057
26.18	31.00	168.00	1758.00	0.0872	0.0232	99.9750	129.32	0.0671	0.0066
31.00	38.36	138.00	1441.00	0.0874	0.0279	99.9650	99.45	0.0630	0.0074
38.36	47.03	96.00	880.00	0.0984	0.0340	99.9750	67.37	0.0690	0.0100
47.03	57.22	76.00	574.00	0.1169	0.0411	99.9750	53.67	0.0826	0.0133
57.22	69.18	54.00	332.00	0.1399	0.0492	99.9450	38.81	0.1006	0.0189
69.18	83.20	25.00	201.00	0.1106	0.0584	99.9250	13.35	0.0591	0.0229
83.20	100.00	28.00	133.00	0.1739	0.0689	99.8650	19.56	0.1215	0.0329
100.00	127.90	18.00	115.00	0.1353	0.0831	99.8750	8.30	0.0624	0.0342
127.90	162.60	15.00	81.00	0.1562	0.1008	99.7250	6.62	0.0690	0.0442
162.60	206.00	7.00	27.00	0.2059	0.1195	98.9950	3.78	0.1113	0.0846
206.00	260.00	4.00	16.00	0.2000	0.1407	96.5650	1.49	0.0748	0.1150
260.00	350.00	4.00	15.00	0.2105	0.1612	90.7550	0.93	0.0497	0.1245

Table B.2 BDT Selection. Tracker pattern: Inner Tracker + P9 within P1 Acceptance

Emin	Emax	Ne^+	Ne^-	$e^+/(e^+ + e^-)$	C.C.	Purity(%)	N$^{\rm true}$e$^+$	$e^+/(e^+ + e^-)Corr.$	σ^{stat}
2.00	2.41	1913.00	27862.00	0.0642	0.0019	99.9750	1863.00	0.0626	0.0014
2.41	3.04	3019.00	48806.00	0.0583	0.0019	99.9850	2931.36	0.0566	0.0010
3.04	3.75	3155.00	52345.00	0.0568	0.0019	99.9850	3061.08	0.0552	0.0010
3.75	4.55	2988.00	51800.00	0.0545	0.0019	99.9850	2895.01	0.0528	0.0010
4.55	5.43	2655.00	48696.00	0.0517	0.0019	99.9850	2567.46	0.0500	0.0010
5.43	6.42	2377.00	43945.00	0.0513	0.0019	99.9850	2298.05	0.0496	0.0010
6.42	7.50	1945.00	37469.00	0.0493	0.0019	99.9850	1877.55	0.0476	0.0011
7.50	8.69	1694.00	30865.00	0.0520	0.0019	99.9850	1638.53	0.0503	0.0012
8.69	10.00	1365.00	23973.00	0.0539	0.0019	99.9950	1322.02	0.0522	0.0014
10.00	12.01	1389.00	24539.00	0.0536	0.0019	99.9950	1344.72	0.0519	0.0014
12.01	14.26	1068.00	17348.00	0.0580	0.0019	99.9850	1036.39	0.0563	0.0017
14.26	16.78	795.00	12875.00	0.0582	0.0020	99.9850	771.12	0.0564	0.0020
16.78	19.59	666.00	10161.00	0.0615	0.0020	99.9850	646.73	0.0597	0.0023
19.59	22.71	569.00	7923.00	0.0670	0.0021	99.9850	553.53	0.0652	0.0027
22.71	26.18	417.00	5573.00	0.0696	0.0022	99.9850	405.63	0.0677	0.0033
26.18	31.00	339.00	4530.00	0.0696	0.0023	99.9750	329.07	0.0676	0.0037
31.00	38.36	295.00	3527.00	0.0772	0.0026	99.9650	286.39	0.0749	0.0043
38.36	47.03	193.00	2020.00	0.0872	0.0031	99.9750	187.28	0.0846	0.0060
47.03	57.22	107.00	1198.00	0.0820	0.0038	99.9750	102.80	0.0788	0.0076
57.22	69.18	86.00	687.00	0.1113	0.0048	99.9450	83.02	0.1074	0.0114
69.18	83.20	53.00	411.00	0.1142	0.0063	99.9250	50.66	0.1092	0.0149
83.20	100.00	36.00	297.00	0.1081	0.0085	99.8650	33.68	0.1012	0.0172
100.00	127.90	38.00	232.00	0.1407	0.0124	99.8750	35.49	0.1315	0.0214
127.90	162.60	13.00	126.00	0.0935	0.0192	99.7250	10.71	0.0771	0.0252
162.60	206.00	17.00	69.00	0.1977	0.0303	98.9950	15.15	0.1765	0.0442
206.00	260.00	11.00	42.00	0.2075	0.0482	96.5650	8.95	0.1700	0.0579
260.00	350.00	12.00	22.00	0.3529	0.0831	90.7550	9.78	0.2974	0.0880

Table B.3 BDT Selection. Tracker Pattern: Inner Tracker + P1

Emin	Emax	Ne^+	Ne^-	$e^+/(e^+ + e^-)$	C.C.	Purity(%)	N$^{\mathrm{true}}$e$^+$	$e^+/(e^+ + e^-)Corr.$	σ^{stat}
2.00	2.41	2060.00	30175.00	0.0639	0.0021	99.9750	1998.96	0.0620	0.0014
2.41	3.04	3227.00	52862.00	0.0575	0.0021	99.9850	3119.80	0.0556	0.0010
3.04	3.75	3315.00	56714.00	0.0552	0.0021	99.9850	3199.82	0.0533	0.0009
3.75	4.55	3187.00	55835.00	0.0540	0.0021	99.9850	3073.50	0.0521	0.0009
4.55	5.43	2953.00	52357.00	0.0534	0.0021	99.9850	2846.46	0.0515	0.0010
5.43	6.42	2630.00	47368.00	0.0526	0.0021	99.9850	2533.38	0.0507	0.0010
6.42	7.50	2243.00	40698.00	0.0522	0.0021	99.9850	2159.70	0.0503	0.0011
7.50	8.69	1815.00	32931.00	0.0522	0.0022	99.9850	1747.27	0.0503	0.0012
8.69	10.00	1421.00	26216.00	0.0514	0.0022	99.9950	1366.79	0.0495	0.0013
10.00	12.01	1628.00	26947.00	0.0570	0.0022	99.9950	1571.94	0.0550	0.0014
12.01	14.26	1142.00	19358.00	0.0557	0.0022	99.9850	1100.75	0.0537	0.0016
14.26	16.78	918.00	14655.00	0.0589	0.0023	99.9850	886.01	0.0569	0.0019
16.78	19.59	753.00	11849.00	0.0598	0.0024	99.9850	726.19	0.0576	0.0021
19.59	22.71	632.00	9184.00	0.0644	0.0025	99.9850	610.35	0.0622	0.0025
22.71	26.18	480.00	6567.00	0.0681	0.0027	99.9850	463.68	0.0658	0.0030
26.18	31.00	441.00	5472.00	0.0746	0.0029	99.9750	426.36	0.0721	0.0034
31.00	38.36	347.00	4473.00	0.0720	0.0032	99.9650	333.44	0.0692	0.0037
38.36	47.03	220.00	2718.00	0.0749	0.0038	99.9750	210.39	0.0716	0.0049
47.03	57.22	150.00	1563.00	0.0876	0.0046	99.9750	143.46	0.0837	0.0069
57.22	69.18	112.00	975.00	0.1030	0.0056	99.9450	107.07	0.0985	0.0093
69.18	83.20	72.00	579.00	0.1106	0.0069	99.9250	68.41	0.1051	0.0124
83.20	100.00	65.00	401.00	0.1395	0.0085	99.8650	62.00	0.1331	0.0162
100.00	127.90	63.00	310.00	0.1689	0.0110	99.8750	60.14	0.1613	0.0196
127.90	162.60	26.00	213.00	0.1088	0.0147	99.7250	23.09	0.0967	0.0204
162.60	206.00	16.00	95.00	0.1441	0.0203	98.9950	14.17	0.1278	0.0339
206.00	260.00	19.00	51.00	0.2714	0.0321	96.5650	17.23	0.2484	0.0542
260.00	350.00	17.00	43.00	0.2833	0.0749	90.7550	13.00	0.2225	0.0611

Table B.4 BDT Selection. Tracker Pattern: Inner Tracker + P1 + P9

Emin	Emax	Ne^+	Ne^-	$e^+/(e^+ + e^-)$	C.C.	Purity(%)	N$^{\rm true}$e$^+$	$e^+/(e^+ + e^-)Corr.$	σ^{stat}
2.00	2.41	7320.00	108288.00	0.0633	0.0008	99.9750	7241.82	0.0626	0.0007
2.41	3.04	11665.00	188169.00	0.0584	0.0008	99.9850	11523.52	0.0577	0.0005
3.04	3.75	11817.00	199877.00	0.0558	0.0008	99.9850	11658.69	0.0551	0.0005
3.75	4.55	11289.00	195980.00	0.0545	0.0009	99.9850	11125.19	0.0537	0.0005
4.55	5.43	10006.00	182983.00	0.0518	0.0009	99.9850	9844.17	0.0510	0.0005
5.43	6.42	8800.00	164577.00	0.0508	0.0010	99.9850	8646.04	0.0499	0.0005
6.42	7.50	7509.00	140017.00	0.0509	0.0010	99.9850	7370.55	0.0500	0.0006
7.50	8.69	6145.00	112890.00	0.0516	0.0011	99.9850	6027.10	0.0506	0.0006
8.69	10.00	4852.00	87901.00	0.0523	0.0012	99.9950	4755.48	0.0513	0.0007
10.00	12.01	5010.00	89483.00	0.0530	0.0012	99.9950	4905.20	0.0519	0.0007
12.01	14.26	3710.00	62871.00	0.0557	0.0013	99.9850	3630.76	0.0545	0.0009
14.26	16.78	2839.00	47117.00	0.0568	0.0014	99.9850	2775.43	0.0556	0.0010
16.78	19.59	2429.00	37444.00	0.0609	0.0015	99.9850	2375.34	0.0596	0.0012
19.59	22.71	1884.00	28307.00	0.0624	0.0016	99.9850	1841.04	0.0610	0.0014
22.71	26.18	1400.00	20003.00	0.0654	0.0017	99.9850	1368.09	0.0639	0.0017
26.18	31.00	1181.00	16043.00	0.0686	0.0018	99.9750	1154.02	0.0670	0.0019
31.00	38.36	1015.00	12598.00	0.0746	0.0019	99.9650	992.74	0.0729	0.0023
38.36	47.03	614.00	7274.00	0.0778	0.0020	99.9750	600.75	0.0762	0.0030
47.03	57.22	421.00	4073.00	0.0937	0.0020	99.9750	413.59	0.0920	0.0044
57.22	69.18	255.00	2539.00	0.0913	0.0020	99.9450	250.30	0.0896	0.0055
69.18	83.20	155.00	1509.00	0.0931	0.0020	99.9250	152.20	0.0915	0.0071
83.20	100.00	123.00	1020.00	0.1076	0.0020	99.8650	121.02	0.1059	0.0092
100.00	127.90	97.00	858.00	0.1016	0.0023	99.8750	95.09	0.0996	0.0098
127.90	162.60	60.00	430.00	0.1224	0.0036	99.7250	58.50	0.1194	0.0148
162.60	206.00	41.00	228.00	0.1524	0.0069	98.9950	39.27	0.1462	0.0219
206.00	260.00	24.00	144.00	0.1429	0.0142	96.5650	21.41	0.1281	0.0267
260.00	350.00	23.00	94.00	0.1966	0.0282	90.7550	18.68	0.1627	0.0357

Table B.5 BDT Selection. Tracker Pattern: Inner Tracker out of P1 Acceptance

Emin	Emax	Ne^+	Ne^-	$e^+/(e^+ + e^-)$	C.C.	Purity(%)	N$^{\rm true}$e$^+$	$e^+/(e^+ + e^-)Corr.$	σ^{stat}
2.00	2.41	1832.00	25936.00	0.0660	0.0019	99.9750	1785.09	0.0643	0.0015
2.41	3.04	3024.00	46933.00	0.0605	0.0021	99.9850	2932.91	0.0587	0.0011
3.04	3.75	3080.00	50872.00	0.0571	0.0022	99.9850	2972.95	0.0551	0.0010
3.75	4.55	2979.00	50613.00	0.0556	0.0024	99.9850	2862.93	0.0534	0.0010
4.55	5.43	2712.00	48074.00	0.0534	0.0026	99.9850	2591.12	0.0510	0.0010
5.43	6.42	2419.00	43561.00	0.0526	0.0029	99.9850	2298.45	0.0500	0.0010
6.42	7.50	2252.00	37913.00	0.0561	0.0032	99.9850	2136.53	0.0532	0.0012
7.50	8.69	1762.00	31287.00	0.0533	0.0036	99.9850	1656.00	0.0501	0.0012
8.69	10.00	1507.00	25010.00	0.0568	0.0040	99.9950	1413.08	0.0533	0.0014
10.00	12.01	1647.00	25686.00	0.0603	0.0045	99.9950	1537.21	0.0562	0.0014
12.01	14.26	1257.00	18663.00	0.0631	0.0053	99.9850	1163.99	0.0584	0.0017
14.26	16.78	1001.00	13845.00	0.0674	0.0062	99.9850	920.30	0.0620	0.0021
16.78	19.59	788.00	11036.00	0.0666	0.0073	99.9850	712.11	0.0602	0.0023
19.59	22.71	703.00	8735.00	0.0745	0.0086	99.9850	632.85	0.0671	0.0027
22.71	26.18	515.00	6423.00	0.0742	0.0101	99.9850	454.08	0.0654	0.0032
26.18	31.00	502.00	5391.00	0.0852	0.0121	99.9750	441.14	0.0749	0.0037
31.00	38.36	436.00	4486.00	0.0886	0.0152	99.9650	372.20	0.0756	0.0041
38.36	47.03	306.00	2627.00	0.1043	0.0196	99.9750	258.62	0.0882	0.0058
47.03	57.22	176.00	1539.00	0.1026	0.0251	99.9750	139.99	0.0816	0.0076
57.22	69.18	93.00	938.00	0.0902	0.0317	99.9450	64.36	0.0624	0.0093
69.18	83.20	75.00	606.00	0.1101	0.0394	99.9250	52.22	0.0767	0.0127
83.20	100.00	56.00	393.00	0.1247	0.0481	99.8650	37.98	0.0846	0.0167
100.00	127.90	55.00	300.00	0.1549	0.0589	99.8750	38.56	0.1086	0.0208
127.90	162.60	32.00	182.00	0.1495	0.0703	99.7250	19.64	0.0918	0.0271
162.60	206.00	26.00	97.00	0.2114	0.0796	98.9950	18.99	0.1547	0.0409
206.00	260.00	20.00	58.00	0.2564	0.0942	96.5650	14.82	0.1917	0.0554
260.00	350.00	14.00	41.00	0.2545	0.1845	90.7550	4.43	0.0825	0.0825

Table B.6 BDT Selection. Tracker Pattern: Inner Tracker + P9 out of P1 Acceptance

Emin	Emax	Ne^+	Ne^-	$e^+/(e^+ + e^-)$	C.C.	Purity(%)	N$^{\rm true}$e$^+$	$e^+/(e^+ + e^-)Corr.$	σ^{stat}
2.00	2.41	7155.00	102368.00	0.0653	0.0009	99.9750	7063.28	0.0645	0.0007
2.41	3.04	11495.00	180357.00	0.0599	0.0010	99.9850	11325.98	0.0590	0.0005
3.04	3.75	11706.00	194708.00	0.0567	0.0010	99.9850	11513.20	0.0558	0.0005
3.75	4.55	10999.00	191585.00	0.0543	0.0011	99.9850	10798.09	0.0533	0.0005
4.55	5.43	10103.00	179599.00	0.0533	0.0012	99.9850	9903.47	0.0522	0.0005
5.43	6.42	8753.00	162600.00	0.0511	0.0012	99.9850	8561.16	0.0500	0.0005
6.42	7.50	7540.00	138150.00	0.0518	0.0013	99.9850	7367.26	0.0506	0.0006
7.50	8.69	6223.00	113308.00	0.0521	0.0014	99.9850	6072.78	0.0508	0.0006
8.69	10.00	4896.00	88974.00	0.0522	0.0015	99.9950	4771.30	0.0508	0.0007
10.00	12.01	5164.00	90212.00	0.0541	0.0016	99.9950	5028.65	0.0527	0.0007
12.01	14.26	3854.00	63974.00	0.0568	0.0017	99.9850	3750.13	0.0553	0.0009
14.26	16.78	2853.00	46984.00	0.0572	0.0019	99.9850	2770.62	0.0556	0.0010
16.78	19.59	2373.00	36588.00	0.0609	0.0020	99.9850	2304.17	0.0591	0.0012
19.59	22.71	2000.00	28325.00	0.0660	0.0021	99.9850	1943.13	0.0641	0.0014
22.71	26.18	1529.00	20266.00	0.0702	0.0023	99.9850	1485.66	0.0682	0.0017
26.18	31.00	1292.00	16518.00	0.0725	0.0025	99.9750	1253.99	0.0704	0.0019
31.00	38.36	1068.00	12955.00	0.0762	0.0027	99.9650	1035.51	0.0738	0.0022
38.36	47.03	684.00	7285.00	0.0858	0.0030	99.9750	664.17	0.0833	0.0031
47.03	57.22	408.00	4239.00	0.0878	0.0033	99.9750	395.22	0.0850	0.0042
57.22	69.18	249.00	2537.00	0.0894	0.0037	99.9450	240.26	0.0862	0.0054
69.18	83.20	192.00	1457.00	0.1164	0.0044	99.9250	186.21	0.1129	0.0079
83.20	100.00	132.00	975.00	0.1192	0.0056	99.8650	127.00	0.1147	0.0098
100.00	127.90	98.00	791.00	0.1102	0.0085	99.8750	91.91	0.1034	0.0106
127.90	162.60	61.00	404.00	0.1312	0.0151	99.7250	55.49	0.1194	0.0159
162.60	206.00	38.00	240.00	0.1367	0.0298	98.9950	31.20	0.1124	0.0212
206.00	260.00	30.00	127.00	0.1911	0.0602	96.5650	22.25	0.1427	0.0332
260.00	350.00	28.00	102.00	0.2154	0.1365	90.7550	11.03	0.0865	0.0439

Table B.7 Shower Shape Selection. Tracker Pattern: Inner Tracker within P1 Acceptance

Emin	Emax	Ne^+	Ne^-	$e^+/(e^+ + e^-)$	C.C.	Purity(%)	N$^{\rm true}$e$^+$	$e^+/(e^+ + e^-)Corr.$	σ^{stat}
2.00	2.41	571.00	8051.00	0.0662	0.0017	99.9250	557.99	0.0647	0.0027
2.41	3.04	856.00	13326.00	0.0604	0.0021	99.9550	829.06	0.0585	0.0020
3.04	3.75	869.00	14277.00	0.0574	0.0026	99.9650	833.12	0.0550	0.0019
3.75	4.55	872.00	14115.00	0.0582	0.0032	99.9650	828.62	0.0553	0.0019
4.55	5.43	841.00	13873.00	0.0572	0.0039	99.9650	789.60	0.0537	0.0019
5.43	6.42	749.00	12814.00	0.0552	0.0046	99.9550	692.39	0.0511	0.0020
6.42	7.50	636.00	11047.00	0.0544	0.0054	99.9550	578.58	0.0495	0.0021
7.50	8.69	541.00	8978.00	0.0568	0.0063	99.9650	486.87	0.0511	0.0024
8.69	10.00	454.00	7261.00	0.0588	0.0073	99.9650	403.44	0.0523	0.0027
10.00	12.01	493.00	7403.00	0.0624	0.0086	99.9650	432.48	0.0548	0.0027
12.01	14.26	340.00	5375.00	0.0595	0.0102	99.9550	287.36	0.0503	0.0032
14.26	16.78	288.00	4196.00	0.0642	0.0121	99.9550	239.56	0.0534	0.0037
16.78	19.59	247.00	3268.00	0.0703	0.0141	99.9450	202.98	0.0577	0.0044
19.59	22.71	215.00	2603.00	0.0763	0.0164	99.9350	174.41	0.0619	0.0051
22.71	26.18	160.00	1893.00	0.0779	0.0189	99.9350	125.86	0.0613	0.0061
26.18	31.00	155.00	1589.00	0.0889	0.0220	99.9250	121.81	0.0699	0.0070
31.00	38.36	122.00	1302.00	0.0857	0.0265	99.9050	88.82	0.0624	0.0077
38.36	47.03	89.00	773.00	0.1032	0.0324	99.9050	65.24	0.0757	0.0108
47.03	57.22	65.00	498.00	0.1155	0.0393	99.8750	46.46	0.0825	0.0142
57.22	69.18	43.00	300.00	0.1254	0.0472	99.8350	29.54	0.0861	0.0191
69.18	83.20	22.00	174.00	0.1122	0.0563	99.7350	12.30	0.0628	0.0245
83.20	100.00	23.00	116.00	0.1655	0.0670	99.7650	15.75	0.1133	0.0346
100.00	127.90	17.00	96.00	0.1504	0.0817	99.6450	9.22	0.0816	0.0383
127.90	162.60	12.00	65.00	0.1558	0.1009	98.8550	5.14	0.0669	0.0491
162.60	206.00	5.00	26.00	0.1613	0.1228	97.1150	1.41	0.0458	0.0827
206.00	260.00	4.00	11.00	0.2667	0.1495	92.7150	2.15	0.1464	0.1427
260.00	350.00	2.00	15.00	0.1176	0.1839	85.7250	0.00	0.0000	0.0000

Table B.8 Shower Shape Selection. Tracker Pattern: Inner Tracker + P9 within P1 Acceptance

Emin	Emax	Ne^+	Ne^-	$e^+/(e^+ + e^-)$	C.C.	Purity(%)	N$^{\rm true}$e$^+$	$e^+/(e^+ + e^-)Corr.$	σ^{stat}
2.00	2.41	1876.00	27590.00	0.0637	0.0020	99.9250	1822.83	0.0619	0.0014
2.41	3.04	2812.00	45519.00	0.0582	0.0020	99.9550	2725.15	0.0564	0.0011
3.04	3.75	2881.00	48051.00	0.0566	0.0020	99.9650	2789.89	0.0548	0.0010
3.75	4.55	2749.00	47932.00	0.0542	0.0020	99.9650	2658.35	0.0525	0.0010
4.55	5.43	2508.00	45621.00	0.0521	0.0020	99.9650	2421.95	0.0503	0.0010
5.43	6.42	2269.00	41593.00	0.0517	0.0020	99.9550	2190.64	0.0499	0.0011
6.42	7.50	1836.00	35320.00	0.0494	0.0020	99.9550	1769.58	0.0476	0.0011
7.50	8.69	1583.00	28943.00	0.0519	0.0019	99.9650	1529.01	0.0501	0.0013
8.69	10.00	1279.00	22441.00	0.0539	0.0019	99.9650	1237.30	0.0522	0.0015
10.00	12.01	1289.00	22884.00	0.0533	0.0019	99.9650	1246.46	0.0516	0.0014
12.01	14.26	993.00	16118.00	0.0580	0.0019	99.9550	962.96	0.0563	0.0018
14.26	16.78	735.00	11906.00	0.0581	0.0020	99.9550	712.60	0.0564	0.0021
16.78	19.59	617.00	9257.00	0.0625	0.0020	99.9450	599.29	0.0607	0.0024
19.59	22.71	526.00	7205.00	0.0680	0.0021	99.9350	511.87	0.0662	0.0029
22.71	26.18	372.00	5108.00	0.0679	0.0021	99.9350	361.60	0.0660	0.0034
26.18	31.00	308.00	4114.00	0.0697	0.0023	99.9250	299.11	0.0676	0.0038
31.00	38.36	267.00	3118.00	0.0789	0.0025	99.9050	259.56	0.0767	0.0046
38.36	47.03	172.00	1785.00	0.0879	0.0029	99.9050	167.09	0.0854	0.0064
47.03	57.22	92.00	1067.00	0.0794	0.0036	99.8750	88.37	0.0763	0.0080
57.22	69.18	79.00	633.00	0.1110	0.0045	99.8350	76.33	0.1072	0.0118
69.18	83.20	47.00	372.00	0.1122	0.0059	99.7350	44.92	0.1072	0.0155
83.20	100.00	33.00	250.00	0.1166	0.0080	99.7650	31.16	0.1101	0.0192
100.00	127.90	35.00	207.00	0.1446	0.0117	99.6450	32.82	0.1357	0.0228
127.90	162.60	11.00	118.00	0.0853	0.0181	98.8550	8.86	0.0688	0.0249
162.60	206.00	15.00	62.00	0.1948	0.0287	97.1150	13.12	0.1714	0.0458
206.00	260.00	9.00	39.00	0.1875	0.0464	92.7150	6.78	0.1431	0.0568
260.00	350.00	10.00	21.00	0.3226	0.0828	85.7250	7.34	0.2482	0.0875

Table B.9 Shower Shape Selection. Tracker Pattern: Inner Tracker + P1

Emin	Emax	Ne^+	Ne^-	$e^+/(e^+ + e^-)$	C.C.	Purity(%)	$N^{true}e^+$	$e^+/(e^+ + e^-)Corr.$	σ^{stat}
2.00	2.41	2021.00	30198.00	0.0627	0.0014	99.9250	1979.52	0.0614	0.0014
2.41	3.04	3043.00	49469.00	0.0579	0.0014	99.9550	2975.86	0.0567	0.0010
3.04	3.75	3031.00	52162.00	0.0549	0.0014	99.9650	2960.37	0.0536	0.0010
3.75	4.55	2922.00	51400.00	0.0538	0.0014	99.9650	2852.28	0.0525	0.0010
4.55	5.43	2764.00	48779.00	0.0536	0.0014	99.9650	2697.68	0.0523	0.0010
5.43	6.42	2457.00	44841.00	0.0519	0.0014	99.9550	2395.44	0.0506	0.0010
6.42	7.50	2084.00	38232.00	0.0517	0.0014	99.9550	2031.15	0.0504	0.0011
7.50	8.69	1707.00	30794.00	0.0525	0.0014	99.9650	1664.22	0.0512	0.0012
8.69	10.00	1320.00	24348.00	0.0514	0.0015	99.9650	1285.68	0.0501	0.0014
10.00	12.01	1496.00	24901.00	0.0567	0.0015	99.9650	1460.29	0.0553	0.0014
12.01	14.26	1062.00	17761.00	0.0564	0.0016	99.9550	1035.54	0.0550	0.0017
14.26	16.78	843.00	13417.00	0.0591	0.0016	99.9550	822.13	0.0577	0.0020
16.78	19.59	681.00	10795.00	0.0593	0.0017	99.9450	663.15	0.0578	0.0022
19.59	22.71	581.00	8285.00	0.0655	0.0018	99.9350	566.33	0.0639	0.0026
22.71	26.18	429.00	5805.00	0.0688	0.0020	99.9350	417.86	0.0670	0.0032
26.18	31.00	389.00	4892.00	0.0737	0.0023	99.9250	378.53	0.0717	0.0036
31.00	38.36	310.00	3909.00	0.0735	0.0026	99.9050	300.13	0.0711	0.0040
38.36	47.03	199.00	2348.00	0.0781	0.0032	99.9050	191.79	0.0753	0.0053
47.03	57.22	131.00	1351.00	0.0884	0.0041	99.8750	125.84	0.0849	0.0074
57.22	69.18	97.00	842.00	0.1033	0.0051	99.8350	92.98	0.0990	0.0100
69.18	83.20	61.00	487.00	0.1113	0.0065	99.7350	58.04	0.1060	0.0135
83.20	100.00	55.00	344.00	0.1378	0.0082	99.7650	52.47	0.1316	0.0174
100.00	127.90	52.00	282.00	0.1557	0.0106	99.6450	49.32	0.1478	0.0200
127.90	162.60	24.00	186.00	0.1143	0.0140	98.8550	21.39	0.1020	0.0221
162.60	206.00	13.00	84.00	0.1340	0.0188	97.1150	11.23	0.1162	0.0346
206.00	260.00	16.00	44.00	0.2667	0.0289	92.7150	13.94	0.2369	0.0568
260.00	350.00	15.00	38.00	0.2830	0.0675	85.7250	10.90	0.2143	0.0624

Table B.10 Shower Shape Selection. Tracker Pattern: Inner Tracker + P1 + P9

Emin	Emax	Ne^+	Ne^-	$e^+/(e^+ + e^-)$	C.C.	Purity(%)	N$^{\rm true}$e$^+$	$e^+/(e^+ + e^-)Corr.$	σ^{stat}
2.00	2.41	7266.00	108295.00	0.0629	0.0007	99.9250	7192.29	0.0622	0.0007
2.41	3.04	10972.00	175660.00	0.0588	0.0007	99.9550	10849.35	0.0581	0.0005
3.04	3.75	10840.00	184106.00	0.0556	0.0008	99.9650	10704.58	0.0549	0.0005
3.75	4.55	10457.00	181021.00	0.0546	0.0008	99.9650	10315.25	0.0539	0.0005
4.55	5.43	9314.00	170994.00	0.0517	0.0009	99.9650	9171.11	0.0509	0.0005
5.43	6.42	8268.00	156073.00	0.0503	0.0009	99.9550	8128.07	0.0495	0.0005
6.42	7.50	7027.00	131810.00	0.0506	0.0010	99.9550	6901.14	0.0497	0.0006
7.50	8.69	5753.00	105866.00	0.0515	0.0010	99.9650	5646.05	0.0506	0.0007
8.69	10.00	4506.00	82047.00	0.0521	0.0011	99.9650	4417.81	0.0510	0.0008
10.00	12.01	4645.00	83042.00	0.0530	0.0012	99.9650	4549.16	0.0519	0.0008
12.01	14.26	3433.00	58271.00	0.0556	0.0013	99.9550	3360.11	0.0545	0.0009
14.26	16.78	2619.00	43487.00	0.0568	0.0014	99.9550	2560.46	0.0555	0.0011
16.78	19.59	2243.00	34251.00	0.0615	0.0015	99.9450	2193.60	0.0601	0.0013
19.59	22.71	1724.00	25820.00	0.0626	0.0016	99.9350	1684.29	0.0612	0.0015
22.71	26.18	1263.00	18158.00	0.0650	0.0017	99.9350	1233.58	0.0635	0.0018
26.18	31.00	1048.00	14360.00	0.0680	0.0018	99.9250	1023.48	0.0664	0.0020
31.00	38.36	883.00	11247.00	0.0728	0.0019	99.9050	862.75	0.0711	0.0024
38.36	47.03	544.00	6454.00	0.0777	0.0019	99.9050	532.06	0.0760	0.0032
47.03	57.22	370.00	3535.00	0.0948	0.0019	99.8750	363.39	0.0931	0.0047
57.22	69.18	235.00	2294.00	0.0929	0.0019	99.8350	230.70	0.0912	0.0058
69.18	83.20	136.00	1328.00	0.0929	0.0018	99.7350	133.44	0.0912	0.0076
83.20	100.00	114.00	893.00	0.1132	0.0018	99.7650	112.30	0.1116	0.0100
100.00	127.90	87.00	765.00	0.1021	0.0021	99.6450	85.25	0.1001	0.0104
127.90	162.60	54.00	388.00	0.1222	0.0034	98.8550	52.25	0.1184	0.0155
162.60	206.00	40.00	214.00	0.1575	0.0067	97.1150	37.66	0.1489	0.0226
206.00	260.00	24.00	137.00	0.1491	0.0134	92.7150	20.68	0.1298	0.0270
260.00	350.00	22.00	88.00	0.2000	0.0231	85.7250	17.18	0.1608	0.0355

Table B.11 Shower Shape Selection. Tracker Pattern: Inner Tracker Out of P1 Acceptance

Emin	Emax	Ne^+	Ne^-	$e^+/(e^+ + e^-)$	C.C.	Purity(%)	N$^{\rm true}$e$^+$	$e^+/(e^+ + e^-)Corr.$	σ^{stat}
2.00	2.41	1893.00	26129.00	0.0676	0.0008	99.9250	1872.77	0.0668	0.0015
2.41	3.04	2866.00	43532.00	0.0618	0.0010	99.9550	2825.11	0.0609	0.0011
3.04	3.75	2795.00	46679.00	0.0565	0.0012	99.9650	2740.95	0.0554	0.0010
3.75	4.55	2718.00	46227.00	0.0555	0.0015	99.9650	2652.48	0.0542	0.0010
4.55	5.43	2471.00	44346.00	0.0528	0.0018	99.9650	2394.87	0.0512	0.0010
5.43	6.42	2283.00	41055.00	0.0527	0.0021	99.9550	2198.46	0.0507	0.0011
6.42	7.50	2099.00	35186.00	0.0563	0.0025	99.9550	2013.40	0.0540	0.0012
7.50	8.69	1639.00	28947.00	0.0536	0.0030	99.9650	1556.09	0.0509	0.0013
8.69	10.00	1380.00	23006.00	0.0566	0.0035	99.9650	1303.01	0.0534	0.0015
10.00	12.01	1479.00	23543.00	0.0591	0.0042	99.9650	1384.78	0.0553	0.0015
12.01	14.26	1149.00	16970.00	0.0634	0.0051	99.9550	1066.55	0.0589	0.0018
14.26	16.78	910.00	12488.00	0.0679	0.0062	99.9550	836.78	0.0625	0.0022
16.78	19.59	706.00	9920.00	0.0664	0.0075	99.9450	635.74	0.0598	0.0024
19.59	22.71	613.00	7738.00	0.0734	0.0089	99.9350	547.94	0.0656	0.0029
22.71	26.18	457.00	5609.00	0.0753	0.0106	99.9350	401.01	0.0661	0.0034
26.18	31.00	439.00	4700.00	0.0854	0.0128	99.9250	382.91	0.0745	0.0040
31.00	38.36	366.00	3831.00	0.0872	0.0160	99.9050	308.45	0.0735	0.0044
38.36	47.03	249.00	2232.00	0.1004	0.0203	99.9050	206.71	0.0833	0.0062
47.03	57.22	155.00	1290.00	0.1073	0.0257	99.8750	124.11	0.0859	0.0084
57.22	69.18	83.00	826.00	0.0913	0.0319	99.8350	57.58	0.0634	0.0100
69.18	83.20	58.00	519.00	0.1005	0.0388	99.7350	38.47	0.0667	0.0132
83.20	100.00	48.00	324.00	0.1290	0.0463	99.7650	33.80	0.0909	0.0185
100.00	127.90	42.00	258.00	0.1400	0.0554	99.6450	28.40	0.0947	0.0216
127.90	162.60	26.00	146.00	0.1512	0.0650	98.8550	16.71	0.0973	0.0298
162.60	206.00	23.00	68.00	0.2527	0.0765	97.1150	18.21	0.2016	0.0496
206.00	260.00	14.00	49.00	0.2222	0.1082	92.7150	8.01	0.1292	0.0595
260.00	350.00	8.00	30.00	0.2105	0.2751	85.7250	0.00	0.0000	0.0000

Table B.12 Shower Shape Selection. Tracker Pattern: Inner Tracker + P9 out of P1 Acceptance

Emin	Emax	Ne^+	Ne^-	$e^+/(e^+ + e^-)$	C.C.	Purity(%)	N$^{\rm true}$e$^+$	$e^+/(e^+ + e^-)Corr.$	σ^{stat}
2.00	2.41	7110.00	102119.00	0.0651	0.0010	99.9250	7008.36	0.0642	0.0007
2.41	3.04	10663.00	166513.00	0.0602	0.0011	99.9550	10485.45	0.0592	0.0006
3.04	3.75	10650.00	176622.00	0.0569	0.0012	99.9650	10444.41	0.0558	0.0005
3.75	4.55	9952.00	173759.00	0.0542	0.0013	99.9650	9729.85	0.0530	0.0005
4.55	5.43	9206.00	164643.00	0.0530	0.0015	99.9650	8975.55	0.0516	0.0005
5.43	6.42	8102.00	151346.00	0.0508	0.0016	99.9550	7869.69	0.0494	0.0006
6.42	7.50	6915.00	127587.00	0.0514	0.0017	99.9550	6702.24	0.0498	0.0006
7.50	8.69	5646.00	103764.00	0.0516	0.0019	99.9650	5459.26	0.0499	0.0007
8.69	10.00	4464.00	80995.00	0.0522	0.0020	99.9650	4306.75	0.0504	0.0008
10.00	12.01	4680.00	81753.00	0.0541	0.0022	99.9650	4507.61	0.0522	0.0008
12.01	14.26	3420.00	57564.00	0.0561	0.0024	99.9550	3287.48	0.0539	0.0009
14.26	16.78	2527.00	41987.00	0.0568	0.0026	99.9550	2422.55	0.0544	0.0011
16.78	19.59	2140.00	32428.00	0.0619	0.0028	99.9450	2053.99	0.0594	0.0013
19.59	22.71	1740.00	24991.00	0.0651	0.0029	99.9350	1670.08	0.0625	0.0015
22.71	26.18	1301.00	17655.00	0.0686	0.0031	99.9350	1249.71	0.0659	0.0018
26.18	31.00	1122.00	14211.00	0.0732	0.0032	99.9250	1079.58	0.0704	0.0021
31.00	38.36	882.00	10982.00	0.0743	0.0032	99.9050	848.79	0.0715	0.0024
38.36	47.03	563.00	6081.00	0.0847	0.0031	99.9050	545.29	0.0821	0.0034
47.03	57.22	356.00	3637.00	0.0892	0.0029	99.8750	346.05	0.0867	0.0045
57.22	69.18	222.00	2179.00	0.0925	0.0026	99.8350	216.46	0.0902	0.0059
69.18	83.20	163.00	1207.00	0.1190	0.0026	99.7350	159.89	0.1167	0.0088
83.20	100.00	113.00	830.00	0.1198	0.0031	99.7650	110.53	0.1172	0.0106
100.00	127.90	78.00	662.00	0.1054	0.0055	99.6450	74.49	0.1007	0.0113
127.90	162.60	47.00	352.00	0.1178	0.0127	98.8550	42.47	0.1066	0.0162
162.60	206.00	33.00	219.00	0.1310	0.0287	97.1150	26.36	0.1050	0.0215
206.00	260.00	25.00	110.00	0.1852	0.0542	92.7150	17.90	0.1344	0.0341
260.00	350.00	19.00	88.00	0.1776	0.0710	85.7250	10.36	0.0993	0.0369

C

The AMS-02 Positron Fraction Publication

On April 5th 2013, an AMS-02 publication [9] describing the measurement of the positron fraction has been released. In this chapter, we present a comparison with the published results.

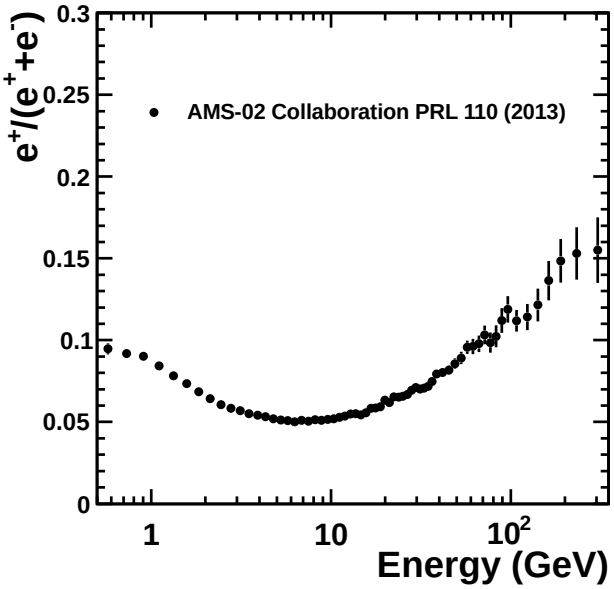

Figure C.1: AMS-02 published result on the positron fraction.

C.1 Comparison with the Published Result

First of all, the analysis presented in this work are compatible with the published one. Minute discrepancies appear in the analysis however, as a result of different data selection and methodologies. In spite of this, these discrepancies agree within statistical and systematic uncertainties. In the next figures we present a comparative of the published result with the positron fraction analysis presented in this work.

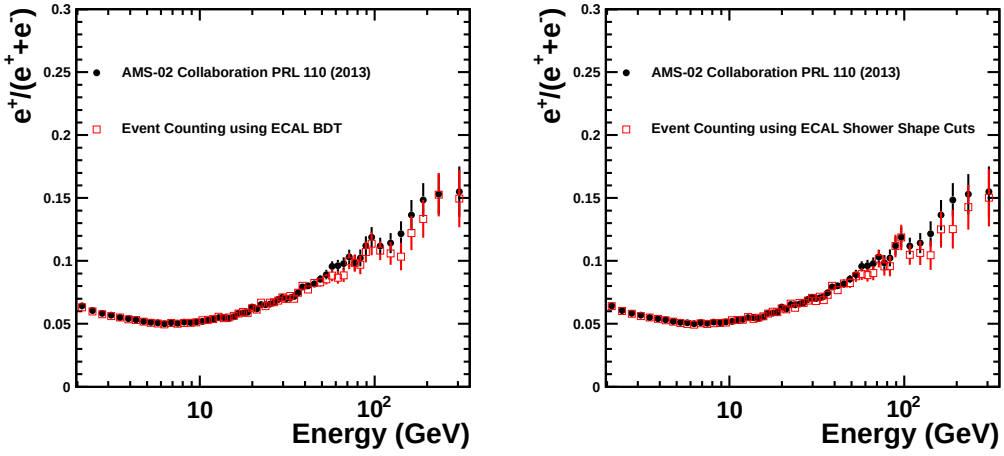

Figure C.2: Event-counting analysis for both Ecal selections.

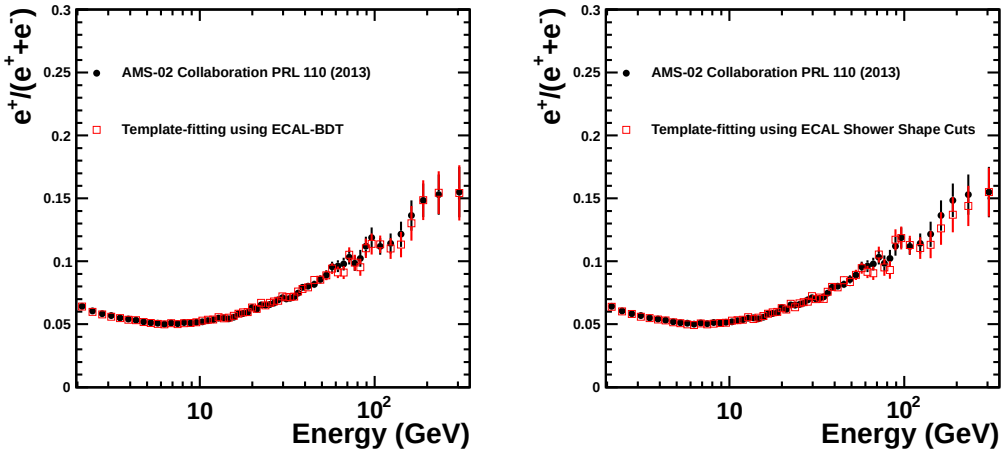

Figure C.3: Template-fitting analysis for both Ecal selections.

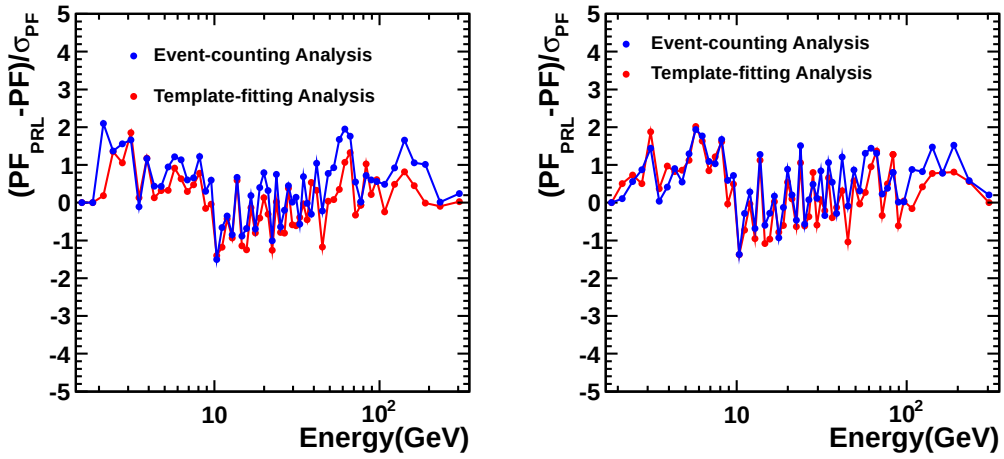

Figure C.4: Relative difference between the published analysis and the ones worked out in this thesis. BDT Selection (Left) and Shower Shape Selection (Right).

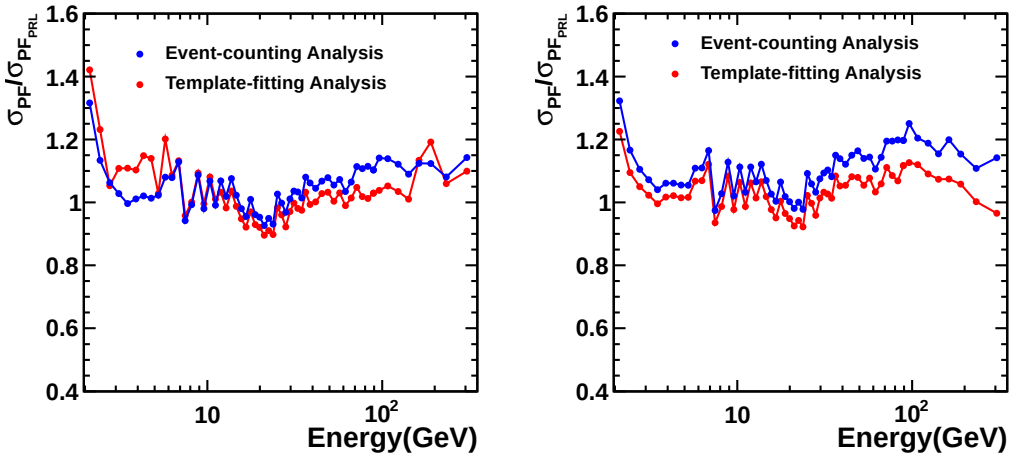

Figure C.5: Ratio of statistical errors between the published analysis and the ones worked out in this thesis. BDT Selection (Left) and Shower Shape Selection (Right).

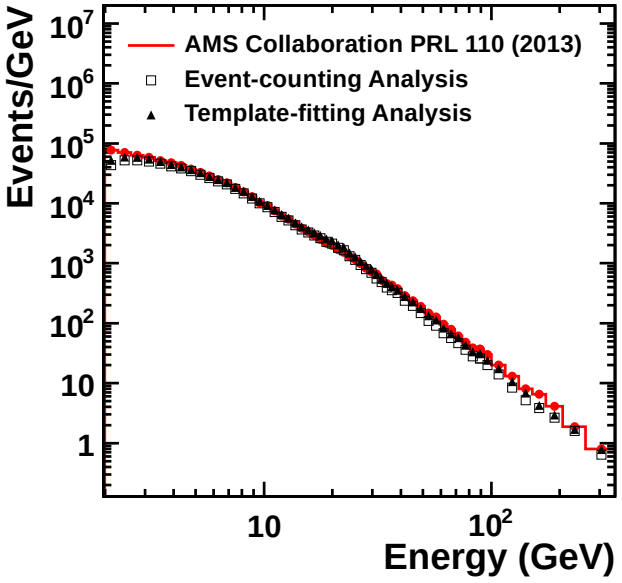

Figure C.6: Number of events per energy selected in the published analysis and the ones worked out in this thesis using a BDT Selection

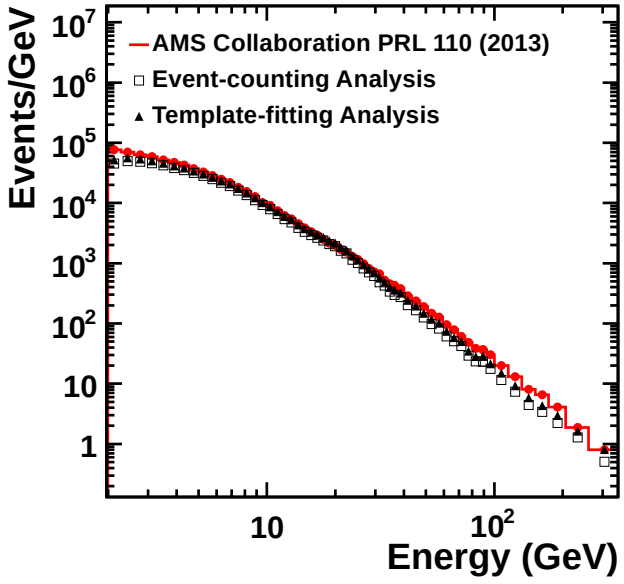

Figure C.7: Number of events per energy selected in the published analysis and the ones worked out in this thesis using a Shower Shape Selection.

C.2 Minimal Model

In this section we present the minimal model parameters for the published positron fraction data and the BDT selection and template fitting analysis.

Table C.1: Minimal model parameters for the positron fraction publication and the BDT selection and template fitting analysis.

Analysis	$\gamma_{e-} - \gamma_{e+}$	K_{e+}/K_{e-}	$\gamma_{e-} - \gamma_s$	K_s/K_{e-}	$1/E_c$	$\chi^2/ndof$
Published analysis	-0.63 ± 0.03	0.091 ± 0.001	0.66 ± 0.05	0.0078 ± 0.0012	$1/0.0013 \pm 1/0.0007$	28.5/57[a]
This analysis	-0.66 ± 0.05	0.090 ± 0.002	0.63 ± 0.05	0.0089 ± 0.0015	$1/0.0015 \pm 1/0.0008$	40.9/53

[a] Statistical + Systematic errors

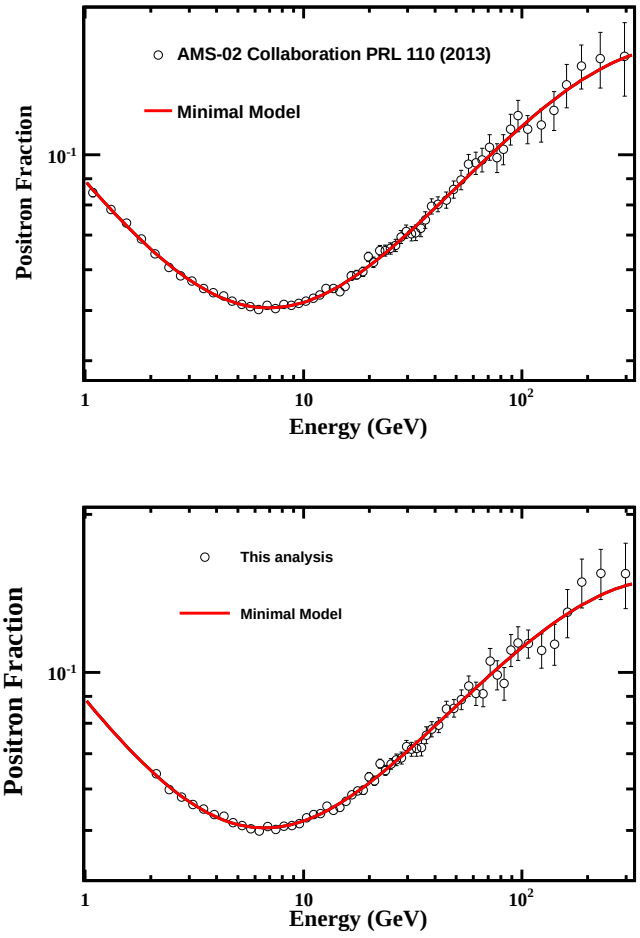

Figure C.8: Minimal model results in the positron fraction publication (upper plot) and the BDT selection and template fitting analysis (lower plot).

D

Tables

Table D.1: Raw positron fraction, positron and electron abundances and proton background estimation as a function of energy for the two selections (BDT cut/Shower Shape cuts)

Emin	Emax	Ne^+	Ne^-	$e^+/(e^+ + e^-)$	Purity(%)	Prot.bkg
2.00	2.41	20856.00	302693.00	0.0645	99.9750	5.22
		20737.00	302382.00	0.0642	99.9250	5.55
2.41	3.04	33344.00	531357.00	0.0590	99.9850	5.00
		31212.00	494019.00	0.0594	99.9550	14.04
3.04	3.75	34030.00	570101.00	0.0563	99.9850	5.10
		31066.00	521897.00	0.0562	99.9650	10.87
3.75	4.55	32383.00	561235.00	0.0546	99.9850	4.86
		29670.00	514454.00	0.0545	99.9650	10.39
4.55	5.43	29321.00	526564.00	0.0527	99.9850	4.40
		27104.00	488256.00	0.0526	99.9650	9.49
5.43	6.42	25784.00	475608.00	0.0514	99.9850	3.87
		24128.00	447722.00	0.0511	99.9550	10.86
6.42	7.50	22164.00	405994.00	0.0518	99.9850	3.32
		20597.00	379182.00	0.0515	99.9550	9.27
7.50	8.69	18222.00	330856.00	0.0522	99.9850	2.73
		16869.00	307292.00	0.0520	99.9650	5.90
8.69	10.00	14522.00	259862.00	0.0529	99.9950	0.73
		13403.00	240098.00	0.0529	99.9650	4.69
10.00	12.01	15364.00	264869.00	0.0548	99.9950	0.77
		14082.00	243526.00	0.0547	99.9650	4.93

12.01	14.26	11407.00	188062.00	0.0572	99.9850	1.71
		10397.00	172059.00	0.0570	99.9550	4.68
14.26	16.78	8715.00	140055.00	0.0586	99.9850	1.31
		7922.00	127481.00	0.0585	99.9550	3.56
16.78	19.59	7276.00	110661.00	0.0617	99.9850	1.09
		6634.00	99919.00	0.0623	99.9450	3.65
19.59	22.71	6021.00	85385.00	0.0659	99.9850	0.90
		5399.00	76642.00	0.0658	99.9350	3.51
22.71	26.18	4514.00	60940.00	0.0690	99.9850	0.68
		3982.00	54228.00	0.0684	99.9350	2.59
26.18	31.00	3923.00	49712.00	0.0731	99.9750	0.98
		3461.00	43866.00	0.0731	99.9250	2.60
31.00	38.36	3299.00	39480.00	0.0771	99.9650	1.15
		2830.00	34389.00	0.0760	99.9050	2.69
38.36	47.03	2113.00	22804.00	0.0848	99.9750	0.53
		1816.00	19673.00	0.0845	99.9050	1.73
47.03	57.22	1338.00	13186.00	0.0921	99.9750	0.33
		1169.00	11378.00	0.0932	99.8750	1.46
57.22	69.18	849.00	8008.00	0.0959	99.9450	0.47
		759.00	7074.00	0.0969	99.8350	1.25
69.18	83.20	572.00	4763.00	0.1072	99.9250	0.43
		487.00	4087.00	0.1065	99.7350	1.29
83.20	100.00	440.00	3219.00	0.1203	99.8650	0.59
		386.00	2757.00	0.1228	99.7650	0.91
100.00	127.90	369.00	2606.00	0.1240	99.8750	0.46
		311.00	2270.00	0.1205	99.6450	1.10
127.90	162.60	207.00	1436.00	0.1260	99.7250	0.57
		174.00	1255.00	0.1218	98.8550	1.99
162.60	206.00	145.00	756.00	0.1609	98.9950	1.46
		129.00	673.00	0.1608	97.1150	3.72
206.00	260.00	108.00	438.00	0.1978	96.5650	3.71
		92.00	390.00	0.1909	92.7150	6.70
260.00	350.00	98.00	317.00	0.2361	90.7550	9.06
		76.00	280.00	0.2135	85.7250	10.90

Table D.2: BDT Selection: Weighted Results

Emin	Emax	Ne^+	Ne^-	CC	Purity(%)	N$^{\mathrm{true}}$e$^+$	$e^+/(e^+ + e^-)$	σ_{stat}
2.00	2.41	20856.00	302693.00	0.0012	99.97	20517.40	0.0634	0.0004
2.41	3.04	33344.00	531357.00	0.0012	99.99	32722.13	0.0579	0.0003
3.04	3.75	34030.00	570101.00	0.0013	99.99	33326.54	0.0552	0.0003
3.75	4.55	32383.00	561235.00	0.0014	99.99	31650.53	0.0533	0.0003
4.55	5.43	29321.00	526564.00	0.0014	99.99	28591.03	0.0514	0.0003
5.43	6.42	25784.00	475608.00	0.0015	99.99	25082.86	0.0500	0.0003
6.42	7.50	22164.00	405994.00	0.0016	99.99	21525.33	0.0502	0.0003
7.50	8.69	18222.00	330856.00	0.0017	99.99	17666.16	0.0506	0.0004
8.69	10.00	14522.00	259862.00	0.0019	100.00	14054.21	0.0512	0.0004
10.00	12.01	15364.00	264869.00	0.0020	100.00	14846.30	0.0529	0.0004
12.01	14.26	11407.00	188062.00	0.0022	99.99	10998.70	0.0551	0.0005
14.26	16.78	8715.00	140055.00	0.0025	99.99	8377.33	0.0562	0.0006
16.78	19.59	7276.00	110661.00	0.0027	99.99	6981.02	0.0592	0.0007
19.59	22.71	6021.00	85385.00	0.0030	99.99	5766.20	0.0630	0.0008
22.71	26.18	4514.00	60940.00	0.0034	99.99	4310.11	0.0658	0.0010
26.18	31.00	3923.00	49712.00	0.0038	99.97	3733.90	0.0695	0.0011
31.00	38.36	3299.00	39480.00	0.0045	99.96	3119.73	0.0729	0.0013
38.36	47.03	2113.00	22804.00	0.0053	99.97	1988.58	0.0795	0.0018
47.03	57.22	1338.00	13186.00	0.0066	99.97	1248.73	0.0860	0.0024
57.22	69.18	849.00	8008.00	0.0079	99.94	783.82	0.0881	0.0031
69.18	83.20	572.00	4763.00	0.0099	99.93	523.06	0.0980	0.0043
83.20	100.00	440.00	3219.00	0.0112	99.86	401.25	0.1094	0.0054
100.00	127.90	369.00	2606.00	0.0133	99.88	329.49	0.1088	0.0061
127.90	162.60	207.00	1436.00	0.0201	99.72	174.06	0.1065	0.0083
162.60	206.00	145.00	756.00	0.0277	99.00	122.54	0.1344	0.0125
206.00	260.00	108.00	438.00	0.0422	96.57	86.15	0.1530	0.0173
260.00	350.00	98.00	317.00	0.0844	90.75	57.85	0.1495	0.0229

Table D.3: Shower Shape Selection: Weighted Results

Emin	Emax	Ne^+	Ne^-	CC	Purity(%)	N$^{\mathrm{true}}$e$^+$	$e^+/(e^+ + e^-)$	σ_{stat}
2.00	2.41	20737.00	302382.00	0.0010	99.93	20433.77	0.0632	0.0004
2.41	3.04	31212.00	494019.00	0.0011	99.96	30689.98	0.0584	0.0003
3.04	3.75	31066.00	521897.00	0.0012	99.96	30473.32	0.0551	0.0003
3.75	4.55	29670.00	514454.00	0.0013	99.96	29036.82	0.0534	0.0003
4.55	5.43	27104.00	488256.00	0.0014	99.96	26450.76	0.0513	0.0003
5.43	6.42	24128.00	447722.00	0.0015	99.96	23474.68	0.0497	0.0003
6.42	7.50	20597.00	379182.00	0.0016	99.96	19996.10	0.0500	0.0003
7.50	8.69	16869.00	307292.00	0.0018	99.96	16341.51	0.0504	0.0004
8.69	10.00	13403.00	240098.00	0.0019	99.96	12954.00	0.0511	0.0004
10.00	12.01	14082.00	243526.00	0.0021	99.96	13580.77	0.0527	0.0004
12.01	14.26	10397.00	172059.00	0.0024	99.96	10000.00	0.0548	0.0005
14.26	16.78	7922.00	127481.00	0.0026	99.96	7594.09	0.0560	0.0006
16.78	19.59	6634.00	99919.00	0.0029	99.94	6348.75	0.0596	0.0007
19.59	22.71	5399.00	76642.00	0.0032	99.93	5154.91	0.0628	0.0009
22.71	26.18	3982.00	54228.00	0.0036	99.93	3789.62	0.0651	0.0010
26.18	31.00	3461.00	43866.00	0.0039	99.93	3285.42	0.0693	0.0012
31.00	38.36	2830.00	34389.00	0.0046	99.90	2668.51	0.0717	0.0014
38.36	47.03	1816.00	19673.00	0.0052	99.90	1708.17	0.0793	0.0019
47.03	57.22	1169.00	11378.00	0.0062	99.88	1094.23	0.0871	0.0026
57.22	69.18	759.00	7074.00	0.0075	99.83	703.59	0.0897	0.0034
69.18	83.20	487.00	4087.00	0.0093	99.74	447.07	0.0974	0.0046
83.20	100.00	386.00	2757.00	0.0099	99.76	356.01	0.1134	0.0059
100.00	127.90	311.00	2270.00	0.0117	99.64	279.50	0.1070	0.0064
127.90	162.60	174.00	1255.00	0.0179	98.86	146.83	0.1029	0.0087
162.60	206.00	129.00	673.00	0.0256	97.11	107.99	0.1314	0.0129
206.00	260.00	92.00	390.00	0.0396	92.71	69.46	0.1430	0.0177
260.00	350.00	76.00	280.00	0.0515	85.72	45.78	0.1503	0.0228

Table D.4: Template-Fitting. Shower Shape Selection. Weighted Results

Emin	Emax	$\mathrm{N^{true}e^{+}}$	$e^+/(e^+ + e^-)$	σ_{stat}
2.00	2.41	23522.78	0.0630	0.0004
2.41	3.04	34287.72	0.0585	0.0003
3.04	3.75	33159.15	0.0549	0.0003
3.75	4.55	31374.35	0.0533	0.0003
4.55	5.43	28528.09	0.0513	0.0003
5.43	6.42	25373.33	0.0498	0.0003
6.42	7.50	21615.76	0.0500	0.0003
7.50	8.69	17827.25	0.0506	0.0004
8.69	10.00	14181.49	0.0512	0.0004
10.00	12.01	14919.04	0.0527	0.0004
12.01	14.26	11129.37	0.0550	0.0005
14.26	16.78	8518.86	0.0565	0.0006
16.78	19.59	7129.81	0.0596	0.0007
19.59	22.71	5829.95	0.0630	0.0008
22.71	26.18	4334.37	0.0655	0.0010
26.18	31.00	3775.15	0.0696	0.0011
31.00	38.36	3128.75	0.0727	0.0013
38.36	47.03	2015.95	0.0806	0.0018
47.03	57.22	1311.14	0.0886	0.0024
57.22	69.18	833.73	0.0910	0.0031
69.18	83.20	538.41	0.0980	0.0042
83.20	100.00	428.40	0.1135	0.0054
100.00	127.90	358.17	0.1140	0.0059
127.90	162.60	189.83	0.1095	0.0081
162.60	206.00	140.34	0.1389	0.0118
206.00	260.00	88.31	0.1443	0.0160
260.00	350.00	73.00	0.1550	0.0193

Table D.5: Template-Fitting. BDT Selection. Weighted Results

Emin	Emax	$\mathrm{N^{true}e^{+}}$	$e^+/(e^+ + e^-)$	σ_{stat}
2.00	2.41	23975.49	0.0632	0.0004
2.41	3.04	35341.47	0.0581	0.0003
3.04	3.75	35778.52	0.0550	0.0003
3.75	4.55	33668.72	0.0533	0.0003
4.55	5.43	30427.74	0.0515	0.0003
5.43	6.42	27001.13	0.0501	0.0003
6.42	7.50	23068.01	0.0503	0.0003
7.50	8.69	19042.28	0.0509	0.0004
8.69	10.00	15261.85	0.0515	0.0004
10.00	12.01	16099.99	0.0530	0.0004
12.01	14.26	12070.44	0.0552	0.0005
14.26	16.78	9260.46	0.0566	0.0006
16.78	19.59	7764.11	0.0595	0.0007
19.59	22.71	6480.85	0.0638	0.0008
22.71	26.18	4875.28	0.0664	0.0010
26.18	31.00	4245.56	0.0700	0.0011
31.00	38.36	3587.61	0.0737	0.0012
38.36	47.03	2288.92	0.0801	0.0017
47.03	57.22	1508.81	0.0889	0.0023
57.22	69.18	947.28	0.0913	0.0030
69.18	83.20	639.15	0.0999	0.0039
83.20	100.00	479.53	0.1096	0.0050
100.00	127.90	414.50	0.1141	0.0056
127.90	162.60	232.44	0.1154	0.0077
162.60	206.00	136.75	0.1436	0.0126
206.00	260.00	93.00	0.1531	0.0166
260.00	350.00	72.07	0.1545	0.0215

Table D.6: Systematic error due to the uncertainty in the determination of the charge confusion for the BDT selection (Left) and Shower Shape (Right column) selections.

Emin	Emax	σ_{BDTsys}(C.C.)	σ_{SSsys}(C.C.)
2.00	2.41	0.0007	0.0006
2.41	3.04	0.0007	0.0007
3.04	3.75	0.0007	0.0006
3.75	4.55	0.0007	0.0006
4.55	5.43	0.0006	0.0006
5.43	6.42	0.0006	0.0006
6.42	7.50	0.0006	0.0006
7.50	8.69	0.0006	0.0006
8.69	10.00	0.0006	0.0006
10.00	12.01	0.0006	0.0006
12.01	14.26	0.0006	0.0007
14.26	16.78	0.0008	0.0008
16.78	19.59	0.0007	0.0007
19.59	22.71	0.0008	0.0008
22.71	26.18	0.0008	0.0008
26.18	31.00	0.0009	0.0009
31.00	38.36	0.0009	0.0009
38.36	47.03	0.0010	0.0010
47.03	57.22	0.0010	0.0010
57.22	69.18	0.0010	0.0011
69.18	83.20	0.0011	0.0011
83.20	100.00	0.0012	0.0015
100.00	127.90	0.0014	0.0022
127.90	162.60	0.0018	0.0021
162.60	206.00	0.0023	0.0028
206.00	260.00	0.0039	0.0049
260.00	350.00	0.0077	0.0077

Bibliography

[1] The First Fermi-LAT Catalog of Sources Above 10 GeV. 2013.

[2] Rasha Abbasi and Paolo Desiati. Large Scale Cosmic Ray Anisotropy With IceCube. 2009.

[3] O. Adriani et al. An anomalous positron abundance in cosmic rays with energies 1.5-100 GeV. *Nature*, 458(7238):607–609, 2009.

[4] O. Adriani et al. PAMELA results on the cosmic-ray antiproton flux from 60 MeV to 180 GeV in kinetic energy. *Phys.Rev.Lett.*, 105:121101, 2010.

[5] M. Aguilar et al. Cosmic-ray positron fraction measurement from 1 to 30 GeV with AMS-01. *Physics Letters B*, 646(4):145–154, 2007.

[6] Markus Ahlers, Philipp Mertsch, and Subir Sarkar. On cosmic ray acceleration in supernova remnants and the FERMI/PAMELA data. *Phys.Rev.*, D80:123017, 2009.

[7] Amenomori et al. Anisotropy and corotation of galactic cosmic rays. *Science*, 314(5798):439 – 443, 2006.

[8] M. Amenomori. Anisotropy and Corotation of Galactic Cosmic Rays. *Science*, 314:439–443, 2006.

[9] AMS Collaboration. First Result from the Alpha Magnetic Spectrometer on the International Space Station: Precision Measurement of the Positron Fraction in Primary Cosmic Rays of 0.5ˆ1350 GeV. *Phys. Rev. Lett.*, 110:141102, Apr 2013.

[10] I. Anatoly. The Yakutsk array experiment: Main results and future directions. In *European Physical Journal Web of Conferences*, volume 53 of *European Physical Journal Web of Conferences*, page 4003, June 2013.

[11] Igor V. Moskalenko Andrew W. Strong and Vladimir S. Ptuskin. Cosmic-ray propagation and interactions in the Galaxy. *Annual Review of Nuclear and Particle Systems*, vol. 57(1):85–327, 2007.

[12] T. Antoni et al. Large scale cosmic - ray anisotropy with KASCADE. *Astrophys.J.*, 604:687–692, 2004.

[13] Nima Arkani-Hamed, Douglas P. Finkbeiner, Tracy R. Slatyer, and Neal Weiner. A theory of dark matter. *Phys. Rev. D*, 79:015014, Jan 2009.

[14] A. M. Atoyan, F. A. Aharonian, and H. J. Völk. Electrons and positrons in the galactic cosmic rays. *Phys. Rev. D*, 52(6):3265–3275, 1995.

[15] B. Bertucci on behalf of the AMS Collaboration. Precision measurement of the electron plus positron spectrum with AMS. In *Procceedings of the 33rd International Cosmic Ray Conference*, July 2013.

[16] E. Baltz and A. Edsjo. Positron propagation and fluxes from neutralino annihilation in the halo. *Phys. Rev. D*, 59(2):023511, 1998.

[17] S. W. Barwick et al. Measurements of the Cosmic-Ray Positron Fraction from 1 to 50 GeV. *Astrophys. J.*, 482:191–194, 1997.

[18] K. G. Begeman, A. H. Broeils, and R. H. Sanders. Extended rotation curves of spiral galaxies - Dark haloes and modified dynamics. *Monthly Notices of the Royal Astronomical Society*, 249:523–537, Apr 1991.

[19] Giuseppe Di Bernardo, Carmelo Evoli, Daniele Gaggero, Dario Grasso, and Luca Maccione. Unified interpretation of cosmic ray nuclei and antiproton recent measurements. *Astroparticle Physics*, 34(5):274 – 283, 2010.

[20] G. Bertone, D. Hooper, and J. Silk. Particle dark matter: evidence, candidates and constraints. *Physics Reports*, 405:279–390, Jan 2005.

[21] Pasquale Blasi. The origin of the positron excess in cosmic rays. *Phys.Rev.Lett.*, 103:051104, 2009.

[22] Pasquale Blasi and Pasquale D. Serpico. High-energy antiprotons from old supernova remnants. *Phys.Rev.Lett.*, 103:081103, 2009.

[23] Johannes Blümer, Ralph Engel, and Jörg R. Hörandel. Cosmic rays from the knee to the highest energies. *Progress in Particle and Nuclear Physics*, 63(2):293 – 338, 2009.

[24] Torsten Bringmann, Julien Lavalle, and Pierre Salati. Intermediate mass black holes and nearby dark matter point sources: A critical reassessment. *Phys. Rev. Lett.*, 103(16):161301, 2009.

[25] Pierre Brun, Timur Delahaye, Jürg Diemand, Stefano Profumo, and Pierre Salati. Cosmic ray lepton puzzle in the light of cosmological n-body simulations. *Phys. Rev. D*, 80(3):035023, 2009.

[26] I. Büsching, O. C. de Jager, M. S. Potgieter, and C. Venter. A Cosmic-Ray Positron Anisotropy due to Two Middle-Aged, Nearby Pulsars? *ApJ*, 678(1):L39–L42, 2008.

[27] Ignacio Cernuda. Anisotropies in the cosmic-ray electron spectrum: A way to discriminate between exotic and astrophysical sources? pages 513–518, 2010.

[28] Ignacio Cernuda. Cosmic-ray electron anisotropies as a tool to discriminate between exotic and astrophysical sources. *Astroparticle Physics*, 34:59–69, September 2010.

[29] J. Chang et al. An excess of cosmic ray electrons at energies of 300-800 GeV. *Nature*, 456:362–365, 2008.

[30] Pascal Chardonnet, Jean Orloff, and Pierre Salati. The production of anti-matter in our galaxy. *Physics Letters B*, 409(1-4):313 – 320, 1997.

[31] X. Chi, K. S. Cheng, and E. C. M. Young. Pulsar-Wind Origin of Cosmic-Ray Positrons. *ApJ*, 459(2):L83–L86, 1996.

[32] Marco Cirelli, Mario Kadastik, Martti Raidal, and Alessandro Strumia. Model-independent implications of the e+, e-, anti-proton cosmic ray spectra on properties of Dark Matter. *Nucl. Phys.*, B813:1–21, 2009.

[33] J. M. Clem, D. P. Clements, J. Esposito, P. Evenson, D. Huber, J. L'Heureux, P. Meyer, and C. Constantin. Solar Modulation of Cosmic Electrons. *Apj*, 464:507, June 1996.

[34] AMS Collaboration. Search for antihelium in cosmic rays. *Physics Letters B*, 461(4):387–396, 1999.

[35] AMS Collaboration. Cosmic protons. *Physics Letters B*, 490(1-2):27–35, 2000.

[36] AMS Collaboration. Helium in near earth orbit. *Physics Letters B*, 494(3-4):193–202, 2000.

[37] AMS Collaboration. Leptons in near earth orbit. *Physics Letters B*, 484(1-2):10–22, 2000.

[38] AMS Collaboration. Protons in near earth orbit. *Physics Letters B*, 472(1-2):215–226, 2000.

[39] AMS Collaboration. A study of cosmic ray secondaries induced by the mir space station using ams-01. *Nuclear Instruments and Methods in Physics Research Section B*, 234(3):321–323, 2005.

[40] AMS Collaboration. Relative composition and energy spectra of light nuclei in cosmic rays: Results from ams-01. *The Astrophysical Journal*, 724(1):111, 2010.

[41] AMS Collaboration. Isotopic composition of light nuclei in cosmic rays: Results from ams-01. *The Astrophysical Journal*, 736(2):105, 2011.

[42] AMS-01 Collaboration. Cosmic-ray positron fraction measurement from 1 to 30 gev with ams-01. *Physics Letters B*, 646(4):145–154, 2007.

[43] Pamela Collaboration. Search for cosmic ray electron-positron anisotropies with the pamela data. *Journal of Physics: Conference Series*, 409(1):012055, 2013.

[44] Super-Kamiokande Collaboration. Observation of the anisotropy of 10 tev primary cosmic ray nuclei flux with the super-kamiokande-i detector. *Phys. Rev. D*, 75:062003, Mar 2007.

[45] A. H. Compton and I. A. Getting. An Apparent Effect of Galactic Rotation on the Intensity of Cosmic Rays. *Physical Review*, 47:817–821, June 1935.

[46] Stephane Coutu, Steven W. Barwick, James J. Beatty, Amit Bhattacharyya, Chuck R. Bower, et al. Cosmic ray positrons: Are there primary sources? *Astropart.Phys.*, 11:429–435, 1999.

[47] W. J. G. de Blok. The Core-Cusp Problem. *Advances in Astronomy*, 2010, 2010.

[48] T. Delahaye, R. Lineros, F. Donato, N. Fornengo, J. Lavalle, P. Salati, and R. Taillet. Galactic secondary positron flux at the Earth. *Astronomy and Astrophysics*, 501(3):821–833, 2009.

[49] T. Delahaye, R. Lineros, F. Donato, N. Fornengo, and P. Salati. Positrons from dark matter annihilation in the galactic halo: Theoretical uncertainties. *Physical Review D*, 77(6), 2008.

[50] G. Di Sciascio. Measurement of Cosmic Ray Spectrum and Anisotropy with ARGO-YBJ. *EPJ Web Conf.*, 52:04004, 2013.

[51] Boris Dolgoshein. Transition radiation detectors and particle identification. *Nuclear Instruments and Methods in Physics Research Section A: Accelerators, Spectrometers, Detectors and Associated Equipment*, 252(2–3):137 – 144, 1986.

[52] A. A. Abdo et al. The large-scale cosmic-ray anisotropy as observed with milagro. *The Astrophysical Journal*, 698(2):2121, 2009.

[53] Ackermann et al. Fermi LAT observations of cosmic-ray electrons from 7 GeV to 1 TeV. *Physical Review D*, 82(9):092004, nov 2010.

[54] Ackermann et al. Searches for cosmic-ray electron anisotropies with the fermi large area telescope. *Phys. Rev. D*, 82:092003, Nov 2010.

[55] Ackermann et al. Measurement of Separate Cosmic-Ray Electron and Positron Spectra with the Fermi Large Area Telescope. *Physical Review Letters*, 108(1):011103, jan 2012.

[56] Adriani et al. Cosmic-Ray Electron Flux Measured by the PAMELA Experiment between 1 and 625 GeV. *Physical Review Letters*, 106(20):201101, May 2011.

[57] Adriani et al. PAMELA Measurements of Cosmic-Ray Proton and Helium Spectra. *Science*, 332:69–, April 2011.

[58] Aharonian et al. Energy Spectrum of Cosmic-Ray Electrons at TeV Energies. *Physical Review Letters*, 101(26):261104, dec 2008.

[59] Beringer et al. Review of particle physics. *Phys. Rev. D*, 86:010001, Jul 2012.

[60] J. Tada et al. Analysis of cosmic ray anisotropy around 1015 ev using network observation data of air showers. *Nuclear Physics B - Proceedings Supplements*, 151(1):485 – 488, 2006.

[61] J. L. Feng. Dark Matter Candidates from Particle Physics and Methods of Detection. *Anual Review of Astronomy and Astrophysics*, 48:495–545, Sep 2010.

[62] FERMI/LAT collaboration. Measurement of the Cosmic Ray e+ plus e- spectrum from 20 GeV to 1 TeV with the Fermi Large Area Telescope. *Phys. Rev. Lett.*, 102(18), 2009.

[63] Quan-Gui Gao, Ze-Jun Jiang, and Li Zhang. Possible Contribution of Mature Gamma;-Ray Pulsars to Cosmic-ray Positrons. *Chinese Journal of Astronomy and Astrophysics*, 8(1):87–95, 2008.

[64] M. Garcia-Munoz, P. Meyer, K. R. Pyle, and J. A. Simpson. The Dependence of Solar Modulation on the Sign of the Cosmic Ray Particle Charge : Further Study of a 22 Year Solar Magnetic Cycle. In *International Cosmic Ray Conference*, volume 3 of *International Cosmic Ray Conference*, page 303, 1987.

[65] V.L. Ginzburg and S.I. Syrovatskii. *The origin of cosmic rays*. Pergaemon, Oxford, 1964.

[66] L. J. Gleeson and W. I. Axford. Solar Modulation of Galactic Cosmic Rays. *Apj*, 154:1011, December 1968.

[67] D. Grasso et al. On Possible Intepretations of the high Energy Electron-Positron Spectrum measured by the Fermi Large Area Telescope. *Astroparticle Physics*, 32(2):140–151, 2009.

[68] Kenneth Greisen. End to the cosmic-ray spectrum? *Phys. Rev. Lett.*, 16:748–750, Apr 1966.

[69] Guenter Grindhammer and S. Peters. The Parameterized simulation of electromagnetic showers in homogeneous and sampling calorimeters. 1993.

[70] A. K. Harding and R. Ramaty. The Pulsar Contribution to Galactic Cosmic Ray Positrons. In *International Cosmic Ray Conference*, volume 2 of *International Cosmic Ray Conference*, pages 92–+, 1987.

[71] S. Heinz and R. Sunyaev. Cosmic rays from microquasars: A narrow component to the CR spectrum? *Astron. Astroph.*, 390:751–766, August 2002.

[72] A. M. Hillas. The Origin of Ultra-High-Energy Cosmic Rays. *Araa*, 22:425–444, 1984.

[73] Andreas Hoecker, Peter Speckmayer, Joerg Stelzer, Jan Therhaag, Eckhard von Toerne, and Helge Voss. TMVA: Toolkit for Multivariate Data Analysis. *PoS*, ACAT:040, 2007.

[74] Dan Hooper, Pasquale Blasi, and Pasquale Serpico. Pulsars as the Sources of High Energy Cosmic Ray Positrons. *Journal of Cosmology and Astroparticle Physics*, 1:25–+, 2009.

[75] L. Hui. Unitarity Bounds and the Cuspy Halo Problem. *Physical Review Letters*, 86:3467–3470, apr 2001.

[76] K. Ioka. A Gamma-Ray Burst/Pulsar for Cosmic Ray Positrons with a Dark Matter-Like Spectrum. *Progress of Theoretical Physics*, 123:743–755, April 2010.

[77] K. Ioka and P. Mészáros. Hypernova and Gamma-ray Burst Remnants as TeV Unidentified Sources. *Apj*, 709:1337–1342, February 2010.

[78] Norita Kawanaka, Kunihito Ioka, , and Mihoko M. Nojiri. Is cosmic-ray electron excess from pulsars is spiky or smooth? continuous and multiple electron/positron injections. *The Astrophysical Journal*, 710(2):958–963, 2010.

[79] L.Zhang and K.S.Cheng. Cosmic-ray positrons from mature gamma-ray pulsars. *A&A*, 368(3):1063–1070, 2001.

[80] Dmitry Malyshev, Ilias Cholis, and Joseph Gelfand. Pulsars versus dark matter interpretation of ATIC/PAMELA. *Phys. Rev. D*, 80(6):063005, 2009.

[81] R. N. Manchester, G. B. Hobbs, A. Teoh, and M. Hobbs. The ATNF pulsar catalogue. *Astron. J.*, 129:1993–2006, 2005.

[82] C.Y. Mao and C.S Shen. Anisotropy and diffusion of cosmic ray electrons. *Chinese Journal of Physics*, 10(1):16–28, 1971.

[83] M.A. Mariscotti. A method for automatic identification of peaks in the presence of background and its application to spectrum analysis. *Nuclear Instruments and Methods*, 50(2):309 – 320, 1967.

[84] D. MAURIN. *USINE: a new public cosmic ray propagation code Basic phenomenology, sample results, and a bit of USINE*, chapter 56, pages 420–434.

[85] Patrick Meade, Michele Papucci, Alessandro Strumia, and Tomer Volansky. Dark Matter Interpretations of the Electron/Positron Excesses after FERMI. *arXiv:0905.0480*, 2009.

[86] P. Mertsch. Cosmic ray backgrounds for dark matter indirect detection. *ArXiv e-prints*, December 2010.

[87] Philipp Mertsch and Subir Sarkar. Testing astrophysical models for the PAMELA positron excess with cosmic ray nuclei. *Phys.Rev.Lett.*, 103:081104, 2009.

[88] Miroslav Morhac, Jan Kliman, Vladislav Matouisek, Martin Veselsky, and Ivan Turzo. Identification of peaks in multidimensional coincidence gamma-ray spectra. *Nuclear Instruments and Methods in Physics Research Section A: Accelerators, Spectrometers, Detectors and Associated Equipment*, 443(1):108 – 125, 2000.

[89] I. V. Moskalenko and A. W. Strong. Production and propagation of cosmic-ray positrons and electrons. *The Astrophysical Journal*, 493(2):694, 1998.

[90] J. F. Navarro, C. S. Frenk, and S. D. M. White. The Structure of Cold Dark Matter Halos. *Astrophysical Jornal*, 462:563, may 1996.

[91] International Association of Geomagnetism and Aeronomy. International geomagnetic reference field: the eleventh generation. *Geophysical Journal International*, 183(3):1216–1230, 2010.

[92] E.N. Parker. The passage of energetic charged particles through interplanetary space. *Planetary and Space Science*, 13(1):9 – 49, 1965.

[93] Miguel Pato, Lidia Pieri, and Gianfranco Bertone. Multi-messenger constraints on the annihilating dark matter interpretation of the positron excess. *Phys.Rev.*, D80:103510, 2009.

[94] Lidia Pieri, Julien Lavalle, Gianfranco Bertone, and Enzo Branchini. Implications of high-resolution simulations on indirect dark matter searches. *Phys. Rev. D*, 83:023518, Jan 2011.

[95] Pierre Auger Collaboration, J. Abraham, P. Abreu, M. Aglietta, C. Aguirre, D. Allard, I. Allekotte, J. Allen, P. Allison, C. Alvarez, and et al. Correlation of the Highest-Energy Cosmic Rays with Nearby Extragalactic Objects. *Science*, 318:938–, November 2007.

[96] Planck Collaboration, P. A. R. Ade, N. Aghanim, C. Armitage-Caplan, M. Arnaud, M. Ashdown, F. Atrio-Barandela, J. Aumont, C. Baccigalupi, A. J. Banday, and et al. Planck 2013 results. I. Overview of products and scientific results. *ArXiv e-prints*, mar 2013.

[97] Stefano Profumo. Dissecting Pamela (and ATIC) with Occam's Razor: Existing,well known Pulsars naturally account for the "anomalous" Cosmic-Ray Elec tron and Positron Data. *arXiv:0812.4457*, 2008.

[98] David Crespo Roces. Prestaciones del detector AMS-02 para el estudio del canal de positrones de los rayos cósmicos. *UCM eprints*, July 2012.

[99] B. P. Roe, H.-J. Yang, J. Zhu, Y. Liu, I. Stancu, and G. McGregor. Boosted decision trees as an alternative to artificial neural networks for particle identification. *Nuclear Instruments and Methods in Physics Research A*, 543:577–584, May 2005.

[100] Philip Schuster, Natalia Toro, Neal Weiner, and Itay Yavin. High Energy Electron Signals from Dark Matter Annihilation in the Sun. *Phys.Rev.*, D82:115012, 2010.

[101] P. D. Serpico. Astrophysical models for the origin of the positron "excess". *Astroparticle Physics*, 39:2–11, Dec 2012.

[102] Z.K. Silagadze. A New algorithm for automatic photopeak searches. *Nucl.Instrum.Meth.*, A376:451–454, 1996.

[103] Torbjorn Sjostrand, Stephen Mrenna, and Peter Z. Skands. PYTHIA 6.4 Physics and Manual. *JHEP*, 0605:026, 2006.

[104] Torbjorn Sjostrand, Stephen Mrenna, and Peter Z. Skands. A Brief Introduction to PYTHIA 8.1. *Comput.Phys.Commun.*, 178:852–867, 2008.

[105] P. Sokolsky. Final results from the high solution fly's eye (hires) experiment. *Nuclear Physics B - Proceedings Supplements*, 212–213(0):74 – 78, 2011. Proceedings of the Cosmic Ray International Seminars (CRIS 2010) 100 years of Cosmic Ray Physics: from pioneering experiments to physics in space.

[106] V. Springel, J. Wang, M. Vogelsberger, A. Ludlow, A. Jenkins, A. Helmi, J. F. Navarro, C. S. Frenk, and S. D. M. White. The Aquarius Project: the subhaloes of galactic haloes. *MNRAS*, 391:1685–1711, Dec 2008.

[107] C. Størmer. On the Trajectories of Electric Particles in the Field of a Magnetic Dipole with Applications to the Theory of Cosmic Radiation. Sixth Communication. With 17 Figures in the Text. *Astrophysica Norvegica*, 2:193, January 1937.

[108] Andrew W. Strong, Igor V. Moskalenko, and Vladimir S. Ptuskin. Cosmic-ray propagation and interactions in the Galaxy. *Ann.Rev.Nucl.Part.Sci.*, 57:285–327, 2007.

[109] D. Thompson et al. EGRET high-energy gamma-ray pulsar studies. 1: Young spin powered pulsar. *ApJ*, 436(1):229–238, 1994.

[110] S. Torii et al. High-energy electron observations by PPB-BETS flight in Antarctica. *arXiv:0809.0760*, 2008.

[111] T. Yamamoto, K. Mase, M. Takeda, N. Sakaki, and M. Teshima. Signatures of ultra-high energy cosmic ray composition from propagation of nuclei in intergalactic photon fields. *Astroparticle Physics*, 20(4):405 – 412, 2004.

[112] Hasan Yüksel, Matthew D. Kistler, and Todor Stanev. TeV Gamma Rays from Geminga and the Origin of the GeV Positron Excess. *Phys. Rev. Lett.*, 103(5):051101, 2009.

[113] G. T. Zatsepin and V. A. Kuz'min. Upper Limit of the Spectrum of Cosmic Rays. *Soviet Journal of Experimental and Theoretical Physics Letters*, 4:78, August 1966.

[114] L. Zhang and K.S. Cheng. High-energy radiation from rapidly spinning pulsars with thick outer gaps. *ApJ*, 487(1):370–379, 1997.